

Dynamics of Branched Polymers: Motion, Scattering and Rheology



Laurence George Demosthenis Hawke
Department of Applied Mathematics
University of Leeds

Submitted in accordance with the requirements for the degree of Doctor
of Philosophy

October 2013

The candidate confirms that the work submitted is his own, except where work which has formed part of jointly-authored publications has been included. The contribution of the candidate and the other authors to this work has been explicitly indicated below. The candidate confirms that appropriate credit has been given within the thesis where reference has been made to the work of others.

This copy has been supplied on the understanding that it is copyright material and that no quotation from the thesis may be published without proper acknowledgement.

© 2013 The University of Leeds and Laurence George Demosthenis
Hawke

To my mother

Details of contributions to jointly authored publications:

P. Bačová, L.G.D. Hawke, D.J. Read, and A.J. Moreno. Dynamics of branched polymers: A combined study by molecular dynamics simulations and tube theory. *Macromolecules*, 46(11):4633-4650, 2013.

I was a co-author mainly contributing to the theoretical sections of the paper. In particular, I contributed to the development of the theoretical expressions for the mean square displacement correlation functions and the writing of the first draft of the theoretical sections. P. Bačová was the lead author providing the Molecular Dynamics simulations and the first draft of the sections about the simulations. D.J. Read and A.J. Moreno provided supervision and feedback on the paper. They also engaged in discussions about the results and modified the manuscript. The work presented in this paper is reproduced in chapter 2 of my thesis.

Acknowledgements

I wish to express my sincere gratitude to my supervisor Dr. Daniel J. Read for his guidance, constant support and encouragement throughout my PhD. This thesis would not have been completed without his uncomplaining help and invaluable insights. It has been a pleasure to work with him. I would also like to thank him for giving me the opportunity to play football on Sundays which helped me to unwind research stress and maintain my weight in double digits! In addition, I would like to thank Prof. Peter D. Olmsted for fruitful discussions and for being my co-supervisor.

This PhD project was supported financially by the Marie Curie Initial Training Network DYNACOP (DYNamics of Architecturally COMplex Polymers) in the Seventh Framework (FP7) program of the European Commission (Grant Agreement No.: 214627). I consider myself a very lucky person to have been a member of the DYNACOP project and I would like to thank all the DYNACOP colleagues for the many stimulating discussions which I very much appreciated. Special thanks to Petra Bačová and Dr. Angel J. Moreno for the wonderful collaboration and their hospitality during my exchange visit at the Centro de Física de Materiales in San Sebastian. Also, special thanks to Dr. Qian Huang and Prof. Ole Hassager for introducing me to the world of experimental rheology and for their hospitality during my exchange visit at the Technical University of Denmark (DTU). I also thank them for providing me with their FSR data. I also wish to thank my fellow DYNACOP ESRs and ERs for the great time we had during conferences and workshops over the last three and a half years. I will hardly forget the good time we had at Capri, Lisbon and Crete.

Moreover, I would like to thank Dr. Michaela Zamponi and Dr. Wim Pyckhout-Hintzen from Forschungszentrum Jülich for useful discussions as regards the NSE technique and for providing me with their data. For sharing with me his knowledge about cross-slot flow experiments and modelling extensional viscosity overshoots I would like to thank Dr. David M. Hoyle from University of Durham.

Thanks go to my fellow students in the Satellite area for making the office a pleasant and friendly place to work. Some of them have also been very good friends and made my stay in Leeds enjoyable. Finally, I wish to thank my mother for her affection, tireless support and encouragement during my studies as well as my relatives and friends in Greece.

Abstract

Here, molecular models for the description of the dynamics and flow properties of melts of entangled branched polymers are developed. Their predictions are compared against data from MD simulations, NSE spectroscopy, and rheological measurements.

Following an introductory chapter, in chapters 2 and 3 the attention is drawn to local branch point motion. Expressions for the MSD correlation functions are derived. The expression for the segmental MSD is compared against MD results [1], obtained from simulations in which arm ends are motionless, i.e. standard CR events are suppressed. This comparison suggests an apparent slow relaxation of the branch point localisation at early times; here, this process is referred to as “early tube dilation” (ETD). Standard CR events are also taken into account by utilizing the dynamic dilution hypothesis [2]. It is shown that the theoretical expression matches MSD data from simulations in which chain ends are mobile provided that CR and ETD are accounted for in the model. The theoretical MSD correlation functions are also used, in the context of a dynamic version of the RPA, for the calculation of the scattering signal from the branch point; the predicted signal is compared against NSE data [3].

Chapters 4 and 5 deal with the flow properties of pom-pom melts. FSR and cross-slot flow measurements [4, 5, 6, 7], from industrial melts, indicate a viscosity overshoot in extension. In chapter 4 this phenomenon is modelled by introducing the overshoot model, a variant of the pom-pom model of McLeish and Larson [8]. Following the approach of Inkson et al. [9], a multimode version of the overshoot model is employed to fit the FSR data for the industrial resin DOW150R [6, 7]. In chapter 5, CR events are incorporated. They are modelled by means of Rouse-like hops in common with Refs. [10, 11, 12, 13]. In analogy with Refs. [14, 15], the physical picture of thin and fat tubes is adopted in the description of the dynamics of the system. The model predicts strain hardening (thinning) at extension (shear) during start up of the flow. The maximum stretch, however, becomes dependent on flow-rate.

Contents

1	Introduction	1
1.1	Overview	1
1.2	Rheology	5
1.2.1	The stress tensor	5
1.2.2	Deformation tensors	6
1.2.3	Solids, liquids and viscoelasticity	10
1.2.4	Linear viscoelasticity	12
1.2.5	Non-linear viscoelasticity	16
1.2.6	Uniaxial Extensional Rheometers	17
1.3	Scattering	19
1.3.1	The Neutron Spin Echo Technique	21
1.4	Molecular Models: linear chains	26
1.4.1	Gaussian chains	27
1.4.2	A simple constitutive equation: The dumbbell model	28
1.4.3	Dynamics of unentangled linear polymers: the Rouse model	29
1.4.4	Dynamics of entangled polymers	34
1.4.5	Other relaxation mechanisms	39
1.5	Molecular Models: branched polymers	44

1.5.1	Relaxation in Star polymers	44
1.5.2	The pom-pom molecule	46
1.6	Molecular Dynamics	54
1.7	Summary and outline of the thesis	58
2	Dynamics of star polymers: branch point motion	61
2.1	Introduction	61
2.2	Dynamics in the unentangled regime	62
2.2.1	The Rouse model for symmetric polymer stars	62
2.2.2	Results for the MSD correlation functions	67
2.2.3	The correlation function $\psi_\ell^R(t)$	69
2.3	Dynamics in the entangled regime	72
2.3.1	Localising springs	72
2.3.2	Results for the MSD correlation functions	76
2.3.3	Comparison with the Vilgis and Boué expressions	79
2.4	Comparison with MD simulations	80
2.4.1	Simulations with fixed chain ends	80
2.4.2	Simulations with free chain ends	85
2.5	Conclusions	91
3	Description of NSE data using tube theory and the RPA	93
3.1	Introduction	93
3.2	Random Phase Approximation (RPA)	98
3.2.1	A homopolymer melt of Gaussian (ideal) chains	98
3.2.2	A copolymer melt with two components	99
3.2.3	Structure Factors for Copolymers of Arbitrary Architecture	102

3.2.4	Scattering behaviour at equilibrium: static RPA	106
3.3	Dynamic RPA: theory	111
3.3.1	Applying the RPA to obtain $\langle \rho_{\mathbf{q}}^H \rangle_{\rho}$	113
3.3.2	RPA to obtain $\overline{\langle \varphi_{-\mathbf{q}}^H \rangle_{\varphi} \langle \rho_{\mathbf{q}}^H \rangle_{\rho,0}}$ and $\overline{\langle \varphi_{-\mathbf{q}}^H \rangle_{\varphi} \langle \rho_{\mathbf{q}}^D \rangle_{\rho,0}}$	115
3.3.3	Comparison with NSE data: the melt of symmetric stars	117
3.4	Comparison with MD	124
3.5	Conclusions and future work	127
4	Modifying the pom-pom model for extensional viscosity overshoots	131
4.1	Introduction	131
4.2	The overshoot model	136
4.2.1	The physical concept	136
4.2.2	Constitutive equation	138
4.3	Predictions of the model: single mode	145
4.3.1	The <i>relaxation case</i> : testing the three versions of the evolutionary equation of the backbone orientation	145
4.3.2	<i>Normal case</i> and <i>relaxation case</i> : comparing options B and C	147
4.3.3	Option C: varying the values of the model parameters	150
4.3.4	A rough guide for fitting data with the overshoot model	157
4.4	Predictions of the model: multimode version	158
4.4.1	The full model	158
4.4.2	Minimal model	160
4.4.3	Comments on the pom-pom spectra	165
4.5	Conclusions and future work	166

5	Constraint Release events in a pom-pom melt	171
5.1	A pom-pom molecule with constraint release under shear and uniaxial extensional flows	171
5.1.1	An alternative model for the pom-pom molecule	172
5.1.2	A simple CCR rate for the pom-pom backbone: the 1CR model	175
5.1.3	Modeling two CR rates in a pom-pom melt: the 2CR model	178
5.2	Conclusions and future work	186
6	Concluding Remarks and future work	189
6.1	Local branch point motion in branched polymers	189
6.2	Constitutive modelling of industrial complexity melts	191
	Appendix	193
A	Unentangled stars.	193
A.1	‘Diagonal’ terms which contain $\Psi_{p'}^c \Psi_p^c$ and $\Psi_{q'}^{s_i} \Psi_q^{s_i}$ and ‘non diagonal’ terms which contain $\Psi_{q'}^{s_i} \Psi_p^c$ and $\Psi_{q'}^{s_i} \Psi_q^{s_j}$	193
A.2	Mean square displacement correlation functions.	195
B	Entangled stars: Mean square displacement correlation functions.	198
C	Tube survival probability from the simulations.	201
C.1	The correlation function $\Psi_{s_\ell}^{MD}(t)$ for the Cayley tree.	201
C.2	Relaxation spectra and the fit of $\psi(t)$ to KWW functions.	203
D	Numerical solution for the 1CR and 2CR models	205
E	Nomenclature	208
	Bibliography	217

List of figures

- 1.1 Examples of polymer architectures. Upper: The simplest possible topology of a linear chain (left) and the structure of a typical complex branched macromolecule encountered in industrial applications (right). Bottom: Some well defined branched architectures synthesised by living anionic polymerisation. 2
- 1.2 Upper: A polymer melt resembles a plate of cooked spaghetti. Chain motion is restricted by the mutual entanglements. Bottom: Simple shear flow produced between two parallel plates (left). Uniaxial extensional flow produced between two plates which separate at an exponential rate (right). Elements of the polymeric fluid specimen (red colour) are separated exponentially in time in the direction of stretch (x-direction). . . 3
- 1.3 Left: A typical film blowing line. During the processing and before solidification, which occurs at the so-called freeze line height, the polymer melt is subjected to shear and extensional deformations. Right: As molten polymer exits the die is stretched in the machine direction (MD), and in the transverse direction (TD). In the normal direction (ND) contraction occurs. The TD is perpendicular to the plane of the page. 4
- 1.4 The definition of shear and extensional strain in terms of ratios of measurements before and after the deformation. 9
- 1.5 Different responses of Newtonian liquids (viscous), solids (elastic) and polymeric fluids (viscoelastic) to a step shear strain (left) and to a steady shear flow (right). 11

- 1.6 G'/G_0 (black solid line) and G''/G_0 (black dashed line) vs the dimensionless frequency $\omega\tau$ for a single Maxwell model. The respective quantities for a Newtonian liquid and an elastic solid are also depicted as red and blue lines, respectively. The low and high frequency limits of G' and G'' are also shown as labels. 14
- 1.7 Comparison of G' and G'' for monodisperse linear and star polyisoprene melts. Figure from Ref. [2]. 15
- 1.8 Upper: Larmor precession for a neutron spin, \mathbf{n}_s , placed at an angle θ to a magnetic field \mathbf{B} . The direction in which \mathbf{n}_s rotates is shown by the red arrow. ϕ_L is the precession angle. Bottom: A NSE spectrometer. The events at “regions” 1-11 are described in the text. 22
- 1.9 Upper: $\langle \mathbf{u}_\ell(0) \cdot \mathbf{R}(t) \rangle$ vs \tilde{t}_R for various segments along the chain; $\xi = 0, 0.15, 0.30$ correspond to magenta, green, and blue solid lines, respectively; dashed lines of the same colour refer to symmetric segments. Red line $\xi = 0.5$. The black line shows $\langle \mathbf{R}(t) \cdot \mathbf{R}(0) \rangle$. Bottom: Schematic illustration of the conformational relaxation of the chain at early and late times (left and right side respectively). 32
- 1.10 Left: The entanglements from the matrix chains to the test chain are depicted as black dots. The blue line represents the conformation of the test chain for length scales smaller than a . Right: The tube-like region that the constraints form to the test chain. The primitive path is shown in both sides as a bold black line. 35
- 1.11 Upper: Segmental MSD of the actual chain vs time, as predicted by the tube model (CLF is included). The plots suggests the existence of four distinct regimes. Bottom: Schematic illustration of the chain motion at these four distinct regimes. 36

- 1.12 DE tube theory in step shear. Left: $\frac{G(t)}{G_N^0}$ against $\frac{t}{\tau_{b1}}$. The solid (dashed) line refers to chains of entanglement length Z_1 ($\frac{Z_2}{Z_1} = 2$) and reptation time τ_{b1} ($\frac{\tau_{b2}}{\tau_{b1}} = 8$). Up to $t \approx \tau_e$, $\frac{G(t)}{G_N^0}$ displays Rouse behaviour. Then, it establishes a plateau; the width of the plateau region increases with increasing chain length. Right: $\frac{G(t,\gamma)}{G_N^0}$ against $\frac{t}{\tau_b}$ for $\frac{\tau_b}{\tau_R} = 10^2$. Stress relaxation at high strains ($\gamma = 5, 20$) is a two stage process; the abrupt initial decay (final decline) is attributed to stretch (orientation) relaxation. 38
- 1.13 Thermal CR events in a bi-disperse melt of short (red colour) and long (green colour) linear chains. A given long chain can make local hops and explore the space that was previously occupied by the much faster reptating short chains. 42
- 1.14 Hierarchical relaxation of a pom-pom molecule. Upper left: The initial conformation of the chain immediately after an imposed strain. Upper right: At a later time, $t \ll \tau_a$, branch points and backbone segments are essentially pinned; only sections of the arms close to the arm tips renew their conformation. Bottom left: At times $t \gtrsim \tau_a$, each time an arm fully retracts, the branch points make diffusive hops. Bottom right: At much later times, $t \gg \tau_a$, backbones relax via renormalised reptation in a dilated tube. 48
- 1.15 The predictions of the pom-pom model in continuous shear (dashed lines) and uniaxial extension (solid lines) for three different rates; $\dot{\gamma}, \dot{\epsilon} = 0.01s^{-1}$ (black), $\dot{\gamma}, \dot{\epsilon} = 1s^{-1}$ (red), and $\dot{\gamma}, \dot{\epsilon} = 10s^{-1}$ (blue). The model predicts transient extensional hardening and transient shear thinning. $G_0 = 1Pa, \tau_b = 5s, \tau_b/\tau_s = 4, q = 10$ and $\phi_b = 1$ 50

- 1.16 Segmental MSD, as obtained from MD simulations on entangled three arm symmetric stars (open circles) and on entangled linear chains (lines), for various entanglement segments along the chains; for the correspondence between colours and entanglement segments see the legend. Black and red open symbols refer to the MSD of the simulation branch point, as calculated from simulations in which chain ends were free and fixed, respectively. All data are provided by P. Bačová and Dr. A. J. Moreno. 56
- 2.1 Schematic illustration of an unentangled star. The position vector $\mathbf{r} = \mathbf{r}_{\alpha,\ell,t}$ of the ℓ th segment in arm α at time t is shown. We label segments as $\ell = 0, 1, \dots, N_a$ starting from the branch point where $\ell = 0$ and ending at the arm tip where $\ell = N_a$ 63
- 2.2 The first four modes (waves) of a cosine (black solid lines) and a sine (blue solid lines) eigenmode traveling along an arm of a symmetric star. The chain tension related to these modes is also shown with dashed lines of respective colour. 65
- 2.3 Segmental MSD normalised by $N_a b^2 \sqrt{t_{R_a}}$, as predicted by the model, for an unentangled three arm polymer star. Different colours correspond to different positions along the arm; $\xi = \ell/N_a = 0.001$ (blue), $\xi = 0.005$ (green), and $\xi = 0.01$ (red). The grey line refers to the branch point while the black line refers to a linear chain. 69
- 2.4 Tangent correlation function (eq. 2.13) for unentangled stars. The solid lines refer to ‘half-correlation’ ($B' = C' = -1/2$) while the dashed lines to ‘full-correlation’ ($B' = C' = -1$). Different colours correspond to different Rouse segments along the arm: $\xi = 0.15$ (black), 0.3 (magenta), 0.5 (red), 0.7 (green), and 0.85 (blue). 71

- 2.5 Left: Schematic illustration of the tube model. Entanglements are modeled by confining the actual chain in a tube-like region. The black line represents the primitive path. Right: An alternative description of the entanglements. In this case entanglements are modeled by localising springs (constraints). The black line shows the mean path which can be thought of as the analogous of the primitive path of the tube model. 72
- 2.6 Left: Segmental MSD in the entangled regime (i.e. $\langle(\mathbf{r}_{\alpha,s,t} - \mathbf{r}_{\alpha,s,t'})^2\rangle$ of table 2.2), normalised by a^2 , for three different segments along an arm of a star with 3 arms: $s = 0.05$ (blue), $s = 0.25$ (green), and $s = 1$ (red). The grey and black lines refer to unentangled chains; grey - branch point; black - a segment of a linear chain. Right: The same quantities as in the left panel, together with the segmental MSD in the unentangled regime (i.e. $\langle(\mathbf{r}_{\alpha,\ell,t} - \mathbf{r}_{\alpha,\ell,t'})^2\rangle$ of table 2.1), represented as solid curves (colour codes correspond to same values of s). In this case the MSD has been normalised by $a^2\sqrt{t_e}$ 78
- 2.7 MD results for the MSD of the “simulation branch point” of the star (red circles) and of the central “simulation branch point” of the Cayley tree (blue circles), with their respective error bars. Filled triangles refer to the the average MSD up to $t \sim 10^6\tau_0^{MD}$. The grey line refers to the theoretical MSD without ETD. The dashed grey line shows an alternative fit that describes well the Rouse and the plateau regimes but fails to describe the crossover between these two regimes. The black line shows the theoretical prediction when ETD is accounted for. MD data are provided by P. Bačová and Dr. A. J. Moreno [1]. 81
- 2.8 For a selected star in the simulations with fixed ends, trajectory of the branch point (orange dots) and mean paths of the three arms (black, blue and green). A deep fluctuation of the branch point along the green arm is clearly observed. The figure is provided by P. Bačová and Dr. A. J. Moreno [1]. 83

- 2.9 Due to CR and/or early tube dilation the fast Rouse modes (transverse motion about the mean path) evolve within a tube that smoothly dilates with time. Motion along the mean path is supposed quenched. Black solid lines show the undilated tube. Black dashed lines and red lines represent the dilated tube at different timescales. 86
- 2.10 The correlator $\Psi_{s_\ell}^{MD}(t)$ for three different segments s_ℓ along the arm of the star (squares) and the long arm of the Cayley tree (circles). Some KWW fitting functions are shown by lines. The figure is provided by P. Bačová and Dr. A. J. Moreno [1]. 88
- 2.11 Tube survival probability of the star and of the Cayley tree, as computed from the simulations. The computation has been done by P. Bačová and Dr. A. J. Moreno [1]. 89
- 2.12 MSD of the branch point of the stars (left) and Cayley trees (right) with free ends. MD data are shown as open black circles. Their error is shown with black bars. The cyan (magenta) line refers to the theoretical MSD using $\alpha_d = 1$ ($\alpha_d = 4/3$) and accounts for CR and ETD. The MD data for fixed arm ends (filled circles with their error bars) are also included. The MD data are provided by P. Bačová and Dr. A. J. Moreno [1]. 91
- 3.1 Schematic drawing of the studied systems. Left: A melt of star polymers with a short labelling (protonated monomers) near the branch point (blue colour). The rest of the molecule is deuterated (red colour). Right: Centre-labelled linear chains embedded in a matrix of fully deuterated chains. 94
- 3.2 Left: A melt prior to incompressibility. Monomer density is not constant at all points in space. Thus different chains highly overlap. Right: A melt after enforcing incompressibility. Monomer density must be constant everywhere in the melt and thus configurations that do not satisfy this criterion are eliminated. In this case, chain overlap is not as high as before the introduction of incompressibility. 101

- 3.3 Left: Definition of a block. Here, the blue colour corresponds to protonated species H while the black colour to deuterated species D . Right: Showing the variables that relate to two given blocks (labelled 1 and 2) in a chain. The blocks 1 and 2 are separated by the blocks a, b, c, etc. \mathbf{h}_b is the end-to-end vector of block b (green arrow). 103
- 3.4 Splitting the chains into blocks. Dashed (solid) lines refer to the H (D) species. The labels ($0, Z_H, Z_D$, etc.) show how the chain length is expressed in terms of tube coordinates. Left: The star copolymer. Here, the labels 1 to 6 count blocks. Right: The mixture of linear chains. 105
- 3.5 $n_c^{-1}S^{tot}(q)$ as a function of $|\mathbf{q}|$ for the melt of copolymer stars. The black, red, and blue lines refer to stars with $f = 3, f = 4$, and $f = 6$, respectively. The same quantity for the blend of linear chains is plotted for comparison with a green line. The inset shows the finite value of scattering at zero $|\mathbf{q}|$ for the mixture of linear chains. Open symbols in this figure (also in Figs. 3.6 and 3.7) correspond to the values of the plotted quantities at the available experimental $|\mathbf{q}|$ values. 108
- 3.6 Left: The static scattering function in terms of the normalised wavevector $Q_a = |\mathbf{q}|R_{ga}$ for the star copolymer melts. Solid lines: EV interactions are included. Dashed lines: EV interactions are ignored. Different colours correspond to different number of arms in exactly the same way as in Fig. 3.5. Right: S_0^{HH}/S_{cor} as a function $|\mathbf{q}|$ for the star copolymers and the mixture of linear chains (green line). 109
- 3.7 The ratio I_{coh}/I_{inc} as a function of $|\mathbf{q}|$ for both examined systems. The correspondence between colour and number of arms is the same as in Figs. 3.5 and 3.6 (see also the label). The green colour refers to the blend of linear chains. The open symbols show the values of I_{coh}/I_{inc} at the experimental values of $|\mathbf{q}|$ 110

- 3.8 Schematic representation of the chain configurations at time $t' = 0$ (black colour) and at time $t' = t$ (red colour). Between these two stages the quenched variables are the localising springs (the “tubes”) and slow Rouse modes. The annealed variables are fast Rouse modes and so the chain configurations at time t have locally changed. 112
- 3.9 Theoretical (lines) and experimental (symbols) $P(q, t)$, for the PE star melt, at several $|\mathbf{q}|$. Black, red, blue, and green colours refer to $|\mathbf{q}| = 0.5\text{nm}^{-1}, 0.77\text{nm}^{-1}, 0.96\text{nm}^{-1}$, and 1.15nm^{-1} , respectively. Left: $P(q, t)$ in the presence (solid lines) and absence (dotted lines) of EV interactions (correlations) when both the coherent and incoherent signals are included. Right: $P(q, t)$ with and without the incoherent signal (solid and dotted lines, respectively), in the presence of correlations. The NSE data [3] are provided by Dr. M. Zamponi. 120
- 3.10 Theoretical $P(q, t)$ using the expressions of table 2.2 for the MSD correlation functions (solid lines). The same quantity using the expressions of Vilgis and Boué for the MSD functions (dotted lines). EV interactions (correlations) are disregarded. Both the coherent and incoherent signals are accounted for. NSE data are represented by filled circles. The correspondence between colours and \mathbf{q} values is the same as in Fig. 3.9; a, b, W_R same as for Fig. 3.9. The NSE data [3] are provided by Dr. M. Zamponi. 121
- 3.11 Predicted $P(q, t)$ when early tube dilation (ETD) is included (thick solid lines). The dotted and thin solid lines refer to $g(t) = 1$ (neglect of ETD) and are obtained using $a = 3.5\text{nm}$ and $a = 4.04\text{nm}$, respectively. NSE data, with their error bars, are show with open squares. The correspondence between colours and \mathbf{q} values is the same as in Figs. 3.9 and 3.10. The NSE data [3] are provided by Dr. M. Zamponi. 123

- 3.12 The normalised incoherent scattering function, as obtain from the MD simulations (open symbols with their error bars) and the theoretical expressions (lines) for several $|\mathbf{q}|$ values. Thick (thin) lines refer to $\alpha_d = 1$ ($\alpha_d = 4/3$). The theoretical predictions account for ETD and CR. Left: For $g(t)$ we use eq 2.31. Right: for $g(t)$ we use $\tilde{g}(t)$ (see text). The MD data are provided by P. Bačová and Dr. A. J. Moreno. 125
- 3.13 The normalised coherent scattering function, as obtain from the MD simulations (open symbols) and our theoretical expressions (lines) for several $|\mathbf{q}|$ values. Thick (thin) lines refer to $\alpha_d = 1$ ($\alpha_d = 4/3$). The theoretical predictions account for ETD and CR. For the correspondence between colours and $|\mathbf{q}|$ values see the text. The MD data are provided by P. Bačová and Dr. A. J. Moreno. 127
- 4.1 Left: A long chain branched (LCB) polymer. Right: A LCB polymer melt can be modelled as a series of individual pom-pom molecules. The inner parts of the LCB chain stretch more than the outer ones. Therefore the pom-pom molecules that represent the inner sections are decorated with higher q values. 133
- 4.2 FSR measurements for the industrial sample DOW150R. Left: Uniaxial extensional viscosity [6], under steady flow, for several extensional rates. Right: The same quantity at $\dot{\epsilon} = 0.1\text{s}^{-1}$ [7]; black and blue symbols refer to flow cessation before the overshoot (**BO**) and after the overshoot (**AO**), respectively. The data are provided by Dr. Qian Huang and Prof. Ole Hassager. 134
- 4.3 Up: A given backbone, prior to branch point withdrawal, entangles with both blue and green surrounding chains. The flow tends to stretch the backbone beyond the maximum stretch and so $\lambda > q$. Bottom: Branch point withdrawal occurs since the maximum stretch, $\lambda = q$, should be maintained. This process is instantaneous on the flow timescale and hence some entanglements (the blue ones) are stripped off. Here, the backbone only entangles with the green chains and so it is confined within a dilated tube. 137

4.4 Left: The backbone tube at three different times during entanglement stripping. All tubes have undergone the same deformation history and identical fractional amount of chain retraction and thus $S_1 = S_2 = S_3$, $\lambda_1 = \lambda_2 = \lambda_3$. Right: The backbone tube at three different times during entanglement reformation. In this case “thinner” tubes equilibrate within “fatter” tubes, i.e. $S_1 \neq S_2 \neq S_3$, $\lambda_1 \neq \lambda_2 \neq \lambda_3$. The blue and black crosses represent the entanglements that form the blue and black tube, respectively. 139

4.5 Uniaxial extensional viscosity vs time for the *relaxation case* (RC). The black, red and blue symbols refer to options A, B and C, respectively. The strain rate is $\dot{\epsilon} = 0.1s^{-1}$. The flow is ceased at $t = t_{cf} \simeq 45s$. $G_0 = 72.88Pa$, $\tau_{b0}/\tau_{s0} = 2$, $q = 12$, $\Psi_w = 1$ and $h = 0$. For all three options entanglement stripping is quenched since $\Psi_w = 1$ 146

4.6 The corresponding orientation alignment, $S_{xx} - S_{yy}$ (left), and stretch, λ (right), of the viscosity curves of Fig. 4.5. The flow is ceased at $t = t_{cf} \simeq 45s$. The correspondence between colours and options in the same as in Fig. 4.5. 146

4.7 Uniaxial extensional viscosity vs time for options B and C (red and blue colours, respectively). Left: the *normal case*. Right: the *relaxation case*. In the right panel, open symbols refer to the **AO** case while lines refer to the **BO** case. The mode is parameterised by $G_0 = 72.88Pa$, $\tau_{b0}/\tau_{s0} = 1.5$, $q = 12$, $\Psi_w = 0.5$, $h = 1$ 148

4.8 The corresponding Ψ , τ_s , $S_{xx} - S_{yy}$ and λ of the viscosity curves of the right panel of Fig. 4.7 (i.e. for the *relaxation case*). 148

4.9 Transient uniaxial extensional viscosity vs time of the reference modes with varying τ_{b0}/τ_{s0} (see labels). Panels **a** and **c**: *normal case* (NC) for the slow mode and the fast mode, respectively. Panels **b** and **d**: *relaxation case* (NC) for the slow mode and the fast mode, respectively. For the parameterisation of the reference modes see the text. 151

4.10 Same as Fig. 4.9 with varying q (see labels). 152

- 4.11 Same as Figs. 4.9 and 4.10 with varying Ψ_w (see labels). 152
- 4.12 Same as Figs. 4.9- 4.11 with varying h (see labels). 153
- 4.13 Relaxation behaviour of the fast and slow modes. Panels **a**, **b**, **c** and **d** depict Ψ , τ_s , $S_{xx} - S_{yy}$ and λ , respectively. The results for the fast (slow) mode are shown with green (red) colour and are obtained using $\tau_{b0}/\tau_{s0} = 1.5(1.5)$, $q = 12(8)$, $\Psi_w = 0.2(0.2)$ and $h = 1(1)$. Symbols correspond to the **AO** case while lines to the **BO** case. 156
- 4.14 Comparison between the predictions of the full version of the overshoot model (lines) and the experimental data (symbols) for the DOW150R sample. Upper panel: Using SET I of table 4.2. Bottom panel: Using SET II of table 4.2. The plots on the left (right) side refer to the *normal case* (*relaxation case*). For the correspondence between curves and represented quantities in the *relaxation case* see the labels. The data are provided by Dr. Qian Huang and Prof. Ole Hassager. 159
- 4.15 A comparison between the full and the minimal model for the *normal case*, and for the slowest mode of the SET II spectrum of table 4.2. The full (minimal) model is represented by magenta (black) lines. Panel **a** presents the uniaxial extensional viscosity. Panels **b**, **c** and **d** show Ψ , λ and τ_b , respectively. Here, $\tau_b = \tau_s$ 161
- 4.16 Same as Fig. 4.15 for the *relaxation case*. Symbols correspond to the **AO** case while lines to the **BO** case. 162
- 4.17 Same as Fig. 4.14 using the minimal model and the parameterisation of table 4.3. The data are provided by Dr. Qian Huang and Prof. Ole Hassager. 163
- 5.1 The 1CR model using $q = 5$, $\tau_b = 100\text{s}$, and $\tau_s = 1\text{s}$. Top panel: Shear (left) and elongational (right) viscosities. Bottom panel: The corresponding values of λ . The correspondence between rates and colours is: 0.01s^{-1} (black), 0.1s^{-1} (red), 0.5s^{-1} (blue), 1s^{-1} (magenta), 2s^{-1} (dark yellow), and 5s^{-1} (dark cyan). For the shear case, the dotted lines correspond to the model predictions when CCR events are ignored. 176

5.2 The 2CR model under uniaxial extension. Top: Viscosity vs time. Bottom: λ_{thin} and λ_{fat} (left and right side, respectively). The correspondence between colours and rates at the lowest six rates is the same as in Fig. 5.1. The highest three rates are 10s^{-1} , 50s^{-1} , 100s^{-1} and are represented by wine, orange and grey colours, respectively. At all panels the solid (dotted) lines refer to $\tilde{\tau} = \tau_{CR}$ ($\tilde{\tau} = \tau_{eff}$). For the parameterisation see the text. 185

5.3 Same as Fig. 5.2 but for continuous shear flow. 186

C.1 Upper: Schematic representation of the correlations used for $\Psi_{s_\ell}^{MD}(t)$ of the Cayley tree. The red colour highlights the section of the chain in which $\mathbf{u}_{\alpha,s_\ell,0}$ is embedded. Panels I, II and III refer to the respective cases discussed in the text. The dashed black arrows in panel II indicate the position of the inner and outer sections of the long arm and the position of the side arm on the molecule. Different sections are denoted by $\alpha, \beta, \gamma, \delta$, etc. Moreover, numbers labelling particular sections are the prefactors used in the analogous correlation function of eq 2.33 for the Cayley tree. Bottom: Schematic representation of the correlations used for $\Psi_{s_\ell}^{MD}(t)$ of the three arm symmetric star. In this case α, β, γ refer to different arms. The numbers labelling the arms β and γ are the prefactors B', C' used in eq 2.33. 202

List of tables

1.1	Flow tensors in simple flows	8
1.2	Bound coherent and incoherent scattering lengths	21
2.1	Theoretical predictions for the MSD of unentangled stars	68
2.2	MSD for entangled stars	77
3.1	Molecular characteristics of the chains in the two studied systems	95
3.2	S_0^{HH} , S_0^{DD} and S_0^{HD} single chain correlation functions	107
4.1	Overshoot model equation set.	144
4.2	Parameterisation for the full version of the model	164
4.3	Parameterisation for the minimal model	165
1	The relaxation spectrum of the 888 star as obtained from the simulations.	203
2	The relaxation spectrum of the Cayley tree as obtained from the simulations.	204
3	KWW parameters for the functions $\Xi_\alpha(t)$, $\Xi_\beta(t)$, $\Xi_\gamma(t)$ of the different sections of the Cayley tree.	204

Chapter 1

Introduction

1.1 Overview

Polymer chains are large macromolecules. Their structure is composed of multiple repeat units, known as monomers, which are connected by covalent chemical bonds. The number of monomers, N , is referred to as the degree of polymerisation of the chain and varies substantially between different polymers. On the one hand chemically synthesized polymers like polyethylene (PE) and polystyrene (PS) contain typically about $10^2 - 10^4$ monomers. On the other hand, natural polymers (biopolymers), such as proteins and nucleic acids, usually have larger degree of polymerisation, that is, N may be as high as 10^9 . The degree of polymerisation is proportional to the molecular weight, M_w , of the polymer chain; $M_w = M_{w_0}N$ where M_{w_0} is the molecular weight of a monomer.

Figure 1.1 illustrates schematically various topologies of chemically synthesized chains. The upper panel shows the two extremes of topological complexity; a linear chain (left) and a highly and arbitrary branched chain (right). Between these two extremes lie polymer chains with a star-like, a Cayley tree-like and a pom-pom-like architecture (pom-poms with only two arms per branch point are referred to as H-polymers). These structures are schematically illustrated in the bottom panel of Fig. 1.1. The synthesis of these well defined branched architectures has been possible due to the recent developments in living anionic polymerisation techniques [16, 17, 18, 19].

The chemically synthesized polymers are widely used and in a variety of applications. For example they are used as the matrix material of composites in aerospace and

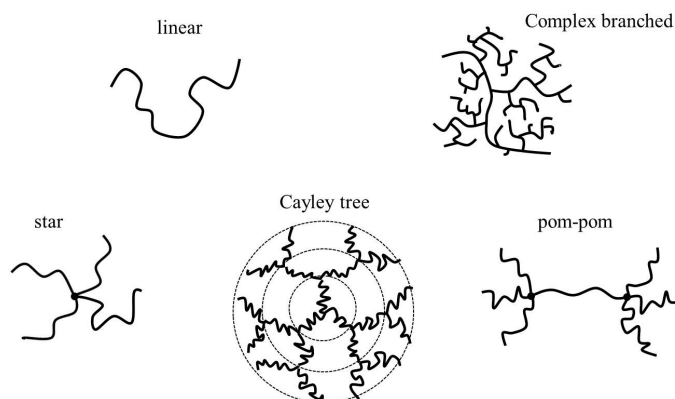


Figure 1.1: Examples of polymer architectures. Upper: The simplest possible topology of a linear chain (left) and the structure of a typical complex branched macromolecule encountered in industrial applications (right). Bottom: Some well defined branched architectures synthesised by living anionic polymerisation.

automobile applications due to their light weight compared to metals [20, 21]. Furthermore, they are extensively used as films for various packaging applications [22, 23]. One of the most common methods of manufacturing these polymeric films is the so-called film blowing process [24]. During the manufacturing of such products molten polymer (polymer melt) is subjected to simple flows, like shear and extension, or/and complex flows which are a combination of shear and extensional deformation (flow).

The motion of a single polymer chain in a polymer melt, which approximately resembles a plate of cooked spaghetti, is significantly restricted by topological constraints, i.e. the impediments to motion created by the inability of the chain to pass through its neighbouring chains [2, 25, 26, 27, 28, 29]. These topological constraints are known as entanglements. The upper panel of Fig. 1.2 shows schematically the mutual entanglements between a given chain (blue) and the rest of the chains in the melt. The presence of entanglements affects macroscopic properties of the melt like its viscosity, which can be thought of as its resistance to an imposed flow. A greater number of entanglements leads to a higher viscosity. In analogy, the difficulty of extracting (pulling) a single strand from the rest of the spaghetti increases when the strands are more entangled.

The bottom panel of Fig. 1.2 depicts schematically a shear flow (left) and an extensional flow (right). In more details, polymeric fluid is subjected to simple shear flow when it is

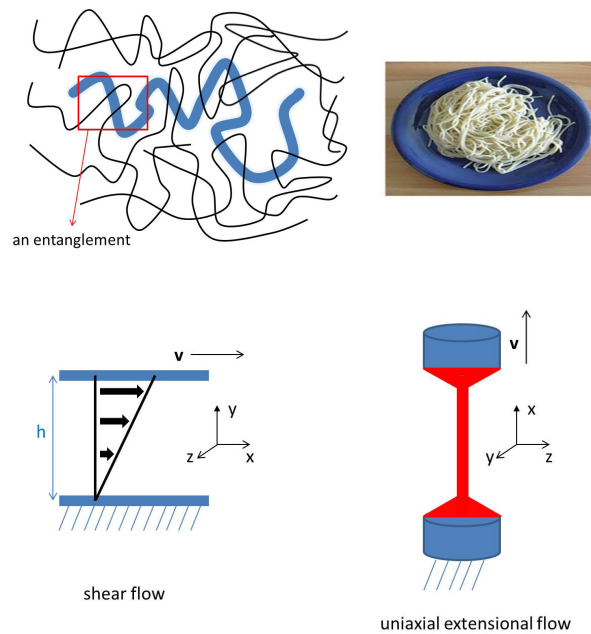


Figure 1.2: Upper: A polymer melt resembles a plate of cooked spaghetti. Chain motion is restricted by the mutual entanglements. Bottom: Simple shear flow produced between two parallel plates (left). Uniaxial extensional flow produced between two plates which separate at an exponential rate (right). Elements of the polymeric fluid specimen (red colour) are separated exponentially in time in the direction of stretch (x -direction).

placed between two plates from which one is moving at speed V whereas the other one remains still [30, 31, 32, 33]. In this type of deformation the material is sheared in the x direction while a velocity gradient exists in the y -direction. The relative distance between two fluid elements in different shear planes is linear in time. Extensional flow can be achieved, for instance, in a Filament Stretching Rheometer (FSR) [4, 5, 6, 7, 34] in which the material is stretched between two plates which move apart at an exponential rate; this particular deformation mode is known as uniaxial extension. In uniaxial extension the dimension of the polymeric fluid specimen in the stretching direction (x direction in our notation) increases whereas the dimensions in the other two directions (y and z) decrease uniformly. Two other typical deformation modes are planar extension and biaxial extension. Planar extension is similar to uniaxial extension, except that the dimension of the sample is held constant in one direction. In biaxial extension, in two directions the fluid elements are stretched, while contraction occurs in the third direction.

Biaxial extension is efficient in producing films. Thereby, it is one of the dominant deformation modes in the film blowing process. The left panel of Fig. 1.3 shows a typical

film blowing line. In more details, air is blown on the polymer melt as it exits the die of the extruder and the pressure inflates the extruded melt into a bubble, that is, the polymer melt is elongated in the so-called transverse direction which is perpendicular to the so-called machine direction [24] (c.f. right panel of Fig. 1.3). In addition, the bubble is pulled upwards from the die, i.e. in the machine direction, by a pair of nip rolls. As a result the extruded melt is subjected to biaxial extension [24]. However, some studies [35] indicate that elongation in the transverse direction starts later and so immediately after the die exit the extruded melt is elongated only in the machine direction. During the time the melt is in the die it is subjected to shear stresses.

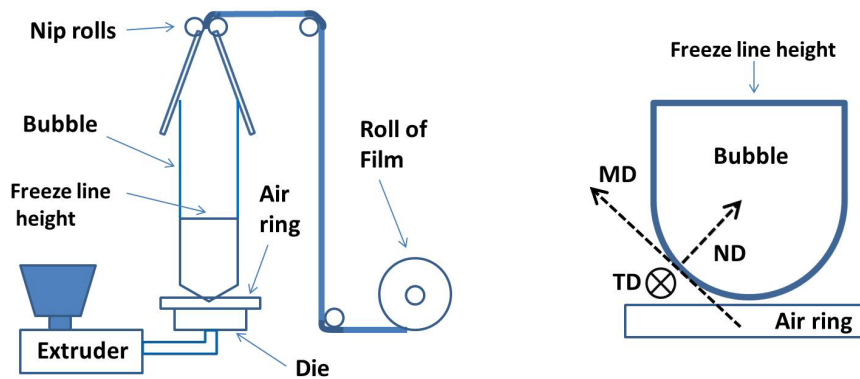


Figure 1.3: Left: A typical film blowing line. During the processing and before solidification, which occurs at the so-called freeze line height, the polymer melt is subjected to shear and extensional deformations. Right: As molten polymer exits the die is stretched in the machine direction (MD), and in the transverse direction (TD). In the normal direction (ND) contraction occurs. The TD is perpendicular to the plane of the page.

The properties of the final product and the ease of processing depend strongly on phenomena like melt fracture and die swell [24, 36, 37]. The former is generally defined as surface roughness of the extrudate while the latter is the expansion of the polymer melt at the die exit. These phenomena depend strongly on the dynamics of the polymer chains in their melt state and on the response of the molten polymer to the applied deformations.

From the above it becomes apparent that it is of practical interest to understand and to be able to predict the flow behaviour (rheology) of polymer melts. Furthermore, it is important to acquire the knowledge to tackle questions such as: Do polymer

melts of different architecture exhibit a different flow behaviour? If they do, which architecture possesses the desirable flow properties. The development of models, based on the molecular scale physics of polymer chains, that describe the dynamics and the flow behaviour of polymer melts plays a key role in answering such questions. The development of such models, for branched architectures, is the main goal of this thesis.

The ultimate goal is to reverse the industrial design arrow, that is, identify polymeric materials with the desirable flow properties using molecular models and flow simulations (in both simple and complex geometries) rather than discovering them by empiricism. Advanced rheological and scattering techniques, Molecular Dynamics (MD) simulations and modelled chemistry play also a crucial part towards the achievement of this overall goal. Within the DYNACOP (DYNamics of Architecturally Complex Polymers) project, in which the author had the opportunity to participate, all the aforementioned methods and techniques were employed in order to synthesise well defined branched polymers and study thoroughly their dynamics and flow properties.

1.2 Rheology

Rheology is the study of deformation of matter. From the experimental point of view the response (stress) of a material to several deformation modes can be measured. On the other hand, the aim of molecular rheology is to construct molecular models that relate the deformation history with the present state of stress. This section presents established knowledge, much of which is covered in Refs. [2, 26, 27, 29, 30, 31, 38]

1.2.1 The stress tensor

Either in a solution or a melt polymer chains carry forces. These forces can be classified into two types: Molecular forces, which arise from intra-chain and inter-chain interactions between the monomers, and body forces, which are external forces acting on the monomers due to, for example, electromagnetic field or gravity. In the case of a polymer solution one should also include, in the molecular forces, the collisions between the monomers of the chain and the much smaller and faster solvent molecules. Nevertheless, in polymer melts or concentrated solutions, the dominant contribution from

the molecular forces arises to a good approximation from the intra-chain interactions particularly from the entropic spring forces acting between neighbouring monomers (see section 1.4.2 below).

Irrespective of their origin, the forces carried by the polymer chains contribute to stresses. These stresses are represented by the matrix elements of the stress tensor $\boldsymbol{\sigma}$. In particular, $\sigma_{\mu\nu}$ denotes the ν component of the total force per unit area across a plane whose normal is in the μ direction. In other words, $\sigma_{\mu\nu}$ is the ν component of the force exerted by the monomers above the plane on the monomers under the plane, divided by the area of the plane. The non-diagonal components of $\boldsymbol{\sigma}$, i.e. $\mu \neq \nu$, are known as the shear components or shear stresses while the diagonal components, i.e. $\mu = \nu$, are referred to as the normal components or normal stresses.

Experimentally, the normal stresses are typically measured with respect to atmospheric pressure. Therefore the polymer stress is, commonly, expressed as

$$\boldsymbol{\sigma} = \mathbf{T} - p\mathbf{I}, \quad (1.1)$$

where \mathbf{T} is the total measured stress and $p\mathbf{I}$ is the isotropic stress due to the atmospheric pressure p . By measuring differences of the form $T_{\mu\mu} - T_{\nu\nu}$ one can eliminate the contribution of the isotropic stress and obtain the contribution from the polymer chains. For dilute polymer solutions, an extra term $\boldsymbol{\sigma}_s$ is added to the LHS of the previous equation in order to account for the contribution of the solvent particles to the total stress.

An equation that relates $\boldsymbol{\sigma}$ with the deformation history of the material is called a constitutive equation. Constitutive equations based on the underlying molecular scale physics of the material are the aim of molecular rheology. Such constitutive equations are derived in chapters 4 and 5 for melts of branched polymers. A detailed discussion of constitutive equations for polymers can be found in Refs. [29, 38].

1.2.2 Deformation tensors

The development of constitutive equations requires a mathematical description of the imposed deformation on a material element. For such an element, with position vector \mathbf{r} , the local rate of deformation is determined from gradients of the velocity field $\mathbf{v}(\mathbf{r}, t)$, the

so-called velocity gradient tensor,

$$\mathbf{K}(\mathbf{r}, t) = (\nabla \mathbf{v}(\mathbf{r}, t))^{\text{T}}, \quad (1.2)$$

where the superscript T denotes matrix transpose.

A useful simplification is to divide $\mathbf{K}(\mathbf{r}, t)$ into the sum of a symmetric and an antisymmetric tensor, as

$$\mathbf{K} = \mathbf{D} + \mathbf{\Omega} = \frac{1}{2} (\mathbf{K} + \mathbf{K}^{\text{T}}) + \frac{1}{2} (\mathbf{K} - \mathbf{K}^{\text{T}}). \quad (1.3)$$

The symmetric part \mathbf{D} is referred to as the rate of deformation tensor, or strain rate tensor, while the antisymmetric part $\mathbf{\Omega}$ is known as the vorticity tensor. The former part is the one deforming (stretching) the material elements whereas the latter part is related to rotation of the polymeric fluid elements. For flows with no rotation, such as the extensional flows, $\mathbf{\Omega} = 0$. In contrast, for shear flow $\mathbf{\Omega} \neq 0$, that is, shear flow is a combination of (planar) extension and rotation.

Note that $\mathbf{K}(\mathbf{r}, t)$ provides information about the current rate of deformation. Therefore it is suitable for use in constitutive equations of differential form. In constitutive equations of integral form the accumulated deformation should be accounted for. In such cases, the deformation gradient tensor, $\mathbf{E}(t', t)$, is used instead of $\mathbf{K}(\mathbf{r}, t)$ for the mathematical description of the deformation. In this framework, for linear deformations (c.f. section 1.2.4 below), the vector \mathbf{w} connecting two embedded points at time t is related to the respective vector \mathbf{w}' at a later time t' through

$$\mathbf{w}'(t') = \mathbf{E}(t', t) \cdot \mathbf{w}(t). \quad (1.4)$$

For simple flows like shear and extensional $\mathbf{K}(\mathbf{r}, t)$ is independent of \mathbf{r} and the following relationship between $\mathbf{K}(t)$ and $\mathbf{E}(t', t)$ holds

$$\frac{\partial \mathbf{E}(t', t)}{\partial t} = \mathbf{K}(t) \cdot \mathbf{E}(t', t). \quad (1.5)$$

$\mathbf{E}(t', t)$ contains information for both deformation and solid body rotation. According to the principle of frame invariance, however, a purely rotational deformation should not induce any stress on the material. Hence it is more appropriate, in the development of integral constitutive equations, to consider the rotationally invariant tensor,

$$\mathbf{B}(t', t) = \mathbf{E}(t', t) \cdot \mathbf{E}^{\text{T}}(t', t), \quad (1.6)$$

known as the Finger tensor, and its inverse, the so-called Cauchy tensor

$$\mathbf{C}(t', t) = \mathbf{B}^{-1}(t', t). \quad (1.7)$$

Table 1.1 shows the velocity gradient and the deformation gradient tensors for shear flow and for both uniaxial and planar extensional flows.

Table 1.1: Flow tensors in simple flows

Flow Type	Velocity gradient \mathbf{K}	Deformation gradient $\mathbf{E}(t', t)$
Shear	$\begin{pmatrix} 0 & \dot{\gamma} & 0 \\ 0 & 0 & 0 \\ 0 & 0 & 0 \end{pmatrix}$	$\begin{pmatrix} 1 & \gamma & 0 \\ 0 & 1 & 0 \\ 0 & 0 & 1 \end{pmatrix}$
Uniaxial extension	$\begin{pmatrix} \dot{\epsilon} & 0 & 0 \\ 0 & -\dot{\epsilon}/2 & 0 \\ 0 & 0 & -\dot{\epsilon}/2 \end{pmatrix}$	$\begin{pmatrix} e^{\epsilon} & 0 & 0 \\ 0 & e^{-\epsilon/2} & 0 \\ 0 & 0 & e^{-\epsilon/2} \end{pmatrix}$
Planar extension	$\begin{pmatrix} \dot{\epsilon} & 0 & 0 \\ 0 & -\dot{\epsilon} & 0 \\ 0 & 0 & 0 \end{pmatrix}$	$\begin{pmatrix} e^{\epsilon} & 0 & 0 \\ 0 & e^{-\epsilon} & 0 \\ 0 & 0 & 1 \end{pmatrix}$

Shear strain, extensional strain, and viscosity

In table 1.1 the quantities γ and ϵ are called the shear strain and extensional (or Hencky) strain, respectively. Consider the deformation geometry of simple shear shown in the upper panel of Fig. 1.4. The shear strain is defined as $\gamma = \Delta x/h$, i.e. the ratio of the displacement of the upper plate, Δx , to the thickness of the sample, h . The quantity $\dot{\gamma}$, the rate of change of shear strain with time, is known as the shear strain rate. In general, if the upper plate moves with constant velocity then $\dot{\gamma}$ is also constant. In this case $\dot{\gamma}$ is related to the shear strain as follows: $\gamma = \dot{\gamma}\Delta t$, where Δt is the elapsed time from the application of the deformation.

Consider now the deformation geometry of (uniaxial) extension shown in the bottom panel of Fig. 1.4. Before the deformation, the length and the diameter of the cylindrical sample are \tilde{L}_0 and \tilde{D}_0 , respectively. If the length after the deformation is \tilde{L} , then the

extensional strain (or Hencky strain) is defined as $\epsilon = \ln\left(\tilde{L}/\tilde{L}_0\right)$. Note that in an ideal uniaxial extension, in which the strain rate $\dot{\epsilon}(= d\epsilon/dt)$ is constant, $\tilde{L}(t)$ and $\tilde{D}(t)$, the length and the diameter of a cylindrical sample at time t respectively, follow the relationships:

$$\tilde{L}(t) = \tilde{L}_0 \exp(\dot{\epsilon}t), \quad \text{and} \quad \tilde{D}(t) = \tilde{D}_0 \exp\left(-\frac{1}{2}\dot{\epsilon}t\right). \quad (1.8)$$

According to the latter expression, in an ideal uniaxial extension, the diameter remains uniform along the elongated specimen.

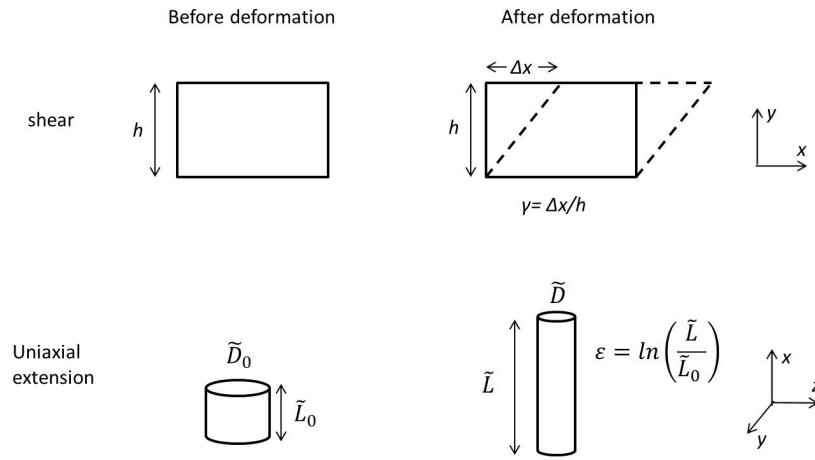


Figure 1.4: The definition of shear and extensional strain in terms of ratios of measurements before and after the deformation.

For the purposes of constitutive modelling, the accumulated shear and extensional strains from time t' to the current time t are defined as

$$\gamma = \int_{t'}^t \dot{\gamma}(t'') dt'', \quad \text{and} \quad \epsilon = \int_{t'}^t \dot{\epsilon}(t'') dt'', \quad (1.9)$$

respectively. $\dot{\gamma}(t'')$ and $\dot{\epsilon}(t'')$ are the local (in time) deformation rates. Equation 1.9 holds for both steady and unsteady flows. For steady flows, the accumulated strains can be converted to time by using $\gamma = \dot{\gamma}\Delta t$ and $\epsilon = \dot{\epsilon}\Delta t$ (where $\Delta t = |t - t'|$).

Measurements of the shear-stress growth coefficient, $\eta(\dot{\gamma}, t)$, and measurements of the (uniaxial) extensional stress growth coefficient, $\eta^+(\dot{\epsilon}, t)$, are among the most common rheological measurements. In such measurements a constant flow rate ($\dot{\gamma}$ or $\dot{\epsilon}$) is applied at time $t = 0$, and $\eta(\dot{\gamma}, t)$ or $\eta^+(\dot{\epsilon}, t)$ are measured as a function of time. In terms of the

notation of the bottom panel of Fig. 1.4 (or Fig. 1.2) for the coordinate system, $\eta(\dot{\gamma}, t)$ and $\eta^+(\dot{\epsilon}, t)$ are defined as

$$\eta(\dot{\gamma}, t) = \frac{\sigma_{xy}(t)}{\dot{\gamma}}, \quad \text{and} \quad \eta^+(\dot{\epsilon}, t) = \frac{\sigma_{xx}(t) - \sigma_{yy}(t)}{\dot{\epsilon}}, \quad (1.10)$$

respectively. For simplicity, hereafter, $\eta(\dot{\gamma}, t)$ and $\eta^+(\dot{\epsilon}, t)$ will be referred to as the shear viscosity and the (uniaxial) extensional viscosity, respectively. The development of constitutive models for the calculation of $\eta(\dot{\gamma}, t)$ and $\eta^+(\dot{\epsilon}, t)$ for melts of branched polymers is the subject of chapters 4 and 5.

1.2.3 Solids, liquids and viscoelasticity

The response of a Newtonian liquid and of an elastic solid to an applied deformation (strain) is completely different. On the one hand liquids are viscous and resist rates of deformation. Thus the stress response is proportional to the applied deformation rate and the total strain is irrelevant. Accordingly, the constitutive equation for a Newtonian liquid is:

$$\boldsymbol{\sigma}^N = 2\eta\mathbf{D}, \quad (1.11)$$

where η is the (time independent) viscosity and \mathbf{D} is the deformation rate tensor.

On the other hand ideal solids are elastic and do not resist rates of deformation but only deformation. In contrast to liquids, elastic solids conserve the elastic energy supplied by the deformation and so restore their original state upon release of the applied strain. For this type of materials the stress is given by Hooke's law,

$$\boldsymbol{\sigma}^E = G_0\mathbf{B}, \quad (1.12)$$

where G_0 is the (time independent) elastic modulus and \mathbf{B} is the Finger tensor.

Viscoelastic materials like polymers exhibit a behaviour which falls between the two aforementioned extremes. Such materials resist both deformation and rate of deformation. A basic constitutive equation, which captures viscoelastic effects, is constructed by combining the viscous and elastic stresses of eqs 1.11 and 1.12, respectively. Specifically, for a shear deformation: $\sigma_{xy}^N = \eta\dot{\gamma}$ and $\sigma_{xy}^E = G_0\gamma$ hence by assuming that a total deformation rate is the sum of an elastic and a viscous deformation one arrives at

$$\frac{1}{\eta}\sigma_{xy}^M + \frac{1}{G_0}\frac{d\sigma_{xy}^M}{dt} = \frac{d\gamma}{dt} = \dot{\gamma}, \quad (1.13)$$

where γ is the accumulated strain, from a time t' to the current time t , given by eq 1.9. Equation 1.13 is the constitutive equation of the so-called Maxwell viscoelastic model. It is readily solved by the integrating factor method. The result reads

$$\sigma_{xy}^M(t) = \int_{-\infty}^t G(t-t') \dot{\gamma}(t') dt', \quad (1.14)$$

where $G(t-t') = G_0 \exp[-(t-t')/\tau]$ is the time dependent relaxation modulus which keeps a memory of the deformation history of the viscoelastic fluid. In $G(t-t')$, τ is the dominant (characteristic) relaxation time also known as the terminal relaxation time. In other words, τ is the time taken for the viscoelastic fluid to relax most of the imposed stress. Assuming $t' = 0$, $G(t-t')$ reduces to

$$G(t) = G_0 \exp\left(\frac{-t}{\tau}\right) \quad (1.15)$$

Figure 1.5 shows, with black lines, the predictions of eq 1.14 for a step shear strain (left) and a steady shear strain (right). In the same figure the respective response of a Newtonian liquid and of an elastic solid is also shown for comparison with a red and a blue line, respectively. The step strain is achieved by applying an instantaneous deformation, of size γ_0 , at time $t = 0$. The corresponding shear rate is $\dot{\gamma} = \gamma_0 \delta(t)$. The steady shear strain is achieved by imposing a constant shear rate, $\dot{\gamma} = \dot{\gamma}_0$, at $t > 0$. In this case the accumulated strain is linear in time, that is $\gamma(t) = \dot{\gamma}_0 t$.

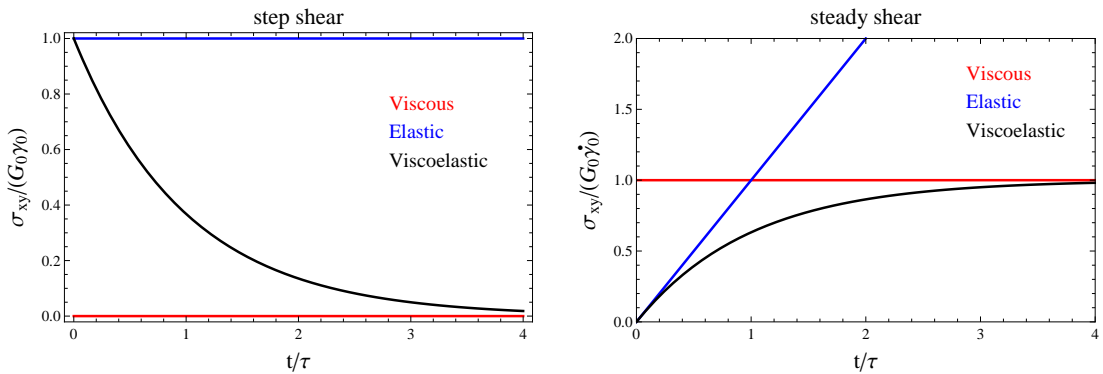


Figure 1.5: Different responses of Newtonian liquids (viscous), solids (elastic) and polymeric fluids (viscoelastic) to a step shear strain (left) and to a steady shear flow (right).

Figure 1.5 demonstrates the radically different response to the deformation of the three materials. Specifically, in the step shear case (left panel), for the Newtonian liquid the stress relaxes instantaneously. In contrast for the elastic solid the stress remains constant,

i.e. $\sigma_{xy}^E(t) = G_0\gamma_0$. According to the Maxwell model, the viscoelastic fluid manifests a solid-like behaviour at early timescales. Then the stress decays to zero in an exponential fashion, that is, $\sigma_{xy}^M(t) \propto \exp(-t/\tau)$. Regarding the steady shear case (right panel), for the Newtonian liquid the stress is the same at all times and equal to $\eta\dot{\gamma}_0$. On the other hand, for the elastic solid the stress increases linearly in time with a slope of gradient $G_0\dot{\gamma}_0$. The viscoelastic fluid displays a cross-over from solid to liquid-like behaviour. This cross-over begins at times of order the terminal relaxation time, τ . At later times, $t \gtrsim 4\tau$, according to the Maxwell model, polymers behave like ordinary (viscous) liquids.

1.2.4 Linear viscoelasticity

Typically, linear viscoelasticity is exhibited by a material that is subjected to a deformation that is very small or very slow. In the linear viscoelastic limit the relaxation modulus at a given temperature is a function of time (or frequency), but not of strain. The Boltzmann superposition principle is another manifestation of linear viscoelasticity. It states that the stress responses to successive deformations are additive. Therefore, for a continuous strain history the stress is expressed as an integral:

$$\boldsymbol{\sigma}(t) = \int_{-\infty}^t 2G(t-t')\mathbf{D}(t')dt', \quad (1.16)$$

where \mathbf{D} is the deformation rate tensor. This equation reduces to eq 1.14 for a shear deformation. By making use of eqs 1.10 and 1.16 one can define, for a slow steady shear flow (that is, $\dot{\gamma} \ll 1\text{s}^{-1}$), the (zero) shear viscosity:

$$\eta(\dot{\gamma}, t) = \eta_0 = \int_0^{\infty} G(t)dt, \quad \text{for } \dot{\gamma} \ll 1\text{s}^{-1}. \quad (1.17)$$

To obtain this expression one has to use the variable transformation $s = t - t'$ in the integral of eq 1.16. In eq 1.17, $G(t)$ is the relaxation modulus of the polymeric material; if the Maxwell model is used to describe the linear viscoelastic behaviour of the polymer then $G(t)$ is given by eq 1.15 and thus η_0 reads

$$\eta_0 = G_0\tau. \quad (1.18)$$

This expression implies that the zero shear viscosity is proportional to the product of the terminal relaxation time and the value of the modulus at that relaxation time.

As discussed in the previous section, step shear and continuous shear deformations are used to probe the linear rheological response of materials. However, the step strain is never completely instantaneous. Moreover, it is not so trivial to establish a constant shear rate experimentally. For these reasons, more often, a small amplitude oscillatory shear (SAOS) deformation is used to probe the linear viscoelastic properties of materials. For this type of deformation mode the imposed strain profile, $\gamma(t)$, reads

$$\gamma(t) = \gamma_0 \sin \omega t, \quad (1.19)$$

where γ_0 is the strain amplitude, and ω is the frequency of the sine function. The corresponding strain rate, at time t , is

$$\dot{\gamma}(t) = \dot{\gamma}_0 \cos \omega t = \Re(\dot{\gamma}_0 \exp(i\omega t)), \quad (1.20)$$

where $\dot{\gamma}_0 = \gamma_0 \omega$.

The stress response to small amplitude oscillatory shear can be obtained by substituting eq 1.20 into eq 1.16. (That is, one has to use $\mathbf{D}(t) = D_{xy}(t) = \dot{\gamma}(t)/2$ in eq 1.16.) The result is

$$\sigma_{xy}(t) = \gamma_0 \sin(\omega t)G' + \gamma_0 \cos(\omega t)G''. \quad (1.21)$$

The quantities G' and G'' are frequency-dependent. They are known as the storage modulus and the loss modulus, respectively. The former represents the portion of the shear stress wave that is in phase with the imposed strain wave and therefore is associated with the storage of the elastic energy supplied by the deformation. The latter represents the portion of the stress wave that is out of phase with the strain wave and hence is related to the dissipation of the elastic energy. In other words, G' and G'' are indicative of solid-like and liquid-like behaviour, respectively. Accordingly, for an elastic solid $G' = G_0$ and $G'' = 0$ whereas for a Newtonian liquid $G' = 0$ and $G'' = G_0 \omega \tau = \eta \omega$. It is worth mentioning that the complex modulus, G^* , can be defined in terms of the storage modulus, G' , and the loss modulus, G'' , as follows:

$$G^*(\omega) = G' + iG''. \quad (1.22)$$

That is, G' and G'' correspond to the real part and the imaginary part of the complex modulus, respectively.

For the Maxwell model (eq 1.14), the explicit formulae for G' and G'' are given by:

$$G' = G_0 \left(\frac{\omega^2 \tau^2}{1 + \omega^2 \tau^2} \right) \quad \text{and} \quad G'' = G_0 \left(\frac{\omega \tau}{1 + \omega^2 \tau^2} \right). \quad (1.23)$$

Figure 1.6 shows G'/G_0 and G''/G_0 (eq 1.23) as a function of the dimensionless frequency $\omega\tau$. In particular, the dimensionless storage modulus, G'/G_0 , is presented as a black solid line while the dimensionless loss modulus, G''/G_0 , is presented as a black dashed line. The respective quantities for a Newtonian liquid and an elastic solid are also depicted as red and blue lines, respectively. As is readily seen from Fig. 1.6, the Maxwell fluid behaves as a liquid at low frequencies, whereas at high frequencies it behaves as a solid. It crosses over from viscous to elastic behaviour at the intermediate (cross-over) frequency, $\omega\tau = 1$, at which G' crosses G'' . So, in the Maxwell model, the cross-over frequency is the exact reciprocal of the terminal relaxation time (τ) and, moreover, it coincides with the frequency at which the maximum of G'' occurs.

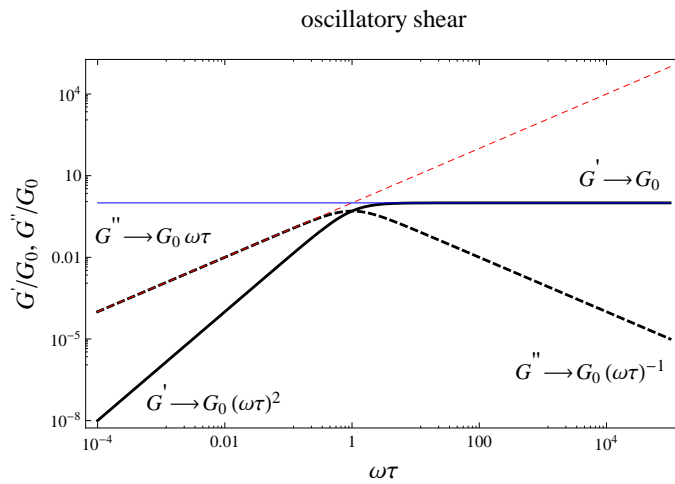


Figure 1.6: G'/G_0 (black solid line) and G''/G_0 (black dashed line) vs the dimensionless frequency $\omega\tau$ for a single Maxwell model. The respective quantities for a Newtonian liquid and an elastic solid are also depicted as red and blue lines, respectively. The low and high frequency limits of G' and G'' are also shown as labels.

Although the Maxwell model shows the correct qualitative behaviour, to fit G' and G'' data of real polymer melts, it is typically necessary to use a sum of Maxwell modes with parameters $[G_{0_i}, \tau_i]$. This set is referred to as the linear spectrum of the polymer melt and describes its response to linear deformations. In this case the relaxation modulus is given by

$$G(t) = \sum_i G_{0_i} \exp\left(\frac{-t}{\tau_i}\right). \quad (1.24)$$

In chapter 4 the linear spectrum of an industrial melt is extracted by fitting G' and G'' data to a finite number of Maxwell modes. The fitting has been performed using the freely

available RepTate software [39].

It is worth mentioning that G' and G'' often reveal the molecular topology of monodisperse (i.e. all chains have the same M_w) polymer melts. For example, a comparison of G' and G'' for linear and star polyisoprene melts [40] (with the M_w of the span of the stars being the same as the M_w of the linear chains) reveals the following (see Fig. 1.7): for the linear polyisoprene melt, the maximum in G'' is close to the cross-over, indicating the existence of a dominant relaxation time. (In this discussion we ignore the behaviour of G' and G'' at the high frequency domain.) For the star polyisoprene melt, however, the cross-over frequency is positioned about four orders of magnitude toward lower frequencies relatively to the frequency at which the maximum in G'' occurs. This indicates the existence of a much broader spectrum of relaxation times for the star polymer. This is also suggested by the broad, sloping solder of G'' itself; to reconstruct this solder one would have to superpose Maxwell modes over three orders of magnitude in frequency [2].

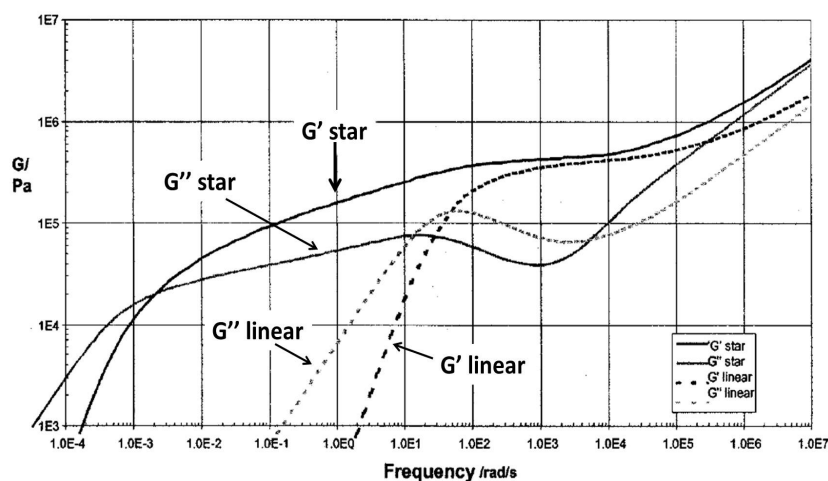


Figure 1.7: Comparison of G' and G'' for monodisperse linear and star polyisoprene melts. Figure from Ref. [2].

Another example is the shape of G' and G'' for a melt of H-polymers. In this case G'' manifests two different “humps” indicating a big separation in the relaxation times associated with the backbone and arm material; the lower frequency hump is attributed to the backbone while the high frequency broad solder arises from the arms [41]. These two examples imply that linear polymers relax their configuration via different mechanisms

compared to branched polymers. The relaxation mechanisms for linear and branched chains are discussed in sections 1.4 and 1.5, respectively.

1.2.5 Non-linear viscoelasticity

Normally, non-linear viscoelasticity is exhibited by a material that is subjected to a deformation that is neither very small nor very slow. In the non-linear viscoelastic limit, the relaxation modulus becomes strain dependent. Also, the Boltzmann superposition principle breaks down. In contrast to the linear viscoelastic limit, the configurations of polymer chains are significantly different from those at equilibrium: a polymer chain, which appears as a random coil in the absence of flow, can be stretched out when the flow rate is of similar order or faster than the inverse of the stretch relaxation time of the chain.

The response of a polymeric material to a non-linear deformation depends both on the type of flow and on the molecular topology. For instance, complex branched polymers exhibit radically different behaviour in extension than in shear. A LDPE melt is strain hardening in uniaxial extension whereas is strain softening (thinning) in shear [42]. This means that the transient extensional viscosity $\eta^+(\dot{\epsilon}, t)$ rises above the linear viscoelastic curve, i.e. above $\eta^+(\dot{\epsilon} \ll 1\text{s}^{-1}, t)$, at non-linear rates whereas the transient shear viscosity $\eta(\dot{\gamma}, t)$ drops below the linear viscoelastic response $\eta(\dot{\gamma} \ll 1\text{s}^{-1}, t)$ at the respective rates. On the other hand, ordinary unbranched melts are strain softening in both shear and uniaxial extension.

Non-linear flows are commonly encountered in processing flows. Thus the understanding of the flow properties of polymer chains in the non-linear viscoelastic regime is of practical interest. In chapters 4 and 5 the flow behaviour of branched polymers under fast (strong) flows, especially extensional, is examined. Experimentally, the non-linear behaviour of polymer melts and solutions has been studied with several different types of rheometers; some of the more frequently used extensional rheometers are presented in the next section.

1.2.6 Uniaxial Extensional Rheometers

The first reliable and accurate extensional rheometer is the one developed by Meissner [43]. In this kind of apparatus the two edges of a sample (which is supported by floating it in a hot oil bath) are squeezed in between a pair of gears that rotate in the opposite direction. The rotation of the gears generates a constant velocity at the points of gripping. Thus the section of the sample between the gripped ends is uniaxially stretched with a (as far as possible) constant Hencky strain rate, provided that no slip of the specimen occurs. This instrument has been further improved by Laun and Münstedt [44].

In a modified version of the original fixture the pair of rotating gears is replaced by sets of ribbed metal belts and the sample is suspended over an air table rather than being floated on an oil bath [45]. Commercialised versions of this instrument are known as RME rheometers and can achieve maximum strain rates of 1s^{-1} [46].

Another type of apparatus that measures uniaxial extensional properties of polymer melts is the Münstedt tensile rheometer (MTR) [47, 48]. The specimen is glued to two metal plates with the lower one being attached to a force transducer. The upper metal plate is connected to a pull rod which is vertically displaced by a toothed belt driven by a motor. For this reason a MTR is referred to as an end-separation type of instrument.

The last decade saw the development of the Sentmanat Extension Rheometer (SER) [49, 50]. The behaviour of melts and elastomers in uniaxial extension is commonly investigated using this device (c.f. example [18, 51, 52]). The basic component of a SER is a pair of counter-rotating drums upon which the sample is wound. The ends of the sample are secured to the drums by means of securing clamps, hence the rotational motion of the drums results in the polymer sample being stretched. The force in the sample is determined from the torque exerted by the drums. A big advantage of a SER is that the entire device can be mounted on a standard shear rheometer. Nevertheless, measurements using this type of rheometer are limited to Hencky strains ≈ 4 . At higher strains the sample no longer experiences homogeneous deformation and usually breaks up. As a result a viscosity steady state value is not reached. SER and MTR instruments also suffer from the same problem.

An end-separation type of instrument that overcomes this problem and hence it appears to be able to reach Hencky strains of order of seven (and consequently an apparent steady

state) is the Filament Stretching Rheometer (FSR) [4, 5, 6, 7, 34]. In a FSR a cylindrical polymeric fluid bridge (filament) is stabilised between two cylindrical plates which in turn are accommodated in a drive train. The bottom plate is stationary (see bottom panel of Fig. 1.2, right). The upper plate is set to motion in the x -direction, at time $t = 0$, and the resulting midpoint diameter of the filament $\tilde{D}_{mid}(t)$ and tensile force $F_z(t)$ (exerted by the elongating filament) are measured. Knowing the time evolution of these quantities one can calculate the stress response and the extensional viscosity of the polymeric fluid. Measurements on a highly branched industrial melt (the so-called DOW150R sample) using this kind of apparatus indicate an extensional viscosity overshoot [6, 7]. A constitutive equation that captures this effect is introduced in chapter 4.

The feature that enables the FSR to measure a viscosity steady state value is the use of an active feedback throughout the measurement. In an ideal uniaxial extension the diameter along the elongating column remains uniform. However, in experiments the diameter near the attached (to the plates) ends is slightly bigger than in the rest of the filament. This creates a non uniform deformation history along the liquid bridge and the middle regions have to flow radially inwards at a faster rate to conserve the volume. Therefore, if the the upper plate is set to motion using an input velocity profile that resembles ideal uniaxial extension, i.e. $d\tilde{L}/dt = \tilde{L}_0\dot{\epsilon}_0 \exp(\dot{\epsilon}t)$, then the measured midpoint diameter $\tilde{D}_{mid}(t)$ does not obey eq 1.8 [34, 53]. The key feature of the FSR is the inclusion of the feedback mechanism that continuously monitors $\tilde{D}_{mid}(t)$ and adjusts the velocity profile of the upper plate to ensure that $\tilde{D}_{mid}(t)$ fulfills eq 1.8; that is, regions in the middle of the filament experience a homogeneous deformation (constant strain rate) hence measurements at higher Hencky strains can be obtained compared to the SER. Note that the overall extension rate of the filament, however, is non-uniform.

Measurements obtained from a cross-slot extensional rheometer (CSER) [54, 55] can complement the aforementioned stretching experiments. A CSER consists of perpendicular bisecting channels with flow through opposing inlets and outlets. This type of flow generates a point of zero flow velocity (stagnation point) at the centre of the cross-slot. The stress response of the material is measured by looking at the resulting optical birefringence patterns (i.e. counting the number of fringes) and using the stress-optical law. The flow profile approximates planar extensional along the stagnation line whereas simple shear dominates near the outer walls [56, 57, 58, 59].

A comparison between steady state (planar) viscosity data from CSER and respective data (for uniaxial extension) obtained by SER, for the DOW150R sample, strongly indicates an extensional viscosity overshoot [60, 61, 62]. This finding supports the aforementioned experimental outcome of the filament stretching rheometer [6]. Note that the comparison between the SER and CSER measurements is possible because at the non-linear rates of interest the difference between uniaxial and planar extension is nominal [9, 63].

1.3 Scattering

Scattering can complement rheological experiments by providing a measure of the deformation and dynamics of polymer molecules. When a beam of neutrons, with average wavelength λ , hits a nucleus two events can happen. A neutron can either be absorbed or scattered. Here, we are only concerned with the latter case. The radius of a nucleus is many orders of magnitude smaller than the wavelength λ of the incoming beam and so nuclei can be considered as structureless points described by delta functions $\delta(\mathbf{r} - \mathbf{r}_i(t))$, where $\mathbf{r}_i(t)$ is the position vector of the nucleus of atom i at time t . If nuclei are assumed structureless and “bound” (i.e. after collision with the neutron they will not move) the nucleus-neutron interaction can be model by the Fermi pseudopotential [64, 65, 66]:

$$V(\mathbf{r}) = \frac{2\pi\hbar^2}{m_n} b_i \delta(\mathbf{r}), \quad (1.25)$$

where \hbar is the reduced Planck constant, m_n is the neutron mass, and \mathbf{r} is the position of the neutron relative to nucleus i . In eq 1.25, b_i is the so-called scattering length (amplitude) of the atomic nucleus i . It depends on the nucleus mass, hence different isotopes have different values of b_i , and the relative orientation between the nucleus spin \mathbf{n}_s and the neutron spin \mathbf{s} . In what follows quantities averaged over isotopes and spin states are denoted by $\langle \dots \rangle_{\text{isot}}^{\text{spin}}$.

The scattering length plays a significant role in scattering experiments because it is related to the measured quantity of such experiments, namely the absolute scattering I_{abs} (here, the subscript *abs* is short for absolute). This quantity has units of reciprocal length, and removes all factors to do with experimental set-up from the experimentally reported scattering signal. Theoretically, its evaluation involves a double sum over all nuclei of the

system:

$$I_{abs} = \frac{1}{\Omega} \sum_{i,j} b_i b_j \exp(i\mathbf{q} \cdot (\mathbf{r}_i - \mathbf{r}_j)), \quad (1.26)$$

where Ω is the total volume of the system and \mathbf{q} is the so-called scattering vector (or momentum transfer vector). If the scattering event is treated in terms of wave physics, then both the incoming and scattered neutron beams are considered plane waves of wave vectors \mathbf{k} and \mathbf{k}' , respectively. In this representation $\mathbf{q} = \mathbf{k}' - \mathbf{k}$; hereafter, the magnitude of \mathbf{q} is denoted by q , i.e. $|\mathbf{q}| = q$. Since b_i, b_j depend upon the isotope and the relative direction between \mathbf{n}_s and \mathbf{s} , to evaluate eq 1.26, one has to consider averages of the form $\langle b_i b_j \rangle_{\text{isot}}^{\text{spin}}$. Let $\langle b_i \rangle_{\text{isot}}^{\text{spin}}$ be the average scattering length of nucleus i , generally known as the coherent scattering length, b_i^{coh} , of the nucleus i . In view of this definition, $\langle b_i b_j \rangle_{\text{isot}}^{\text{spin}}$ can be expressed as

$$\langle b_i b_j \rangle_{\text{isot}}^{\text{spin}} = \langle b_i^{\text{coh}} b_j^{\text{coh}} + b_i b_j - b_i^{\text{coh}} b_j^{\text{coh}} \rangle_{\text{isot}}^{\text{spin}} = b_i^{\text{coh}} b_j^{\text{coh}} + \langle b_i b_j - b_i^{\text{coh}} b_j^{\text{coh}} \rangle_{\text{isot}}^{\text{spin}}.$$

Note that under ordinary conditions isotopes and spin states are randomly distributed, that is, there is no correlation between the occupations of site i and site j by these possible choices. Hence, one gets for $i \neq j$ and $i = j$, respectively:

$$\begin{aligned} \langle b_i b_j - b_i^{\text{coh}} b_j^{\text{coh}} \rangle_{\text{isot}}^{\text{spin}} &= \langle b_i \rangle_{\text{isot}}^{\text{spin}} \langle b_j \rangle_{\text{isot}}^{\text{spin}} - b_i^{\text{coh}} b_j^{\text{coh}} = 0, \\ \langle b_i b_i - b_i^{\text{coh}} b_i^{\text{coh}} \rangle_{\text{isot}}^{\text{spin}} &= \langle b_i^2 \rangle_{\text{isot}}^{\text{spin}} - (b_i^{\text{coh}})^2 = (b_i^{\text{inc}})^2. \end{aligned}$$

The quantity b_i^{inc} is called the incoherent scattering length of the nucleus i .

As a result of the above considerations eq 1.26 can be rewritten as a sum of two independent contributions, coherent and incoherent:

$$\begin{aligned} I_{abs} &= \underbrace{\frac{1}{\Omega} \sum_{i,j} b_i^{\text{coh}} b_j^{\text{coh}} \exp(i\mathbf{q} \cdot (\mathbf{r}_i - \mathbf{r}_j))}_{\text{coherent}} + \underbrace{\frac{1}{\Omega} \sum_i (b_i^{\text{inc}})^2}_{\text{incoherent}} \\ &= I_{coh} + I_{inc}. \end{aligned} \quad (1.27)$$

The coherent signal is interpreted as the scattering that the same system would provide, if all scatterers had the same scattering amplitude b_i^{coh} (in this interpretation $b_i^{\text{coh}} = b_j^{\text{coh}}$ in the first term of eq 1.27). The incoherent signal arises from the fluctuations, of the actual system, about b_i^{coh} . The coherent signal I_{coh} provides information about correlations between positions of different atoms at the same and different times. Therefore, it reveals information about collective phenomena and structural issues of the system [65, 66]. In

contrast, I_{inc} is related to the self-motion of an atomic nucleus no matter if this motion is related to a collective process [65, 66].

In chapter 3 we attempt to interpret experimental data from polyethylene (PE) polymer melts. In this particular experiment [3] the chains have some parts protonated (i.e. they contain the ^1H isotope of hydrogen) and other parts deuterated (i.e. they contain the ^2H isotope of hydrogen). The remaining constituent of PE, carbon, has two natural stable isotopes, ^{12}C and ^{13}C . The former is by far the most common (natural abundance of 98.9%) among both. Thus, the precursors of synthetic polymers like ethylene and butadienes are enriched in ^{12}C . Therefore, in polymer melts ^{12}C is the dominant carbon isotope. For this reason in the interpretation of the data we disregard the isotopic effect of ^{13}C in the scattering length of carbon. The coherent (averaged over all possible spin states) and incoherent scattering lengths of ^1H , ^2H and ^{12}C [64, 65] are shown in table 1.2 together with their natural abundance. A negative sign in a nucleus scattering amplitude indicates a phase shift of the scattered wave by 180 degrees, relative to the phase shift that the same scattering centre would produce if it had a positive scattering length. It is worth mentioning that the neutron scattering lengths of nuclei differ from their X-ray scattering lengths (e.g. all X-ray scattering lengths are positive).

Table 1.2: Bound coherent and incoherent scattering lengths

Atomic nucleus	Natural abundance %	b^{coh} (10^{-15}m)	b^{inc} (10^{-15}m)
^{12}C	98.9	6.6511	0
^1H	99.985	-3.7406	25.274
^2H	0.015	6.671	4.04

1.3.1 The Neutron Spin Echo Technique

Before I present the Neutron Spin Echo (NSE) technique it is sensible to introduce the very basic physics of neutron spin motion in a magnetic field. In a magnetic field \mathbf{B} the neutron spin \mathbf{n}_s experiences a torque causing it to precess around the direction of the magnetic field. This motion of the spin is known as the Larmor precession, and is illustrated schematically in the upper panel of Fig. 1.8. The precession angle, ϕ_L , is independent of

θ the angle between the magnetic field and the neutron spin. It depends only on the time the neutron spends in the field: that is, ϕ_L is related to ν_n , the neutron velocity, and ℓ_L , the variable that “measures” the traveled distance of the neutron in the field, as follows:

$$\phi_L = \gamma_n \frac{\int |\mathbf{B}| d\ell_L}{\nu_n}, \quad (1.28)$$

where γ_n is the gyromagnetic ratio of the neutron. Note that the precession angle can only be determined to mod (2π) . (ϕ_L can be seen in the upper panel of Fig. 1.8.) Larmor precession is exploited in NSE while neutrons are traveling through two identical magnetic fields before and after interacting with the sample.

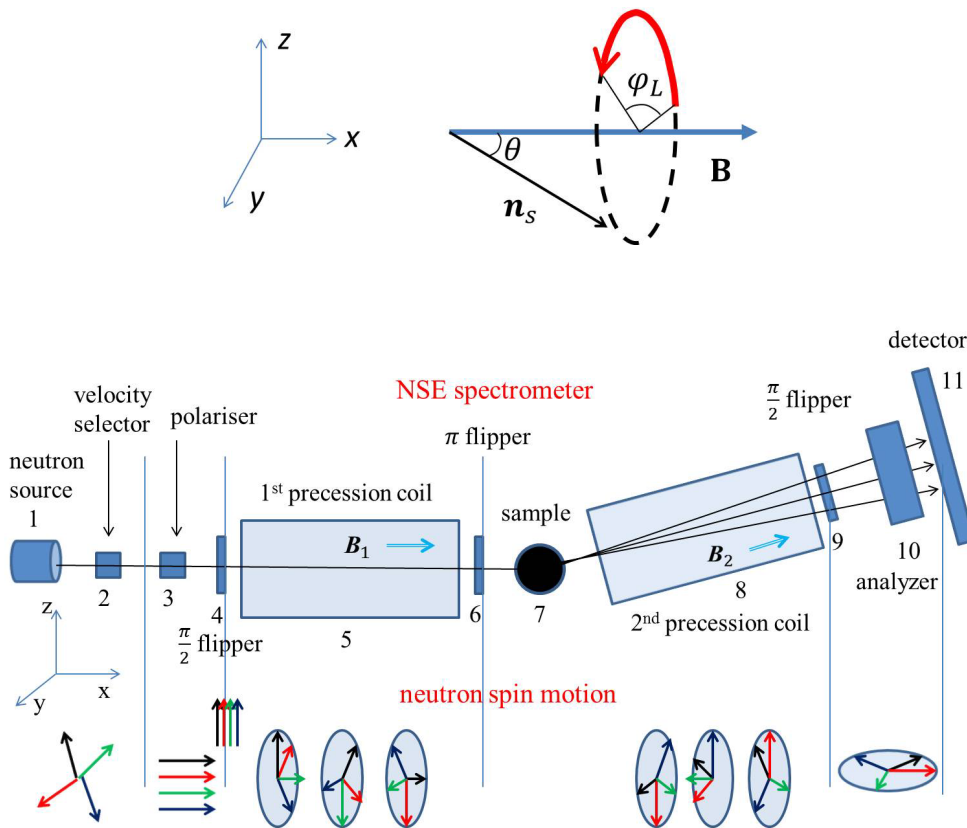


Figure 1.8: Upper: Larmor precession for a neutron spin, \mathbf{n}_s , placed at an angle θ to a magnetic field \mathbf{B} . The direction in which \mathbf{n}_s rotates is shown by the red arrow. ϕ_L is the precession angle. Bottom: A NSE spectrometer. The events at “regions” 1-11 are described in the text.

The detection of tiny changes in the neutron velocity (energy) following a scattering event is the essence of the NSE technique. This is achieved by manipulations of the neutrons spin in a NSE spectrometer. These spin manipulations finally yield the (time

dependent) normalised scattering signal, $P(q, t)$ (eq 1.29 below), which reflects the influence of the sample on the neutrons (and therefore it provides information about the chain dynamics). The bottom panel of Fig. 1.8 shows the layout of a typical NSE spectrometer. The basic events during the implementation of the technique are the following:

1. A neutron source emits neutrons that have a broad distribution of velocities (wavelengths).
2. The beam is coarsely monochromatized by a velocity selector. After exiting the velocity selector the neutron beam has a wavelength distribution of 10%-20%.
3. After, the neutron beam, which has a random distribution of spins, is guided through a polariser. The polarising device transmits only neutrons that have their spins aligned to the velocity direction x .
4. Then the beam goes through a $\frac{\pi}{2}$ flipper which changes the spin direction perpendicular to the magnetic field \mathbf{B}_1 of the first coil in order to initiate Larmor precession when the beam enters \mathbf{B}_1 . At this point, i.e. before entering the first precession coil, the average polarisation of the beam at the z direction $\langle P_z \rangle$ is equal to unity.
5. When the beam travels through \mathbf{B}_1 each neutron spin performs a Larmor precession around the direction of the magnetic field. According to eq 1.28 faster neutrons spend less time in the coil than slow ones and their final precession angle is smaller. Typically, each spin has undergone several thousand full rotations and at the end of the coil the beam is completely depolarised. At that point $\langle P_z \rangle < 1$.
6. Before the neutrons interact with the sample a π flipper rotates the spin direction by 180 degrees around the z axis. Hence, the y component of the spins change sign. If the sample is magnetic the flipper is not necessary.
7. The neutron beam is scattered by the sample. If the scattering is inelastic then the scattered neutrons have their energy and velocity changed. On the contrary, if the scattering is elastic the energy and momentum of the scattered neutrons are preserved.

8. After interacting with the sample the scattered neutrons are guided through a second precession coil identical to the first one. Neutrons that have interacted with the beam elastically restore their initial (i.e. before entering the first coil) polarisation in the z direction when they exit \mathbf{B}_2 . Neutrons that have exchanged velocity with the sample, while traveling through \mathbf{B}_2 , have their spins undergoing a Larmor precession with different precession angle compared to the one in \mathbf{B}_1 . Therefore, the overall resulting polarisation $\langle P_z \rangle$ is less than unity.
9. A $\frac{\pi}{2}$ flipper projects the spins onto the xy plane. If all neutrons have interacted elastically with the sample $\langle P_x \rangle = 1$. Otherwise $\langle P_x \rangle < 1$.
10. An analyzer transmits the scattered neutrons with probability proportional to the cosine of the angle between the x direction and the projected neutron spin orientation onto the xy plane.
11. A detector collects the resulting signal.

Detailed studies concerning the Neutron Spin Echo (NSE) technique and its applications to different systems can be found in Refs. [66, 67, 68, 69, 70]. In the following, we limit ourselves to a discussion concerning issues which are directly related to the work that will be presented in chapter 3.

Neutrons are fermions with quantum spin number $1/2$ thus relative to a specified axis (known as the polarisation axis) can be in two different spin states, i.e. either in the spin up state u_\uparrow or in the spin down state u_\downarrow . In regards with the initial (before scattering) and the final (after scattering) spin state of the neutron, four possible cases occur during a scattering event [65, 66, 67, 70]. These are

$$\left. \begin{array}{l} u_\uparrow u_\uparrow \\ u_\downarrow u_\downarrow \end{array} \right\} \begin{array}{l} \text{no flip of} \\ \text{the neutron spin} \end{array} \qquad \left. \begin{array}{l} u_\uparrow u_\downarrow \\ u_\downarrow u_\uparrow \end{array} \right\} \begin{array}{l} \text{flip of} \\ \text{the neutron spin} \end{array}$$

In a NSE experiment the polariser and the analyser are able to detect the spin state of the neutrons and hence the initial and final spin state of the neutrons is known. Coherent scattering events do not cause flip of the neutron spin. On the other hand, two-thirds of incoherent events (from hydrogen nuclei) do cause a spin flip. These events, therefore, convert two-thirds of the scattering intensity into “non-polarized” (incoherent) background, which has to be subtracted from the final signal. The remaining one-third of

incoherent events cause no spin flip and thus the scattering intensity that arises from these events has to be added to the coherent signal. So the total (time dependent) normalised scattering signal, $P(q, t)$, reads [66, 70]:

$$P(q, t) = \frac{I_{coh}(q, t) - \frac{1}{3}I_{inc}(q, t)}{I_{coh}(q, t) - \frac{1}{3}I_{inc}(q)}, \quad (1.29)$$

where $I_{coh}(q, t)$ and $I_{coh}(q)$ denote the coherent signal at time t and at time zero, respectively. $I_{inc}(q, t)$ is the incoherent signal at time t , while $I_{inc}(q)$ is the static incoherent signal (i.e. the incoherent signal at time zero).

One of the advantages of the NSE method is that complex systems may be selectively studied by variation of the contrast among the structural units (or molecular groups) of the polymer chain. That is, the dynamics of specific sections of the polymer chain may be selectively studied by isotopic substitution of hydrogen (H) by deuterium (D). The motion of the branch point of a symmetric star polymer can be examined, for example, when the branch point is protonated and the arms are deuterated [3]. (The interpretation of the NSE data from this system will be the subject of chapter 3.)

On the one hand, with partly labelled chains in a matrix of fully un-labelled chains, the NSE method (in principle) measures the coherent scattering function, $S^{tot}(q, t)$. (Nevertheless, some incoherent signal may be detected due to spin incoherent scattering from hydrogen nuclei as discussed above.) $S^{tot}(q, t)$ and its static counterpart, $S^{tot}(q)$, are related to the position vectors of the labelled monomers (nuclei), m , (where $m = H$ or $m = D$) of the system as follows:

$$S^{tot}(q, t) = \left\langle \sum_{k,j \in m} \exp [i\mathbf{q} \cdot (\mathbf{r}_k(t) - \mathbf{r}_j(0))] \right\rangle, \quad (1.30a)$$

$$S^{tot}(q) = \left\langle \sum_{k,j \in m} \exp [i\mathbf{q} \cdot (\mathbf{r}_k(0) - \mathbf{r}_j(0))] \right\rangle, \quad (1.30b)$$

where \mathbf{r}_k and \mathbf{r}_j are the position vectors of nuclei k and j , respectively. In such experiments one studies the correlated motions of monomeric pairs. Note that the coherent NSE signals $I_{coh}(q, t)$ and $I_{coh}(q)$, which appear in eq 1.29, can be expressed in terms of the coherent scattering functions, $S^{tot}(q, t)$ and $S^{tot}(q)$, as follows:

$$I_{coh}(q, t) = \frac{\rho}{m_{mon}} \frac{(\tilde{b}_{coh,H} - \tilde{b}_{coh,D})^2}{N_{tot}} S^{tot}(q, t), \quad (1.31a)$$

$$I_{coh}(q) = \frac{\rho}{m_{mon}} \frac{(\tilde{b}_{coh,H} - \tilde{b}_{coh,D})^2}{N_{tot}} S^{tot}(q), \quad (1.31b)$$

where ρ is the density of the polymer, m_{mon} is the molar mass of a monomer, and N_{tot} is the total number of monomers in the system; the quantities $\tilde{b}_{coh,H}$ and $\tilde{b}_{coh,D}$ are the coherent scattering lengths of a protonated (H) and a deuterated (D) monomer, respectively.

On the other hand, with a fully protonated sample or randomly labelled chains, the NSE method measures the incoherent scattering function, $S_{inc}(q, t)$:

$$S_{inc}(q, t) = \left\langle \tilde{b}_{inc,H}^2 \sum_{j \in H} \exp [i\mathbf{q} \cdot (\mathbf{r}_j(t) - \mathbf{r}_j(0))] + \tilde{b}_{inc,D}^2 \sum_{j \in D} \exp [i\mathbf{q} \cdot (\mathbf{r}_j(t) - \mathbf{r}_j(0))] \right\rangle \quad (1.32)$$

with $\tilde{b}_{inc,H}$ ($\tilde{b}_{inc,D}$) and ϕ_H (ϕ_D) being the incoherent scattering length of a protonated (deuterated) monomer and the volume fraction of the protonated (deuterated) material, respectively. In such cases, one investigates self-motion of monomers (nuclei). In terms of $S_{inc}(q, t)$, the incoherent NSE signals, i.e. $I_{inc}(q, t)$ and $I_{inc}(q)$, are given by:

$$I_{inc}(q, t) = \frac{\rho}{m_{mon}} \frac{1}{N_{tot}} S_{inc}(q, t), \quad (1.33a)$$

$$I_{inc}(q) = I_{inc} = \frac{\rho}{m_{mon}} \left(\phi_H \tilde{b}_{inc,H}^2 + \phi_D \tilde{b}_{inc,D}^2 \right). \quad (1.33b)$$

In chapter 3 the above equations (that is, eqs 1.30 to 1.33) and, in turn, eq 1.29 will be calculated for a melt of polyethylene symmetric stars, which contain a small label (protonated segments) at the branch point.

1.4 Molecular Models: linear chains

In this section molecular models that describe the dynamics of linear chains are outlined. The simplest of them is the dumbbell model which represents the polymer chain as an elastic dumbbell. At the next level of complexity the chain is represented by a collection of dumbbells; this level of treatment is generally known as the Rouse model [71]. This model describes successfully the dynamics of the chain at early times before entanglement effects become important. The entanglement effects are accounted for in the mean field approach of Doi and Edwards [26] by localising a single chain in a tube-like region and prohibiting lateral motion beyond a characteristic length scale (the tube diameter).

Thus in the original tube model the chain is allowed to relax its configuration by means of diffusion along the tube axis (reptation). However, this approach, when compared with certain experiments, displays some major limitations which can only be overcome if additional relaxation mechanisms are included. Much of the well established knowledge presented in this section is contained in Refs. [2, 26, 27, 28, 29, 72]

1.4.1 Gaussian chains

The random walk model is the simplest model to describe the statistical properties of a flexible polymer chain. It views the chain as a random walk of $N - 1$ steps (there are N segments) of fixed length, b , the Kuhn length, which is defined as the ratio of the mean-square end-to-end distance of the chain to the contour length of the chain (that is, $b = \langle \mathbf{R}^2 \rangle / L$). The orientation of each step is chosen from an isotropic distribution and therefore is completely uncorrelated with the previous step. As a result the separation vector, $\mathbf{x}_{\ell, \ell'} = \mathbf{r}_{\ell'} - \mathbf{r}_{\ell}$, of two segments of a Gaussian (ideal) chain follows standard random walk statistics, that is

$$\langle \mathbf{x}_{\ell, \ell'} \rangle = 0, \quad \langle \mathbf{x}_{\ell, \ell'}^2 \rangle = |\ell - \ell'| b^2. \quad (1.34)$$

From this equation it is apparent that the end-to-end vector, $\mathbf{R} = \mathbf{r}_N - \mathbf{r}_0$, obeys the relationships $\langle \mathbf{R} \rangle = 0$ and $\langle \mathbf{R}^2 \rangle = Nb^2$; \mathbf{R} is the sum of many (i.e. $N \gg 1$) independent bond vectors (Kuhn steps) of fixed length b and so according to the central limit theorem its probability distribution is, to a good approximation, Gaussian:

$$P(N, \mathbf{R}) = \left(\frac{3}{2\pi^2 Nb^2} \right)^{\frac{3}{2}} \exp \left(\frac{-3\mathbf{R}^2}{2Nb^2} \right). \quad (1.35)$$

The corresponding free energy, $F(N, \mathbf{R})$, reads

$$F(N, \mathbf{R}) = \frac{3k_B T}{2Nb^2} \mathbf{R}^2 + F(N, 0), \quad (1.36)$$

where k_B is the Boltzmann constant, T is the temperature, and $F(N, 0) = U(N, 0) - TS(N, 0)$ is the free energy of a chain that has both its ends at the same point, i.e. has an end-to-end vector $\mathbf{R} = 0$. According to eq 1.36, $F(N, \mathbf{R})$ is minimised when $\mathbf{R} = 0$. Thus the configuration of an ideal chain that has both its ends at the same point corresponds to the minimum free energy and the maximum entropy. To hold the chain at a

fixed end-to-end vector \mathbf{R} one has to apply equal and opposite forces (that are proportional to \mathbf{R}) on the chain ends. In other words, when extended, Gaussian chains exhibit an elastic response that tends to restore a configuration which maximises the entropy. This elastic response is expressed by the entropic tension:

$$\mathbf{f} = -\frac{\partial F(N, \mathbf{R})}{\partial \mathbf{R}} = -\frac{3k_B T}{Nb^2} \mathbf{R}. \quad (1.37)$$

1.4.2 A simple constitutive equation: The dumbbell model

A molecular expression for the stress of polymer chains can be obtained as follows. One may consider a cubic box, of length L_b , containing cL_b^3/N chains where c is the monomer concentration. Note that the chains should have achieved local equilibrium below a characteristic length scale, which is typically considered to be the Kuhn length b . A chain will cross a plane with normal in the μ direction with probability R_μ/L_b , where R_μ is the μ th component of the end-to-end vector of the chain. According to eq 1.37, the ν th component of the force transmitted by this chain across the plane is $f_\nu = 3k_B T(Nb^2)^{-1}R_\nu$. Since the box contains cL_b^3/N polymer chains the total stress reads

$$\sigma_{\mu\nu} = c \frac{3k_B T}{N^2 b^2} \langle R_\mu R_\nu \rangle, \quad (1.38)$$

where $\langle \dots \rangle$ denotes an ensemble average.

From eq 1.38 it is apparent that the calculation of the stress requires the knowledge of the time evolution of $d\langle R_\mu R_\nu \rangle/dt$. Nevertheless, it is convenient to make the rescaling $\langle R_\mu R_\nu \rangle = \langle A_{\mu\nu} \rangle Nb^2/3$ and seek an expression for $d\langle A_{\mu\nu} \rangle/dt$. Such an expression can be derived by treating the polymer chain as a dumbbell (spring), that is, the chain is represented by two beads (segments) of segmental friction ζ_0 and separation vector \mathbf{R} , leading to

$$\frac{d\langle A_{\mu\nu} \rangle}{dt} = K_{\mu\lambda} \langle A_{\lambda\nu} \rangle + \langle A_{\mu\lambda} \rangle K_{\lambda\nu}^T - \frac{1}{\tau_{dl}} (\langle A_{\mu\nu} \rangle - \delta_{\mu\nu}), \quad (1.39)$$

where $\tau_{dl} = \zeta_0(4k)^{-1}$ is the relaxation time of the dumbbell; $k = 3k_B T/b^2$ is the spring constant. In eq 1.39 the first two terms represent the effect of the flow and the last term represents the elastic response of the dumbbell. The polymer stress (eq 1.38) is rewritten as $\sigma = G_{dl} \mathbf{A}$, where $G_{dl} = ck_B T N^{-1}$ is the elastic modulus. This expression together with eq 1.39 constitute the upper convected Maxwell (UCM) model.

1.4.3 Dynamics of unentangled linear polymers: the Rouse model

In the Rouse model the polymer chain is represented as a set of N beads (segments), that are connected with their neighbours with linear force law spring. If the ℓ th bead has position vector \mathbf{r}_ℓ then the spring force acting on this bead is given by

$$\mathbf{f}_\ell = k(-2\mathbf{r}_\ell + \mathbf{r}_{\ell+1} + \mathbf{r}_{\ell-1}). \quad (1.40)$$

The factor $k = 3k_B T b^{-2}$ is the entropic spring constant where b is the Kuhn (segmental) length, k_B is the Boltzmann constant, and T the temperature.

The Langevin equation of the Rouse model (Rouse equation), for the ℓ th bead, in the continuous limit is written as

$$\zeta_0 \frac{\partial \mathbf{r}_\ell(t)}{\partial t} = k \frac{\partial^2 \mathbf{r}_\ell(t)}{\partial \ell^2} + \mathbf{g}_\ell(t). \quad (1.41)$$

The boundary conditions of this equation are $\frac{\partial \mathbf{r}_\ell(t)}{\partial \ell} = 0$ at $\ell = 0$ and $\ell = N$. In terms of physics these boundary conditions express the absence of chain tension at the free ends. The Rouse equation is a force balance between the friction, spring, and random Brownian forces acting on a bead. The friction force $\zeta_0 \frac{\partial \mathbf{r}_\ell(t)}{\partial t}$ can be thought of as the force needed to pull the ℓ th bead from the solvent with a constant velocity; ζ_0 is the segmental friction coefficient. The $k \frac{\partial^2 \mathbf{r}_\ell(t)}{\partial \ell^2}$ term is the analogue of eq 1.40 in the continuous limit. Finally the Brownian force \mathbf{f}_ℓ represents the random collisions of the bead with the much smaller solvent molecules. The moments of this random force are given by

$$\langle \mathbf{g}_\ell(t) \rangle = 0 \quad (1.42a)$$

$$\langle g_{\ell\mu}(t) g_{\ell'\nu}(t') \rangle = 2\zeta_0 k_B T \delta(\ell - \ell') \delta(t - t') \delta_{\mu\nu}. \quad (1.42b)$$

In the latter expression the indexes ℓ and ℓ' denote beads whereas the indexes μ and ν denote cartesian coordinates.

Equation 1.41 is solved by Fourier transform, using the normal coordinates [2, 26]:

$$\mathbf{X}_p(t) = \frac{1}{N} \int_0^N \mathbf{r}_\ell(t) \cos\left(\frac{p\pi\ell}{N}\right) d\ell \quad (1.43a)$$

$$\mathbf{r}_\ell(t) = \mathbf{X}_0(t) + 2 \sum_{p=1}^{\infty} \mathbf{X}_p(t) \cos\left(\frac{p\pi\ell}{N}\right). \quad (1.43b)$$

The transformation 1.43b essentially splits the spacecurve describing the chain contour into p subchains (domains), the so-called ‘‘Rouse modes’’ of the polymer chain. These

modes are indexed by the mode number p . The motion of the subchains (each of them contains N/p segments) is associated with the vector amplitudes $\mathbf{X}_p(t)$. Moreover, each domain relaxes as an independent chain of N/p segments. The corresponding relaxation time τ_p reads

$$\tau_p = \frac{\zeta_p}{k_p} = \tau_0 \left(\frac{N}{p} \right)^2 = \frac{\tau_R}{p^2}, \quad (1.44)$$

where $k_p = 6k_B T p^2 \pi^2 / (N b^2)$, $\zeta_p = 2N \zeta_0$, and $\tau_0 = \zeta_0 b^2 / (3\pi^2 k_B T)$ is the relaxation time of a Rouse segment; $\tau_R = \tau_0 N^2$ is the relaxation time of the whole chain, i.e. $p = 1$, and is referred to as the Rouse relaxation time of the polymer chain. Note that $X_0(t) = \frac{1}{N} \int_0^N \mathbf{r}_\ell(t) d\ell$ is associated with motion of the center of mass of the chain.

For $p \geq 1$, substitution of eq 1.43b into eq 1.41 yields

$$\zeta_p \frac{\partial \mathbf{X}_p(t)}{\partial t} = -k_p \mathbf{X}_p(t) + \mathbf{g}_p(t). \quad (1.45)$$

The second moment of the noise term $\mathbf{g}_p(t)$ is $\langle g_{p\mu}(t) g_{p\nu}(t') \rangle = 2\zeta_p k_B T \delta(t - t') \delta_{pq} \delta_{\mu\nu}$. By use of $\langle g_{p\mu}(t) g_{p\nu}(t') \rangle$ and of the integrating factor method to solve eq 1.45 one obtains the time correlation function of the vector amplitudes:

$$\langle \mathbf{X}_p(t) \cdot \mathbf{X}_q(t') \rangle = \frac{3k_B T}{k_p} \delta_{pq} \exp\left(-\frac{|t - t'|}{\tau_p}\right). \quad (1.46)$$

Motion of the Rouse chain

Having obtained $\langle \mathbf{X}_p(t) \cdot \mathbf{X}_q(t') \rangle$ various time correlation functions can be calculated readily. With respect to chain motion, the main features of the Rouse model can be illustrated by looking at the correlators $\langle \mathbf{u}_\ell(0) \cdot \mathbf{R}(t) \rangle$ and $\langle \mathbf{R}(t) \cdot \mathbf{R}(0) \rangle$. In these correlators $\mathbf{u}_\ell(0) = \partial \mathbf{r}_\ell(0) / \partial \ell$ represents the tangent vector at the ℓ th segment at time 0 (c.f. red small arrow at the bottom panel of Fig. 1.9) while $\mathbf{R}(t) = \mathbf{r}_N(t) - \mathbf{r}_0(t)$ and $\mathbf{R}(0) = \mathbf{r}_N(0) - \mathbf{r}_0(0)$ are the end-to-end vectors at time t and time 0, respectively (c.f. long blue and black arrows at the bottom panel of Fig. 1.9). Using the normal modes, i.e. eq 1.43b (ignoring the $X_0(t)$ term), one arrives at

$$\langle \mathbf{u}_\ell(0) \cdot \mathbf{R}(t) \rangle = \frac{4}{\pi} b^2 \sum_{p \text{ odd}} \frac{\sin(p\pi\xi) \times \exp(-p^2 \tilde{t}_R)}{p} \quad (1.47a)$$

$$\langle \mathbf{R}(t) \cdot \mathbf{R}(0) \rangle = \frac{8}{\pi^2} N b^2 \sum_{p \text{ odd}} \frac{\exp(-p^2 \tilde{t}_R)}{p^2}, \quad (1.47b)$$

where $\xi = \ell/N$ and $\tilde{t}_R = t/\tau_R$.

The upper panel of Fig. 1.9 presents eqs 1.47 as a function of the normalised time \tilde{t}_R . These curves are obtained using $p_{max} = 501$. Results for larger p_{max} are indistinguishable from those of Fig. 1.9. In this figure $\langle \mathbf{R}(t) \cdot \mathbf{R}(0) \rangle$ is depicted with a solid black line. The correlator $\langle \mathbf{u}_\ell(0) \cdot \mathbf{R}(t) \rangle$ is shown for various segments along the chain contour. In particular, the solid magenta, green, and blue lines correspond to $\xi = 0$, $\xi = 0.15$, and $\xi = 0.30$, respectively. The respective dashed lines refer to the symmetric segments on the other half of the chain. Finally, the red solid line refers to the central section of the chain ($\xi = 0.5$).

According to this plot, for the inner sections of the chain, the correlator $\langle \mathbf{u}_\ell(0) \cdot \mathbf{R}(t) \rangle$ stays to unity up to times of $\tilde{t}_R \simeq 0.1$ (red and blue curves). Then it decays rapidly to zero. Moreover, the green lines, which correspond to segments at the outer part of the chain, start to drop about a decade earlier. On the other hand, for the chain ends (magenta curves) the correlator is zero throughout the $10^{-5} \leq \tilde{t}_R \leq 10$ time window. Concerning the end-to-end vector correlator (black curve) it starts to decay at $\tilde{t}_R \sim 10^{-4}$. Nevertheless, the decay up to $\tilde{t}_R \simeq 0.1$ is moderate compared to the final decay in the remaining time interval.

These features can be explained in terms of the ‘‘Rouse modes’’. At early times, $\tilde{t}_R \ll 1$, only modes with high index (fast Rouse modes) are active, that is, the chain is ‘‘split’’ into numerous small subchains. Therefore, conformational changes occur only locally and the overall conformation of the chain is almost unchanged (c.f. left side of the bottom panel of Fig. 1.9 for a schematic representation). In contrast, at times close to τ_R the active Rouse modes are the slower ones (low p) and conformational changes occur on the length scale of the entire chain (also the chain has diffused distances of the order of its own radius of gyration-c.f. right side of bottom panel of Fig. 1.9). This relaxation of the slow modes causes the rapid decay of $\langle \mathbf{u}_\ell(t) \cdot \mathbf{R}(t) \rangle$ of the inner segments in the time window $0.1 \lesssim \tilde{t}_R \lesssim 1$, and the acceleration in the decay of $\langle \mathbf{R}(t) \cdot \mathbf{R}(0) \rangle$ in the same time interval. Note that for $\xi = 0.15$ and $\xi = 0.75$ the correlator $\langle \mathbf{u}_\ell(t) \cdot \mathbf{R}(t) \rangle$ starts to decay earlier on because sections towards the chain ends are more sensitive to higher Rouse modes.

By use of eqs 1.43b and 1.46 an analytical expression for the segmental mean square displacement can be derived [2]:

$$\langle (\mathbf{r}_\ell(t) - \mathbf{r}_\ell(0))^2 \rangle = 6D_{CM}\tau_R\tilde{t}_R + A\frac{Nb^2}{3\pi^2}(\tilde{t}_R)^{\frac{1}{2}}, \quad A \simeq 1.77. \quad (1.48)$$

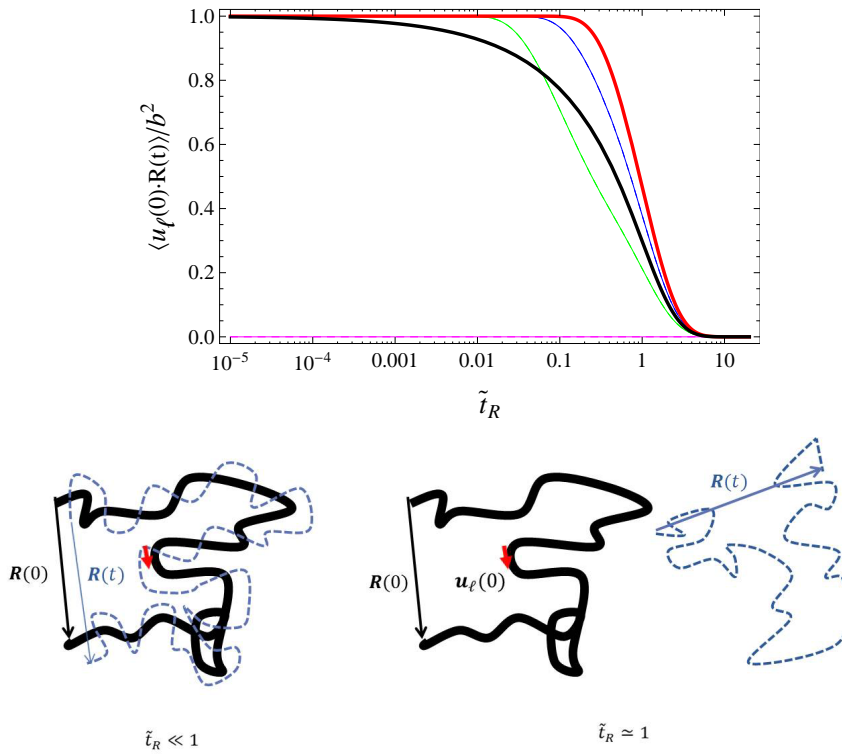


Figure 1.9: Upper: $\langle \mathbf{u}_\ell(0) \cdot \mathbf{R}(t) \rangle$ vs \tilde{t}_R for various segments along the chain; $\xi = 0, 0.15, 0.30$ correspond to magenta, green, and blue solid lines, respectively; dashed lines of the same colour refer to symmetric segments. Red line $\xi = 0.5$. The black line shows $\langle \mathbf{R}(t) \cdot \mathbf{R}(0) \rangle$. Bottom: Schematic illustration of the conformational relaxation of the chain at early and late times (left and right side respectively).

At times $\tilde{t}_R < 1$ the monomers execute sub-Fickian diffusion and the segmental mean-square displacement scales as $t^{0.5}$. In this regime, to move a distance $\Delta \mathbf{r}$, the ℓ th segment has to drag only the $\Delta \mathbf{r}^2 / b^2$ other monomers in the region spanned by $\Delta \mathbf{r}$. At times $\tilde{t}_R \approx 1$ every segment has realised that it belongs to a chain so ordinary diffusion takes place and $\langle (\mathbf{r}_\ell(t) - \mathbf{r}_\ell(0))^2 \rangle \approx 6D_{CM}t$. In this case a segment moves with the rest of the chain and the effective drag arises from the whole chain. Hence the diffusion coefficient associated with this motion is $D_{CM} = k_B T / (N\zeta_0)$.

The Rouse model in flow

Under a shear step deformation the relaxation modulus $G(t)$, plotted as a function of \tilde{t}_R in a log-log scale, displays two distinct regimes; for times $\tilde{t}_R < 1$ it decays with a slope of a half while a crossover to an exponential decay begins at $\tilde{t}_R \approx 1$. This behaviour can

also be explained in terms of the Rouse modes. Specifically, if unrelaxed, each of the N/p subchains (modes) contributes $k_B T$ to the relaxation modulus. Therefore, by using the time dependence of the mode index from eq 1.44, i.e. $p \approx (\tilde{t}_R)^{-1/2}$, one arrives at $G(t) \propto k_B T (\tilde{t}_R)^{-1/2}$ which is valid up to $\tilde{t}_R \approx 1$. As soon as the Rouse relaxation time is reached there are no larger subchains (modes) left to decorrelate and so there is a crossover to the final exponential decay. The explicit formula for the relaxation modulus of the Rouse model is

$$G(t) = \frac{ck_B T}{N} \sum_{p=1}^{\infty} \exp(-2p^2 \tilde{t}_R) \quad (1.49)$$

In oscillatory shear, the Rouse model predicts that both the storage and loss moduli are proportional to $\omega^{1/2}$ at high frequencies. At low frequencies $G' \propto \omega^2$ and $G'' \propto \omega^1$ as in the simple Maxwell model (Fig. 1.6). Furthermore, the Rouse model predicts that the zero shear viscosity scales linearly with the molecular weight of the chain. Indeed this is the case for linear polymer melts up to a critical value of molecular weight, M_{w_c} . However, according to measurements [73, 74], for molecular weights higher than M_{w_c} , the scaling exponent changes to ≈ 3.4 .

Validity of the Rouse model

The Rouse model describes well the dynamics of polymer melts when the chains are shorter than the critical molecular weight, M_{w_c} . Regardless of the molecular weight of the chain, it also describes well the melt dynamics when time-scales are shorter than some critical time (the entanglement relaxation time, see eq 1.50 below). Nevertheless, the model fails for dilute solutions where polymer chains are not entangled. It also fails for polymer melts when the molecular weight of the chains is above M_{w_c} .

For the former system the failure of the Rouse model is attributed to the neglect of hydrodynamic interactions (HI). HI are long-range interactions between different monomers. They are mediated by the solvent. In particular, movement of a given chain segment (monomer) generates the motion of the surrounding solvent molecules in the same direction; this motion of the solvent can, in turn, induce motion of another monomer in the same direction. A model that accounts for hydrodynamic interactions has been developed by Zimm [75]. (This model assumes that the moving polymer chain drags along the adjacent solvent molecules, forming a compact object that moves through the

medium.) As in dilute solutions, hydrodynamic interactions in concentrated solutions or melts also exist, however, it is generally believed that they are fully screened to the level of individual monomers. The underlying mechanism of the screening of hydrodynamic interactions has been a subject of considerable debate (see for example Ref. [76]).

For polymer melts, the failure of the Rouse model to predict the molecular weight scaling exponent of 3.4 (in the regime $M_w > M_{wc}$) is mainly attributed to the neglect of the topological interactions of neighbouring chains (entanglements). For $M_w > M_{wc}$, an alternative model that takes into account the mutual entanglements between the chains is required. This is the tube model of Doi and Edwards [26], and is presented in the next section. According to this model, the dominant relaxation mechanism in a melt of linear polymer chains is reptation. (The reptation process was first suggested by de Gennes [25].)

1.4.4 Dynamics of entangled polymers

Doi-Edwards (DE) tube model

To account for the entanglement effect Doi and Edwards [26], in their so-called tube model, adopted a mean field approach which reduced the many body problem to that of a single chain. In this approach the entanglements are replaced by a set of topological constraints that confine the chain in a tube-like region; the only available way for the chain to renew its configuration is by diffusing back and forth along its own contour length since lateral movement, beyond a particular length scale, is severely restricted. This length scale is known as the tube diameter a . However, it should be thought of as the spatial region between entanglements. Such a region consists of N_e segments so $a^2 = N_e b^2$, where b is the segmental distance (Kuhn length). N_e is referred to as the entanglement degree of polymerization. The relaxation time, τ_e , of these N_e segments is known as the entanglement relaxation time and it follows Rouse dynamics (eq 1.44). Hence it reads

$$\tau_e = \frac{\zeta_0 b^2}{3\pi^2 k_B T} N_e^2 = \tau_0 N_e^2. \quad (1.50)$$

Note that the finer details of the structure of the chain at length scales smaller than a are ignored. At these length scales the entanglement effect is unimportant and the dynamics

of the chain is described by the Rouse model.

The DE tube model is mainly concerned with the dynamics of a coarse grained chain, referred to as the primitive path (PP), which has the same topology as the tube itself relative to the topological constraints (c.f. Fig. 1.10 for a schematic representation). This primitive path follows Gaussian statistics at large length-scales; furthermore, at equilibrium, its mean square end-to-end distance $\langle \mathbf{R}_{pp}^2 \rangle$ is the same as the mean square end-to-end distance $\langle \mathbf{R}^2 \rangle$ of the actual chain. In other words the primitive path, hence the tube itself, is a random walk of step length a , thus

$$\langle \mathbf{R}_{pp}^2 \rangle = \langle \mathbf{R}^2 \rangle \Leftrightarrow a^2 Z = Nb^2 = aL, \quad (1.51)$$

where Z is the number of entanglements acting on the primitive path and L the equilibrium contour length of the PP.

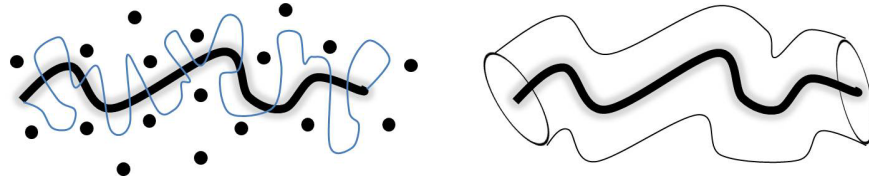


Figure 1.10: Left: The entanglements from the matrix chains to the test chain are depicted as black dots. The blue line represents the conformation of the test chain for length scales smaller than a . Right: The tube-like region that the constraints form to the test chain. The primitive path is shown in both sides as a bold black line.

Since this primitive path diffuses back and forth, i.e. it reptates, along the tube axis it satisfies a one-dimensional diffusion equation. The diffusion coefficient of this process (pure reptation) is $D_{CM} = k_B T (N \zeta_0)^{-1}$, i.e. the diffusion coefficient of the center of mass of a Rouse chain. Under the assumption of a constant contour length of the primitive path, Doi and Edwards solved the diffusion equation and obtained the tube survival probability $\psi(t)$:

$$\psi(t) = \sum_{p \text{ odd}}^{\infty} \frac{8}{p^2 \pi^2} \exp\left(-\frac{p^2 t}{\tau_b}\right). \quad (1.52)$$

The tube survival probability can be interpreted as the average (over all PPs of the system) fraction of the tube that remains occupied by the chain after a waiting time t , assuming that the whole chain is initially in the tube (that is, at $t = 0$, $\psi(0) = 1$). The

form of $\psi(t)$ implies that the longest relaxation time of the reptation process is τ_b . This characteristic time corresponds to the time taken for the entire primitive chain to escape by pure reptation from the tube it was initially confined within. It is known as the reptation time of the chain and is given by

$$\tau_b = \frac{\zeta_0 b^4 N^3}{\pi^2 k_B T a^2} = 3Z\tau_R. \quad (1.53)$$

This equation indicates that as the chain becomes longer the reptation time increases significantly ($\tau_b \propto N^3$). Furthermore, τ_b becomes much larger than τ_R for large N . This demonstrates the crucial effect of entanglements on the characteristic relaxation time of polymer chains.

Apart from the dynamics of the PP, Doi and Edwards [26] calculated the mean square displacement (MSD), $\Delta \mathbf{r}^2 = \langle (\mathbf{r}_\ell(t) - \mathbf{r}_\ell(0))^2 \rangle$, of a segment of the actual chain. The upper panel of Fig. 1.11 shows their prediction in a log-log scale (this plot is adopted from Ref. [26]). This plot suggests the existence of four distinct regimes, which have been identified in NSE experiments [70] and MD simulations (c.f. section 1.6 below).

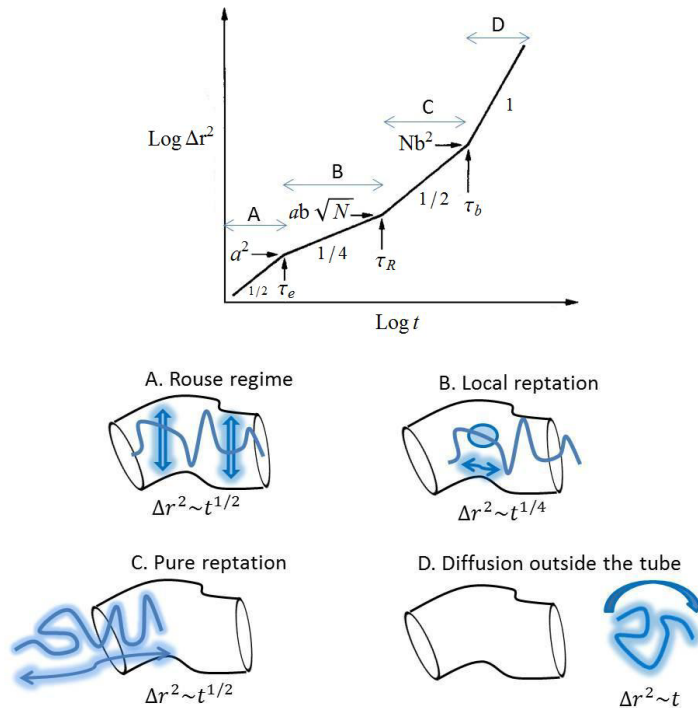


Figure 1.11: Upper: Segmental MSD of the actual chain vs time, as predicted by the tube model (CLF is included). The plots suggests the existence of four distinct regimes. Bottom: Schematic illustration of the chain motion at these four distinct regimes.

The first regime spans timescales up to τ_e . At these early times the segments have not yet realised the existence of the tube and $\Delta \mathbf{r}^2$ exhibits Rouse-like behaviour, that is, transverse (fast) Rouse modes dominate the dynamics and $\Delta \mathbf{r}^2 \propto t^{1/2}$. The second regime covers the time window $\tau_e < t < \tau_R$. In this regime the segments are constrained to diffuse along the primitive path. However, this diffusion process does not occur by pure reptation but by virtue of longitudinal slow Rouse (local reptative) modes. This regime is known as the ‘‘Rouse in tube’’ (or constrained Rouse) regime and $\Delta \mathbf{r}^2$ scales as $t^{1/4}$. The third regime spans the time interval $\tau_R < t < \tau_b$. Since $t > \tau_R$ all segments have realised that they belong to a chain that is confined in a tube. Therefore, diffusion of the center of mass of the chain (i.e. the pure reptation process described by eq 1.52) takes place in the tube. Finally for $t > \tau_b$, $\Delta \mathbf{r}^2 \propto t$ which indicates that the chain has escaped from the original tube and is able to move distances of its own contour. In other words it explores the melt by means of ordinary diffusion.

Tube model-Rheological predictions and limitations

In this section some of the predictions of the DE tube model for the rheological properties of monodisperse melts of linear chains are discussed. The model is successful in capturing experimental data for the relaxation modulus following a step shear deformation. For linear deformations the relaxation modulus can be estimated by simple arguments [26]. Specifically, at times $t \lesssim \tau_e$ the entanglement field is not yet encountered and dynamics is governed by the Rouse model. Thus $G(t)$ can be calculated from eq 1.49 after approximating the sum as an integral:

$$G(t) = \frac{ck_B T}{N} \int_0^\infty \exp(-2p^2 \tilde{t}_R) dp = \frac{ck_B T}{2\sqrt{2}N} (\tilde{t}_R)^{-\frac{1}{2}}, \quad \text{for } t \lesssim \tau_e. \quad (1.54)$$

For timescales $t \gtrsim \tau_e$ only sections of the chain that are still trapped in the tube contribute to stress, hence

$$G(t) = G_N^{(0)} \psi(t) = G_N^{(0)} \sum_{p,\text{odd}} \frac{8}{p^2 \pi^2} \exp\left(-\frac{p^2 t}{\tau_b}\right), \quad \text{for } t \gtrsim \tau_e, \quad (1.55)$$

where $\psi(t)$ is the tube survival probability (eq 1.52). The constant $G_N^{(0)}$ can be obtained by utilizing the fact that eq 1.54 smoothly crosses over to eq 1.55 at $t = \tau_e$, that is, $G_N^{(0)}$ is given by $G_N^{(0)} \simeq G(\tau_e) \simeq ck_B T N^{-1} (\tau_R/\tau_e)^{0.5}$. The linear relaxation modulus is shown at the left panel of Fig. 1.12. This plot reveals the following two features: (i) at early

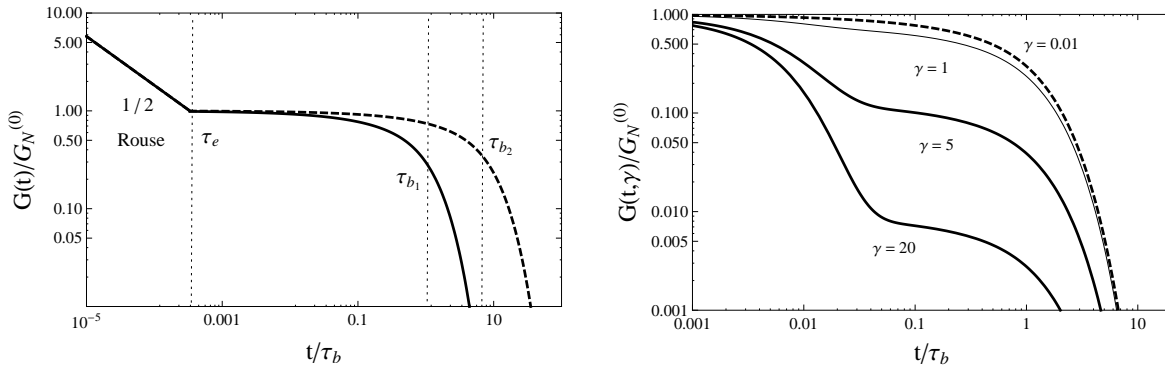


Figure 1.12: DE tube theory in step shear. Left: $\frac{G(t)}{G_N^{(0)}}$ against $\frac{t}{\tau_{b1}}$. The solid (dashed) line refers to chains of entanglement length Z_1 ($\frac{Z_2}{Z_1} = 2$) and reptation time τ_{b1} ($\frac{\tau_{b2}}{\tau_{b1}} = 8$). Up to $t \approx \tau_e$, $\frac{G(t)}{G_N^{(0)}}$ displays Rouse behaviour. Then, it establishes a plateau; the width of the plateau region increases with increasing chain length. Right: $\frac{G(t, \gamma)}{G_N^{(0)}}$ against $\frac{t}{\tau_b}$ for $\frac{\tau_b}{\tau_R} = 10^2$. Stress relaxation at high strains ($\gamma = 5, 20$) is a two stage process; the abrupt initial decay (final decline) is attributed to stretch (orientation) relaxation.

times $G(t)$ decreases with a constant slope of a half indicative of the Rouse behavior. (ii) At times $\tau_e \lesssim t \lesssim \tau_b$ the relaxation modulus forms a plateau as the chains are confined in their tubes; complete relaxation has to "wait" until the chains diffuse (reptate) out of the confining tubes and fully renew their conformations. Since $\tau_b \propto N^3$ an increase in the molecular weight of the chains prolongs the plateau regime. These predictions are in qualitative accordance with measurements [26, 77].

The right panel of Fig. 1.12 shows the non-linear relaxation modulus, $G(t, \gamma) = \sigma_{xy}(t, \gamma)/\gamma$, as a function of t/τ_b for several strains. From this plot it is evident that for the high non-linear strains ($\gamma = 5, 20$) stress relaxation occurs in two stages. During the first stage, that happens at times $t \approx \tau_R$, the PP chains retract along the tube axis and relax the imposed stretch. Throughout the stretch relaxation process, however, the tubes remain aligned in the flow direction and hence a plateau-like region appears at intermediate times. During the second stage, which occurs at times $t \approx \tau_b$, the PP chains reptate out of the tubes (that they are confined within) and alignment is lost. On the other hand, for strains up to $\gamma = 1$ the PP chains are not strongly stretched and stress relaxation is only attributed to reptation. The calculated shape of $G(t, \gamma)$ agrees qualitatively with experimental data [78, 79]; the same data indicate that $G(t, \gamma)$ is time-strain separable at large timescales, whereby it can be expressed as a product of two separate functions,

depending on γ and t respectively. Within the DE theory this separation is possible; for $\tilde{t}_R \gg 1$, $G(t, \gamma) = G(t)h(\gamma)$, where $G(t)$ is the linear viscoelastic modulus (eq 1.55) and $h(\gamma) \approx \left(1 + \frac{4}{15}\gamma^2\right)^{-1}$ is the so-called damping function.

In spite of the success of the Doi-Edwards tube model in capturing several aspects of the rheological properties of monodisperse melts of linear chains, and the inspirational influence to all successive researchers in this field, some of its predictions are not in accordance with experimental data. For instance, one failure of the DE theory arises in steady shear flow where it predicts a maximum for the steady shear stress, $\sigma_{xy}(\dot{\gamma}, t \rightarrow \infty)$, as a function of the shear rate. This maximum occurs at shear rates $\dot{\gamma} \approx \frac{1}{\tau_b}$. In contrast to the theoretical prediction, measurements reveal that the steady shear stress is monotonically increasing [80] or at worst has only a weak maximum [32]. Another shortcoming is found in oscillatory shear. Although the predictions of the DE model for G' and G'' agree qualitatively with experimental data they are insufficient to match the observed G' and (especially) G'' quantitatively [77]. Moreover, the model predicts that the steady state zero shear viscosity scales as M_w^3 whereas measurements [73, 74] suggest a scaling exponent which is closer to 3.4. In conclusion, the slowing down with respect to the Rouse dynamics and the reptation process itself are indisputable, however, the aforementioned discrepancies indicate that reptation is accompanied by additional relaxational mechanisms which are missing from the original DE theory. These physical mechanisms are discussed in the following section. Up to date tube theories that incorporate the missing physics in monodisperse melts of linear chains can be found in Refs. [2, 10, 11, 12, 13, 81].

1.4.5 Other relaxation mechanisms

The relaxation mechanisms which are neglected in the DE theory are namely, contour length fluctuations (CLF), chain stretch, and constraint release (CR). The inclusion of CLF improves the prediction of the DE tube theory with respect to the (incorrect) scaling exponent for viscosity with molecular weight. The CR events (chain stretch) mainly affect the linear (non-linear) viscoelastic properties of polymer melts. Moreover, at fast flow rates, constraint release has its non-linear counterpart known as convective constraint release (CCR).

Contour Length Fluctuation (CLF)

CLF originate from the fact that pure reptation only accounts for the 0th Rouse mode, i.e. the simultaneous motion of all segment mediated by the center of mass diffusion, and not for the full spectrum of Rouse modes. An inclusion of all other Rouse modes (for a 1-d Rouse chain) results in fluctuations of the length of the primitive path [81]. From another point of view, chain ends are subjected to an entropic tension $f_{ex} = 3K_B T/a$, which makes them explore the surrounding melt and therefore drives CLF.

The major effect of the CLF is the acceleration of τ_b relative to the prediction of the pure reptation model (eq 1.53); sections of the chain close to the chain ends can renew (relax) their configuration before the onset of reptation, so the path length that the chain has to diffuse via reptation reduces; the acceleration of τ_b , in turn, affects the zero shear viscosity through the analogous expression of eq 1.18, i.e. through $\eta_0 \propto G_N^{(0)} \tau_b$. It has been shown by Doi (chapter 6 of [26] and Refs. 15 and 16 therein) that the inclusion of CLF leads to an effective reptation time $\tau_b^F = \tau_b (1 - 2C_1 Z^{-0.5} + C_2 Z^{-1} + \dots)$ where C_1, C_2 are numerical constants and Z is the number of entanglements. This expression implies that CLF become less important with increasing chain length. Another contribution from Milner and McLeish [82] gives essentially the same result (c.f. Ref. [81]). These contributions improve the quantitative agreement of the tube model with the experimental data for the zero shear viscosity and the relaxation moduli [82]. However, the improvement is restricted to a range of molecular weights (chain lengths). Furthermore, some of the assumptions of these models are uncontrolled [81].

Likhtman and McLeish [81] used a combined theoretical and stochastic simulation approach to study the CLF. Using this approach the authors were able to calculate the numerical prefactors, C_1, C_2, \dots , in the aforementioned expression for τ_b^F for the whole range of molecular weights. Also, by adding CR, they were able, (i) to fit quantitatively the viscosity measurements of Colby et al. [74], which cover a wide range of molecular weights referring to either side of M_{wc} , and moreover, (ii) produce very good quantitative agreement for the relaxation moduli of monodisperse melts of polystyrene linear chains. A direct observation of CLF is possible using NSE spectroscopy [83, 84].

Chain stretch

When the flow rate is faster than the inverse of the stretch relaxation time, τ_s , polymer chains stretch, that is, the contour length of the chain exceeds the equilibrium value L . However, the contour length does not infinitely increase since its stretching is accompanied by an entropic cost; the chain will retract along the tube axis to maintain its equilibrium contour length. This physical process is known as chain retraction.

Since chain retraction, in linear polymers, occurs at the bare Rouse time of the chain (that is, $\tau_s = \tau_R$) Doi and Edwards assumed that for moderate non-linear (continuous) flows ($\tau_b^{-1} \lesssim \dot{\gamma} \lesssim \tau_R^{-1}$) the stretch, $\lambda = L(t)/L$, of the PP chains is equal to unity at all times. The consequence of this assumption is that the steady state viscosities in shear and extension, $\eta(\dot{\gamma}, t \rightarrow \infty)$ and $\eta^+(\dot{\epsilon}, t \rightarrow \infty)$ respectively, when plotted as a function of the flow rate in a log-log scale, decay monotonically in the region $\dot{\gamma}, \dot{\epsilon} \gtrsim \tau_b^{-1}$; at these rates tubes become aligned in the flow direction, orientation (in turn stress) is saturated, thus the viscosities drop monotonically with a slope of 1 (c.f. eq 1.10).

The assumption $\lambda = 1$ has been relaxed by Marrucci and Grizzuti [85] in the so-called Doi-Edwards-Marrucci-Grizzuti (DEMG) model. In a “toy” version of this model [86] the time evolution of the stretch obeys the differential equation: $d\lambda/dt = \lambda \mathbf{K} : \mathbf{S} - k_s(\lambda) \tau_R^{-1} (\lambda - 1)$ where the second-order tensor, \mathbf{S} , is the pre-averaged orientation of the PP chain. The first term of the latter expression models the affine stretch of the PP chain due to the flow while the second term represents the chain retraction process. The function $k_s(\lambda)$ controls the extensibility of the chain; if the chain is assumed to be infinitely extensible (as in the original DEMG model) then $k_s(\lambda) = 1$; if it is assumed to be finitely extensible then $k_s(\lambda)$ is given by the inverse Langevin function.

According to the DEMG model, the inclusion of chain stretch has a significant effect in extension. In particular, for rates $\dot{\epsilon} \gtrsim \tau_R^{-1}$ an abrupt upturn in the log-log plot of $\eta^+(\dot{\epsilon}, t \rightarrow \infty)$ occurs. This upturn is attributed to the fact that in extension $\mathbf{K} : \mathbf{S} = \dot{\epsilon} (S_{xx} - S_{yy})$ (which becomes simply $\approx \dot{\epsilon}$ after tube alignment in the flow direction), therefore, higher steady state values of stretch, and consequently of stress, are reached with increasing flow rate. These predictions are qualitatively similar with experiments on polymer solutions and polymer melts [87, 88] (some polystyrene melts, however, do not display the aforementioned upturn [89]). Although the inclusion of stretch could in

general lead to a similar behaviour in shear and remove the maximum in $\sigma_{xy}(\dot{\gamma}, t \rightarrow \infty)$, it does not; the flow term in shear approaches zero upon tube alignment since $\mathbf{K} : \mathbf{S} = \dot{\gamma} S_{xy}$ and so it is not strong enough to produce high stretches. For this reason the DEMG model, in the moderate non-linear regime and above, predicts shear-thinning as the original DE tube model. This implies that an additional physical process is missing, which has a major effect in the intermediate and fast flow regimes. This mechanism is constraint release.

Constraint release (CR)

An enlightening example to illustrate (thermal) CR events is a bi-disperse melt of long linear chains and short linear chains; the long (short) chains have molecular weight $M_{w,L}$ ($M_{w,S}$), reptation time $\tau_{b,L}$ ($\tau_{b,S}$), and entanglement length Z_L (Z_S). Provided that the long chains are long enough so as to mutually entangle, two types of entanglements exist: (1) entanglements between long and short chains and (2) entanglements between long chains. Figure 1.13 provides a schematic representation of this system.

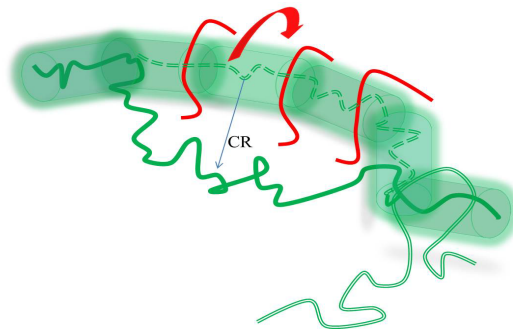


Figure 1.13: Thermal CR events in a bi-disperse melt of short (red colour) and long (green colour) linear chains. A given long chain can make local hops and explore the space that was previously occupied by the much faster reptating short chains.

Consider first the case where there are no entanglements between long chains. Since $\tau_{b,S} \ll \tau_{b,L}$, for time scales $\tau_{b,S} < t < \tau_{b,L}$, long chains can undertake local hops (“kinks”) exploring the space region that is released after the reptation of the short chains and the consequent destruction of the entanglement network. By these hops a long chain can locally renew its configuration and relax a fraction of imposed stress. However, global reconfiguration of a long chain is not possible on the time scale of $\tau_{b,S}$ since short chains can easily re-entangle with the long chain before the latter moves long distances. Thus,

“global conformational relaxation of a long chain requires numerous cycles of reptation of short chains and local motion of the long chain. Essentially, the long chain remains confined in a tube, but this tube is itself relaxing at a rate set by the reptation of the short chains” [29]. This relaxation process approximately resembles the relaxation of a Rouse chain, and for this reason is often referred to as the constraint-release Rouse (CR-Rouse) process [10, 12, 13, 90]. In analogy with $\tau_R = \tau_0 N^2$ the CR-Rouse relaxation time, τ_{CR} , is given by

$$\tau_{CR} \propto \tau_{obs} Z_L^2, \quad (1.56)$$

where τ_{obs} is the relaxation time of the “obstacles” (short chains), that is, $\tau_{obs} = \tau_{b,S} \propto Z_S^3$. Equation 1.56 implies that the effective friction controlling the rate at which a long chain undertakes hops is proportional to the relaxation time, $\tau_{b,S}$, of a short chain rather than proportional to the relaxation time, τ_0 , of a Rouse segment as in the pure Rouse model. When there are, additionally, entanglements between long chains, these provide additional barriers towards global reconfiguration of the long chains.

Note that the presence of the two aforementioned types of entanglements can lead one to conceptually visualise a long chain as being trapped in two tubes (rather than one); a thin tube representing both types of entanglements and a fat tube representing the entanglements between the long chains only [14, 15, 90, 91]. This physical picture gives rise to enriched and more complicated dynamics compared to the dynamics of a chain in a single tube. To quote an example, the terminal time of a long chain can be (in some occasions) the reptation time $\tau_{b,L}$ or (in other occasions) the CR-R relaxation time τ_{CR} . A phase diagram showing the different regimes of terminal relaxation in bi-disperse melts of linear chains has been suggested by Viovy et al. [91]. More recent theories for binary blends, that treat also the non-linear rheology, have been developed by Auhl et al. [14] and Read et al. [15]. The physical picture of the thin and fat tubes will be used in chapter 5 in the modeling of CR events in branched polymers.

In mono-disperse melts, however, there is only one type of entanglements (ideally, in practice one anticipates a range of molecular weights) and thus $\tau_{obs} = \tau_b \propto Z^3$; that is, the reptation time becomes faster than the CR-R relaxation time and therefore one would expect CR events to have a negligible effect on the relaxation dynamics. Nevertheless, it has been shown by Likhtman and McLeish [81] that thermal CR events influence the dynamics at times close to the terminal relaxation time τ_b .

Apart from thermal constraint release Marrucci [92] proposed that constraints are also released when flow rates are faster than τ_b^{-1} . This is because matrix chains are dragged away from a given test chain with subsequent loss of entanglements. This mechanism, as thermal CR, permits the test chain to make hops and relax its local configuration. These hops (i) increase the S_{xy} component of the orientation tensor, \mathbf{S} . Moreover, (ii) they increase the tube length and chain stretch. These two effects, in principal, could increase the σ_{xy} stress component and remove the maximum in $\sigma_{xy}(\dot{\gamma}, t \rightarrow \infty)$ in the intermediate flow regime and above. In fact, this is the case in all models that have included this convective constraint release (CCR) [11, 12, 13, 81, 93]. A molecular observation of CR in polymer melts is possible by means of NSE spectroscopy [94].

1.5 Molecular Models: branched polymers

Since the introduction of the DE tube model there has been an effort to extend this model to branched polymers. Such polymers contain sections which have either one free end or no free ends at all. In these structures reptation is suppressed since it would require multiple parts of the chain to occupy the same section of the tube. Thus the dynamics of branched polymers is governed by a different relaxation mechanism.

1.5.1 Relaxation in Star polymers

Monodisperse star polymers, due to their simplicity in respect to other branched molecules, were the first to be examined. Pearson and Helfand [95] recognized that a star polymer can relax its configuration (and stress) via activated contour length fluctuations (CLF), also known as arm retraction or breathing modes. As discussed in section 1.4.5, in linear chains, these fluctuations relax the conformation of the chain only near the chain ends as they are cut off as soon as reptation sets in. For star polymers, however, reptation is quenched and thus the CLF continues all the way back to the branch point. If these fluctuations are deeper than an entanglement spacing, then the star arm has to manoeuvre around the entanglements in order to fluctuate.

This process is accompanied by an entropic penalty since the chain has to adopt configurations which are entropically unfavourable. The situation is analogous to a

particle diffusing over a potential barrier. This barrier was modelled by Pearson and Helfand [95] by the quadratic potential $U(s_\ell) = \frac{15}{8}Z_a s_\ell^2$, where Z_a is the number of arm entanglements; the time taken for the arm tip to diffuse a fractional distance s_ℓ ($0 < s_\ell < 1$) towards the branch point can be obtained by solving the first passage problem in this type of potential, leading to

$$\tau(s_\ell) = \tau_{\text{pre}} \exp [U(s_\ell)], \quad (1.57)$$

where τ_{pre} is roughly the Rouse relaxation time of the arm. Nevertheless, this calculation is insufficient to match quantitatively experimental data for G' and G'' . In particular, the approach correctly predicts a broadening of the relaxation spectrum relative to that of a linear chain but enormously overestimates the terminal relaxation time [95].

Ball and McLeish [96] noted that eq 1.57 implies a very broad spectrum of relaxation times; when relaxation reaches a fractional distance s_ℓ (from the free end) arm segments with fractional distance $s'_\ell < s_\ell$ have renewed their configurations many times. In other words, all relaxed (non confined) portions of the chain are moving much faster than the unrelaxed portions and so they do not impose any constraints (entanglements) on the motion of the unrelaxed section. As a result of these constraint release events arm retraction takes place into a continuously dilating tube. This progressive dilution of the entanglement network is referred to as “dynamic dilution” and speeds up the arm retraction process. Ball and McLeish suggested this gives rise to a potential barrier which is no longer quadratic in s_ℓ but cubic:

$$U(s_\ell) = \frac{15}{8}Z_a \left(s_\ell^2 - \frac{2}{3}s_\ell^3 \right). \quad (1.58)$$

This equation has been derived under the following two assumptions, entanglement are binary events involving two chains (as schematically shown at the upper panel of Fig. 1.2), and polymer chains are Gaussian. These assumptions imply that the degree of polymerisation scales with the fraction of unrelaxed material, $\phi(s_\ell)$, as $N_e(\phi(s_\ell)) = N_e/\phi(s_\ell)$ where $\phi(s_\ell) = 1 - s_\ell$. As a result, the tube diameter increases with time as $a_{ef}(t) = a\phi(s_\ell)^{-0.5}$ (recall that $a^2 = N_e b^2$).

Colby and Rubinstein [97, 98], however, proposed that the entanglement degree of polymerisation scales as $N_e(\phi(s_\ell)) = N_e/\phi(s_\ell)^{\alpha_d}$, where $\alpha_d = 4/3$ is the so-called

dilution exponent. In this case the effective tube diameter, at time t , reads

$$a_{ef}(t) = \frac{a}{\sqrt{\phi(s_\ell)^{\alpha_d}}}. \quad (1.59)$$

Milner and Mcleish [99], in a refined version of Ref. [96], considered this option and derived the analogous potential of eq 1.58, and the corresponding expression for $\tau(s_\ell)$; the resulting potential is slightly softer than that of eq 1.58 hence the corresponding relaxation times $\tau(s_\ell)$ are faster, particularly in the proximity of the branch point. Furthermore, rather than using the Rouse relaxation time of an arm as an estimate for τ_{pre} , the authors used scaling arguments to derive an expression for τ_{pre} . The incorporation of these effects provides a quantitative agreement with experimental data for G' and G'' over five decades in frequency, from the terminal region up to the start of the high-frequency Rouse regime [99].

Independent of the exact form of $U(s_\ell)$ the (arm retraction) relaxation times $\tau(s_\ell)$ depend exponentially on the number of arm entanglements. This fact is taken into consideration in chapter 4 in the expressions for the reptation time and stretch relaxation time of a pom-pom (eqs 4.3). The concepts of “dynamic dilution” and arm retraction have also been applied to more complicated topologies including the pom-pom molecule, which is discussed in the following section.

1.5.2 The pom-pom molecule

The pom-pom molecule is an idealised molecular structure which has been introduced by McLeish and Larson [8] in order to model the non-linear rheology of industrial resins. A pom-pom molecule consists of two q -armed stars connected by a linear backbone which is also known as the cross-bar. Apart from q , the other structural parameters of a pom-pom polymer are $Z_b(= M_{w_b}/M_e)$ and $Z_a(= M_{w_a}/M_e)$, the number of entanglements acting on the cross-bar and on an arm, respectively. In these expressions M_{w_b} (M_{w_a}) is the molecular weight of the backbone (arm) and M_e is the entanglement molecular weight. Furthermore, the volume fractions of backbone and arm material are respectively defined as

$$\phi_b = \frac{M_{w_b}}{M_{w_b} + 2qM_{w_a}}, \quad \text{and} \quad \phi_a = \frac{2qM_{w_a}}{M_{w_b} + 2qM_{w_a}}. \quad (1.60)$$

A chain of pom-pom topology relaxes its configuration in a hierarchical manner. The different stages of this hierarchical relaxation are shown schematically in Fig. 1.14. First the dangling arms renew their conformation via activated CLF in an identical fashion to a single polymer star. During this arm retraction process the branch points are essentially pinned hence motion of the backbone is to a high degree suppressed. At these timescales the branch points and the segments of the backbone can only fluctuate locally (local motion of the branch points is studied in chapter 2). This physical picture holds for times $t < \tau_a$ (τ_a is the time taken for an arm tip to reach the branch point thus is the time taken for an arm to execute one full retraction). For $t > \tau_a$ each time an arm fully retracts the branch point is able to undertake a diffusive hop (step). The diffusion coefficient for such a step is

$$D_{bp} = \frac{a_{ef}^2(t)p^2}{2\tau_a q}, \quad (1.61)$$

where $a_{ef}(t)$ is the effective tube diameter at time t (eq 1.59) and p is a numerical coefficient which denotes the fraction of the tube diameter that a branch point diffusively hops. The factor of q^{-1} arises from the fact that the branch point has to drag the q arms in order to hop. Note that in this case the fraction of unrelaxed material is defined as $\phi(s_\ell) = \phi_b + \phi_a(1 - s_\ell)$; since arm retraction has reached the branch point, $s_\ell = 1$, and so $\phi(s_\ell)^{\alpha_d} = \phi_b^{\alpha_d}$. By these diffusing hops the backbone is able to relax its stretch, in cases in which its equilibrium primitive path length has been extended by a non-linear flow.

After many cycles of full retractions of the arms, i.e. at times $t \gg \tau_a$, the backbones themselves are the dynamical objects and all arm material acts as a solvent because it exhibits much more rapid dynamics. Therefore the backbones behave essentially as linear chains and reptate. However, the effective drag is not uniformly distributed along the cross-bar but is localized at the two branch points because of the arms. This effective reptation process is accomplished via the diffusive steps of the branch points. According to this physical picture, the reptation time can be estimated from $\tau_b = L_{ef}^2(\pi^2 D)^{-1}$ where L_{ef}^2 is the mean square distance of the dilated backbone primitive path and $D = D_{bp}/2 = k_B T \zeta$ (the drag, ζ_{bp} , of each branch point is additive hence $\zeta = 2\zeta_{bp}$). Using eq 1.61 (assuming however that the hops occur in the undiluted tube a) and $L_{ef} = a_{ef} Z_{b_{ef}} = a_{ef} \phi_b^{\alpha_d} Z_b$ one obtains the orientation relaxation time of the backbone

$$\tau_b = \frac{4q\tau_a Z_b^2}{\pi^2 p^2} \phi_b^{\alpha_d}. \quad (1.62)$$

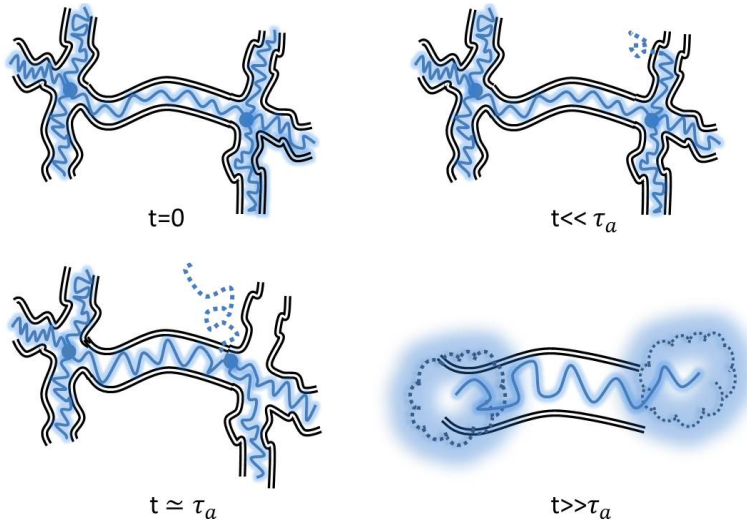


Figure 1.14: Hierarchical relaxation of a pom-pom molecule. Upper left: The initial conformation of the chain immediately after an imposed strain. Upper right: At a later time, $t \ll \tau_a$, branch points and backbone segments are essentially pinned; only sections of the arms close to the arm tips renew their conformation. Bottom left: At times $t \gtrsim \tau_a$, each time an arm fully retracts, the branch points make diffusive hops. Bottom right: At much later times, $t \gg \tau_a$, backbones relax via renormalised reptation in a dilated tube.

The former expression (with $p^2 = 1$ and $\alpha_d = 1$) corresponds to the one presented in the original work of McLeish and Larson [8].

An additional factor of $\phi_b^{\alpha_d}$ arises in eq 1.62 if one assumes that the diffusive steps occur in the dilated tube. On the other hand, $\tau_b = 4q\tau_a Z_b^2 (\pi^2 p^2)^{-1}$ for diffusive hops in the undilated tube and reptation along an undilated primitive path. Regardless of the power law of $\phi_b^{\alpha_d}$, τ_b scales as Z_b^2 and not as Z_b^3 as for ordinary linear chains. This is because the friction is dominated by the branch points so is independent of the length of the cross-bar. Moreover, τ_b is proportional to τ_a hence it depends exponentially on the number of arm entanglements Z_a . In chapter 4, where the original pom-pom model is refined, this dependence is taken into consideration in the equivalent expression of eq 1.62 (eq 4.3a).

A constitutive equation for a monodisperse melt of pom-pom molecules has been developed in Ref. [8]; within this approach, particular attention is paid to the non-linear rheology of the pom-pom molecule, that is, the response of a pom-pom melt to strain (flow) rates faster than the inverse of τ_b , nevertheless slower than the inverse of τ_a , is

more of interest. In this regime of flow rates, the arm relaxation process is effectively instantaneous; arms are considered unstretched hence contribute only to a background Newtonian viscosity. As a result the polymer stress emerges, to a good approximation, only from the cross-bar material. This stress is determined by three dynamical variables. The first one is the pre-averaged backbone tube orientation, $\mathbf{S} = \langle \mathbf{u}\mathbf{u} \rangle$, where \mathbf{u} is a unit vector denoting the orientation of a (backbone) tube segment at time t . The other two variables are the pre-averaged stretch of the backbone, λ , and the length of arm material withdrawn into the backbone tube, s_c .

With respect to \mathbf{S} its time evolution is given by

$$\mathbf{S} = \frac{\mathbf{A}}{\text{tr}\mathbf{A}}, \quad \text{with} \quad \frac{d\mathbf{A}}{dt} = \mathbf{K} \cdot \mathbf{A} + \mathbf{A} \cdot \mathbf{K}^T - \frac{1}{\tau_b} \left(\mathbf{A} - \frac{1}{3}\mathbf{I} \right) \quad (1.63)$$

where \mathbf{A} is an auxiliary tensor, \mathbf{K} is the velocity gradient tensor and τ_b is the reptation (orientation) relaxation time (eq 1.62). The differential approximation of eq 1.63 has been suggested by Dr. O. Harlen to ease the considerable computation effort which is demanded to solve the integral version of \mathbf{S} [8]. As shown in Ref. [8], it predicts qualitatively the same behaviour as the integral approximation is shear and uniaxial extension. However, for (large) non-linear shear step strains, the two versions predict qualitatively different behaviour for the damping function at times beyond τ_b [62, 100]. A review of the differential and integral versions of the orientation tensor of the pom-pom model can be found in Ref. [101]. The differential version is adopted, hereafter, for computational ease.

The dynamics of the backbone stretch, λ , is controlled by the following equation:

$$\frac{d\lambda}{dt} = \lambda \mathbf{K} : \mathbf{S} - \frac{1}{\tau_s} (\lambda - 1), \quad (1.64)$$

with $\tau_s = q\tau_a Z_b/3$ being the stretch relaxation time of the backbone; as for τ_b , factors of $\phi_b^{\alpha_d}$ arise in the expression for τ_s depending on the particular choice of tube diameter (dilated or non dilated) [2]. Note that the ratio τ_b/τ_s is proportional to the number of backbone entanglements Z_b . Equation 1.64 holds for $\lambda < q$. When $\lambda = q$ the spring tension equals the free end tension. Beyond this, the tension at the backbone is sufficient to withdraw the branch points (consequently arm material) into sections of the backbone tube. This arm material becomes aligned with the tube so its contribution to the stress is minor [8]. For this reason the dynamics of s_c , the length of arm material withdrawn into

the backbone tube, is typically ignored [9, 102, 103]. To summarise the stretch dynamics, λ has an upper bound, the so-called maximum stretch condition, $\lambda = q$; at this point two opposing factors contribute to λ . The flow, which tends to stretch the backbone further, and branch point withdrawal, which occurs on the timescale of the Rouse time of the chain (i.e. is instantaneous on the flow timescale), and tends to keep λ equal to q . On the other hand, as long as $\lambda < q$, the evolution of the stretch is governed by eq 1.64.

Finally the contribution of the cross-bar to the stress is: $\sigma = 3G_0\phi_b^2\lambda^2\mathbf{S}$. This expression together with eqs 1.63 and 1.64 are the constitutive equation of the original pom-pom model. In the expression for the stress one factor of ϕ_b comes from tube dilation due to the fully relaxed arms. The second factor arises from the fact that only backbone material contributes to the stress.

Figure 1.15 shows how the model performs in continuous shear and (uniaxial) extension (for the parameterisation set see the caption of the figure). From this figure it is evident that the model predicts a qualitatively different response under the two flows. Specifically, for the non-linear shear (extensional) rates, $\dot{\gamma} = 1, 10\text{s}^{-1}$ ($\dot{\epsilon} = 1, 10\text{s}^{-1}$), the transient response is below (above) the linear one for $\dot{\gamma} = 0.01\text{s}^{-1}$ ($\dot{\epsilon} = 0.01\text{s}^{-1}$). Therefore, the pom-pom model predicts qualitatively the shear thinning and extensional hardening behaviour, of industrial resins, which was discussed in section 1.2.5. The strain

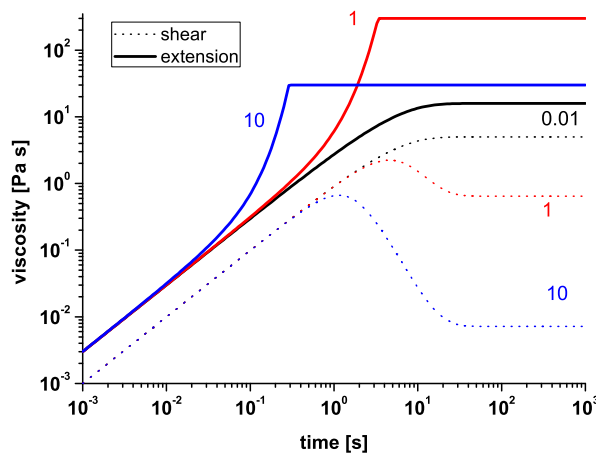


Figure 1.15: The predictions of the pom-pom model in continuous shear (dashed lines) and uniaxial extension (solid lines) for three different rates; $\dot{\gamma}, \dot{\epsilon} = 0.01\text{s}^{-1}$ (black), $\dot{\gamma}, \dot{\epsilon} = 1\text{s}^{-1}$ (red), and $\dot{\gamma}, \dot{\epsilon} = 10\text{s}^{-1}$ (blue). The model predicts transient extensional hardening and transient shear thinning. $G_0 = 1\text{Pa}$, $\tau_b = 5\text{s}$, $\tau_b/\tau_s = 4$, $q = 10$ and $\phi_b = 1$.

hardening in extension is an indirect consequence of the hierarchical relaxation of the molecule; stretch relaxation starts only after an arm has completely retracted and so the flow has enough time to efficiently stretch the backbone.

Note that for $\dot{\epsilon} = 1, 10\text{s}^{-1}$ the extensional viscosity forms a plateau at steady state. This plateau is the result of orientation and stretch saturation. In particular, all tubes are on average aligned in the flow direction (so that $S_{xx} - S_{yy} \approx 1$) and the stretch value is dictated by the maximum stretch condition $\lambda = q$. As a result, the model predicts a steady state plateau for all flow rates which are fast enough to make the backbone achieve its maximum extensibility. This feature renders the original version of the model unsuitable for matching uniaxial extensional viscosity data of industrial melts, which indicate that the viscosity overshoots. In chapter 4 the constitutive equation of the original model is modified so as to enable a viscosity overshoot in uniaxial extension. In the next section some revisions of the original pom-pom model are briefly discussed. However, these refined versions are unable to predict an overshoot in $\eta^+(\dot{\epsilon}, t)$.

Revisions to the pom-pom model

If the steady state values for $\eta^+(\dot{\epsilon}, t \rightarrow \infty)$, as predicted by the original model, are plotted as a function of $\dot{\epsilon}$, then a sharp peak is observed [8]. This behaviour is inconsistent with experimental data for mono-disperse H-polymer melts [41]. Blackwell et al. [102] proposed a modification in the stretch relaxation time which removes this abrupt peak. In more details, the authors considered local branch point displacement (withdrawal) in the backbone tube prior to maximum stretch. As arm material is withdrawn into the cross-bar tube the entanglement path length of the arm material shortens and thus τ_a , in turn, τ_s speed up. By considering local branch point motion within a quadratic potential one can estimate the modified stretch relaxation time [2, 102]:

$$\tau_s \rightarrow \tau_s \exp\left(\frac{-2(\lambda - 1)}{q - 1}\right). \quad (1.65)$$

This modification of the original model, referred to as the drag-strain coupling, produces more moderate values of stretch compared to the original version and so smooths out the aforementioned peak in $\eta^+(\dot{\epsilon}, t \rightarrow \infty)$ [102].

Another drawback of the constitutive equation introduced in Ref. [8] is that it gives a zero second normal stress difference, Ψ_2 , in shear [8]. On the contrary experimental

studies indicate a non zero Ψ_2 [104]. Alternative approximations, such as the extended pom-pom (XPP) model [105] and the double convected pom-pom (DCPP) model [56, 57, 106], have been suggested to resolve this discrepancy. Although these approximations successfully forecast a non zero Ψ_2 they disregard an important piece of physics of the pom-pom model, namely the maximum stretching $\lambda = q$. A version that retains the maximum stretch condition and gives $\Psi_2 \neq 0$ has been introduced by Öttinger [107].

As pointed out by Lee et al. [108], complex flow situations, like contraction-expansion flows and large amplitude oscillatory shear (LAOS) flows, require careful treatment with respect to the orientation relaxation time that one should use in eq 1.63. This is because in such flows there are occasions in which the length of the primitive path is brought below its equilibrium value. Accordingly, the authors of Ref. [108] proposed an effective reptation time, τ_b^* , for $\lambda < 1$, given by $(\tau_b^*)^{-1} = \tau_b^{-1} + \dot{\lambda}/\lambda - \mathbf{K} : \mathbf{S}$.

Multimode versions-randomly branched polymers

The branching structure of industrial grade polymeric material like LDPE is vastly more complex than that of a simple pom-pom; LDPE melts contain chains with multiple (and irregularly spaced) long chain branches. Therefore, a single mode version of the initial pom-pom model (and of the refined versions) fails to predict quantitatively the rheology of commercial melts. A multimode version of the model, however, which successfully captures many aspects of the flow behaviour of LDPEs has been suggested by Inkson et al. [9].

In this multimode approach the complex structure of a complex branched chain is modelled by a superposition of pom-poms (modes) of different relaxation times and arms. Moreover, these modes are assumed decoupled hence their stress contribution is summed, leading to the following expression for the total stress:

$$\boldsymbol{\sigma}_{total} = \sum_i \boldsymbol{\sigma}_i = \sum_i 3G_{0_i} \lambda_i^2 \mathbf{S}_i, \quad (1.66)$$

where i is an index denoting modes; the orientation, \mathbf{S}_i , and stretch, λ_i , of each mode are given by eqs 1.63 and 1.64, respectively. The relaxation times τ_b and τ_s , however, are not given by $\tau_b = 4q\tau_a Z_b^2 \phi_b / \pi^2$ (eq 1.62) and $\tau_s = q\tau_a Z_b / 3$, they are extracted by fitting linear and non-linear viscoelastic data of a given melt. On the one hand, τ_{b_i} together with

G_{0_i} control the linear viscoelastic properties of a melt (as discussed in section 1.2.4) and thus can be determined by fitting G' and G'' ; on the other hand, τ_{s_i} alongside q_i control the non-linear response of a melt, therefore, can be obtained by matching (for instance) the uniaxial extensional viscosity [9]. For this reason the multimode approach of Inkson et al. [9] may be considered as a generalisation of the practise of fitting a set of Maxwell modes to shear oscillatory data. Having obtained the set of parameters, $[G_{0_i}, \tau_{b_i}, \tau_{s_i}, q_i]$, one can use it to calculate the stress response in other simple flows (e.g. shear flow and planar extension) and/or more complex flows (e.g. cross-slot and LAOS) [9, 62, 103, 108].

It is worth emphasising that the range of values for τ_{s_i} and q can be narrowed by arguments based on the pom-pom physics. These arguments are detailed in section 4.1 of chapter 4. The range of $[\tau_{s_i}, q]$ values can be further narrowed by evaluating the performance of the pom-pom model in various flows. For instance, if two different sets of $[\tau_{s_i}, q]$ produce the same result in uniaxial extension, one set can be considered superior to the other if at the same time it describes successfully the flow behaviour in other deformation modes, e.g. exponential shear [103] and LAOS. Nevertheless, the non-linear pom-pom spectrum, $[\tau_{s_i}, q_i]$, does not necessarily provide a precise characterisation of the molecular topology. These parameters are associated with the actual molecular values and give an estimate of the molecular architecture, however, the decoupling of the real structure into individual pom-poms weakens the quantitative link between the parameters and the true molecular values.

In chapter 4 a refined version of the original pom-pom model that enables viscosity overshoots in uniaxial extension is proposed. The decoupling of the real structure of a LDPE into individual pom-poms, suggested by Inkson et al., is adopted in order to capture experimental data of the commercial melt DOW150R. The modification implied by the drag-strain coupling (eq 1.65) is also taken into account, for both τ_s and τ_b . For reasons that will become clear in chapter 4 three different options for the equation of the time evolution of \mathbf{S} are considered. The first of them is eq 1.63. In the second expression τ_b is amplified by λ^2 ; this alteration was first suggested in the XPP model [105] and used subsequently in the DCP model [56, 106]. The third option corresponds to the expression that was ruled out in Ref. [8] for not exhibiting the correct asymptotic behaviour in shear. For all three options the expression for $d\lambda/dt$ is given by eq 1.64.

1.6 Molecular Dynamics

Up to this point we have seen how the dynamics of polymer chains are investigated by means of experimental techniques and analytical/semianalytical studies like the Rouse and the tube models. Another tool, which gains constantly power due to modern computational resources, is the Molecular Dynamics (MD) simulations [109, 110, 111]. The advantage of the MD simulations over the aforementioned models is the fact that the simulations directly examine the multichain problem hence they do not suffer from potentially erroneous approximations as the models do.

In a well entangled melt the relaxation times of the various dynamic processes cover an extremely broad spectrum, ranging from picoseconds (reorientation of the monomeric bonds) to times which can be easily of the order of seconds (reptation, arm retraction). Unfortunately, the current computational capabilities do not allow the running of a single MD simulation that would capture all these phenomena. For this reason polymer melts are typically simulated using a coarse-grained description of the chain that neglects atomistic details, that is, several atoms of the chain are represented by a united bead. Characteristic features of a polymeric liquid such as connectivity and uncrossability are then taken into account by introducing appropriate interactions between the united beads.

The potentials that describe these interactions have been proposed by Grest and Kremer [112]. In particular, excluded volumed interactions (uncrossability effects) are modeled by a repulsive Lennard-Jones (LJ) potential:

$$U_{\text{LJ}}(r) = \begin{cases} 4\epsilon \left[\left(\frac{\sigma}{r}\right)^{12} - \left(\frac{\sigma}{r}\right)^6 + \frac{1}{4} \right] & \text{for } r \leq r_c, \\ 0 & \text{for } r > r_c, \end{cases} \quad (1.67)$$

where the cut-off distance $r_c = 2^{1/6}\sigma$ is chosen so that only the repulsive term of the LJ potential is used. Typically the energy unit is set by $\epsilon = k_B T$ and the length unit by the diameter, σ , of the beads. The corresponding time unit is given by $\tau_0^{MD} = (m_0 \sigma^2 / \epsilon)^{1/2}$ where m_0 is the monomer mass. Connectivity between successive beads is provided by the finitely-extensible non-linear elastic (FENE) potential:

$$U_{\text{FENE}} = \begin{cases} -\frac{1}{2} K_F R_F^2 \ln \left[1 - \left(\frac{r}{R_F}\right)^2 \right] & \text{for } r \leq R_F \\ 0 & \text{for } r > R_F. \end{cases} \quad (1.68)$$

In this equation $K_F = 30\epsilon/\sigma^2$ and $R_F = 1.5\sigma$ are the spring constant and the maximum bond length, respectively.

Apart from $U_{LJ}(r)$ and $U_{FENE}(r)$ subsequent MD studies of polymer melts [1, 113, 114] include a bending potential of the form

$$U_{\text{bend}}(\theta) = k_\theta(1 - \cos \theta), \quad (1.69)$$

where θ is the bending angle in between two adjacent bonds and k_θ is the strength of the bending potential. The latter is set equal to zero and 2ϵ for flexible and semiflexible chains, respectively. With the introduction of some local stiffness chains become more entangled. This is advantageous in terms of computational time since one can simulate, with the same degree of polymerisation N , more strongly entangled systems than by using flexible chains.

Having defined the potentials describing the interactions between the beads the time evolution of the conformations of the chains are obtained by integrating the equations of motion, namely

$$m_0\ddot{\mathbf{r}}_i = -\nabla U(\mathbf{r}_i) - \Gamma\dot{\mathbf{r}}_i + \mathbf{f}_i(t), \quad (1.70)$$

where (for the i th bead) \mathbf{r}_i is the position vector, U is the total interaction potential with the other beads, $\Gamma = -0.5m_0/\tau_0$ is the friction coefficient, and \mathbf{f}_i is a noise term with second moment $\langle \mathbf{f}_i(t) \cdot \mathbf{f}_j(t') \rangle = \delta_{ij}\delta(t - t')6k_B T\Gamma$.

With trajectories at one's disposal many observables are accessible. One of them is the mean square displacement (MSD) of a bead $\langle \Delta \mathbf{r}^2 \rangle = \langle (\mathbf{r}_i(t) - \mathbf{r}_i(0))^2 \rangle$. MD simulations on melts of linear chains have justified the Rouse behaviour at early timescales; the same studies have demonstrated that central monomers obey the predictions of the DE tube model (the four distinct regimes in Fig. 1.11) whereas segments close to the chains ends follow much faster dynamics [1, 113, 114, 115].

MD studies on branched polymer melts have been scarce due to their high computational expense; branched polymers have in general much longer relaxation times than linear ones hence their equilibration is a much more difficult procedure. Fortunately, efficient methods combining Monte Carlo (MC) and MD simulations have been developed recently to equilibrate large-scale conformations with relatively low computational cost [116]. These equilibration methods, together with high parallelization,

render MD simulations on entangled branched architectures plausible with modern computational resources.

Such MD simulations on melts of entangled symmetric three arm stars and Cayley trees have been employed in a cooperative work with P. Bačová, Dr. A. J. Moreno and Dr. D. J. Read [1]. In these simulations eight entanglements long ($Z_a=8$) star arms have been considered. Cayley trees have been constructed by attaching a two entanglements long side arm in the centers of the $Z_a=8$ star arms. The eight entanglements long arms (of the star and of the Cayley tree) have been divided into segments of one entanglement, i.e. into eight entanglement segments per arm, and the average (over equivalent segments on each arm) MSD, $\langle \Delta \mathbf{r}^2 \rangle$, of these segments has been evaluated.

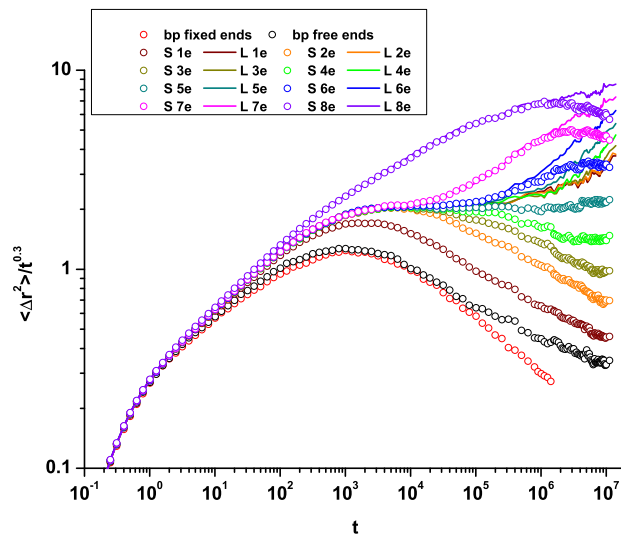


Figure 1.16: Segmental MSD, as obtained from MD simulations on entangled three arm symmetric stars (open circles) and on entangled linear chains (lines), for various entanglement segments along the chains; for the correspondence between colours and entanglement segments see the legend. Black and red open symbols refer to the MSD of the simulation branch point, as calculated from simulations in which chain ends were free and fixed, respectively. All data are provided by P. Bačová and Dr. A. J. Moreno.

Figure 1.16 shows with open circles the obtained $\langle \Delta \mathbf{r}^2 \rangle$, divided by $t^{0.3}$, for the symmetric star as a function of time (for the correspondence between the colours and the entanglement segments see the legend of the figure). The time axis, as in all figures of chapters 2 and 3 that contain MD data, is expressed in simulation units τ_0^{MD} . In the same figure the respective results for a linear chain (which is treated as a two arm symmetric

star and so $Z = 2Z_a = 16$) are included as lines for comparison. The analogous figure for the Cayley tree is published in the joint paper [1]. In figure 1.16, apart from the MSD of every entanglement segment, the MSD of the “simulation branch point” is depicted with open black and open red circles; these symbols correspond to MD with free and fixed chain ends during the simulations, respectively. Hereafter, the term “simulation branch point” refers to the actual branch point of the simulation and the three nearest monomers on each arm. Note that with respect to the Cayley tree the former term refers to the central branch point of the structure. Figure 1.16 reveals several features:

- Up to $\tau_e \approx 1800\tau_0^{MD}$ all segments in both structures follow Rouse behaviour. However, the data in this regime are better described by a scaling exponent of 0.6 instead of the 0.5 exponent anticipated for pure Rouse behaviour. This slight discrepancy can be attributed to the semiflexible character of the chains (here, $k_\theta = 2\epsilon$).
- All segments, except the branch point and the outer entanglement segment of both structures, obey the “Rouse in tube” (constrained Rouse) dynamics for at least a portion of the time window $\tau_e < t < \tau_{Ra}$ where $\tau_{Ra} = \tau_e Z_a^2 \approx 10^5 \tau_0^{MD}$ is the Rouse relaxation time of an arm. Here, this regime appears as a horizontal line since the MSD is divided by $t^{0.3}$. Again, due to semiflexibility, $\langle \Delta \mathbf{r}^2 \rangle$ scales as $t^{0.3}$ rather than $t^{0.25}$ as the DE tube model predicts (c.f. regime B of Fig. 1.16). The departure from the constrained Rouse behaviour depends strongly on the topology. For the linear chains the MSD, for all segments, increases as soon as reptation sets in; this transition to reptation dynamics occurs earlier as the chain end is approached. In contrast, the MSD for the stars spreads out dramatically. Middle sections of the arm (e.g. dark cyan circles) follow the constrained Rouse dynamics longer than the inner (outer) sections which obey much slower (faster) dynamics. These observations are consistent with the arm retraction process discussed in section 1.5.1.
- The MSD of the two outer entanglement segments of the linear chains (violet and magenta lines) and of the star arms (violet and magenta circles) are indistinguishable up to $t \approx 3 \times 10^6 \tau_0^{MD}$; this indicates that the outermost entanglement segments do not probe the characteristic relaxation process associated with each molecular structure, i.e. reptation and arm retraction for the linear and star

chains, respectively; in fact, the MSD of the outermost segment, for both structures, is weakly perturbed from the Rouse behaviour. For longer times, the MSD of the two outer segments of the star arms is lower than the MSD of the respective segments of the linear chains. This is because the outer segments of the star chains remain attached to a more slowly relaxing “object” (the inner sections of the star arm).

- The MSD is slowing down as one approaches the branch point. Moreover, up to $t \approx 10^5 \tau_0^{MD}$ the red and black circles are almost indistinguishable. At longer times the red circles (simulation branch point/fixed ends) fall below the black circles (simulation branch point/free ends), as expected, since in a simulation in which arms tips are fixed constraint release is quenched.

The development of a basic model for the description of the MD data, for the simulation branch point (red and black circles), is the subject of the next chapter.

1.7 Summary and outline of the thesis

In this chapter an outline of experimental rheology, scattering techniques and Molecular Dynamics simulations was given. Furthermore, two basic molecular models, namely the Rouse model and the Doi-Edwards tube model were briefly discussed. The extension of the tube model to branched architectures was also presented. We saw that the dynamics and rheological response of branched polymers can be radically different from the dynamics and flow properties of linear chains. This thesis is mainly concerned with the study of the dynamics and flow behaviour of melts of branched polymers.

In particular, chapter 2 will focus on the dynamics of branch points at times scales far below the time taken for an arm to completely relax its configuration. This chapter will provide a basic model with which to compare the (simulation branch point) MD data of Fig. 1.16. This model will be based on the Rouse model, nevertheless, to incorporate entanglements each Rouse segment will be localised in its own harmonic potential. For both unentangled and entangled systems analytical expressions for the MSD correlation functions will be derived. Then, the expression for the MSD of the branch point will be compared against the MD data that correspond to the simulations with fixed arm ends. As

we will see in section 2.4.1, as soon as the branch point encounters the confining potential the theoretical MSD displays a clear plateau whereas the MD data continue to rise; this finding indicates an apparent slow relaxation of the branch point localisation at times $\tau_e \lesssim t \lesssim \tau_R$; we will refer to this early relaxation process as early tube dilation. Standard constraint release events will also be taken into account by utilizing the dynamic dilution hypothesis [2]. It will be shown that the model matches the MD data from the simulations with free chain ends, provided that standard CR and early tube dilation are accounted for.

Chapter 3 will be dedicated to the calculation of the scattering signal from the labelled sections of polymer melts. Particular attention will be paid to the interpretation of the NSE measurements of Zamponi et al. [3], which refer to short labelled sections (in the close proximity of the branch point) of symmetric three arm stars. Following on the work of Read [117, 118] we will make a clear distinction between fast (annealed) and slow (quenched) variables; in our approach the annealed variables refer to the fast Rouse modes while the quenched variables to the slow Rouse modes and the localising springs. Having this distinction in mind we will apply a dynamic version of the Random Phase Approximation (RPA) in order to obtain an expression for the time dependent scattering function of the system. This expression will depend on single chain structure factors which in turn depend on MSD correlation functions. The analytical expressions (to be developed in chapter 2) will be used for these correlation functions. The theoretical scattering function will be compared against the NSE data of Zamponi et al. [3].

Chapter 4 and onwards is concerned with modifications of the differential version of the pom-pom model of McLeish and Larson [8]. A variant of the original model that enables (uniaxial) extensional viscosity overshoots will be introduced in chapter 4. In our modified model the overshoot originates from entanglement stripping at fast flows. An additional differential equation for the time evolution of the fraction of active backbone entanglements, $\Psi(t)$, will be added to the existing set of equations for the time evolution of the pre-averaged orientation and the pre-averaged stretch. However, three different options (equations) will be considered for the evolution of the orientation. Moreover, two more parameters per mode will be introduced. In line with the work of Inkson et al. [9] a multimode version will be employed to fit the experimental data for the industrial resin DOW150R [6, 7]. As will be shown in sections 4.4.1 and 4.4.2, the full version of the model captures a fair amount of the experimental observations, however, it can not fit all

experimental data with a unique parameterisation. Nevertheless, a minimal version of the model provides a decent fit to all experimental data.

In chapter 5 constraint release events will be incorporated in a pom-pom melt using the model introduced by Read in Ref. [13]. Two particular cases will be considered: (1) convective constraint release events arising from the relative motion between the matrix backbones and the backbone of a test molecule, and (2) constraint release events arising from the relative motion between the backbone material and the much faster relaxing arms. To develop a constitutive equation for this system we will adopt the physical picture of a thin and a fat tube surrounding the backbone chain, in analogy with the works of Auhl et al. [14] and Read et al. [15] for bi-disperse melts of linear chains.

Chapter 2

Dynamics of star polymers: branch point motion

2.1 Introduction

The motivation behind this chapter is to develop a basic model with which to compare the Molecular Dynamics (MD) simulation results, presented in Fig. 1.16 of section 1.6, for the three arm star. Nevertheless, this basic model neglects the relaxation modes of local reptation and arm retraction. Therefore, its predictions, for the segmental self-motion, are suitable for comparison against the MD results for the mean square displacement (MSD), $\langle \Delta r^2 \rangle$, of segments in the close proximity of the branch point. Specifically, the comparison is focused on the so-called “simulation branch point”. As shown in Fig. 1.16, this “segment” is not directly affected by the neglected relaxation modes in the MD time window. An attempt to incorporate arm retraction modes in expressions for the MSD of segments of symmetric stars can be found in Ref. [119].

The model developed in this chapter is essentially an extension of the Rouse model (c.f. section 1.4.3) to symmetric star polymer architectures. However, to model the entanglement (confinement) effect, each Rouse segment (monomer) is localised by a quadratic potential [118, 120, 121, 122, 123, 124]. As a result of this localisation each segment is enforced to fluctuate about an average position. The connection of all average positions leads to the so-called mean path [124] which can be thought of as the analogous of the primitive path of the tube model. The cases of unentangled and entangled chains

are considered separately in sections 2.2 and 2.3, respectively.

For confined linear chains, a similar calculation has been performed by Vilgis and Boué [120] but their expressions for the MSD failed to exhibit Gaussian chain statistics at equilibrium, as expected. As demonstrated in subsection 2.3.3, the reason for this failure is the neglect of the contribution of the mean path. The equations derived in section 2.3 correct this point, and can be used for linear chains if these are treated as two-arm stars.

By using the continuous chain Rouse model, we are explicitly ignoring some complications inherent to the molecular dynamics model, such as the discrete nature of the beads or the bending potential (c.f. eq 1.69 of section 1.6). Nevertheless, the expressions derived in section 2.3 provide a starting point for the analysis of monomer motion near branch points in the MD simulations, when the effects of tube dilation are accounted for in the model. The inclusion of tube dilation in the model is detailed in section 2.4. It must be stressed that the expressions derived in section 2.3 refer only to local branch point motion within the tube and not to the diffusive steps (curvilinear hopping) that a branch point undertakes after an arm has completely retracted [2, 125, 126, 127, 128].

2.2 Dynamics in the unentangled regime

2.2.1 The Rouse model for symmetric polymer stars

For an unentangled symmetric star polymer, the Langevin equation and the free energy read respectively [26, 71]

$$\zeta_0 \frac{\partial \mathbf{r}_{\alpha,\ell,t}}{\partial t} = k \frac{\partial^2 \mathbf{r}_{\alpha,\ell,t}}{\partial \ell^2} + \mathbf{g}(\alpha, \ell, t) \quad (2.1a)$$

$$F_R = \frac{k}{2} \sum_{\alpha=1}^f \sum_{\ell=0}^{N_a} (\mathbf{r}_{\alpha,\ell+1,t} - \mathbf{r}_{\alpha,\ell,t})^2 = \frac{k}{2} \sum_{\alpha=1}^f \int_0^{N_a} \left(\frac{\partial \mathbf{r}_{\alpha,\ell,t}}{\partial \ell} \right)^2 d\ell, \quad (2.1b)$$

where f is the number of arms, and $\mathbf{r} = \mathbf{r}_{\alpha,\ell,t}$ is the position vector of the ℓ th segment in arm α at time t . The Rouse segments in each arm are labelled $\ell = 0, 1, \dots, N_a$ starting from the branch point where $\ell = 0$ and ending at the arm tip where $\ell = N_a$. The labelling of the Rouse segments is illustrated schematically in Fig. 2.1.

As in eq 1.41, ζ_0 and $k(= 3k_B T/b^2)$ are, respectively, the segmental friction and the entropic spring constant. The term $\mathbf{g}(\alpha, \ell, t)$ is the Brownian force acting on the ℓ th

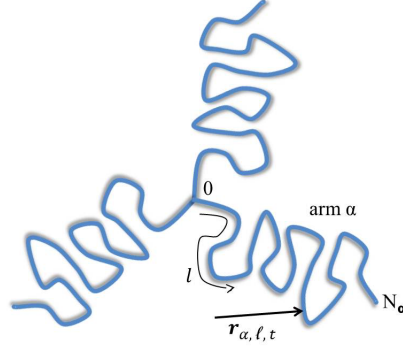


Figure 2.1: Schematic illustration of an unentangled star. The position vector $\mathbf{r} = \mathbf{r}_{\alpha, \ell, t}$ of the ℓ th segment in arm α at time t is shown. We label segments as $\ell = 0, 1, \dots, N_\alpha$ starting from the branch point where $\ell = 0$ and ending at the arm tip where $\ell = N_\alpha$.

segment of the arm α , with averages

$$\langle g_\mu(\alpha, \ell, t) \rangle = 0 \quad (2.2a)$$

$$\langle g_\mu(\alpha, \ell, t) g_\nu(\beta, \ell', t') \rangle = 2\zeta_0 k_B T \delta(\ell - \ell') \delta(t - t') \delta_{\mu\nu} \delta_{\alpha\beta}. \quad (2.2b)$$

Indices μ and ν denote cartesian coordinates while α and β are used to label different arms. These averages are the same as eqs 1.42. The extra term $\delta_{\alpha\beta}$ in eq 2.2b, compared to eq 1.42b, ensures that the random forces acting on bead ℓ on arm α are uncorrelated with the respective forces acting on the same bead on arm β .

However, the boundary conditions of eq 2.1a differ from those of eq 1.41. Specifically, the appropriate boundary conditions for a symmetric star with f arms are

$$\mathbf{r}_{\alpha=1, \ell=0, t} = \mathbf{r}_{\alpha=2, \ell=0, t} = \dots = \mathbf{r}_{\alpha=f, \ell=0, t} \quad (2.3a)$$

$$\left. \frac{\partial \mathbf{r}}{\partial \ell} \right|_{\alpha=1, \ell=0} + \left. \frac{\partial \mathbf{r}}{\partial \ell} \right|_{\alpha=2, \ell=0} + \dots + \left. \frac{\partial \mathbf{r}}{\partial \ell} \right|_{\alpha=f, \ell=0} = 0 \quad (2.3b)$$

$$\left. \frac{\partial \mathbf{r}}{\partial \ell} \right|_{\alpha=1, \ell=N_\alpha} = \left. \frac{\partial \mathbf{r}}{\partial \ell} \right|_{\alpha=2, \ell=N_\alpha} = \dots = \left. \frac{\partial \mathbf{r}}{\partial \ell} \right|_{\alpha=f, \ell=N_\alpha} = 0. \quad (2.3c)$$

Equation 2.3a satisfies the chain connectivity requirement at the branch point while eq. 2.3b represents the force balance at the branch point. Equation 2.3c indicates that there is no external force acting at the free ends of the arms. This boundary condition is independent of the topology of the chain and is the only boundary condition if the chain is linear.

In view of eqs 2.3, $\mathbf{r}_{\alpha, \ell, t}$ can be expressed in terms of two “families” of eigenmodes (eigenfunctions). In particular, cosine eigenmodes, $\Psi_p^c(\ell)$, which have degeneracy of one

and sine eigenmodes, $\Psi_q^{s_i}(\alpha, \ell)$, which have degeneracy of $f' = f - 1$. These two families of eigenmodes are indexed with the mode numbers p and q , respectively, so $\mathbf{r}_{\alpha, \ell, t}$ reads

$$\mathbf{r}_{\alpha, \ell, t} = \sum_p \mathbf{X}_p^c(t) \Psi_p^c(\ell) + \sum_q \left(\mathbf{X}_q^{s_1}(t) \Psi_q^{s_1}(\alpha, \ell) + \dots + \mathbf{X}_q^{s_{f'}}(t) \Psi_q^{s_{f'}}(\alpha, \ell) \right). \quad (2.4)$$

Expansions of similar form have been proposed in the literature [129, 130]. The explicit expressions of the cosine and sine eigenmodes are, respectively, given by

$$\Psi_p^c(\ell) = \cos\left(\frac{p\pi\ell}{N_a}\right) \quad (2.5a)$$

$$\Psi_q^{s_i}(\alpha, \ell) = s_{i\alpha} \sin\left(\frac{(2q-1)\pi\ell}{2N_a}\right). \quad (2.5b)$$

The numerical coefficients $s_{i\alpha}$ of the sine eigenmodes satisfy the following constraints:

$$\sum_{\alpha=1}^f s_{i\alpha} = 0 \quad (2.6a)$$

$$\sum_{\alpha=1}^f s_{i\alpha}^2 = f \quad (2.6b)$$

$$\sum_{\alpha=1}^f s_{i\alpha} s_{j\alpha} = 0, \quad (2.6c)$$

where indices i, j denote the i th and j th sine eigenmode, respectively. Equation 2.6a is a consequence of the force balance at the branch point as expressed by eq 2.3b. Equations 2.6b and 2.6c arise from normalization and orthogonality, respectively.

Figure 2.2 shows a cosine eigenmode $\Psi_p^c(\ell)$ (black solid line) and a sine eigenmode $\Psi_q^{s_i}(\alpha, \ell)$ (blue solid line) for the first four modes, i.e. for $p = 1, 2, 3, 4$ and $q = 1, 2, 3, 4$, as a function of the normalised arm coordinate $\xi = \ell/N_a$. The derivatives of $\Psi_p^c(\ell)$ and $\Psi_q^{s_i}(\alpha, \ell)$ with respect to ℓ (ignoring the terms $p\pi/N_a$ and $(2q-1)\pi/(2N_a)$, respectively) are also shown with dashed lines of respective colour. These derivatives are related to the tension of the chain. All curves of this figure that refer to the sine eigenmode are obtained by setting $s_{i\alpha} = 1$. Figure 2.2 reveals the following:

- At the branch point the contribution of the sine eigenmode to $\mathbf{r}_{\alpha, \ell, t}$ is zero for all modes. Moreover, the arms are excited in a symmetric manner by the cosine eigenmodes and therefore at the branch point $\Psi_p^c(0) = 1$ for every arm (c.f. all blue and black solid lines, respectively, at $\xi = 0$). From these two observations it is apparent that the boundary condition of chain connectivity at the branch point, namely eq 2.3a, is automatically satisfied.

- The chain tension associated with the cosine eigenmode is zero at the branch point. In contrast, it is non-zero for the sine eigenmode (c.f. all black and blue dashed lines, respectively, at $\xi = 0$). As a result, in order to satisfy the boundary condition of zero tension at the branch point (eq 2.3b), one has to excite the arms in such a way so as the numerical coefficients $s_{i\alpha}$ of the sine eigenmode fulfill eqs 2.6. For a three arm star an obvious solution is to set, for example, $s_{i3} = 0$ and excite the two remaining arms in an antisymmetric manner, that is, set $s_{i1} = -s_{i2}$.
- The tension at the arm tips is zero for both the cosine and the sine eigenmode (c.f. black and blue dashed lines at $\xi = 1$). This justifies that eq 2.3c is satisfied. It is worth mentioning that if the sine eigenmode was chosen to be of the form $\sin\left(\frac{q\pi\ell}{N_\alpha}\right)$ then the tension at the arm tips would have been non-zero.

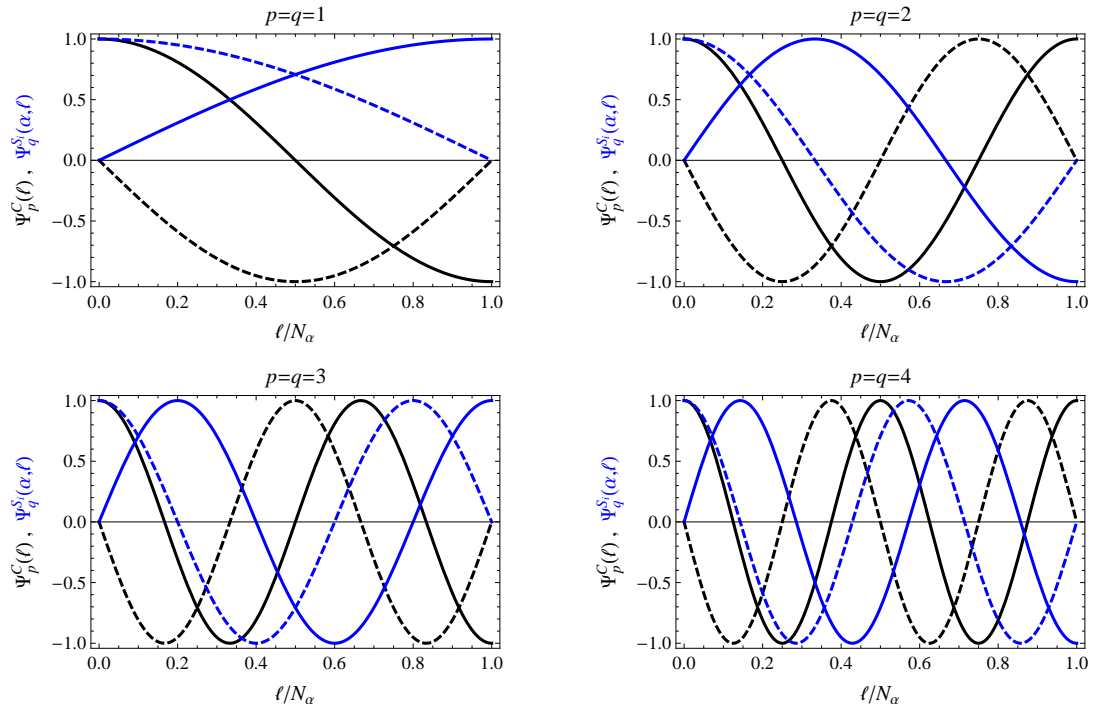


Figure 2.2: The first four modes (waves) of a cosine (black solid lines) and a sine (blue solid lines) eigenmode traveling along an arm of a symmetric star. The chain tension related to these modes is also shown with dashed lines of respective colour.

The first step toward the calculation of the MSD is substitution of eq 2.4 into eq 2.1a.

This substitution yields

$$\begin{aligned} & \zeta_0 \sum_p \left[\frac{\partial \mathbf{X}_p^c(t)}{\partial t} \Psi_p^c \right] + \zeta_0 \sum_q \left[\frac{\partial \mathbf{X}_q^{s_1}(t)}{\partial t} \Psi_q^{s_1} + \dots + \frac{\partial \mathbf{X}_q^{s_{f'}}(t)}{\partial t} \Psi_q^{s_{f'}} \right] = \\ & -k \sum_p \left[\frac{p^2 \pi^2}{N_a^2} \mathbf{X}_p^c(t) \Psi_p^c \right] - k \sum_q \left[\left(\frac{2q-1}{2N_a} \right)^2 \pi^2 \left(\mathbf{X}_q^{s_1}(t) \Psi_q^{s_1} + \dots + \mathbf{X}_q^{s_{f'}}(t) \Psi_q^{s_{f'}} \right) \right] + \\ & \mathbf{g}(\alpha, \ell, t). \end{aligned} \quad (2.7)$$

The first step in order to obtain the evolutionary equations for the eigenmodes amplitudes

$\mathbf{X}_p^c, \mathbf{X}_q^{s_1}, \dots, \mathbf{X}_q^{s_{f'}}$ is to multiply the above equation by the following sums

$$\sum_{\alpha=1}^f \int_0^{N_a} \sum_{p'} \Psi_{p'}^c(\ell) d\ell, \quad \sum_{\alpha=1}^f \int_0^{N_a} \sum_{q'} \Psi_{q'}^{s_1}(\alpha, \ell) d\ell, \quad \dots, \quad \sum_{\alpha=1}^f \int_0^{N_a} \sum_{q'} \Psi_{q'}^{s_{f'}}(\alpha, \ell) d\ell.$$

Then one needs to integrate over the arm coordinate ℓ and sum over arms α . During this procedure only “diagonal” terms which contain products of the form $\Psi_{p'}^c \Psi_p^c$ and $\Psi_{q'}^{s_i} \Psi_q^{s_i}$ are non-zero because of eqs 2.6a and 2.6c. (See Appendix A.1.) The final expressions are as follows:

$$\begin{aligned} \zeta_p \frac{\partial \mathbf{X}_p^c(t)}{\partial t} &= -k_p^c \mathbf{X}_p^c(t) + \mathbf{g}_p^c(t) \\ \zeta_q \frac{\partial \mathbf{X}_q^{s_1}(t)}{\partial t} &= -k_q^{s_1} \mathbf{X}_q^{s_1}(t) + \mathbf{g}_q^{s_1}(t) \\ &\vdots \\ \zeta_q \frac{\partial \mathbf{X}_q^{s_{f'}}(t)}{\partial t} &= -k_q^{s_{f'}} \mathbf{X}_q^{s_{f'}}(t) + \mathbf{g}_q^{s_{f'}}(t). \end{aligned} \quad (2.8)$$

All equations that refer to sine eigenmodes are identical so in practice only two of the above equations need to be solved. In particular, the one that refers to \mathbf{X}_p^c and one of the remaining $f-1$ that refer to $\mathbf{X}_q^{s_1} = \dots = \mathbf{X}_q^{s_{f'}} = \mathbf{X}_q^{s_i}$. In the system of eqs 2.8, $\zeta_p = \zeta_q = f\zeta_0 N_a/2$, $k_p^c = fp^2\pi^2 3k_B T / (2N_a b^2)$, $k_q^{s_i} = f(2q-1)^2\pi^2 3k_B T / (8N_a b^2)$; moreover

$$\mathbf{g}_p^c = \sum_{\alpha=1}^f \int_0^{N_a} \mathbf{g}(\alpha, \ell, t) \Psi_p^c d\ell \quad (2.9a)$$

$$\mathbf{g}_q^{s_i} = \sum_{\alpha=1}^f \int_0^{N_a} \mathbf{g}(\alpha, \ell, t) \Psi_q^{s_i} d\ell. \quad (2.9b)$$

The solutions for \mathbf{X}_p^c and $\mathbf{X}_q^{s_i}$ are obtained using the integrating factor method and are:

$$\mathbf{X}_p^c(t) = \frac{1}{\zeta_p} \exp\left(\frac{-t}{\tau_p^c}\right) \int_{-\infty}^t \mathbf{g}_p^c \exp\left(\frac{t'}{\tau_p^c}\right) dt' \quad (2.10a)$$

$$\mathbf{X}_q^{s_i}(t) = \frac{1}{\zeta_q} \exp\left(\frac{-t}{\tau_q^{s_i}}\right) \int_{-\infty}^t \mathbf{g}_q^{s_i} \exp\left(\frac{t'}{\tau_q^{s_i}}\right) dt', \quad (2.10b)$$

where $\tau_p^c = \zeta_p/k_p^c$ and $\tau_q^{s_i} = \zeta_q/k_q^{s_i}$.

The next step is to compute the correlation functions $\langle X_{p\mu}^c(t)X_{p'\nu}^c(t') \rangle$ and $\langle X_{q\mu}^{s_i}(t)X_{q'\nu}^{s_i}(t') \rangle$. To do this, one first needs to work out the averages that involve the noise terms, namely $\langle g_{p\mu}^c g_{p'\nu}^c \rangle$ and $\langle g_{q\mu}^{s_i} g_{q'\nu}^{s_i} \rangle$, using eqs 2.9a, 2.9b and 2.2b. Having obtained $\langle g_{p\mu}^c g_{p'\nu}^c \rangle$ and $\langle g_{q\mu}^{s_i} g_{q'\nu}^{s_i} \rangle$ eqs 2.10 can be used in order to obtain the final result, which is

$$\langle \mathbf{X}_p^c(t) \cdot \mathbf{X}_{p'}^c(t') \rangle = \frac{2N_a b^2 \delta_{pp'}}{f\pi^2 p^2} \exp(-\tilde{t}_{R_a} p^2) \quad (2.11a)$$

$$\langle \mathbf{X}_q^{s_i}(t) \cdot \mathbf{X}_{q'}^{s_i}(t') \rangle = \frac{8N_a b^2 \delta_{qq'}}{f\pi^2 (2q-1)^2} \exp\left(\frac{-\tilde{t}_{R_a} (2q-1)^2}{4}\right) \quad (2.11b)$$

where $\tilde{t}_{R_a} = |t-t'|/\tau_{R_a}$ is the normalised time; τ_{R_a} is the Rouse relaxation time of an arm given by $\tau_{R_a} = \zeta_0 b^2 N_a^2 (3\pi^2 k_B T)^{-1}$. We note that ‘‘non diagonal’’ correlation functions of the form $\langle X_{p\mu}^c(t)X_{q'\nu}^{s_i}(t') \rangle$ and $\langle X_{q\mu}^{s_i}(t)X_{q'\nu}^{s_j}(t') \rangle$ vanish since they contain terms like $\Psi_p^c \Psi_{q'}^{s_i}$ and $\Psi_q^{s_i} \Psi_{q'}^{s_j}$. The contribution of these terms, as shown in Appendix A.1, is zero because of eqs 2.6a and 2.6c.

At equilibrium eqs 2.11a and 2.11b reduce, respectively, to

$$\langle \mathbf{X}_p^c(0) \cdot \mathbf{X}_{p'}^c(0) \rangle = \frac{2N_a b^2 \delta_{pp'}}{f\pi^2 p^2} \quad (2.12a)$$

$$\langle \mathbf{X}_q^{s_i}(0) \cdot \mathbf{X}_{q'}^{s_i}(0) \rangle = \frac{8N_a b^2 \delta_{qq'}}{f\pi^2 (2q-1)^2}. \quad (2.12b)$$

It is worth mentioning that these equilibrium correlation functions can be calculated by making use of the equipartition theorem, after substitution of eq 2.4 into the free energy of the system (eq 2.1b).

Having obtained eqs 2.12 it is a straightforward procedure to obtain the expressions for the MSD correlation functions. This is done by substituting eq 2.4 into the general expression for the MSD, which is

$$\langle (\mathbf{r}_{\alpha,\ell,t} - \mathbf{r}_{\beta,\ell',t'})^2 \rangle = \langle \mathbf{r}_{\alpha,\ell,t} \cdot \mathbf{r}_{\alpha,\ell,t} \rangle + \langle \mathbf{r}_{\beta,\ell',t'} \cdot \mathbf{r}_{\beta,\ell',t'} \rangle - 2 \langle \mathbf{r}_{\alpha,\ell,t} \cdot \mathbf{r}_{\beta,\ell',t'} \rangle,$$

and making use of eqs 2.11. This calculation is detailed in Appendix A.2.

2.2.2 Results for the MSD correlation functions

The final expressions for the MSD correlation functions are presented in table 2.1. In these expressions, $\Phi(x)$ is the error function given by $\Phi(x) = (2/\sqrt{\pi}) \int_0^x e^{-u^2} du$.

Furthermore, $\langle(\mathbf{r}_{\alpha,\ell,t} - \mathbf{r}_{\alpha,\ell',t'})^2\rangle$ and $\langle(\mathbf{r}_{\alpha,\ell,t} - \mathbf{r}_{\beta,\ell',t'})^2\rangle$ refer, respectively, to the MSD of segments placed in the same and in different arms. The expression for the segmental self-motion (i.e. for $\alpha = \beta$, $\ell = \ell'$) is shown in the third row of table 2.1. This expression reduces to $\langle(\mathbf{r}_{\alpha,0,t} - \mathbf{r}_{\alpha,0,t'})^2\rangle = 4N_a b^2 \sqrt{\tilde{t}_{Ra}} / (f\pi^{1.5})$ for the branch point (fourth row of table 2.1), which is lower by a factor of $2/f$ compared to segmental motion in a linear chain of polymerization degree N_a [26, 71]. We stress that the expressions of table 2.1 are consistent in the limit case of linear chains. Indeed if we set $f = 2$ these expressions provide the well-known Rouse behaviour for the segmental motion of unentangled linear chains. We note that our reduced, for linear chains, expression for $\langle(\mathbf{r}_{\alpha,\ell,t} - \mathbf{r}_{\alpha,\ell',t'})^2\rangle$ is a closed expression, in contrast to the respective equation in [26] (i.e. eq 4.III.9 on page 134). Moreover, at equilibrium ($t = t'$) the Gaussian chain limit is recovered independently of f . Indeed $\langle(\mathbf{r}_{\alpha,\ell,t} - \mathbf{r}_{\alpha,\ell',t'})^2\rangle$ and $\langle(\mathbf{r}_{\alpha,\ell,t} - \mathbf{r}_{\beta,\ell',t'})^2\rangle$ reduce, for $t = t'$, to the Gaussian chain result $b^2|\ell - \ell'|$ and $b^2(\ell + \ell')$, respectively.

Table 2.1: Theoretical predictions for the MSD of unentangled stars

MSD	Expression
$\langle(\mathbf{r}_{\alpha,\ell,t} - \mathbf{r}_{\alpha,\ell',t'})^2\rangle$	$\frac{2N_a b^2}{\pi^{1.5}} \sqrt{\tilde{t}_{Ra}} \exp\left(\frac{-\pi^2 \ell - \ell' ^2}{4\tilde{t}_{Ra} N_a^2}\right) - \frac{2(f-2)N_a b^2}{f\pi^{1.5}} \sqrt{\tilde{t}_{Ra}} \exp\left(\frac{-\pi^2(\ell + \ell')^2}{4N_a^2 \tilde{t}_{Ra}}\right) -$ $\frac{(f-2)b^2(\ell + \ell')}{f} \left[\Phi\left(\frac{\pi(\ell + \ell')}{2N_a \sqrt{\tilde{t}_{Ra}}}\right) - 1 \right] + b^2 \ell - \ell' \Phi\left(\frac{\pi \ell - \ell' }{2N_a \sqrt{\tilde{t}_{Ra}}}\right)$
$\langle(\mathbf{r}_{\alpha,\ell,t} - \mathbf{r}_{\beta,\ell',t'})^2\rangle$	$\frac{b^2(\ell + \ell')}{f} \left[(f-2) + 2\Phi\left(\frac{\pi(\ell + \ell')}{2N_a \sqrt{\tilde{t}_{Ra}}}\right) \right] + \frac{4N_a b^2}{f\pi^{1.5}} \sqrt{\tilde{t}_{Ra}} \exp\left(\frac{-\pi^2(\ell + \ell')^2}{4N_a^2 \tilde{t}_{Ra}}\right)$
$\langle(\mathbf{r}_{\alpha,\ell,t} - \mathbf{r}_{\alpha,\ell,t'})^2\rangle$	$2b^2\ell \left(\frac{f-2}{f}\right) \left[1 - \Phi\left(\frac{\pi\ell}{\sqrt{\tilde{t}_{Ra}} N_a}\right) \right] + \frac{2N_a b^2}{\pi^{1.5}} \sqrt{\tilde{t}_{Ra}} \left[1 - \left(\frac{f-2}{f}\right) \exp\left(\frac{-\pi^2 \ell^2}{\tilde{t}_{Ra} N_a^2}\right) \right]$
$\langle(\mathbf{r}_{\alpha,0,t} - \mathbf{r}_{\alpha,0,t'})^2\rangle$	$\frac{2}{f} \frac{2N_a b^2}{\pi^{1.5}} \sqrt{\tilde{t}_{Ra}}$

Figure 2.3 shows the segmental MSD (i.e. the expression presented at the third row of table 2.1), as a function of the normalised time \tilde{t}_{Ra} , for a three arm polymer star. Predictions are shown for three different Rouse segments along the arm. The blue, green and red lines correspond to $\xi = 0.001$, $\xi = 0.005$ and $\xi = 0.01$, respectively; $\xi = \ell/N_a$. The MSD of the branch point, $\langle(\mathbf{r}_{\alpha,0,t} - \mathbf{r}_{\alpha,0,t'})^2\rangle = 4N_a b^2 \sqrt{\tilde{t}_{Ra}} / (f\pi^{1.5})$, is also presented with a grey line. Moreover, the segmental MSD of an unentangled

linear chain is depicted with a black line. We have divided the MSD by $N_a b^2 \sqrt{\tilde{t}_{R_a}}$ to facilitate comparison of the blue, green and red curves with the grey and black lines. In this particular plot the normalised mean square displacement of the branch point and of a segment of a linear chain appear as horizontal lines. The ratio of these two curves is $2/f$. From Fig. 2.3, it is apparent that the arm segments initially obey the segmental dynamics of the linear chain. Then a cross over to the branch point dynamics occurs. This cross over happens earlier for segments closer to the branch point. Finally, we emphasise that,

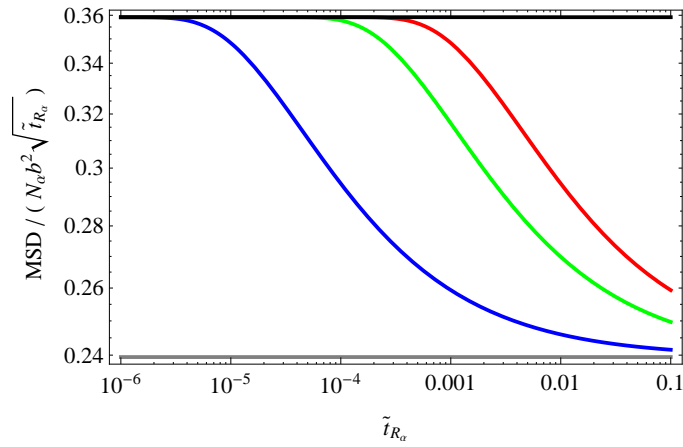


Figure 2.3: Segmental MSD normalised by $N_a b^2 \sqrt{\tilde{t}_{R_a}}$, as predicted by the model, for an unentangled three arm polymer star. Different colours correspond to different positions along the arm; $\xi = \ell/N_a = 0.001$ (blue), $\xi = 0.005$ (green), and $\xi = 0.01$ (red). The grey line refers to the branch point while the black line refers to a linear chain.

in the derivation of the expressions of table 2.1 we have made the approximation that the fast Rouse modes dominate the dynamics. Consequently, we expect these expressions to be valid only for $t \ll \tau_{R_a}$ (or equivalently for $\tilde{t}_{R_a} \ll 1$).

2.2.3 The correlation function $\psi_\ell^R(t)$

A chain segment can renew its orientation by two different ways: by mechanisms that involve local reorganisation of the chain such as local constraint release (CR) and fast (local) Rouse modes, or by mechanisms that involve global reconfiguration of the chain like the terminal Rouse relaxation and tube escape (e.g. reptation, arm retraction). The latter processes require motion of the chain ends, whereas the former ones do not. The principal concern here and in section 2.4.2 below is to develop a correlation function

(correlator) that is sensitive to global reconfiguration of the chain only. Section 2.4.2 will deal with entangled polymer stars. Here, unentangled polymer stars are considered only. Therefore, the correlator to be developed below should relax at timescales of order the Rouse relaxation time of the chain, but remain close to unity at early times.

The calculation of the correlator for the unentangled star chains is similar to the calculation of the correlator $\langle \mathbf{u}_\ell(0) \cdot \mathbf{R}(t) \rangle$ for the linear chains (section 1.4.3). However, in this case one needs to correlate the tangent vector of a Rouse segment not only with the end-to-end vector of the arm that the segment is placed on, but also with the end-to-end vectors of all other arms. Specifically, for a three arm symmetric star the analogous correlator to $\langle \mathbf{u}_\ell(0) \cdot \mathbf{R}(t) \rangle$ of a linear chain, reads

$$\psi_\ell^R(t) = \langle \mathbf{u}_{\alpha,\ell,0} \cdot (\mathbf{R}_{\alpha,t}^e + B' \mathbf{R}_{\beta,t}^e + C' \mathbf{R}_{\gamma,t}^e) \rangle, \quad (2.13)$$

where $\mathbf{u}_{\alpha,\ell,0} = \partial \mathbf{r}_{\alpha,\ell,0} / \partial \ell$ represents the tangent vector at the ℓ th segment in the arm α at time 0, and $\mathbf{R}_{\alpha,t}^e = \mathbf{r}_{\alpha,N_\alpha,t} - \mathbf{r}_{\alpha,0,t}$ is the end-to-end vector of the arm α at time t . The three indices $\alpha, \beta, \gamma \in \{1, 2, 3\}$ are different and denote the three arms of the star. The numerical coefficients B' and C' provide the weight of the correlations between the arm α and the other two arms β and γ .

Concerning the values of the coefficients B' and C' we consider two options. The first option corresponds to $B' = C' = -1/2$ (“half correlation”) and leads to

$$\begin{aligned} \psi_\ell^{R_{\text{hc}}}(t) &= \left\langle \mathbf{u}_{\alpha,\ell,0} \cdot \left(\mathbf{R}_{\alpha,t}^e - \frac{1}{2} \mathbf{R}_{\beta,t}^e - \frac{1}{2} \mathbf{R}_{\gamma,t}^e \right) \right\rangle \\ &= \frac{4b^2}{\pi} \sum_{p \text{ odd}} \frac{1}{p} \left[\cos \left(\frac{p\pi\xi}{2} \right) \sin \left(\frac{p\pi}{2} \right) \exp \left(\frac{-\tilde{t}_{R_a} p^2}{4} \right) \right], \end{aligned} \quad (2.14)$$

where $\xi = \ell(N_a)^{-1}$. The second option, $B' = C' = -1$ (“full correlation”), yields

$$\begin{aligned} \psi_\ell^{R_{\text{fc}}}(t) &= \langle \mathbf{u}_{\alpha,\ell,0} \cdot (\mathbf{R}_{\alpha,t}^e - \mathbf{R}_{\beta,t}^e - \mathbf{R}_{\gamma,t}^e) \rangle \\ &= \frac{4b^2}{3\pi} \sum_{p \text{ odd}} \frac{1}{p} \left[4 \cos \left(\frac{p\pi\xi}{2} \right) \sin \left(\frac{p\pi}{2} \right) \exp \left(\frac{-\tilde{t}_{R_a} p^2}{4} \right) - \sin(p\pi\xi) \exp(-\tilde{t}_{R_a} p^2) \right], \end{aligned} \quad (2.15)$$

To derive eqs 2.14 and 2.15 we have expressed the tangent vector and the end-to-end vectors in terms of the Rouse modes using eq 2.4. Furthermore, we have used eqs 2.11.

Figure 2.4 depicts both the “half correlation” (solid lines) function, $\psi_\ell^{R_{\text{hc}}}(t)$, and the “full correlation” (dashed lines) function, $\psi_\ell^{R_{\text{fc}}}(t)$, against \tilde{t}_{R_a} , for various Rouse segments

along an arm of the star. In particular, the black, magenta, red, green, and blue curves correspond to $\xi = 0.15, 0.3, 0.5, 0.7,$ and $0.85,$ respectively. In the usual continuous approximation, the sum in eqs 2.14 and 2.15 extends from $p = 1$ to $p = p_{\max} \rightarrow \infty$. To obtain this figure a cut-off value of $p_{\max} = 1000$ has been used. Results for larger p_{\max} are indistinguishable. Figure 2.4 demonstrates two important points which are taken into consideration when the analogous correlation function of $\psi_\ell^R(t)$, for entangled systems, is estimated from the MD simulations (subsection 2.4.2 below).

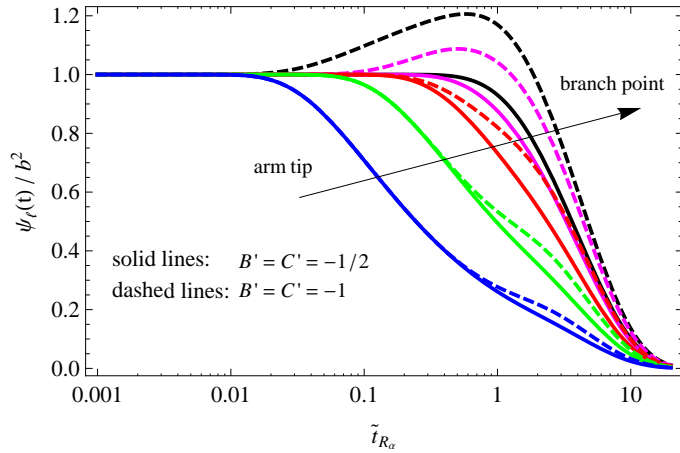


Figure 2.4: Tangent correlation function (eq. 2.13) for unentangled stars. The solid lines refer to ‘half-correlation’ ($B' = C' = -1/2$) while the dashed lines to ‘full-correlation’ ($B' = C' = -1$). Different colours correspond to different Rouse segments along the arm: $\xi = 0.15$ (black), 0.3 (magenta), 0.5 (red), 0.7 (green), and 0.85 (blue).

First, for inner sections of the chain (c.f. black and magenta curves), both $\psi_\ell^{R_{fc}}(t)$ and $\psi_\ell^{R_{hc}}(t)$ start to decay at $\tilde{t}_{R_a} \approx 1$ indicating that they are insensitive to higher order Rouse modes. For chain sections close to chain ends, the initial decay is seen at a timescale set by the Rouse time of the $(1-\xi)$ section of the chain, i.e. by $\tau_{R_{(1-\xi)}} = \tau_{mon} N_a^2 (1-\xi)^2$. Second, the full correlator, $\psi_\ell^{R_{fc}}(t)$, exceeds the maximum expected value of unity and gives undesirable peaks for segments close to the branch point (c.f. black and magenta dashed curves); this peak is undesirable because it implies that the correlator is not only sensitive to the global reorganisation of the chain, but it is also sensitive to local reconfiguration of the chain. On the other hand, the half correlator exhibits the desired behaviour: that is, it remains close to unity at early times, and relaxes at timescales of order the terminal relaxation time.

2.3 Dynamics in the entangled regime

2.3.1 Localising springs

In a polymer melt, the entanglements imposed by the surrounding chains on a test chain localise it in space. This effect is not incorporated in eqs 2.1, which refer to an unentangled chain. Therefore, for describing effects due to entanglements, an alternative model is required. Following on from the earlier works [118, 120, 121, 122, 123] and that of Read et al. [124], in order to model the entanglement effect, we localise each monomer of a Rouse chain by a harmonic potential centred at a fixed point $\mathbf{R}_{\alpha,l}$ (c.f. Fig. 2.5). This approach provides an alternative description of the entanglement effect to the tube model (presented in section 1.4.4) and is referred to as the Warner and Edwards “picture” of the tube [121, 122]. The strength of the harmonic potential is parameterised by h_s . Alternatively, one may consider the localizing potential be represented by a virtual anchoring chain of N_s monomers, where $N_s = 1/h_s$.

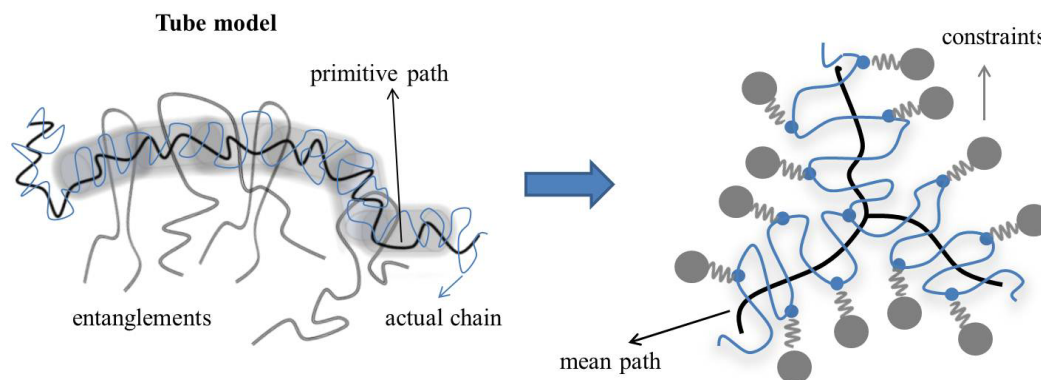


Figure 2.5: Left: Schematic illustration of the tube model. Entanglements are modeled by confining the actual chain in a tube-like region. The black line represents the primitive path. Right: An alternative description of the entanglements. In this case entanglements are modeled by localising springs (constraints). The black line shows the mean path which can be thought of as the analogous of the primitive path of the tube model.

The Langevin equation and the free energy in this model read respectively:

$$\zeta_0 \frac{\partial \mathbf{r}_{\alpha,\ell,t}}{\partial t} = k \frac{\partial^2 \mathbf{r}_{\alpha,\ell,t}}{\partial \ell^2} + kh_s(\mathbf{R}_{\alpha,\ell} - \mathbf{r}_{\alpha,\ell,t}) + \mathbf{g}(a, \ell, t) \quad (2.16)$$

$$F = \frac{k}{2} \sum_{\alpha=1}^f \sum_{\ell=0}^{N_\alpha} [(\mathbf{r}_{\alpha,\ell+1,t} - \mathbf{r}_{\alpha,\ell,t})^2 + h_s (\mathbf{R}_{\alpha,\ell} - \mathbf{r}_{\alpha,\ell,t})^2]. \quad (2.17)$$

Equations 2.16 and 2.17 differ from the respective equations of the Rouse model, namely eqs 2.1a and 2.1b, by the additional terms $kh_s(\mathbf{R}_{\alpha,\ell} - \mathbf{r}_{\alpha,\ell,t})$ and $kh_s(\mathbf{R}_{\alpha,\ell} - \mathbf{r}_{\alpha,\ell,t})^2$, respectively. These terms represent the effect of the localizing potential. The introduction of the harmonic potential restricts chain motion so each monomer fluctuates about a position averaged over entanglement relaxation time τ_e (since $\mathbf{R}_{\alpha,\ell}$'s are fixed). Hence one may express the position vector of each segment as

$$\mathbf{r}_{\alpha,\ell,t} = \widehat{\mathbf{r}}_{\alpha,\ell} + \Delta_{\alpha,\ell,t}, \quad (2.18)$$

where $\widehat{\mathbf{r}}_{\alpha,\ell}$ is the time independent average position of the ℓ th monomer in arm α , and $\Delta_{\alpha,\ell,t}$ denotes the fluctuations about this average position. When all average positions are connected the mean path is obtained. As demonstrated by Read et al. [124], the mean path is obtained from eq 2.17 by requiring that

$$\frac{\partial F}{\partial \mathbf{r}_{\alpha,\ell,t}} = 0 \quad \text{at} \quad \mathbf{r}_{\alpha,\ell,t} = \widehat{\mathbf{r}}_{\alpha,\ell},$$

which yields

$$\mathbf{R}_{\alpha,\ell} = \widehat{\mathbf{r}}_{\alpha,\ell} - \frac{1}{h_s} (\widehat{\mathbf{r}}_{\alpha,\ell+1} + \widehat{\mathbf{r}}_{\alpha,\ell-1} - 2\widehat{\mathbf{r}}_{\alpha,\ell}) = \widehat{\mathbf{r}}_{\alpha,\ell} - \frac{1}{h_s} \frac{\partial^2 \widehat{\mathbf{r}}_{\alpha,\ell}}{\partial \ell^2}. \quad (2.19)$$

Substitution of this equation into eq 2.17 leads to reexpression of the free energy (in the continuous chain limit) as a sum of two independent contributions:

$$\begin{aligned} F &= F_{\text{mean path}} + F_{\Delta} \\ &= \underbrace{\frac{k}{2} \sum_{\alpha=1}^f \int_0^{N_\alpha} \left[\left(\frac{\partial \widehat{\mathbf{r}}_{\alpha,\ell}}{\partial \ell} \right)^2 + \frac{1}{h_s} \left(\frac{\partial^2 \widehat{\mathbf{r}}_{\alpha,\ell}}{\partial \ell^2} \right)^2 \right] d\ell}_{\text{mean path}} + \\ &\quad \underbrace{\frac{k}{2} \sum_{\alpha=1}^f \int_0^{N_\alpha} \left[\left(\frac{\partial \Delta_{\alpha,\ell,t}}{\partial \ell} \right)^2 + h_s (\Delta_{\alpha,\ell,t})^2 \right] d\ell}_{\text{fluctuations}}, \end{aligned} \quad (2.20)$$

one depending only on the mean path (first term) and another depending only on the fluctuations about the mean path (second term). From the above equation it is apparent

that the mean path contribution $F_{\text{mean path}}$ contains the usual Gaussian chain stretching energy term, namely $k \left(\frac{\partial \hat{\mathbf{r}}_{\alpha, \ell}}{\partial \ell} \right)^2$, and a second term, $\frac{k}{h_s} \left(\frac{\partial^2 \hat{\mathbf{r}}_{\alpha, \ell}}{\partial \ell^2} \right)^2$, which penalises bending of the mean path. Equation 2.20 itself is adequate for the description of the equilibrium configuration of the chain. In contrast, it does not provide any information on the conformational changes of the chain as a function of time.

For this reason, one needs to examine the time evolution of the fluctuation term $\Delta_{a, \ell, t}$ in order to obtain the expressions for the MSD correlation functions of the entangled stars. Substitution of eq 2.19 in eq 2.16 gives the appropriate Langevin equation

$$\zeta_0 \frac{\partial \Delta_{a, \ell, t}}{\partial t} = k \frac{\partial^2 \Delta_{a, \ell, t}}{\partial \ell^2} - kh_s \Delta_{a, \ell, t} + \mathbf{g}(a, \ell, t), \quad (2.21)$$

which is the starting point of this calculation. In a manner similar to eq 2.4 of section 2.2.1, $\Delta_{\alpha, \ell, t}$ can be expanded as a series of eigenmodes:

$$\Delta_{\alpha, \ell, t} = \sum_p \mathbf{Y}_p^c(t) \Psi_p^c(\ell) + \sum_q \left(\mathbf{Y}_q^{s_1}(t) \Psi_q^{s_1}(\alpha, \ell) + \dots + \mathbf{Y}_q^{s_{f'}}(t) \Psi_q^{s_{f'}}(\alpha, \ell) \right), \quad (2.22)$$

where the eigenmodes $\Psi_p^c(\ell)$ and $\Psi_q^{s_i}(\alpha, \ell)$ are the same as in eq 2.4 and their explicit expressions are given by eqs 2.5. However, the eigenmode amplitudes $\mathbf{Y}_p^c(t)$ and $\mathbf{Y}_q^{s_i}(t)$ differ from those of the unentangled case, namely $\mathbf{X}_p^c(t)$ and $\mathbf{X}_q^{s_i}(t)$, because of the additional $-kh_s \Delta_{a, \ell, t}$ term in the Langevin equation of the Warner-Edwards model (compare the structure of eqs 2.1a and 2.21).

The correlation functions $\langle \mathbf{Y}_p^c(t) \cdot \mathbf{Y}_{p'}^c(t') \rangle$ and $\langle \mathbf{Y}_q^{s_i}(t) \cdot \mathbf{Y}_{q'}^{s_i}(t') \rangle$ are calculated following exactly the same procedure as for the calculation of $\langle \mathbf{X}_p^c(t) \cdot \mathbf{X}_{p'}^c(t') \rangle$ and $\langle \mathbf{X}_q^{s_i}(t) \cdot \mathbf{X}_{q'}^{s_i}(t') \rangle$ in the unentangled case. The results are

$$\langle \mathbf{Y}_p^c(t) \cdot \mathbf{Y}_{p'}^c(t') \rangle = \frac{2N_a b^2 \delta_{pp'} \times \exp\left(-\tilde{t}_{R_a} \left[p^2 + \left(\sqrt{h_s} \frac{N_a}{\pi} \right)^2 \right]\right)}{f \pi^2 \left[p^2 + \left(\sqrt{h_s} \frac{N_a}{\pi} \right)^2 \right]} \quad (2.23a)$$

$$\langle \mathbf{Y}_q^{s_i}(t) \cdot \mathbf{Y}_{q'}^{s_i}(t') \rangle = \frac{8N_a b^2 \delta_{qq'} \times \exp\left(-\frac{1}{4} \tilde{t}_{R_a} \left[(2q-1)^2 + \left(2\sqrt{h_s} \frac{N_a}{\pi} \right)^2 \right]\right)}{f \pi^2 \left[(2q-1)^2 + \left(2\sqrt{h_s} \frac{N_a}{\pi} \right)^2 \right]}. \quad (2.23b)$$

These expressions reduce to

$$\langle \mathbf{Y}_p^c(0) \cdot \mathbf{Y}_{p'}^c(0) \rangle = \frac{2N_a b^2 \delta_{pp'}}{f \pi^2 \left[p^2 + \left(\sqrt{h_s} \frac{N_a}{\pi} \right)^2 \right]} \quad (2.24a)$$

$$\langle \mathbf{Y}_q^{s_i}(0) \cdot \mathbf{Y}_{q'}^{s_i}(0) \rangle = \frac{8N_a b^2 \delta_{qq'}}{f \pi^2 \left[(2q-1)^2 + \left(2\sqrt{h_s} \frac{N_a}{\pi} \right)^2 \right]}, \quad (2.24b)$$

at equilibrium. Moreover, they are consistent with eqs 2.11 in the limit $h_s \rightarrow 0$.

An alternative way to evaluate $\langle \mathbf{Y}_p^c(0) \cdot \mathbf{Y}_{p'}^c(0) \rangle$, $\langle \mathbf{Y}_q^{s_i}(0) \cdot \mathbf{Y}_{q'}^{s_i}(0) \rangle$ and consequently $\langle (\Delta_{\alpha,\ell,0} - \Delta_{\alpha,\ell',0})^2 \rangle$, $\langle (\Delta_{\alpha,\ell,0} - \Delta_{\beta,\ell',0})^2 \rangle$, is to use F_Δ together with the equipartition theorem. In particular, first eq 2.22 is inserted into F_Δ yielding

$$F_\Delta = \frac{kf}{2} \left[\sum_{p,p'} \left(\frac{\pi^2 p^2}{2N_a} + \frac{h_s N_a}{2} \right) \langle \mathbf{Y}_p^c(0) \cdot \mathbf{Y}_{p'}^c(0) \rangle \delta_{pp'} + \sum_{q,q'} \left(\frac{\pi^2 (2q-1)^2}{8N_a} + \frac{h_s N_a}{2} \right) \left(\langle \mathbf{Y}_q^{s_1}(0) \cdot \mathbf{Y}_{q'}^{s_1}(0) \rangle + \dots + \langle \mathbf{Y}_q^{s_{f'}}(0) \cdot \mathbf{Y}_{q'}^{s_{f'}}(0) \rangle \right) \delta_{qq'} \right]. \quad (2.25)$$

Then the equipartition theorem is used, that is, each Cartesian component of the correlation functions $\langle \mathbf{Y}_p^c(0) \cdot \mathbf{Y}_{p'}^c(0) \rangle$ and $\langle \mathbf{Y}_q^{s_i}(0) \cdot \mathbf{Y}_{q'}^{s_i}(0) \rangle$ is assigned an energy of $k_B T/2$, leading to eqs 2.24.

Once the equilibrium correlation functions of the mode amplitudes are determined it is a straightforward procedure to obtain $\langle (\Delta_{\alpha,\ell,0} - \Delta_{\alpha,\ell',0})^2 \rangle$ and $\langle (\Delta_{\alpha,\ell,0} - \Delta_{\beta,\ell',0})^2 \rangle$ (c.f. Appendix B). We note that in the remainder of this section the expressions are presented in terms of tube coordinates using the transformations $s = \ell/N_e$, $a^2 = N_e b^2$ and $\tilde{t}_e = |t - t'|/\tau_e = \tilde{t}_{Ra} (N_a/N_e)^2$. As shown in Appendix B, for segments on the same arm:

$$\langle (\Delta_{\alpha,s,0} - \Delta_{\alpha,s',0})^2 \rangle = a^2 \sqrt{k_b} \left[1 - \exp \left(-\frac{|s - s'|}{\sqrt{k_b}} \right) \right] - \frac{a^2 \sqrt{k_b}}{2} \left(\frac{f-2}{f} \right) \left[\exp \left(\frac{-s}{\sqrt{k_b}} \right) - \exp \left(\frac{-s'}{\sqrt{k_b}} \right) \right]^2. \quad (2.26a)$$

For segments on different arms:

$$\langle (\Delta_{\alpha,s,0} - \Delta_{\beta,s',0})^2 \rangle = a^2 \sqrt{k_b} \left[1 - \frac{2}{f} \exp \left(\frac{-(s+s')}{\sqrt{k_b}} \right) \right] - \frac{a^2 \sqrt{k_b}}{2} \left(\frac{f-2}{f} \right) \left[\exp \left(\frac{-2s}{\sqrt{k_b}} \right) + \exp \left(\frac{-2s'}{\sqrt{k_b}} \right) \right]. \quad (2.26b)$$

The factor k_b appearing in these expressions (also in eqs 2.27 and table 2.2 below) is equal to N_s/N_e^2 . The appropriate selection for k_b , according to Ref. [124], is $k_b = 1/4$.

The next step toward the calculation of the MSD is to obtain the contribution of the mean path. Since the chains in our theory are assumed to be Gaussian we know that at equilibrium $\langle (\mathbf{r}_{\alpha,s,0} - \mathbf{r}_{\alpha,s',0})^2 \rangle = a^2 |s - s'|$ and $\langle (\mathbf{r}_{\alpha,s,0} - \mathbf{r}_{\beta,s',0})^2 \rangle = a^2 (s + s')$. Subsequently, the mean path contribution to the MSD can be calculated by using $\langle (\hat{\mathbf{r}}_{\alpha,s} - \hat{\mathbf{r}}_{\alpha,s'})^2 \rangle = a^2 |s - s'| - \langle (\Delta_{\alpha,s,0} - \Delta_{\alpha,s',0})^2 \rangle$ and $\langle (\hat{\mathbf{r}}_{\alpha,s} - \hat{\mathbf{r}}_{\beta,s'})^2 \rangle = a^2 (s + s') -$

$\langle(\Delta_{\alpha,s,0} - \Delta_{\beta,s',0})^2\rangle$. The results for segments on the same arm (i.e. $\alpha = \beta$) and on different arms ($\alpha \neq \beta$) are, respectively:

$$\langle(\widehat{\mathbf{r}}_{\alpha,s} - \widehat{\mathbf{r}}_{\alpha,s'})^2\rangle = a^2|s - s'| - a^2\sqrt{k_b} \left[1 - \exp\left(\frac{-|s - s'|}{\sqrt{k_b}}\right) \right] + \frac{a^2\sqrt{k_b}}{2} \left(\frac{f-2}{f}\right) \left[\left(\exp\left(\frac{-s}{\sqrt{k_b}}\right) - \exp\left(\frac{-s'}{\sqrt{k_b}}\right) \right)^2 \right], \quad (2.27a)$$

$$\langle(\widehat{\mathbf{r}}_{\alpha,s} - \widehat{\mathbf{r}}_{\beta,s'})^2\rangle = a^2(s + s') - a^2\sqrt{k_b} + \frac{2a^2\sqrt{k_b}}{f} \exp\left(\frac{-(s + s')}{\sqrt{k_b}}\right) + \frac{a^2\sqrt{k_b}}{2} \left(\frac{f-2}{f}\right) \left[\exp\left(\frac{-2s}{\sqrt{k_b}}\right) + \exp\left(\frac{-2s'}{\sqrt{k_b}}\right) \right]. \quad (2.27b)$$

2.3.2 Results for the MSD correlation functions

Having obtained the contribution of the mean path one can work out the final expressions for the MSD correlation functions using $\langle(\mathbf{r}_{\alpha,s,t} - \mathbf{r}_{\alpha,s',t'})^2\rangle = \langle(\widehat{\mathbf{r}}_{\alpha,s} - \widehat{\mathbf{r}}_{\alpha,s'})^2\rangle + \langle(\Delta_{\alpha,s,t} - \Delta_{\alpha,s',t'})^2\rangle$ and $\langle(\mathbf{r}_{\alpha,s,t} - \mathbf{r}_{\beta,s',t'})^2\rangle = \langle(\widehat{\mathbf{r}}_{\alpha,s} - \widehat{\mathbf{r}}_{\beta,s'})^2\rangle + \langle(\Delta_{\alpha,s,t} - \Delta_{\beta,s',t'})^2\rangle$ after working out the $\langle\Delta_{\alpha,s,t} \cdot \Delta_{\alpha,s',t'}\rangle$, $\langle\Delta_{\alpha,s,t} \cdot \Delta_{\beta,s',t'}\rangle$ terms using equations 2.22 and 2.23 (c.f. Appendix B). The final results are presented in table 2.2.

The left panel of Fig. 2.6 shows $\langle(\mathbf{r}_{\alpha,s,t} - \mathbf{r}_{\alpha,s',t'})^2\rangle/a^2$ (dashed lines), as a function of \tilde{t}_e , for three different segments along an arm of a $f = 3$ polymer star. The blue, green and red dashed curves correspond to $s = 0.05$ (near the branch point), $s = 0.25$ and $s = 1$ (one entanglement segment from the branch point), respectively. In the same panel, we plot the MSD of the branch point of an unentangled star (fourth expression of table 2.1) and of a segment of an unentangled linear chain with grey and black lines, respectively (as in Fig. 2.3). The ratio of these two lines is $2/f$. In order to obtain the grey and black lines we have converted the corresponding expressions for the MSD (table 2.1) in tube coordinates using $\tilde{t}_{Ra} = \tilde{t}_e (N_e/N_a)^2$, $a^2 = N_e b^2$ and $s = \ell/N_e$. In the right panel of Fig. 2.6 we plot the same MSD (as in the left panel), normalised by $a^2\sqrt{\tilde{t}_e}$. We have also included the MSD of specific segments of unentangled stars, according to $\langle(\mathbf{r}_{\alpha,\ell,t} - \mathbf{r}_{\alpha,\ell,t'})^2\rangle$ of table 2.1 converted to tube coordinates. In analogy with the data sets for entangled stars, the blue, green, and red solid curves for the unentangled case correspond to $s = 0.05$, $s = 0.25$ and $s = 1$, respectively. All dashed curves of Fig. 2.6 have been obtained by using $k_b = 1/4$.

Table 2.2: MSD for entangled stars

MSD	Expression
$\langle (\mathbf{r}_{\alpha,s,t} - \mathbf{r}_{\alpha,s',t'})^2 \rangle$	$a^2 s - s' + a^2 \sqrt{k_b}$ $\times \left[\exp\left(\frac{- s-s' }{\sqrt{k_b}}\right) - \frac{(f-2)}{f} \exp\left(\frac{-(s+s')}{\sqrt{k_b}}\right) \right] -$ $a^2 \sqrt{k_b} \cosh\left(\frac{ s-s' }{\sqrt{k_b}}\right) +$ $\frac{1}{2} a^2 \sqrt{k_b} (\Omega_-^A(s, s', \tilde{t}_e) + \Omega_+^A(s, s', \tilde{t}_e)) +$ $a^2 \sqrt{k_b} \frac{(f-2)}{f} \cosh\left(\frac{(s+s')}{\sqrt{k_b}}\right) +$ $\frac{1}{2} a^2 \sqrt{k_b} \frac{(f-2)}{f} (\Omega_-^B(s, s', \tilde{t}_e) + \Omega_+^B(s, s', \tilde{t}_e))$
$\langle (\mathbf{r}_{\alpha,s,t} - \mathbf{r}_{\beta,s',t'})^2 \rangle$	$a^2 (s + s') + \frac{2}{f} a^2 \sqrt{k_b} \exp\left(\frac{-(s+s')}{\sqrt{k_b}}\right) -$ $\frac{2}{f} a^2 \sqrt{k_b} \cosh\left(\frac{(s+s')}{\sqrt{k_b}}\right) +$ $\frac{2}{f} a^2 \sqrt{k_b} (\Omega_-^B(s, s', \tilde{t}_e) + \Omega_+^B(s, s', \tilde{t}_e))$
$\langle (\mathbf{r}_{\alpha,s,t} - \mathbf{r}_{\alpha,s,t'})^2 \rangle$	$a^2 \sqrt{k_b} \Phi\left(\frac{\sqrt{\tilde{t}_e}}{\pi \sqrt{k_b}}\right) - \frac{1}{2} a^2 \sqrt{k_b} \frac{(f-2)}{f}$ $\times \exp\left(\frac{-2s}{\sqrt{k_b}}\right) \left[1 + \Phi\left(\frac{\sqrt{\tilde{t}_e}}{\pi \sqrt{k_b}} - \frac{\pi s}{\sqrt{\tilde{t}_e}}\right) \right] +$ $\frac{1}{2} a^2 \sqrt{k_b} \frac{(f-2)}{f} \exp\left(\frac{2s}{\sqrt{k_b}}\right) \left[1 - \Phi\left(\frac{\sqrt{\tilde{t}_e}}{\pi \sqrt{k_b}} + \frac{\pi s}{\sqrt{\tilde{t}_e}}\right) \right]$
$\langle (\mathbf{r}_{\alpha,0,t} - \mathbf{r}_{\alpha,0,t'})^2 \rangle$	$\frac{2}{f} a^2 \sqrt{k_b} \Phi\left(\frac{\sqrt{\tilde{t}_e}}{\pi \sqrt{k_b}}\right)$

where $\Phi(x) = \frac{2}{\sqrt{\pi}} \int_0^x e^{-u^2} du$ and

$$\Omega_-^A(s, s', \tilde{t}_e) = \exp\left(\frac{-|s-s'|}{\sqrt{k_b}}\right) \Phi\left(\frac{\sqrt{\tilde{t}_e}}{\pi \sqrt{k_b}} - \frac{\pi |s-s'|}{2\sqrt{\tilde{t}_e}}\right)$$

$$\Omega_+^A(s, s', \tilde{t}_e) = \exp\left(\frac{|s-s'|}{\sqrt{k_b}}\right) \Phi\left(\frac{\sqrt{\tilde{t}_e}}{\pi \sqrt{k_b}} + \frac{\pi |s-s'|}{2\sqrt{\tilde{t}_e}}\right)$$

$$\Omega_-^B(s, s', \tilde{t}_e) = \exp\left(\frac{-(s+s')}{\sqrt{k_b}}\right) \Phi\left(\frac{\sqrt{\tilde{t}_e}}{\pi \sqrt{k_b}} - \frac{\pi (s+s')}{2\sqrt{\tilde{t}_e}}\right)$$

$$\Omega_+^B(s, s', \tilde{t}_e) = \exp\left(\frac{(s+s')}{\sqrt{k_b}}\right) \Phi\left(\frac{\sqrt{\tilde{t}_e}}{\pi \sqrt{k_b}} + \frac{\pi (s+s')}{2\sqrt{\tilde{t}_e}}\right)$$

From the right panel of Fig. 2.6 it is apparent that the segment closer to the branch point (blue dashed curve) follows at very early timescales, up to $\tilde{t}_e \approx 0.01$, the segmental dynamics of an unentangled linear chain (black line). For $0.02 \gtrsim \tilde{t}_e \gtrsim 0.1$ a cross over to the branch point dynamics of the unentangled star occurs, that is, the dashed and solid blue lines coincide in this time window. At later timescales the segment starts to experience

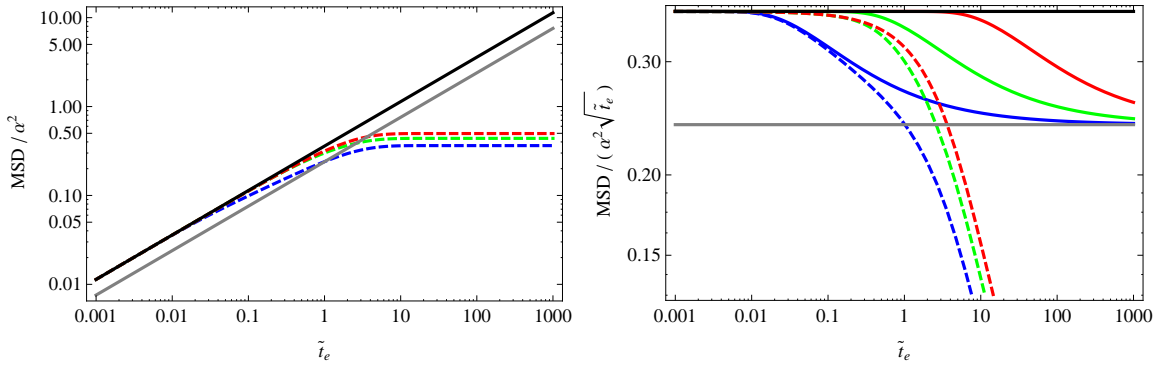


Figure 2.6: Left: Segmental MSD in the entangled regime (i.e. $\langle(\mathbf{r}_{\alpha,s,t} - \mathbf{r}_{\alpha,s,t'})^2\rangle$ of table 2.2), normalised by a^2 , for three different segments along an arm of a star with 3 arms: $s = 0.05$ (blue), $s = 0.25$ (green), and $s = 1$ (red). The grey and black lines refer to unentangled chains; grey - branch point; black - a segment of a linear chain. Right: The same quantities as in the left panel, together with the segmental MSD in the unentangled regime (i.e. $\langle(\mathbf{r}_{\alpha,\ell,t} - \mathbf{r}_{\alpha,\ell,t'})^2\rangle$ of table 2.1), represented as solid curves (colour codes correspond to same values of s). In this case the MSD has been normalised by $a^2\sqrt{t_e}$.

the localising effects and a final cross over to a plateau in the MSD occurs. This plateau arises at timescales $\tilde{t}_e \gtrsim 1$ and shows up as a horizontal line or a line of $-1/2$ slope in the left and right panels of Fig. 2.6, respectively. The other two segments that are located further from the branch point ($s = 0.25$ and $s = 1$) realise that are localised before they “feel” the presence of the branch point. As a result, their MSD exhibits a crossover from the unentangled linear chain behaviour to the plateau regime directly, without following at all the branch point dynamics of the unentangled star.

The expressions of table 2.2, as those of table 2.1, have been derived under the assumption that the internal (fast) Rouse modes dominate the dynamics. Furthermore, they do not include any other relaxation modes such as local reptation and arm retraction. Hence, they are valid for timescales $t \ll \tau_{R_a}$ and for segments in the close proximity of a branch point. In section 2.4, $\langle(\mathbf{r}_{\alpha,s,t} - \mathbf{r}_{\alpha,s,t'})^2\rangle$ is compared against the MD data for the MSD, $\langle\Delta r^2\rangle$, of the “simulation branch point” since the motion of this portion of the chain is unaffected by the omitted relaxation modes. Furthermore, the model developed in this chapter can be used for making predictions for other observables. For example, the first two expressions of table 2.2, i.e. $\langle(\mathbf{r}_{\alpha,s,t} - \mathbf{r}_{\alpha,s',t'})^2\rangle$ and $\langle(\mathbf{r}_{\alpha,s,t} - \mathbf{r}_{\beta,s',t'})^2\rangle$, can be used for the calculation of the dynamic structure factor of an entangled three arm star.

This calculation together with comparison with available experimental NSE data [3], for the branch point, is presented in chapter 3. In the following subsection $\langle(\mathbf{r}_{\alpha,s,t} - \mathbf{r}_{\alpha,s',t'})^2\rangle$ is compared against the respective expression of Vilgis and Boué [120].

2.3.3 Comparison with the Vilgis and Boué expressions

Vilgis and Boué considered the dynamics of a cross-linked chain in a network far above the gel point [120]. In this study the cross-links were modelled in the same way as the entanglements in the model presented in section 2.3.1, that is, the cross-links were represented by localising springs (with fixed centres). Therefore, the expression for the MSD correlation function, $\langle(\mathbf{r}_{s,t} - \mathbf{r}_{s',t'})^2\rangle_{VB}$, of Ref. [120] can be compared with $\langle(\mathbf{r}_{\alpha,s,t} - \mathbf{r}_{\alpha,s',t'})^2\rangle$ of table 2.2, if one sets $f = 2$ in the latter expression.

In terms of the tube variables $a^2 = N_e b^2 = 2(\sqrt{h_s})^{-1} b^2$, $s = \ell/N_e$ and $\tilde{t}_e = |t - t'|/\tau_e$, used in the previous subsection, $\langle(\mathbf{r}_{s,t} - \mathbf{r}_{s',t'})^2\rangle_{VB}$ is expressed as

$$\langle(\mathbf{r}_{s,t} - \mathbf{r}_{s',t'})^2\rangle_{VB} = \frac{a^2}{2} \left[1 - \frac{1}{2} (2 \cosh(2|s - s'|) - \Omega_-^A(s, s', \tilde{t}_e) - \Omega_+^A(s, s', \tilde{t}_e)) \right], \quad (2.28)$$

where the functions $\Omega_-^A(s, s', \tilde{t}_e)$ and $\Omega_+^A(s, s', \tilde{t}_e)$ are given in table 2.2. On the other hand, $\langle(\mathbf{r}_{\alpha,s,t} - \mathbf{r}_{\alpha,s',t'})^2\rangle$ of table 2.2, for $f = 2$ and $k_b = 1/4$, reduces to

$$\langle(\mathbf{r}_{\alpha,s,t} - \mathbf{r}_{\alpha,s',t'})^2\rangle = a^2 |s - s'| - \frac{a^2}{2} [1 - \exp(-2|s - s'|)] + \frac{a^2}{2} \left[1 - \frac{1}{2} (2 \cosh(2|s - s'|) - \Omega_-^A(s, s', \tilde{t}_e) - \Omega_+^A(s, s', \tilde{t}_e)) \right]. \quad (2.29)$$

In this equation the first two terms correspond to the contribution of the mean path while the third term represents the contribution of the fluctuations. Equations 2.28 and 2.29 differ only by the mean path contribution.

However, the mean path term is vital for maintaining the Gaussian statistics of the chain. In particular, at equilibrium ($\tilde{t}_e = 0$), $\Omega_-^A(s, s', \tilde{t}_e) = -\exp(-2|s - s'|)$ and $\Omega_+^A(s, s', \tilde{t}_e) = \exp(2|s - s'|)$ leading to $\langle(\mathbf{r}_{\alpha,s,0} - \mathbf{r}_{\alpha,s',0})^2\rangle = a^2 |s - s'|$, which coincides with the Gaussian chain result as expected. In contrast, the respective result of Vilgis and Boué is $\langle(\mathbf{r}_{s,0} - \mathbf{r}_{s',0})^2\rangle_{VB} = \frac{a^2}{2} [1 - \exp(-2|s - s'|)]$ indicating that the conformation of the chain is Gaussian at short length scales only, i.e. for $|s - s'| \ll 1$.

Equation 2.28 has been used in the literature in the interpretation of neutron spin echo experiments [3]. In this particular study the authors used $\langle (\mathbf{r}_{s,t} - \mathbf{r}_{s',t'})^2 \rangle_{VB}$ to describe the motion of labelled segments in the vicinity of the branch point of a three arm symmetric polymer star. Essentially, the labelled section of the chain was treated as a two arm star. However, the segmental friction, ζ_0 , of this effective linear chain was increased by the factor $f/2$ ($f = 3$) to account for the reduced mobility due to the branch point. As shown in Fig. 2.6 the expressions developed in this chapter incorporate directly the effects of the stronger friction at the branch point. In chapter 3 both the Vilgis and Boué equation and the expressions developed in the previous subsection are used, in the comparison of the theoretical scattering function with the NSE data.

2.4 Comparison with MD simulations

2.4.1 Simulations with fixed chain ends

As discussed in section 1.6, in the MD simulations of entangled stars with free ends several relaxation modes are active at different timescales. Specifically, at early timescales ($t < \tau_e$) the dynamics of the chain is dominated by Rouse motion. The Rouse regime is followed by local reptative motion (“Rouse in tube”) or arm retraction depending on the position of the segment along the arm (additionally arm retraction contributes continuously to constraint release). These features are also evident in the respective results for the Cayley trees [1]. Since the theoretical expression for segmental self-motion (i.e. $\langle (\mathbf{r}_{\alpha,s,t} - \mathbf{r}_{\alpha,s,t'})^2 \rangle$ of table 2.2) accounts only for internal Rouse modes, its validity should be initially tested against MD simulations where all other relaxation mechanisms are to a high degree inactive.

In view of these ideas, simulations of symmetric stars and Cayley trees in which the free ends of all arms are fixed in space have been performed [1]. The points at which the ends are fixed simply correspond to the positions that the ends have at the beginning of the simulation. Notice that the configurations of the chains at the beginning of the simulation (that is, the initial configurations) correspond to configurations of an equilibrated melt. The immobilization of the ends suppresses arm retraction, as well as constraint release events driven by arm retraction, hence these simulations provide MSD results that can be

directly compared with $\langle(\mathbf{r}_{\alpha,s,t} - \mathbf{r}_{\alpha,s,t'})^2\rangle$ of table 2.2. Figure 2.7 presents the simulation results for the MSD of the “simulation branch points”, with their respective error bars, as a function of time. In particular, red and blue circles refer to the star and Cayley tree, respectively. In the same figure the average MSD (up to time scales of $t \sim 10^6\tau_0^{MD}$ for which data for both branch points exist) is also shown with small filled triangles. The results demonstrate that there are no differences, within statistics, between the MSD of the branch point in the star and in the Cayley tree in the time window of the simulation.

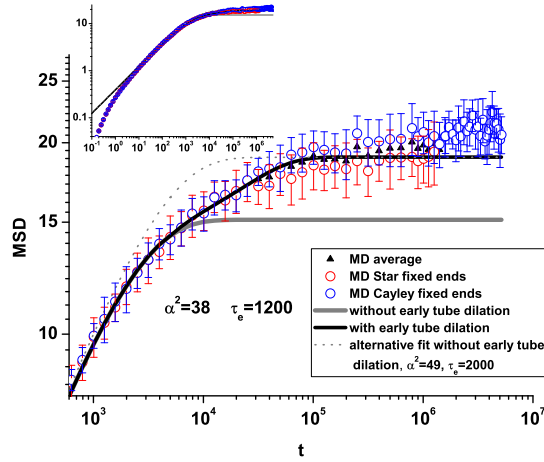


Figure 2.7: MD results for the MSD of the “simulation branch point” of the star (red circles) and of the central “simulation branch point” of the Cayley tree (blue circles), with their respective error bars. Filled triangles refer to the the average MSD up to $t \sim 10^6\tau_0^{MD}$. The grey line refers to the theoretical MSD without ETD. The dashed grey line shows an alternative fit that describes well the Rouse and the plateau regimes but fails to describe the crossover between these two regimes. The black line shows the theoretical prediction when ETD is accounted for. MD data are provided by P. Bačová and Dr. A. J. Moreno [1].

Figure 2.7 also includes our theoretical prediction, i.e. $\langle(\mathbf{r}_{\alpha,s,t} - \mathbf{r}_{\alpha,s,t'})^2\rangle$, of table 2.2 as a solid grey line. In a similar manner to the average performed in the MSD of the simulations, we have averaged over the MSD for the continuous chain between $s = 0$ and $s = 3/N_e$ for each arm. The solid grey line has been constructed using the values $a^2 = 38\sigma$ and $\tau_e = 1200\tau_0^{MD}$ (these values correspond to simulation units). This line compares very well with the simulation data up to $t \approx 6 \times 10^3\tau_0^{MD}$. However, it significantly underestimates the value of the average MSD of the simulation (small triangles) in the

apparent plateau region. By adjusting the parameters a^2 and τ_e we can construct curves which compare well with the solid triangles in the Rouse regime (i.e. up to $t \approx 10^3 \tau_0^{MD}$) and in the plateau-like region of the simulation. Nevertheless, these curves fail to describe the crossover between these two regimes (in the interval $10^3 \tau_0^{MD} \lesssim t \lesssim 10^5 \tau_0^{MD}$). One example of such a curve is shown in Fig. 2.7 with a dashed grey line. This curve has been constructed using $a^2 = 49\sigma$ and $\tau_e = 2000\tau_0^{MD}$. Thus, we have forced the values of $a^2 = 38\sigma$ and $\tau_e = 1200\tau_0^{MD}$ in order to match the theoretical and the simulation MSD in the Rouse and crossover regime. Obviously, since the model predicts Rouse dynamics at $t \rightarrow 0$, it does not account for the early ballistic motion observed in MD, that is, independently of the values of a^2 and τ_e our predictions do not match the MD data at timescales $t < 1\tau_0^{MD}$ (c.f. inset of Fig. 2.7).

We note that the theoretical entanglement time $\tau_e = 1200\tau_0^{MD}$ is somewhat smaller than the value $\tau_e = 1800\tau_0^{MD}$ estimated from previous simulation [127]. Nevertheless, taking into account that local stiffness effects in the simulated chains are not implemented in the theoretical model and that there are some uncertainties in the method of estimation of τ_e from the simulation, these two values are in a relatively good agreement.

The most noticeable feature in Fig. 2.7 is that the MD data continue to rise at times $t > \tau_e$ whilst the theoretical MSD (solid grey line) establishes a clear plateau. The plateau in the theory is fully expected since no other relaxation modes, apart from internal (fast) Rouse modes, are included in the model. In contrast, the MD data clearly indicate that, even if the arm ends are fixed, there is some relaxation of the entanglement constraints experienced by the branch point. This relaxation occurs after the branch point has explored its initial entanglement cage at the timescale τ_e .

A possible interpretation of this observation is that there is some process occurring after τ_e , giving rise to an apparent slow relaxation of the branch point localisation. We refer to this process as an (early) “tube dilation” (ETD), as it shares some features with the processes softening the tube. However, we stress that this process is not a dilation in a sense of widening of the tube due to “standard” constraint release events which arise from the retraction of the arms. This is because the chain ends are fixed in these particular simulations hence the arm retraction process is quenched.

We can only speculate as to the mechanisms involved in this early tube dilation process.

It could be due to tension equilibration along the constraining chains, which would occur at the Rouse time of the arms. In an earlier work Zhou and Larson [113] investigated, by MD of a similar bead-spring model, melts of linear chains with fixed chain ends. They also reported tube dilation and attributed it to a new type of constraint release (c.f. Fig. 7 in Ref. [113]), called ‘end looping’ constraint release (ELCR), which occurred through Rouse motion. ELCR in melts of linear chains has also been studied at the level of primitive paths [131]. However, for strongly entangled chains this process is only effective near the chain ends [113], and we do not expect it to be relevant for relaxation of the branch point in the systems investigated here.

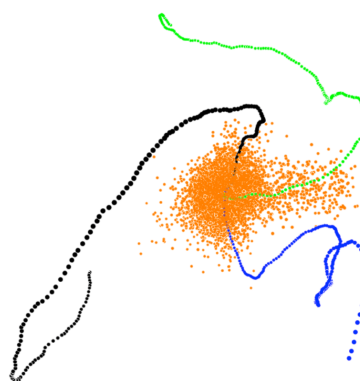


Figure 2.8: For a selected star in the simulations with fixed ends, trajectory of the branch point (orange dots) and mean paths of the three arms (black, blue and green). A deep fluctuation of the branch point along the green arm is clearly observed. The figure is provided by P. Bačová and Dr. A. J. Moreno [1].

An alternative explanation is that the branch point makes short excursions along the tubes of each arm (known as “diving modes” [132]), which in entropic terms are not so unfavourable as end looping. Still, it is worth mentioning that visual inspection of branch point trajectories, in the MD simulations with fixed ends, gives some indications of the diving modes. Concretely, the branch point diving can be seen in roughly half of the branch point trajectories of Cayley tree and symmetric stars. Figure 2.8 shows an example for a selected star. Orange dots represent the trajectory of the branch point (plotted at intervals of $t \sim 0.1\tau_e$). The three curves formed by the black, blue and green lines are the ‘mean paths’ of the three arms. These have been obtained by averaging the monomer positions over the whole trajectory of the simulation with fixed arms, and provide an estimation of the tube contour. The shape of the trajectory in the figure is not

spherical and reveals a deep exploration of one of the tubes (green arm) by the branch point. Such a deep withdrawal of the branch point in only one particular direction occurs rarely, in the most cases the trajectory has an elliptical or triangular shape, indicating much milder branch point excursions in two or three arm tubes.

A precise characterization of the microscopic mechanisms involved in the early tube dilation process is beyond the scope of this work. Nevertheless, irrespective of its origin, we can quantify the magnitude of the effect of this process by treating it as a weak tube dilation, as follows. We assume that the tube enlargement depends weakly on time so there is a separation of timescale between fast Rouse motion within the tube and a slower "tube enlargement" process. Therefore, we may still use the expression for $\langle(\mathbf{r}_{\alpha,s,t} - \mathbf{r}_{\alpha,s,t'})^2\rangle$ of table 2.2 after rescaling appropriately the model parameters as

$$a^2(t) = \frac{a^2}{g(t)}, \tau_e(t) = \frac{\tau_e}{g^2(t)}, s(t) = s_0 g(t). \quad (2.30)$$

Here, as in the rest of the chapter, is assumed that $t' = 0$ in $\langle(\mathbf{r}_{\alpha,s,t} - \mathbf{r}_{\alpha,s,t'})^2\rangle$. Under this renormalisation the early Rouse behaviour of the chain in the tube remains unchanged. The term $g(t)$ is a slowly varying tube dilation function which is obtained by minimising the error between the theory and the averaged branch point MD data (i.e. the small filled triangles of Fig. 2.7) using trial values in the range $[0, 1]$. The so-obtained function $g(t)$ can be fitted to

$$g(t) = \begin{cases} g_0 + g_1, & \text{if } t \leq t_0 \\ g_0 + g_1 \exp(- (t - t_0)/\tau_g), & \text{if } t > t_0 \end{cases} \quad (2.31)$$

with $g_0 \approx 0.75$, $g_1 \approx 0.25$, $\tau_g \approx 22600.0\tau_0^{MD}$, and $t_0 = 5010.0\tau_0^{MD}$ for both stars and Cayley trees (since the respective MSD from simulations are identical within statistics). The black line in Fig. 2.7 represents the theoretical MSD of the branch point after incorporating the effect of tube dilation as described above. It is worth mentioning that $g(t)$ at the longest MD time approaches a value of 0.75, which can be interpreted as an increase of the original tube diameter a of the order of 15%. The effective relaxation time τ_g for the tube dilation is about five times smaller than the Rouse relaxation time of an arm. Having analyzed the mean square displacement for the branch point in the MD with fixed arm ends, we can move on to assess the effects of constraint release in the case of the free ends. We present our findings in the following subsection.

2.4.2 Simulations with free chain ends

In this section we extend the comparison between our model and the MD simulations to MSD data obtained from simulated systems with free chain ends. Since the chain ends in the simulations are free the arm retraction process is active. As a result “standard” constraint release events occur, that is, as the arms retract toward the branch point they remove entanglements on surrounding chains. In order to compare our model predictions for the MSD with the simulation results we need to quantify the effects of these constraint release events. The dynamic dilution hypothesis, discussed in section 1.5.2, provides a means of quantifying constraint release in terms of $\psi(t)$, the tube survival probability which represents the fraction of arm material still not visited by arm retraction (i.e. yet unrelaxed) after a waiting time t . We stress that in the upper limit of the simulation time window ($2 \times 10^7 \tau_0^{MD}$), $\psi(t) \approx 0.3$ and $\psi(t) \approx 0.4$ for the star and the Cayley tree, respectively (c.f. Fig. 2.11 below). Therefore, for both simulated systems the dynamics of the inner section of the chain, close to the branch point, is not affected by the arm retraction mechanism directly.

We take the aforementioned ideas and facts into consideration and argue, in addition, that at the end of the MD simulation the dynamics of the unrelaxed portion of the chain, in the vicinity of the branch point, is still dominated by chain motion within a localising potential (“tube”). In other words, we assume that the dynamics of the aforementioned section of the chain is dictated by fast Rouse modes which express fluctuations (transverse motion) about the mean path. (We suppose that local motion along the tube is not yet active.) Nevertheless, these modes evolve within a tube which slowly dilates as a function of time. (See Fig. 2.9 for a schematic illustration.) Thus, we anticipate that $\langle (\mathbf{r}_{\alpha,s,t} - \mathbf{r}_{\alpha,s,t'})^2 \rangle$ of table 2.2 can still be used to describe the segmental self-motion, if the model parameters are renormalised (rescaled) as

$$a^2(t) = \frac{a^2}{g(t)\psi^{\alpha_d}(t)}, \quad \tau_e(t) = \frac{\tau_e}{g(t)^2\psi^{2\alpha_d}(t)}, \quad s(t) = s_0 g(t)\psi^{\alpha_d}(t). \quad (2.32)$$

In this equation, $g(t)$ is the function obtained in the previous subsection (c.f. eq 2.31) describing the early tube dilation process and $\psi(t)$ is the tube survival probability. We note that these rescaling rules differ from the respective rules of eq 2.30 only by $\psi(t)$. This is because, in terms of our model, constraint release is considered to provide an additional rescaling of the tube diameter over and above the early tube dilation process discussed in

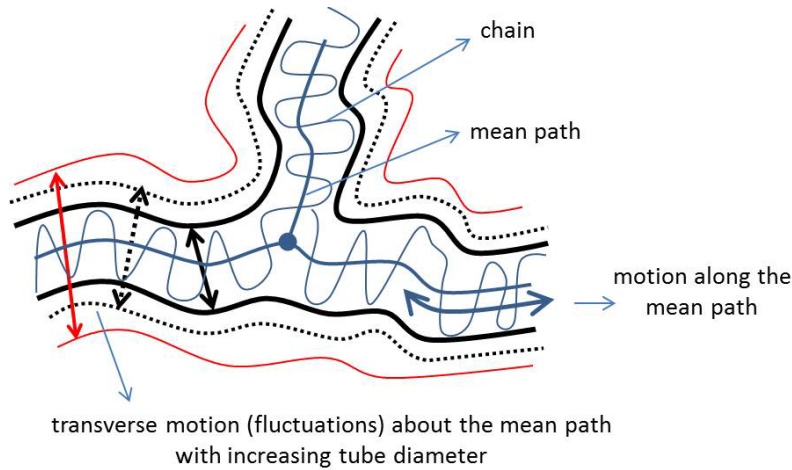


Figure 2.9: Due to CR and/or early tube dilation the fast Rouse modes (transverse motion about the mean path) evolve within a tube that smoothly dilates with time. Motion along the mean path is supposed quenched. Black solid lines show the undilated tube. Black dashed lines and red lines represent the dilated tube at different timescales.

the previous section. In other words, we assume that though constraint release and early tube dilation produce a similar effect, i.e. widening of the tube, they act independently. The exponent α_d is the so-called dilution exponent, often assumed to be 1 or $4/3$ [98]. In our comparison we investigate both values of α_d (c.f. figure 2.12 below). It is apparent that in order to use the expressions of table 2.2, under the renormalisation of eq 2.32, one needs to estimate $\psi(t)$ first. The estimation of $\psi(t)$ can be done directly from the MD simulations. It has been done by P. Bačová and Dr. A. J. Moreno and the results are presented in the joint publication [1]. Here, the procedure for obtaining $\psi(t)$ is reproduced for completeness.

First, the correlation function,

$$\Psi_{s_\ell}^{MD}(t) = \langle \mathbf{u}_{\alpha, s_\ell, 0} \cdot (\mathbf{R}_{\alpha, t}^e - \frac{1}{2} \mathbf{R}_{\beta, t}^e - \frac{1}{2} \mathbf{R}_{\gamma, t}^e) \rangle, \quad (2.33)$$

is computed. This is the analogous correlation function of eq 2.13 of section 2.2.3 in the entangled regime. Since $B' = C' = -1/2$ the undesirable peaks of the “full correlation” function are avoided (c.f. Fig. 2.4) and therefore eq 2.33 is sensitive to tube escape, but not to local reorganisation of the chain. (Notice that the choice $B' = C' = 0$ is not suitable because the correlator will become sensitive to local orientation relaxation due to constraint release.) Nevertheless, it is stressed that eq 2.13 refers to unentangled stars and has been calculated using the Rouse modes of eq 2.4, whereas eq 2.33 refers to entangled

stars and has been computed using the MD trajectories of the chain, that is, the tangent vector $\mathbf{u}_{\alpha,s_\ell,0}$ at time $t' = 0$ and the end-to-end vectors $\mathbf{R}_{\alpha,t}^e$, $\mathbf{R}_{\beta,t}^e$ and $\mathbf{R}_{\gamma,t}^e$ at time t are obtained from the coordinates of the chain in the simulation box. The extension of eq 2.33 to Cayley trees is discussed in Appendix C.1. In the simulations $\mathbf{u}_{\alpha,s_\ell,0}$ has been approximated by the end-to-end vector of an arm segment of length equal to ten monomeric units. This segment size is chosen as a compromise to both achieving good statistics and averaging fast monomer fluctuations (not captured within the model). It is worth mentioning that correlation functions similar to equation 2.33 have been proposed in a MD study of polymer melts of linear chains [133]. In this study instead of the trajectories of the chain the trajectories of the mean path are used. The latter are obtained by averaging over τ_e the trajectories of the (actual) chain [133]. In other words, this average is performed over short-time (fast) internal modes of the chain. However, as demonstrated in Fig. 2.4, for the inner sections of the chain, which are of interest, the analogous correlation function of $\Psi_{s_\ell}^{MD}(t)$ is insensitive to these fast Rouse modes for times up to $\tau_{Ra} \gg \tau_e$. This justifies that the use of chain coordinates rather than the mean path has no significant effect on the computation of $\Psi_{s_\ell}^{MD}(t)$. The same applies when tube dilation is present as it simply introduces a few more fast Rouse modes to average over.

Second, for different segments s_ℓ along the arms, $\Psi_{s_\ell}^{MD}(t)$ is plotted as a function of time and the data are fitted to stretched exponential (KWW) functions:

$$x_{s_\ell}(t) = \exp(-(t/\tau_{s_\ell})^\beta), \quad (2.34)$$

where β is the stretching exponent and τ_{s_ℓ} is the relaxation time of the s_ℓ th segment. This relaxation time is interpreted as the time taken for the arm retraction process to reach the s_ℓ th segment. From the fitting procedure one obtains a set of points $[s_\ell; \tau_{s_\ell}]$, which provide the information about the consecutive relaxation of the segments along the arms, and the individual values of β for each segment. The obtained spectrums of $[s_\ell; \tau_{s_\ell}]$ for the stars and the Cayley trees are presented in tables 1 and 2 of Appendix C.2, respectively. Figure 2.10 shows $\Psi_{s_\ell}^{MD}(t)$ with open squares (filled circles) for three different segments of the symmetric stars (Cayley trees). In particular, the red, green and blue curves correspond to $s_\ell = 0.3, 0.5,$ and $0.8,$ respectively. For the Cayley trees these values refer to segments placed along the long arm ($Z=8$) of the molecule. In the same figure with solid lines some KWW fitting functions are also presented for comparison. From Fig. 2.10 it is evident that not all functions fully relax within the MD time window. For

example, in both systems the inner segments remain, on average, confined in their tubes, that is, for $s_\ell = 0.3$ (red symbols) the correlator $\Psi_{s_\ell}^{MD}(t)$ barely drops to the value ≈ 0.7 (≈ 0.8) for the stars (Cayley trees) at the end of the simulation. For such segments $\Psi_{s_\ell}^{MD}(t)$ is not fitted to eq 2.34.

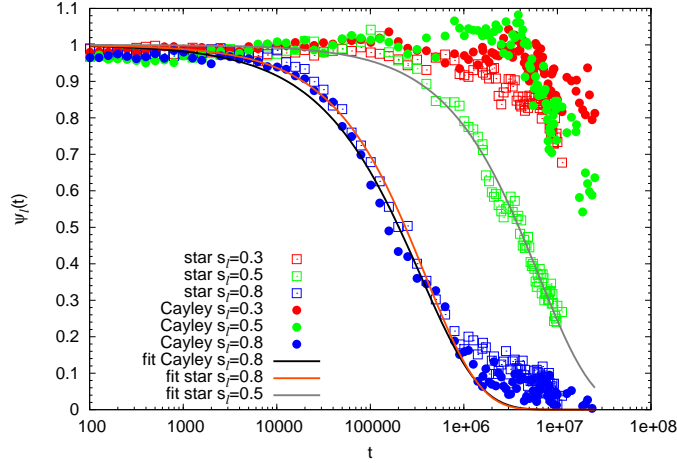


Figure 2.10: The correlator $\Psi_{s_\ell}^{MD}(t)$ for three different segments s_ℓ along the arm of the star (squares) and the long arm of the Cayley tree (circles). Some KWW fitting functions are shown by lines. The figure is provided by P. Bačová and Dr. A. J. Moreno [1].

Third, the relaxation spectrums $[s_\ell; \tau_{s_\ell}]$ of the arms of the stars and of the Cayley trees, presented in Appendix C.2, are used in order to construct functions $\Xi_\alpha(t)$, $\Xi_\beta(t)$ and $\Xi_\gamma(t)$ that represent the fraction of material still not visited by arm retraction on the respective part α, β and γ of the molecule. For the star the indices α, β, γ denote the three arms while for the Cayley tree refer to the inner and outer sections of the long arms and to the attached side arm. Essentially, the discrete set of points $[s_\ell; \tau_{s_\ell}]$ of each part α, β, γ is fitted to some model function, in order to obtain the respective continuous functions $\Xi_{\alpha, \beta, \gamma}(t)$. Two model functions have been used as possible candidates, specifically a pure exponential function and a KWW function of the form of eq 2.34. However, the data show strong deviations from pure exponential behaviour and are much better described by a KWW function [1]. The functions $\Xi_{\alpha, \beta, \gamma}(t)$ are normalised so that $\Xi_{\alpha, \beta, \gamma}(0) = 1$ (that is, all the material is confined in the original tube at $t = 0$) and decay with time in an exponential-like manner until all the material in the respective part is relaxed, that is, $\Xi_{\alpha, \beta, \gamma}(\tau_a^{\alpha, \beta, \gamma}) = 0$ when arm retraction reaches the branch point of part α, β, γ at $t = \tau_a^{\alpha, \beta, \gamma}$. In the simulation, this limit is encountered for the side arm and the outer

section of the long arm of the Cayley tree only. The explicit expressions of the functions $\Xi_{\alpha,\beta,\gamma}(t)$, for both architectures, can be found in Appendix C.2.

Finally, having estimated the tube survival probabilities of each arm (part) of the star (Cayley tree), i.e. the functions $\Xi_{\alpha,\beta,\gamma}(t)$, the overall tube survival probability $\psi(t)$ of the star and of the Cayley tree is calculated according to

$$\psi(t) = \frac{\tilde{A}Z_{\alpha}\Xi_{\alpha}(t) + \tilde{B}Z_{\beta}\Xi_{\beta}(t) + \tilde{C}Z_{\gamma}\Xi_{\gamma}(t)}{\tilde{A}Z_{\alpha} + \tilde{B}Z_{\beta} + \tilde{C}Z_{\gamma}}. \quad (2.35)$$

In this expression Z_{α} , Z_{β} and Z_{γ} denote the number of entanglements on the respective arm (part) α , β and γ of the star (Cayley tree). $\tilde{A} = \tilde{B} = \tilde{C} = 1$ for the star and $\tilde{A} = \tilde{B} = \tilde{C} = 3$ for the Cayley tree. The form of eq 2.35 implies that the total tube survival probability is the weight contribution of the tube survival probability of each arm (part) of the star (Cayley tree). Obviously, for the star, due to symmetry, each arm contributes equally and so $\Xi_{\alpha}(t) = \Xi_{\beta}(t) = \Xi_{\gamma}(t)$.

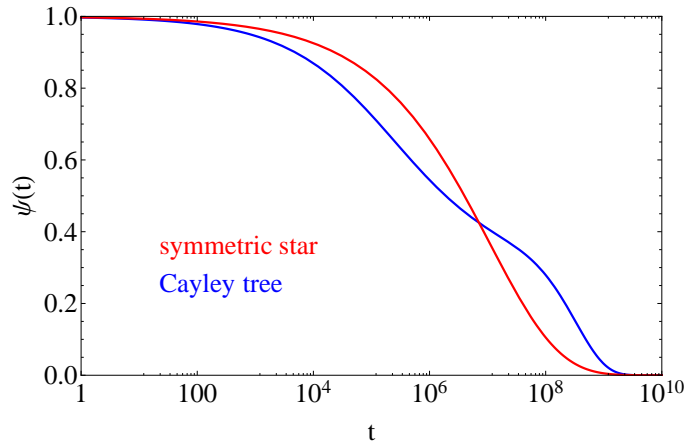


Figure 2.11: Tube survival probability of the star and of the Cayley tree, as computed from the simulations. The computation has been done by P. Bačová and Dr. A. J. Moreno [1].

The tube survival probabilities of the symmetric star and of the Cayley tree, obtained from the methodology described above, are shown in Fig. 2.11 as a function of time. The red and blue lines refer to the three arm symmetric star and the Cayley tree, respectively. These functions extend beyond the MD time window (i.e. $t \gtrsim 2 \times 10^7 \tau_0^{MD}$) and fully decay at $t \sim 10^9 \tau_0^{MD}$. However, this is simply a possible extrapolation of the data. Nothing that follows depends on this. According to Fig. 2.11, at the end of the MD simulation $\psi(t) \approx 0.3$ and $\psi(t) \approx 0.4$ for the star and Cayley tree, respectively. This

justifies that the segments in the vicinity of the branch point are not yet visited by the arm retraction process.

Interestingly, the fraction of unrelaxed material is larger in the star than in the Cayley tree up to $t \approx 7 \times 10^6 \tau_0^{MD}$. Then the two curves cross each other; at longer times tube relaxation is faster in the stars. The observed behaviour can be explained as follows. The Cayley trees possess more free ends than the symmetric stars, as they have short side arms attached. These side arms, up to $t \approx 10^6 \tau_0^{MD}$ at which fully relax, provide extra tube dilation that is reflected in the lower values of $\psi(t)$ for the Cayley tree in this time interval. At timescales $t \gtrsim 10^6 \tau_0^{MD}$ the retracted side arms add friction to the long arms. This additional friction slows down the retraction of the long arms. As a result, the $\psi(t)$ of the Cayley tree is higher than the $\psi(t)$ of the star at long times.

Having obtained the tube survival probability $\psi(t)$ and the early tube dilation function $g(t)$ one can determine the time evolution of the model parameters through eq 2.32 and therefore calculate $\langle (\mathbf{r}_{\alpha,s,t} - \mathbf{r}_{\alpha,s,t'})^2 \rangle$ of table 2.2 and compare it against the MD data. The segmental MSD, as predicted by $\langle (\mathbf{r}_{\alpha,s,t} - \mathbf{r}_{\alpha,s,t'})^2 \rangle$, is presented in Fig. 2.12 with cyan and magenta lines for $\alpha_d = 1$ and $\alpha_d = 4/3$, respectively. In the same figure the MD data for the “simulation branch points”, obtained from simulations in which all chain ends were free, are depicted with open black circles together with their respective error bars. Note that in the majority of cases the width of the error bar is of a similar size to the width of the black open circle. The left panel refers to the symmetric star while the right panel to the Cayley tree. The data of the simulation with fixed ends (small red and small blue circles), previously presented in Fig. 2.7, are also included for comparison.

From Fig. 2.12 it is evident that the MSD of the branch point is larger than its counterpart in the simulation with fixed ends (compare the open black circles with the small filled circles at timescales bigger than $t \sim 10^5 \tau_0^{MD}$). This is because constraint release is active in this case. Moreover, in the time window $10^3 \tau_0^{MD} \lesssim t \lesssim 5 \times 10^6 \tau_0^{MD}$, the branch point in the star is more localised than in the Cayley tree, since at these timescales $\psi(t)$ of the star is bigger than $\psi(t)$ of the Cayley tree (c.f. Fig. 2.11). From the same figure it is clear that the theoretical predictions compare well with the MD data for dilation exponent $\alpha_d = 1$. The good agreement between the model predictions and the MD data demonstrates that one can use the tube survival probability, parameterised by $\psi(t)$, to predict the effective dilation of the tube diameter, measured from the mean square

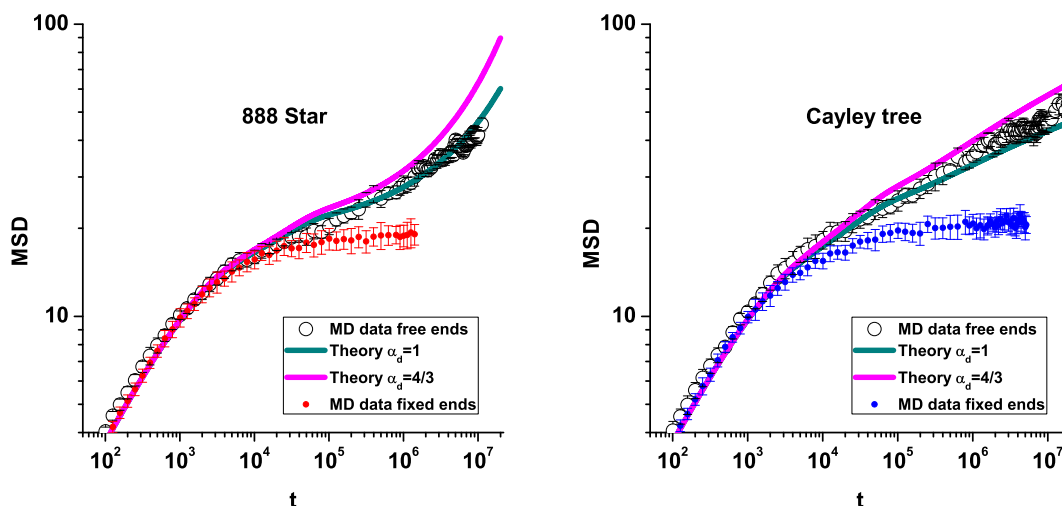


Figure 2.12: MSD of the branch point of the stars (left) and Cayley trees (right) with free ends. MD data are shown as open black circles. Their error is shown with black bars. The cyan (magenta) line refers to the theoretical MSD using $\alpha_d = 1$ ($\alpha_d = 4/3$) and accounts for CR and ETD. The MD data for fixed arm ends (filled circles with their error bars) are also included. The MD data are provided by P. Bačová and Dr. A. J. Moreno [1].

displacement of the branch point. This observation is in accordance with the “dynamic dilution” hypothesis. However, it remains possible that a higher value of α_d , such as $4/3$, could be used, but this would require some form of partial tube dilation, as (for example) suggested by Watanabe et al. [134, 135].

2.5 Conclusions

This chapter dealt with the local motion of a branch point. Both unentangled and entangled symmetric polymer stars were considered. The dynamics of unentangled chains were described by extending the Rouse model [71] to the polymer star structure. Entangled chains were represented by means of localising springs [121, 122]; that is, each segment of a Rouse star was localised by its own harmonic potential and so it was enforced to fluctuate about a mean path [124]. For both unentangled and entangled chains, analytical expressions for the mean square displacement (MSD) correlation functions were derived (c.f. tables 2.1 and 2.2). Moreover, in the case of entangled chains, the expression for the branch point segmental MSD was compared against MD data obtained from simulations in which the chain ends were either free or motionless [1]. In the latter

case the arm retraction process was quenched, thereby the constraint release (CR) events were suppressed in the simulations.

For unentangled chains, it was found that the mobility of the branch point, i.e. the segmental MSD of the branch point, reduces by a factor of $2/f$ compared to the mobility of the middle segment of a linear chain. For entangled systems, it was found that:

- I. The theoretical MSD of the branch point exhibits a plateau as soon as the branch point encounters the confining potential. This is due to the fact that the only source of conformational relaxation, in the context of the model, is fast Rouse modes. These modes are only related to the fluctuations (transverse motion) about the mean path. They do not generate motion along the mean path (tube).
- II. At times $t > \tau_e$, the MSD of the branch point (in the MD simulations in which the arm tips were motionless) continues to grow weakly with increasing time, contrary to the model. The model can capture this behaviour provided that an early tube dilation (ETD) process, which smoothly increases the tube diameter as a function of time, is allowed (c.f. eqs 2.31 and 2.30). It remains possible, however, that the simulation data could be explained by motion along the mean path rather than early tube dilation.
- III. Assuming that CR provides an additional rescaling of the tube diameter over and above the ETD process, the model predictions for the MSD of the branch point, using a dilation exponent of unity ($\alpha_d = 1$), compare well with simulation data obtained from simulations in which the chain ends are free (see Fig. 2.12). This result is in accordance with the “dynamic dilution” hypothesis [2].

Chapter 3

Description of Neutron Spin Echo data using tube theory and the Random Phase Approximation

3.1 Introduction

The aim of this chapter is to describe theoretically the scattering from polymer melts, which consist of partially labelled chains, by using the Random Phase Approximation (RPA) [136, 137] and the Warner-Edwards (WE) picture of the tube [121, 122]. (In this picture of the tube entanglements are modelled by localising springs, as already discussed in section 2.3.1.)

However, we stress that our main concern is the interpretation of the Neutron Spin Echo (NSE) data of Zamponi et al. [3] from the copolymer melt of the three arm symmetric stars (system I below); that is, we intent to compute the total (time dependent) scattering signal, $P(q, t)$, i.e. eq 1.29, for this system. As regards the mixture of linear chains (system II below), we will limit our study to the calculation of the equilibrium scattering signal only (that is, the static scattering at $t = 0$). The two systems of interest are the following:

- I. A copolymer melt of polyethylene (PE) symmetric stars that consist of three arms. Here, each chain contains labelled and non-labelled sections. Specifically, the labelled section of the chain, which is protonated (H), is the branch point itself,

and a fraction of monomers on each arm in the vicinity of the branch point. (In what follows, this part of the chain is simply referred to as the branch point.) The remaining sections of the arms are non-labelled, i.e. they are deuterated (D). Clearly, the copolymer is designed in such a way so that the scattering experiment delivers information about the motion of the branch point only [3].

- II. A polymer mixture (blend) made of centre-labelled (protonated) linear chains, and matrix linear chains, which are fully deuterated, and have molecular weight similar to the molecular weight of the labelled chains [84]. The volume fraction of the centre-labelled chains is $\phi_{c_{\text{lab}}} = 0.2$ whilst the volume fraction of the non-labelled matrix chains is $\phi_{c_{\text{mat}}} = 0.8$.

A schematic drawing of the two systems is shown Fig. 3.1. In this figure, the blue colour refers to the protonated species while the red colour refers to the deuterated species. We note that for both systems the parent material is polybutadiene (PB). The exact molecular characteristics of the parent materials, taken from Refs. [3, 84], are summarised in table 3.1.

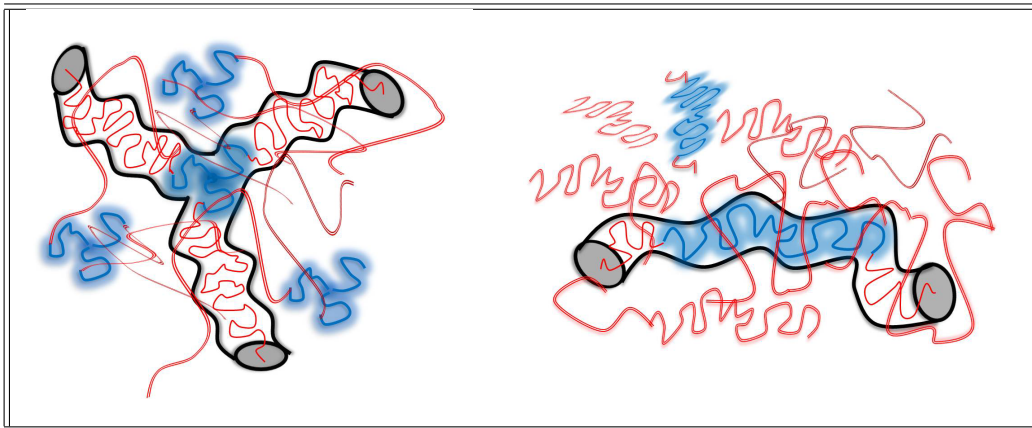


Figure 3.1: Schematic drawing of the studied systems. Left: A melt of star polymers with a short labelling (protonated monomers) near the branch point (blue colour). The rest of the molecule is deuterated (red colour). Right: Centre-labelled linear chains embedded in a matrix of fully deuterated chains.

Due to the fact that the parent material is PB, the structures of the protonated and deuterated monomers are, respectively, $-[CH_2 - CHD - CHD - CH_2]-$ and $-[CD_2 - CD_2 - CD_2 - CD_2]-$. In what follows, the former structure is defined as the labelled (protonated) “monomer” while the latter structure is defined as the unlabelled

Table 3.1: Molecular characteristics of the chains in the two studied systems

System	M_w (kg/mol) of labelled part	overall M_w (kg/mol)
dhd-linear chain	20	28.3
d-linear chain	-	27.6
hd- star polymer	1.05*	26.85*

* The values refer to one arm

(deuterated) “monomer”. The molecular weight of the protonated monomer, \widetilde{M}_{w_H} , and the respective quantity of the deuterated monomer, \widetilde{M}_{w_D} , are given by

$$\widetilde{M}_{w_H} = 4M_{w_C} + 2M_{w_D} + 6M_{w_H}, \quad (3.1a)$$

$$\widetilde{M}_{w_D} = 4M_{w_C} + 8M_{w_D}, \quad (3.1b)$$

where M_{w_C} , M_{w_H} and M_{w_D} are, respectively, the atomic weights of carbon, hydrogen and deuterium; these atomic weights have the following values: $M_{w_C} = 12.0107$ (g/mol), $M_{w_H} = 1.0079$ (g/mol) and $M_{w_D} = 2M_{w_H}$. In view of the molecular characteristics presented in table 3.1 and having obtained \widetilde{M}_{w_H} and \widetilde{M}_{w_D} , one finds that each arm of a star copolymer consists of $N_H \simeq 18$ protonated monomers and $N_D \simeq 402$ deuterated monomers; the total number of monomers per arm is $N_a = N_H + N_D$. Regarding the mixture of linear chains we find that the centred labelled chains contain $N_H \simeq 344$ protonated monomers; each deuterated end of these chains consists of $N_D \simeq 65$ monomers. On the other hand each matrix chain has $N_D^* \simeq 430$ deuterated monomers.

The calculation of the scattering from the aforementioned systems requires the calculation of the coherent and incoherent scattering lengths of the protonated and deuterated “monomers”. Since each protonated monomer consists of four carbon atoms, six hydrogen atoms, and two deuterium atoms its coherent scattering length, $\widetilde{b}_{coh,H}$, and its (squared) incoherent scattering length, $\widetilde{b}_{inc,H}^2$, are given by

$$\widetilde{b}_{coh,H} = 4b_C^{coh} + 6b_H^{coh} + 2b_D^{coh}, \quad (3.2a)$$

$$\widetilde{b}_{inc,H}^2 = 4(b_C^{inc})^2 + 6(b_H^{inc})^2 + 2(b_D^{inc})^2. \quad (3.2b)$$

Regarding the deuterated “monomers” each of them contains four carbons atoms and

eight deuterium atoms, hence the analogous expressions to eqs 3.2 are

$$\tilde{b}_{coh,D} = 4b_C^{coh} + 8b_D^{coh}, \quad (3.3a)$$

$$\tilde{b}_{inc,D}^2 = 4(b_C^{inc})^2 + 8(b_D^{inc})^2. \quad (3.3b)$$

The values of the coherent and incoherent scattering amplitudes for the carbon, hydrogen, and deuterium atoms appearing in eqs 3.2 and 3.3 (i.e. the values of b_X^{coh} and b_X^{inc} with $X = C, H, D$) are given in table 1.2 of section 1.3. By using these values and eqs 3.2 and 3.3 one obtains $\tilde{b}_{coh,H} \simeq 17.5\text{fm}$, $\tilde{b}_{inc,H}^2 \simeq 3865.3\text{fm}^2$, $\tilde{b}_{coh,D} \simeq 80\text{fm}$ and $\tilde{b}_{inc,D}^2 \simeq 130.6\text{fm}^2$.

The basic theoretical tool, that will be used throughout this chapter for the calculation of the scattering signal of the systems, is the Random Phase Approximation. This approximation deals with the statistical mechanics of concentration fluctuations in polymer systems. It has proven to be very useful in the interpretation of scattering experiments of polymer networks [138, 139, 140] and melts [117, 118, 141, 142]. Moreover, it has been used in modelling phase separation of block copolymer melts [143, 144, 145, 146, 147]. Usually, the approximation begins with structure factors calculated in the absence of interactions and uses these to calculate the scattering pattern of the interacting system. One can compute the structure factors in the absence of interactions by using some convenient and appropriate microscopic model for the polymer melt. In this work the Warner-Edwards (WE) model is used for the description of the melt. It should be pointed out that the RPA formalism, to be developed in this chapter, will hold even if the WE model is replaced by another microscopic model.

In an earlier work [117] Read applied a generalisation of the RPA, based on the WE picture of the tube, to a melt of stretched linear triblock copolymers and a melt of stretched H-copolymers. Since an H polymer relaxes hierarchically the physical picture implied by the “dynamic dilution hypothesis” suggests that, at a given experimental timescale, a clear distinction between relaxed and unrelaxed material can be made. In Ref. [117] the author related the rapid relaxation of the material at the arm tips (dangling ends) of the H polymers to “fast” (fluctuating or annealed) variables. On the other hand, the orientationally unrelaxed material still trapped in its original tube at the experimental time window was associated with “slow” (shared or quenched) variables. Read demonstrated that, when fast and slow relaxing tube variables are inter-active at the same lengthscale, detailed consideration of the slow variables is vital. In a refined version of his original

theory [118], Read incorporated the effect of elastic inhomogeneities, that is, he examined how motion of the dangling ends couples to inhomogeneities of the melt, which arise from the fact that different sections of the tube are orientated differently, and captured successfully many aspects of the scattering experimental data [148].

The arms of a star polymer relax in an identical fashion to the arms of an H-polymer. Therefore, a similar level of treatment as in Ref. [117] (with respect to annealed and quenched variables) is expected to hold in the case of the PE symmetric star which is of interest in this chapter. In contrast to [117] we disregard completely arm retraction because this type of relaxation process has not reached the short labelled section (close to the branch point) at the experimental timescale [3]. Hence, in our case, quenched variables are associated with the localising springs (“tubes”) and the slow Rouse modes which activate local reptative motion; in other words, we assume that at the experimental time window these relaxation mechanisms are to a high degree inactive. The annealed variables refer to the fast Rouse modes which are related to the (rapid) fluctuations of the chain about its mean path; this kind of motion does not involve motion along the tube.

The rest of the chapter is organized as follows. In section 3.2 we introduce the basic RPA formalism in the case of (i) an ideal melt of homopolymer chains (subsection 3.2.1) and in the case of (ii) a copolymer melt of two components (subsection 3.2.2). In subsection 3.2.3 we calculate the (static) single chain structure factors for the two studied systems which will be used in the subsequent sections; in subsection 3.2.4, for instance, these static structure factors are used to assess the importance of excluded volume chain-chain interactions (correlations) in our systems, at equilibrium. This subsection, moreover, deals with the estimation of the weight contribution of the coherent and incoherent signals to the total scattering intensity. In section 3.3 we develop a dynamic version of the RPA. This version of the RPA is used for the interpretation of the NSE data of Zamponi et al. [3] for the melt of polymer stars. In section 3.4 we compare our predictions for the coherent and incoherent scattering functions against MD simulations. Finally, in section 3.5 conclusions are given; in this section, also, some issues which demand further study are briefly discussed.

3.2 Random Phase Approximation (RPA)

3.2.1 A homopolymer melt of Gaussian (ideal) chains

Let us consider a melt of identical, in terms of degree of polymerisation, Gaussian chains. The position vector of monomer (segment) ℓ on chain ω is denoted by \mathbf{r}_ℓ^ω . Furthermore, the local polymer density is defined as

$$\rho_{\mathbf{r}} = \sum_{\omega, \ell} \delta(\mathbf{r} - \mathbf{r}_\ell^\omega), \quad (3.4)$$

which has the following Fourier transform

$$\rho_{\mathbf{q}} = \sum_{\omega, \ell} \exp(i\mathbf{q} \cdot \mathbf{r}_\ell^\omega). \quad (3.5)$$

In view of the fact that the density variables $\rho_{\mathbf{q}}$ involve a sum over many (nearly) independent random variables (c.f. eq 3.5) we anticipate that the $\rho_{\mathbf{q}}$ variables are, to first approximation, Gaussian.

A Gaussian distribution in $\rho_{\mathbf{q}}$ is completely specified by the first and second moment averages $\langle \rho_{\mathbf{q}} \rangle$ and $\langle \rho_{\mathbf{q}} \rho_{\mathbf{k}}^* \rangle$. For an equilibrated melt, translational symmetry applies, as the chains are free to move anywhere within the system, and so (for $\mathbf{q} \neq 0$) the two aforementioned moments are given by:

$$\langle \rho_{\mathbf{q}} \rangle = 0 \quad (3.6a)$$

$$\langle \rho_{\mathbf{q}} \rho_{\mathbf{k}}^* \rangle = \langle \rho_{\mathbf{q}} \rho_{-\mathbf{q}} \rangle \delta_{\mathbf{qk}}. \quad (3.6b)$$

Taking into consideration these constraints (eqs 3.6), the only possible Gaussian distribution of the density variables $\rho_{\mathbf{q}}$, in the non-interacting limit, is the following:

$$\Psi_0\{\rho_{\mathbf{q}}\} \sim \exp\left(-\frac{1}{2} \sum_{\mathbf{q}} \frac{\rho_{\mathbf{q}} \rho_{-\mathbf{q}}}{\langle \rho_{\mathbf{q}} \rho_{-\mathbf{q}} \rangle_0}\right), \quad (3.7)$$

where $\langle \dots \rangle_0$ denotes an average over all chains in the absence of monomer-monomer interactions. This distribution is related to the entropy of the system; it indicates that a particular concentration fluctuation $\rho_{\mathbf{q}}$ can be achieved by adjusting the configurations of the chains in a number of different ways.

In terms of the RPA, the quantity of interest is the $\langle \rho_{\mathbf{q}} \rho_{-\mathbf{q}} \rangle_0$ average which corresponds to the static scattering function of the melt, $S_0(q)$. By using eq 3.5 one arrives at:

$$S_0(q) = \langle \rho_{\mathbf{q}} \rho_{-\mathbf{q}} \rangle_0 = \left\langle \sum_{\omega, \ell} \sum_{\omega', \ell'} \exp \left(i\mathbf{q} \cdot \left(\mathbf{r}_{\ell}^{\omega} - \mathbf{r}_{\ell'}^{\omega'} \right) \right) \right\rangle_0. \quad (3.8)$$

In the absence of interactions, there is no correlation between the conformations of different chains and therefore contributions to $S_0(q)$ from different chains ($\omega \neq \omega'$) are zero. Equation 3.8 thus reduces to

$$S_0(q) = n_c \sum_{\ell, \ell'} \langle \exp(i\mathbf{q} \cdot (\mathbf{r}_{\ell} - \mathbf{r}_{\ell'})) \rangle_0 = n_c s_0(q), \quad (3.9)$$

where n_c is the total number of chains in the system, and $s_0(q)$ is the structure factor of a single chain.

The single chain structure factor, $s_0(q)$, can be calculated by assuming some model for the nature of the polymer chains. Consider the Gaussian chain model. Here, the separation vector $(\mathbf{r}_{\ell} - \mathbf{r}_{\ell'})$ is Gaussian with zero mean and second moment average $\langle (\mathbf{r}_{\ell} - \mathbf{r}_{\ell'})^2 \rangle_0 = b^2 |\ell - \ell'|$. So it can be shown [26] that:

$$\langle \exp(i\mathbf{q} \cdot (\mathbf{r}_{\ell} - \mathbf{r}_{\ell'})) \rangle_0 = \exp \left(-\frac{q^2}{6} \langle (\mathbf{r}_{\ell} - \mathbf{r}_{\ell'})^2 \rangle_0 \right) = \exp \left(-\frac{q^2 b^2 |\ell - \ell'|}{6} \right),$$

where $q = |\mathbf{q}|$. By using the previous expression and by converting the sums to integrals (in eq 3.9), for a linear chain of step length b and polymerization degree N , the structure factor $s_0(q)$ reduces to the Debye function $j_D(Q_N^2)$, with $Q_N^2 = q^2 b^2 N/6$ and

$$j_D(u) = \frac{2}{u^2} (\exp(-u) - 1 + u). \quad (3.10)$$

3.2.2 A copolymer melt with two components

Let us now assume that the system consists of two different monomer types, namely A and B (in a neutron scattering experiment the different monomer species correspond to different labelling). We introduce the local density fields $\rho^A(\mathbf{r})$ and $\rho^B(\mathbf{r})$ with their Fourier transforms:

$$\rho_{\mathbf{q}}^A = \sum_{\omega, \ell \in A} \exp(i\mathbf{q} \cdot \mathbf{r}_{\ell}^{\omega}), \quad \rho_{\mathbf{q}}^B = \sum_{\omega, \ell \in B} \exp(i\mathbf{q} \cdot \mathbf{r}_{\ell}^{\omega}), \quad (3.11)$$

where the sum in $\rho_{\mathbf{q}}^A$ and $\rho_{\mathbf{q}}^B$ is over A and B species, respectively. Note that the formalism to be presented below holds for both block-copolymer melts and polymer blends: in terms

of the RPA treatment, the difference between copolymer melts and polymer blends is realised in the single chain structure factors s_0^{AA} , s_0^{BB} , and s_0^{AB} (eq 3.15 below).

The density variables (fields) $\rho_{\mathbf{q}}^A$ and $\rho_{\mathbf{q}}^B$ involve a sum over a large number of nearly independent variables, as the density variables $\rho_{\mathbf{q}}$ above. So $\rho_{\mathbf{q}}^A$ and $\rho_{\mathbf{q}}^B$ are, to a good approximation, Gaussian also. It is possible, however, that they are correlated when individual chains contain both A and B species (as in copolymers). In the non-interacting limit (that is, with $\chi = 0$ and no excluded volume interactions, see discussion below) the density variables $\rho_{\mathbf{q}}^A$ and $\rho_{\mathbf{q}}^B$ are distributed according to:

$$\Psi_0 \{ \rho_{\mathbf{q}}^A, \rho_{\mathbf{q}}^B \} \sim \exp \left[-\frac{1}{2} \sum_{\mathbf{q}} \begin{pmatrix} \rho_{-\mathbf{q}}^A & \rho_{-\mathbf{q}}^B \end{pmatrix} M_{\mathbf{q}}^{-1} \begin{pmatrix} \rho_{\mathbf{q}}^A \\ \rho_{\mathbf{q}}^B \end{pmatrix} \right]. \quad (3.12)$$

This joint distribution represents the (nearly) Gaussian concentration fluctuations of the density fields $\rho_{\mathbf{q}}^A$ and $\rho_{\mathbf{q}}^B$. Similar to eq 3.7, it is related to the entropy of the system (a copolymer melt or polymer blend). $M_{\mathbf{q}}$ is the matrix of correlation functions calculated in the absence of interactions:

$$M_{\mathbf{q}} = \begin{pmatrix} S_0^{AA}(q) & S_0^{AB}(q) \\ S_0^{BA}(q) & S_0^{BB}(q) \end{pmatrix}. \quad (3.13)$$

Hence the matrix elements of $M_{\mathbf{q}}$ are given by

$$S_0^{AB}(q) = S_0^{AB} = \langle \rho_{\mathbf{q}}^A \rho_{-\mathbf{q}}^B \rangle_0 = n_c s_0^{AB}(q), \quad (3.14)$$

where

$$s_0^{AB}(q) = s_0^{AB} = \left\langle \sum_{\ell \in A} \sum_{\ell' \in B} \exp(i\mathbf{q} \cdot (\mathbf{r}_{\ell} - \mathbf{r}_{\ell'})) \right\rangle_0, \quad (3.15)$$

with n_c denoting the total number of chains and s_0^{AB} (similarly s_0^{AA} and s_0^{BB}) denoting the *single chain* structure factors of the non-interacting system.

The RPA formalism allows monomeric interactions to be taken into account by multiplying $\Psi_0 \{ \rho_{\mathbf{q}}^A, \rho_{\mathbf{q}}^B \}$ with the Boltzmann factor $\exp(-U \{ \rho_{\mathbf{q}}^A, \rho_{\mathbf{q}}^B \})$, where

$$U \{ \rho_{\mathbf{q}}^A, \rho_{\mathbf{q}}^B \} = \frac{1}{2\Omega} \sum_{\mathbf{q}} \left\{ V_{ef} |\rho_{\mathbf{q}}^A + \rho_{\mathbf{q}}^B|^2 - \frac{\chi}{2\rho} |\rho_{\mathbf{q}}^A - \rho_{\mathbf{q}}^B|^2 \right\}, \quad (3.16)$$

and then taking the limit $V_{ef} \rightarrow \infty$ at the end of the calculation. The first term of eq 3.16 accounts for incompressibility while the second term models the monomeric interactions. In the same equation, Ω is the volume of the system, ρ is the total

monomer concentration, and χ is the Flory interaction parameter; χ is related to the intra and inter monomer-monomer interactions (that is, interactions between AA, BB and AB monomers). Throughout this work we ignore the Flory parameter, assuming the experiment to be designed so that it is negligibly small. Therefore, we only consider chain-chain excluded volume (EV) interactions leading to incompressibility.

Specifically, by enforcing incompressibility to the polymer blend, we assume that fluctuations in the composition (i.e. the difference between $\rho^A(\mathbf{r})$ and $\rho^B(\mathbf{r})$) are much larger and more important than fluctuations in the overall polymer density (the sum of $\rho^A(\mathbf{r})$ and $\rho^B(\mathbf{r})$) [117, 118]. Consequently, the total monomer density at all points in space is constant and equal to $\rho^A(\mathbf{r}) + \rho^B(\mathbf{r}) = \rho$. This is equivalent to setting $\rho_{\mathbf{q}}^A = -\rho_{\mathbf{q}}^B = \tilde{\rho}_{\mathbf{q}}$. In other words, conformations of the system that do not satisfy incompressibility are eliminated and the number of possible states (configurations) that the system explores is reduced. Hence EV interactions between different polymer chains are imposed on the system (c.f. Fig. 3.2 for a schematic representation).

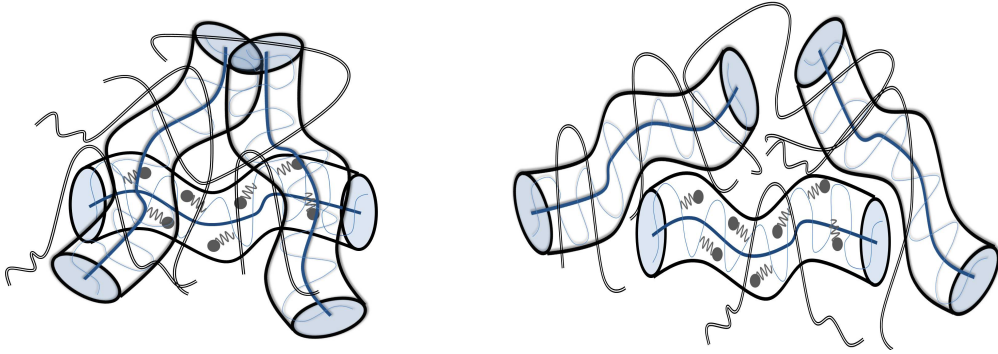


Figure 3.2: Left: A melt prior to incompressibility. Monomer density is not constant at all points in space. Thus different chains highly overlap. Right: A melt after enforcing incompressibility. Monomer density must be constant everywhere in the melt and thus configurations that do not satisfy this criterion are eliminated. In this case, chain overlap is not as high as before the introduction of incompressibility.

If incompressibility is introduced, then eq 3.12 becomes

$$\Psi_{\text{inc}} \{ \tilde{\rho}_{\mathbf{q}} \} \sim \exp \left[-\frac{1}{2} \sum_{\mathbf{q}} \left(\frac{S_0^{AA} + S_0^{BB} + 2S_0^{AB}}{S_0^{AA}S_0^{BB} - (S_0^{AB})^2} \right) \tilde{\rho}_{\mathbf{q}}\tilde{\rho}_{-\mathbf{q}} \right]. \quad (3.17)$$

By comparing the above distribution with eq 3.7 and by using eqs 3.15 one obtains the

static scattering function of a two component incompressible blend:

$$S^{tot}(q) = \frac{S_0^{AA}S_0^{BB} - (S_0^{AB})^2}{S_0^{AA} + S_0^{BB} + 2S_0^{AB}} = n_c \left(\frac{s_0^{AA}s_0^{BB} - (s_0^{AB})^2}{s_0^{AA} + s_0^{BB} + 2s_0^{AB}} \right), \quad (3.18)$$

with the correlation functions S_0^{AA} , S_0^{BB} , S_0^{AB} and the structure factor s_0^{AA} , s_0^{BB} , s_0^{AB} given by eqs 3.14 and 3.15, respectively. Equation 3.18 is applicable for any two component polymer melt independent of the topology of the chains (linear, star, etc.) under the condition that there are no quenched variables, i.e. they are in their equilibrium configuration [117]. As demonstrated in Ref. [117] when quenched and annealed variables are both active at the same lengthscale the naive application of the RPA, as expressed by eq 3.18, gives erroneous results.

3.2.3 Structure Factors for Copolymers of Arbitrary Architecture

In this section, the correlation functions S_0^{AA} , S_0^{BB} and S_0^{AB} (eq 3.14) for the systems I and II presented in section 3.1 are calculated. (The final results are presented in table 3.2.) In what follows, the species of type A and B correspond to the protonated (H) and deuterated (D) monomers of the scattering experiment, respectively.

The calculation is based on Read's method introduced in Ref. [149]. This method provides a useful and rapid way for the evaluation of structure factors of complex architecture polymers. Central to the method is the assumption that the polymer chain can be divided into several blocks. It is convenient to split the chain into different blocks at branch points and include in the same block monomers of the same type. Nevertheless, there should not be correlation between the internal configurations of any two blocks [149].

To illustrate the method let us consider a polymer melt that consists of polymer chains like the one depicted in the left panel of Fig. 3.3. In the following, the calculation of the correlation function S_0^{HH} is described. (The extension to S_0^{HD} and S_0^{DD} is then obvious.) According to eq 3.14, to obtain S_0^{HH} one needs to calculate the single chain structure factor s_0^{HH} . If the chain is divided into blocks then s_0^{HH} reads:

$$s_0^{HH} = \sum_{\substack{\text{blocks} \\ \gamma, \gamma'}} s_{\gamma\gamma'}^{HH} \quad (3.19)$$

where $s_{\gamma\gamma'}^{HH}$ is the contribution to s_0^{HH} of a pair of blocks (γ, γ') .

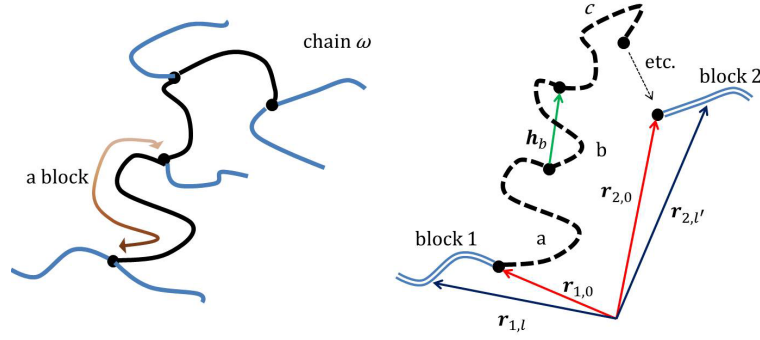


Figure 3.3: Left: Definition of a block. Here, the blue colour corresponds to protonated species H while the black colour to deuterated species D . Right: Showing the variables that relate to two given blocks (labelled 1 and 2) in a chain. The blocks 1 and 2 are separated by the blocks a, b, c, etc. \mathbf{h}_b is the end-to-end vector of block b (green arrow).

The right panel of Fig. 3.3 shows two blocks, labelled 1 and 2, which are separated by a number of other blocks (labelled $\gamma = a, b, c, \dots$, etc.). We now consider the contribution, s_{12}^{HH} , from these two blocks to s_0^{HH} . This is given by

$$s_{12}^{HH} = \sum_{\ell \in \text{block 1}} \sum_{\ell' \in \text{block 2}} \langle \exp [i\mathbf{q} \cdot (\mathbf{r}_{2,\ell'} - \mathbf{r}_{1,\ell})] \rangle_0, \quad (3.20)$$

where $\mathbf{r}_{2,\ell'}$ is the position vector of the ℓ' th segment in block 2, and $\mathbf{r}_{1,\ell}$ is the position vector of the ℓ th segment in block 1 (see Fig. 3.3, right). \mathbf{q} is the scattering vector. The vector $(\mathbf{r}_{2,\ell'} - \mathbf{r}_{1,\ell})$ can be expressed as follows:

$$\mathbf{r}_{2,\ell'} - \mathbf{r}_{1,\ell} = (\mathbf{r}_{2,\ell'} - \mathbf{r}_{2,0}) + \sum_{\gamma} \mathbf{h}_{\gamma} + (\mathbf{r}_{1,0} - \mathbf{r}_{1,\ell}), \quad (3.21)$$

where \mathbf{h}_{γ} is the end-to-end vector of the block γ , and $\mathbf{r}_{1,0}$ and $\mathbf{r}_{2,0}$ are the position vectors of the end monomers of blocks 1 and 2, respectively. By substituting eq 3.21 back into eq 3.20 one arrives at:

$$s_{12}^{HH} = \sum_{\ell \in \text{block 1}} \langle \exp [i\mathbf{q} \cdot (\mathbf{r}_{1,0} - \mathbf{r}_{1,\ell})] \rangle_0 \left\langle \prod_{\gamma} \exp (i\mathbf{q} \cdot \mathbf{h}_{\gamma}) \right\rangle_0 \times \sum_{\ell' \in \text{block 2}} \langle \exp [i\mathbf{q} \cdot (\mathbf{r}_{2,\ell'} - \mathbf{r}_{2,0})] \rangle_0. \quad (3.22)$$

Note that the $\langle \dots \rangle_0$ average (in eq 3.20) has been split into three individual averages, since it is assumed that there is no correlation between the internal configurations of any

two blocks. Hence, eq 3.22 factorises and can be written in a straightforward manner:

$$s_{12}^{HH} = H_1 \prod_{\substack{\gamma=a,b, \\ c,\dots}} G_\gamma H_2, \quad \text{where} \quad (3.23)$$

$$G_\gamma = \langle \exp(i\mathbf{q} \cdot \mathbf{h}_\gamma) \rangle_0, \quad \text{and} \quad H_\gamma = \sum_{\ell \in \text{block } \gamma} \langle \exp(i\mathbf{q} \cdot (\mathbf{r}_{\gamma,\ell} - \mathbf{r}_{\gamma,0})) \rangle_0. \quad (3.24)$$

The quantity G_γ is referred to as the ‘‘propagator’’. It describes the effects on the structure factor from the section of the chain that is placed between the two blocks. The terms H_1 and H_2 denote the contribution from blocks 1 and 2, respectively. (H_γ is referred to as the ‘‘coterm’’ of block γ .) All contributions that involve separate blocks are calculated in a manner similar to eq 3.23. The same-block terms ($\gamma = \gamma'$) in eq 3.19 are all of form

$$s_{\gamma\gamma}^{HH} = J_\gamma = \sum_{\substack{\ell, \ell' \\ \in \text{block } \gamma}} \langle \exp[i\mathbf{q} \cdot (\mathbf{r}_{\gamma,\ell'} - \mathbf{r}_{\gamma,\ell})] \rangle_0. \quad (3.25)$$

In what follows, J_γ is referred to as the ‘‘self-term’’ for block γ .

It is obvious from the above description that, in the non-interacting limit, the single chain structure factors (s_0^{HH} , etc.) and, in turn, the correlation functions S_0^{HH} , S_0^{DD} and S_0^{HD} of complex structures can be conveniently written in terms of propagators, coterms, and self-terms. If a block is assumed to be a Gaussian chain of segmental length b and polymerisation degree N_γ , then eqs 3.24 and 3.25 reduce to the following expressions [149]:

$$G_\gamma = \exp(-Q_\gamma^2), \quad (3.26a)$$

$$H_\gamma = N_\gamma \frac{1}{Q_\gamma^2} [1 - \exp(-Q_\gamma^2)], \quad (3.26b)$$

$$J_\gamma = N_\gamma^2 j_D(Q_\gamma^2), \quad (3.26c)$$

where $Q_\gamma^2 = q^2 b^2 N_\gamma / 6$ is the normalised wavevector, and $j_D(Q_\gamma^2)$ is the Debye structure factor given by eq 3.10. In what follows, the subscript γ in the propagators, coterms, and self-terms will be either H or D denoting protonated or deuterated blocks, respectively.

In view of eqs 3.26 we can move on to apply Read’s technique to our systems. The left panel of Fig. 3.4 shows how the star copolymer is separated into blocks (here, the labels 1 to 6 count the different blocks). In particular, each arm is divided into two blocks. One containing the protonated species ($Z_H = N_H / N_e$ entanglements act on this block), and

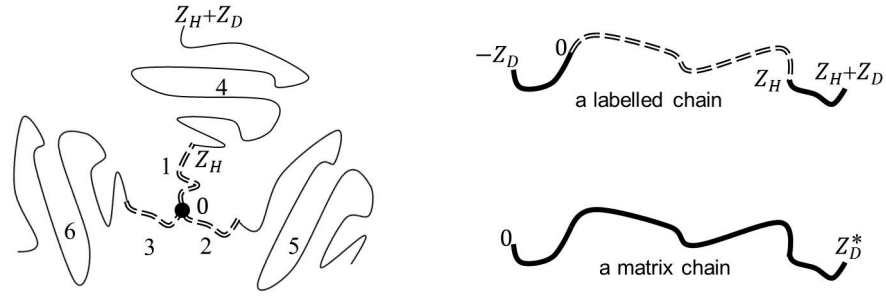


Figure 3.4: Splitting the chains into blocks. Dashed (solid) lines refer to the H (D) species. The labels (0, Z_H , Z_D , etc.) show how the chain length is expressed in terms of tube coordinates. Left: The star copolymer. Here, the labels 1 to 6 count blocks. Right: The mixture of linear chains.

another one containing the deuterated species ($Z_D = N_D/N_e$ entanglements act on this block). According to eq 3.19 (and the labelling in Fig. 3.4) the structure factor s_0^{HH} is calculated as follows:

$$s_0^{HH} = \sum_{\gamma=1,2,3} \sum_{\gamma'=1,2,3} s_{\gamma\gamma'}^{HH}. \quad (3.27)$$

Therefore, there are three self-terms $s_{\gamma\gamma}^{HH} (= J_H)$, one from each protonated section, and six identical $s_{\gamma\neq\gamma'}^{HH}$ terms from the pairs 1-2, 1-3, 2-1, 2-3, 3-1, and 3-2. These terms are calculated according to eq 3.23: that is, each term contributes a factor H_H^2 to s_0^{HH} ; the contribution of such pairs should not contain a propagator since there are no blocks between the protonated sections (blocks). Therefore, the final expression for s_0^{HH} is: $s_0^{HH} = 3J_H + 6H_H^2$. For the structure factor s_0^{DD} , there are again three self-terms $s_{\gamma\gamma}^{DD} (= J_D)$, and six identical terms from the pairs 4-5, 4-6, 5-4, 5-6, 6-4, and 6-5. However, in this case there are two protonated blocks between the deuterated blocks and hence each (deuterated) pair contributes to s_0^{DD} a factor $G_H^2 H_D^2$. Hence, s_0^{DD} is equal to $3J_D + 6G_H^2 H_D^2$. Notice that, in s_0^{HD} , there are no self-terms, since the double sum over blocks includes one sum over all H blocks and one sum over all D blocks:

$$s_0^{HD} = \sum_{\gamma=1,2,3} \sum_{\gamma'=4,5,6} s_{\gamma\gamma'}^{HD}. \quad (3.28)$$

Following eq 3.23, one finds that the pairs 1-4, 2-5 and 3-6 contribute to this structure factor a factor $H_H H_D$, while the remaining six pairs contribute to s_0^{HD} a factor $H_H G_H H_D$. Therefore, $s_0^{HD} = 3H_H H_D (1 + 2G_H)$. Finally, to obtain the correlation functions S_0^{HH} ,

S_0^{DD} and S_0^{HD} , one simply needs to multiply the above expressions for the structure factors by the total number of chains, n_c . The final expressions for S_0^{HH} , S_0^{DD} , and S_0^{HD} are given in table 3.2. Note that the expressions in this table refer to copolymer stars of f arms. Although the case $f = 3$ was described above only, the extension of the method to stars with arbitrary number of arms is straightforward.

Concerning the mixture (blend) of linear chains, the labelled chains (with volume fraction $\phi_{c_{\text{lab}}}$) are divided into three blocks with the protonated part being the central block. This block consists of N_H monomers while the two deuterated blocks consist of N_D monomers each. On the other hand, each deuterated chain is treated as a single block with N_D^* segments; the volume fraction of the matrix chains is $\phi_{c_{\text{mat}}}$. (The right panel of Fig. 3.4 illustrates schematically the separation in blocks for this particular system.) Since we are dealing with a polymer blend rather than a copolymer melt, some extra attention is required in the calculation of the correlation functions. In particular, only polymer chains that contain labelled species contribute to S_0^{HH} and S_0^{HD} . As a result, one finds $S_0^{HH} = n_{c_H} J_H$ and $S_0^{HD} = n_{c_H} 2H_H H_D$, where $n_{c_H} (= n_c \phi_{c_{\text{lab}}})$ is the number of labelled chains in the system. (n_c is the total number of chains, i.e. labelled and non-labelled.) Regarding S_0^{DD} , there are two separate contributions. One from the labelled chains and another one from the matrix chains; there are n_{c_H} labelled chains and $n_{c_D} (= n_c \phi_{c_{\text{mat}}})$ matrix chains, hence S_0^{DD} reads:

$$\begin{aligned} S_0^{DD} &= n_{c_H} \left\langle \sum_{\substack{\ell, \ell' \in D \\ \text{labelled} \\ \text{chains}}} \exp(i\mathbf{q} \cdot (\mathbf{r}_\ell - \mathbf{r}_{\ell'})) \right\rangle_0 + n_{c_D} \left\langle \sum_{\substack{\ell, \ell' \in D \\ \text{matrix} \\ \text{chains}}} \exp(i\mathbf{q} \cdot (\mathbf{r}_\ell - \mathbf{r}_{\ell'})) \right\rangle_0 \\ &= n_{c_H} s_{0_{\text{lab}}}^{DD} + n_{c_D} s_{0_{\text{mat}}}^{DD}, \end{aligned}$$

where $s_{0_{\text{lab}}}^{DD}$ and $s_{0_{\text{mat}}}^{DD}$ are the s_0^{DD} structure factors of the labelled and matrix chains, respectively. Following Read's [149] method we arrive at $s_{0_{\text{lab}}}^{DD} = 2(J_D + H_D^2 G_H)$ and $s_{0_{\text{mat}}}^{DD} = J_D^*$. Table 3.2 summarises the expressions for S_0^{HH} , S_0^{DD} , and S_0^{HD} for both the copolymer melt of symmetric stars and the blend of linear chains.

3.2.4 Scattering behaviour at equilibrium: static RPA

In the previous subsection we calculated the correlation functions S_0^{HH} , S_0^{DD} and S_0^{HD} . One can substitute the expressions of table 3.2 back to eq 3.18, and calculate the static

Table 3.2: S_0^{HH} , S_0^{DD} and S_0^{HD} single chain correlation functions

Star Polymer	Linear chain
$S_0^{HH} = n_c [f J_H + f(f-1)H_H^2]$	$S_0^{HH} = n_c \phi_{\text{clab}} J_H$
$S_0^{DD} = n_c [f J_D + f(f-1)G_H^2 H_D^2]$	$S_0^{DD} = n_c [\phi_{\text{clab}} 2(J_D + H_D^2 G_H) + \phi_{\text{cmat}} J_D^*]$
$S_0^{HD} = n_c f H_H H_D (1 + (f-1)G_H)$	$S_0^{HD} = n_c \phi_{\text{clab}} 2 H_H H_D$

scattering function of the two systems. Moreover, using these expressions one can assess the effects of incompressibility on the system. For this reason it is convenient to rewrite eq 3.18 as

$$\begin{aligned}
 S^{tot}(q) &= S_0^{HH} - \frac{(S_0^{HH} + S_0^{HD})^2}{S_0^{HH} + S_0^{DD} + 2S_0^{HD}} \\
 &= S_0^{HH} - S_{cor}.
 \end{aligned} \tag{3.29}$$

The first term on the RHS of eq 3.29 can be thought of as the coherent scattering from the protonated (labelled) sections in the absence of EV interactions. The second term, i.e. S_{cor} , can be interpreted as a correction to the scattering due to the EV interactions, which are brought about by incompressibility.

Figure 3.5 depicts $S^{tot}(q)/n_c$, as a function of $|\mathbf{q}|$, for the melt of copolymer stars. The black, red, and blue lines refer to stars with $f = 3$, $f = 4$, and $f = 6$ arms, respectively. The same quantity for the blend of linear chains is plotted for comparison with a green line. The open symbols in this figure, and in Figs. 3.6 and 3.7 below, do not refer to experimental data. They refer to the values of the plotted quantities at the $|\mathbf{q}|$ values of the NSE experiment, which measures the (dynamic) normalised scattering signal, $P(q, t)$: open squares and open circles correspond to the $f = 3$ star copolymer melt and the blend of linear chains, respectively. The experimental values of $|\mathbf{q}|$ are the following: $|\mathbf{q}| = 0.05 \text{ \AA}^{-1}$, $|\mathbf{q}| = 0.077 \text{ \AA}^{-1}$, $|\mathbf{q}| = 0.096 \text{ \AA}^{-1}$ and $|\mathbf{q}| = 0.115 \text{ \AA}^{-1}$. All curves of Fig. 3.5, and of Figs. 3.6 and 3.7 below, have been obtained by using the value $b = 8.24 \text{ \AA}$ for the monomeric distance (for both protonated and deuterated species). Moreover, the number of the protonated and deuterated monomers has been calculated by using the molecular characteristics presented in table 3.1, and eqs 3.1. Figure 3.5 reveals several features.

First, for the blend of linear chains there is scattering in the $|\mathbf{q}| \rightarrow 0$ limit. Since

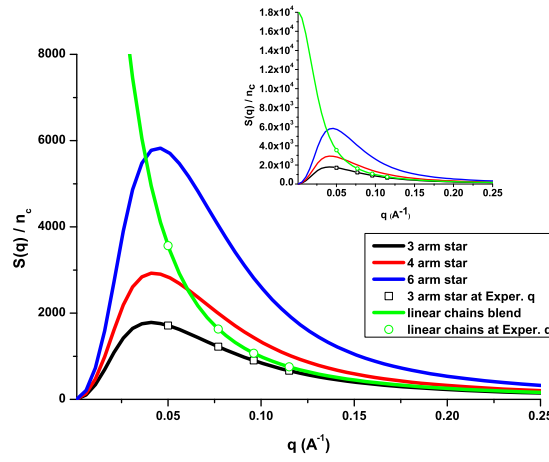


Figure 3.5: $n_c^{-1}S^{tot}(q)$ as a function of $|\mathbf{q}|$ for the melt of copolymer stars. The black, red, and blue lines refer to stars with $f = 3$, $f = 4$, and $f = 6$, respectively. The same quantity for the blend of linear chains is plotted for comparison with a green line. The inset shows the finite value of scattering at zero $|\mathbf{q}|$ for the mixture of linear chains. Open symbols in this figure (also in Figs. 3.6 and 3.7) correspond to the values of the plotted quantities at the available experimental $|\mathbf{q}|$ values.

the blend consists of a small volume fraction of labelled chains, which are embedded in a “sea” of matrix chains, variations in the composition are possible even at large lengthscales. The inset of Fig. 3.5 shows the finite value of scattering at the zero $|\mathbf{q}|$ limit; it is given by: $\lim_{|\mathbf{q}| \rightarrow 0} S_{lin}^{tot}/n_c = \frac{\phi_{c_{mat}}(N_D^*)^2 \phi_{c_{lab}} N_H^2}{\phi_{c_{mat}}(N_D^*)^2 + \phi_{c_{lab}}(N_H + 2N_D)^2}$. Second, for the star copolymer melts, we notice the existence of a peak at a non-zero value of $|\mathbf{q}|$. This peak is referred to as the “correlation hole” peak. It slightly shifts to higher $|\mathbf{q}|$ values as the number of arms increases.

To understand the physical meaning of this peak, in the left panel of Fig. 3.6, I have re-plotted $S^{tot}(q)/n_c$ in terms of the normalised wavevector, $Q_a = |\mathbf{q}|R_{g_a}$. ($R_{g_a} = \sqrt{b^2 N_a/6}$ is the radius of gyration of an arm in the non-interacting limit.) As in Fig. 3.5, the solid black, red, and blue lines correspond to $f = 3$, $f = 4$ and $f = 6$, respectively. In the same panel, the dashed lines show the aforementioned quantity when EV interactions are disregarded: that is, the second term in the RHS of eq 3.29 is neglected. A comparison between solid and dashed lines of the same colour reveals that, in the absence of EV interactions, the correlation hole peak disappears, and there is scattering in the zero $|\mathbf{q}|$ limit. So the physical interpretation of the correlation hole peak is as follows. In the

presence of EV interactions, which are brought about by incompressibility, there are no fluctuations in the concentration profile on large lengthscales. In other words, EV interactions prevent large scale motion of the chains and so variations in the polymer density occur at a finite length. The existence of a maximum around $Q_a = 3$, for all solid lines, indicates that this length is of order $2\pi R_{g_\alpha}/3$. Using $b = 8.24\text{\AA}$ and $N_a \simeq 420$ one finds that $2\pi R_{g_\alpha}/3 \approx 144\text{\AA}$; I note for comparison that, for the $f = 3$ star copolymer melt, this value is approximately five times bigger than the tube diameter (as estimated by matching the theoretical and experimental normalised scattering function, $P(q, t)$, c.f. section 3.3.3 below).

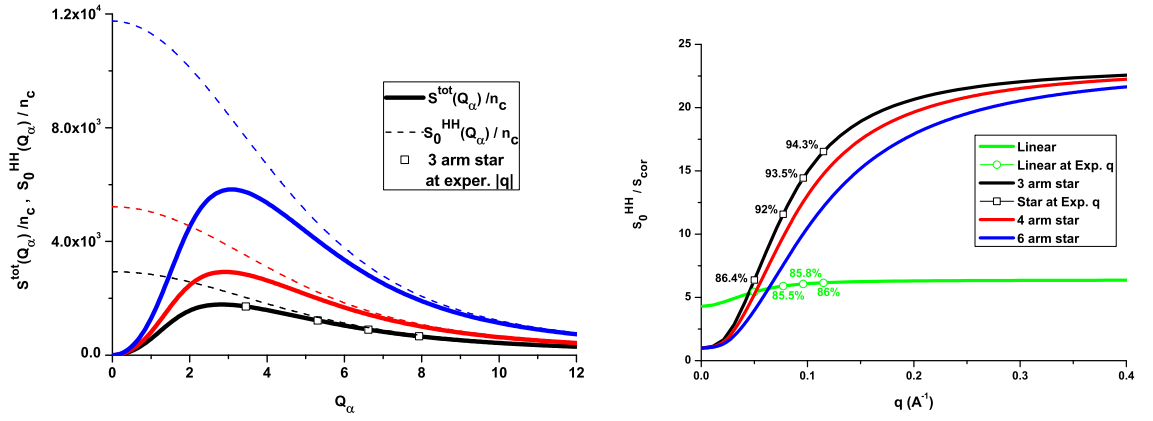


Figure 3.6: Left: The static scattering function in terms of the normalised wavevector $Q_a = |\mathbf{q}|R_{g_a}$ for the star copolymer melts. Solid lines: EV interactions are included. Dashed lines: EV interactions are ignored. Different colours correspond to different number of arms in exactly the same way as in Fig. 3.5. Right: $S_0^{\text{HH}}/S_{\text{cor}}$ as a function $|\mathbf{q}|$ for the star copolymers and the mixture of linear chains (green line).

Furthermore, by comparing the open black symbols with the black dashed line (in the left panel of Fig. 3.6), one realises that, at the experimental $|\mathbf{q}|$ values, EV interactions give a small perturbation to the scattering data for the three arm star copolymer melt. This is also apparent from the right panel of Fig. 3.6 where the $S_0^{\text{HH}}/S_{\text{cor}}$ ratio is plotted as a function $|\mathbf{q}|$. The same quantity for the mixture of linear chains is also shown with green colour revealing a similar trend. At the lowest value of $|\mathbf{q}|$, i.e. at $|\mathbf{q}| = 0.05\text{\AA}^{-1}$, the corresponding value of $S_0^{\text{HH}}/S_{\text{cor}}$ can be interpreted as 86.4% and 85% contribution of S_0^{HH} to $S^{\text{tot}}(q)$ for the star copolymer and the mixture of linear chains, respectively. As the magnitude of the scattering vector (i.e. $|\mathbf{q}|$) increases, EV interactions become

less important and so the ratio S_0^{HH}/S_{cor} reaches a plateau. However, the neglect of interactions at the lower $|\mathbf{q}|$ gives a potential error of order 10%.

We now move on to assess the contribution of coherent and incoherent scattering to the total scattering signal. Figure 3.7 shows the ratio I_{coh}/I_{inc} as a function of $|\mathbf{q}|$ for both examined systems. To obtain I_{coh} and I_{inc} we use eqs 1.31b and 1.33b, respectively. This figure demonstrates that in all examined $|\mathbf{q}|$ values the overall signal is dominated by the coherent term. The incoherent signal becomes comparable to the coherent one only at the high $|\mathbf{q}|$ limit. The neglect of the incoherent signal, however, could give a potential error of order 10% which is of similar magnitude to the neglect of excluded volume chain-chain interactions. For this reason, in the next section, we develop a dynamic version of the RPA that takes into account EV interactions, and moreover, we include the incoherent signal in our comparison with the NSE data.

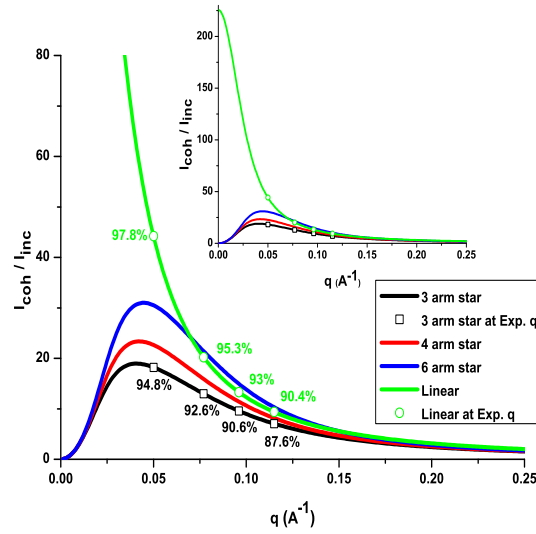


Figure 3.7: The ratio I_{coh}/I_{inc} as a function of $|\mathbf{q}|$ for both examined systems. The correspondence between colour and number of arms is the same as in Figs. 3.5 and 3.6 (see also the label). The green colour refers to the blend of linear chains. The open symbols show the values of I_{coh}/I_{inc} at the experimental values of $|\mathbf{q}|$.

3.3 Dynamic RPA: theory

In this section we apply a dynamic version of the RPA to interpret the NSE data of Zamponi et al. [3], for the melt of symmetric three arm stars. Since the expressions for the dynamical structure factors (eqs 1.30a and 1.32) involve correlation between monomer positions at two different times, we introduce the following Fourier transformed density fields of the protonated and deuterated monomers:

$$\varphi_{\mathbf{q}}^H = \sum_{\omega, \ell \in H} \exp(i\mathbf{q} \cdot \mathbf{r}_{\ell}^{\omega}(0)), \quad \varphi_{\mathbf{q}}^D = \sum_{\omega, \ell \in D} \exp(i\mathbf{q} \cdot \mathbf{r}_{\ell}^{\omega}(0)), \quad (3.30a)$$

$$\rho_{\mathbf{q}}^H = \sum_{\omega, \ell \in H} \exp(i\mathbf{q} \cdot \mathbf{r}_{\ell}^{\omega}(t)), \quad \rho_{\mathbf{q}}^D = \sum_{\omega, \ell \in D} \exp(i\mathbf{q} \cdot \mathbf{r}_{\ell}^{\omega}(t)). \quad (3.30b)$$

The density fields $\varphi_{\mathbf{q}}^H$ and $\varphi_{\mathbf{q}}^D$ are associated with the configuration of the chain at time $t' = 0$ while the density fields $\rho_{\mathbf{q}}^H$ and $\rho_{\mathbf{q}}^D$ are associated with the configuration of the chain at a later time $t' = t$. As explained in section 3.1, during the time interval t , there are some quenched variables (slow Rouse modes, fixed localising springs) shared between the two stages and some annealed variables (fast Rouse modes). Figure 3.8 shows a schematic drawing of the system at time zero and after the time interval t . In what follows averages over annealed and quenched variables, in the absence of chain-chain EV interactions (correlations), are denoted, respectively, by $\langle \dots \rangle_0$ and $\overline{(\dots)}^0$; in the presence of interactions these averages are written as $\langle \dots \rangle$ and $\overline{(\dots)}$, respectively.

Note that, with respect to the annealed variables, averages are taken over two different distributions. In particular, one average is taken over the annealed variables at time $t' = 0$, and a second average is taken over the annealed variables at time $t' = t$. The former average is denoted by $\langle \dots \rangle_{\varphi, 0}$ while the latter average is symbolised by $\langle \dots \rangle_{\rho, 0}$; these two averages, in the presence of interactions imposed at the relevant time, are denoted by $\langle \dots \rangle_{\varphi}$ and $\langle \dots \rangle_{\rho}$, respectively. To simplify the notation, hereafter, the averages $\langle \rho_{\mathbf{q}}^H \rangle_{\varphi, 0}$, $\langle \rho_{\mathbf{q}}^H \rangle_{\varphi}$, and $\langle \rho_{\mathbf{q}}^D \rangle_{\varphi, 0}$, $\langle \rho_{\mathbf{q}}^D \rangle_{\varphi}$ will be omitted, when unnecessary, since the density fields $\rho_{\mathbf{q}}^H$ and $\rho_{\mathbf{q}}^D$ are only associated with the chain configurations at time $t' = t$.

The localising potential acting on a chain prevents it from exploring all its degrees of freedom. Since on the NSE experimental timescale the localising springs (“tubes”) are considered unrelaxed (quenched) each monomer is constrained to fluctuate in a small volume about a mean position. The effect of this constraint on the density fields, $\rho_{\mathbf{q}}^H$

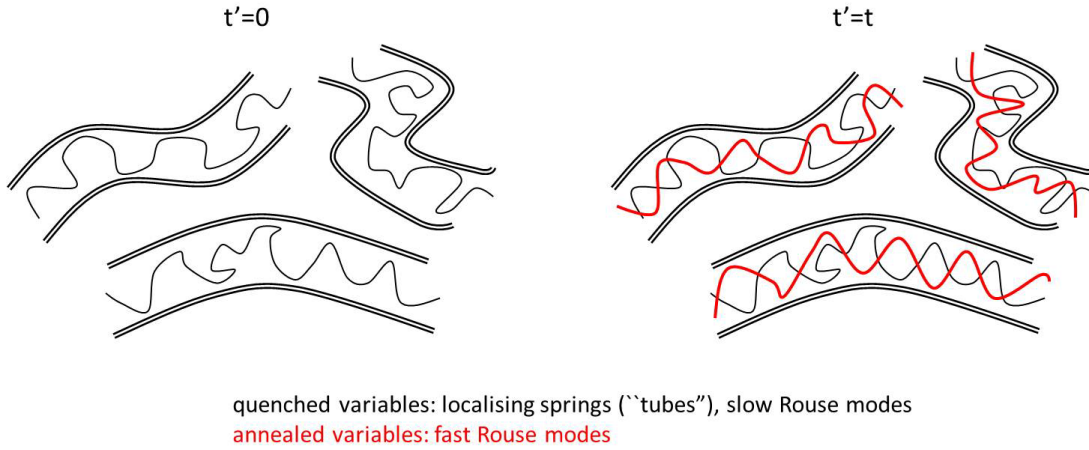


Figure 3.8: Schematic representation of the chain configurations at time $t' = 0$ (black colour) and at time $t' = t$ (red colour). Between these two stages the quenched variables are the localising springs (the “tubes”) and slow Rouse modes. The annealed variables are fast Rouse modes and so the chain configurations at time t have locally changed.

and ρ_q^D , is that they are enforced to fluctuate about a nonzero mean, which in the absence of excluded volume interactions would be $\langle \rho_q^H \rangle_0$ and $\langle \rho_q^D \rangle_0$, respectively. These average values are non zero because in the presence of the localising springs translational symmetry is destroyed, that is, eq 3.6a does not hold in this case. Translational symmetry is restored if one averages over all possible configurations of the slow (quenched) variables; then, $\overline{\langle \rho_q^H \rangle_0}^0$ and $\overline{\langle \rho_q^D \rangle_0}^0$ are equal to zero. It must be stressed that $\langle \rho_q^H \rangle_0$ and $\langle \rho_q^D \rangle_0$ correspond to configurations of the system in the absence of interactions. If interactions are taken into account by means of incompressibility, then, the conformations of the chains change, and consequently, the non zero means of the density fields also change. The change in the non zero means of $\varphi_q^{H,D}$ and $\rho_q^{H,D}$ can be estimated by applying the RPA.

However, before I perform this particular calculation I will explain my strategy for clarity: the overall goal is the calculation of the scattering signal, $P(q, t)$, i.e. the computation of eq 1.29, in the presence of chain-chain EV interactions. This calculation, in turn, requires the calculation of the dynamic scattering functions, $S^{tot}(q, t)$ and $S_{inc}(q, t)$, and their static counterparts. (See eqs 1.29 to 1.33.) With respect to the calculation of the incoherent scattering functions, $S_{inc}(q, t)$ and $S_{inc}(q)$, one does not need to explicitly include the EV interactions, since these scattering functions are concerned

only with the self motion of each monomer, not the potentially correlated motions of monomeric pairs. EV interactions affect these correlations and thus affect the coherent scattering functions, $S^{tot}(q, t)$ and $S^{tot}(q)$. In terms of the density fields $\varphi_{\mathbf{q}}^H$ and $\rho_{\mathbf{q}}^H$, $S^{tot}(q, t)$ reads

$$S^{tot}(q, t) = \overline{\langle \langle \varphi_{\mathbf{q}}^H \rho_{-\mathbf{q}}^H \rangle_{\rho} \rangle_{\varphi}} = \overline{\langle \varphi_{\mathbf{q}}^H \rangle_{\varphi} \langle \rho_{-\mathbf{q}}^H \rangle_{\rho}} = \overline{\langle \varphi_{-\mathbf{q}}^H \rangle_{\varphi} \langle \rho_{\mathbf{q}}^H \rangle_{\rho}}. \quad (3.31)$$

An expression for $S^{tot}(q, t)$ will be developed by applying the RPA twice; (i) one time to obtain an expression for $\langle \rho_{\mathbf{q}}^H \rangle_{\rho}$ in terms of $\langle \rho_{\mathbf{q}}^H \rangle_{\rho, 0}$ and $\langle \rho_{\mathbf{q}}^D \rangle_{\rho, 0}$ (after this step, $S^{tot}(q, t)$, will depend on $\overline{\langle \varphi_{-\mathbf{q}}^H \rangle_{\varphi} \langle \rho_{\mathbf{q}}^H \rangle_{\rho, 0}}$ and $\overline{\langle \varphi_{-\mathbf{q}}^H \rangle_{\varphi} \langle \rho_{\mathbf{q}}^D \rangle_{\rho, 0}}$), and (ii) a second time, to express $\overline{\langle \varphi_{-\mathbf{q}}^H \rangle_{\varphi} \langle \rho_{\mathbf{q}}^H \rangle_{\rho, 0}}$ and $\overline{\langle \varphi_{-\mathbf{q}}^H \rangle_{\varphi} \langle \rho_{\mathbf{q}}^D \rangle_{\rho, 0}}$ in terms of both the static and time dependent structure factors of a single chain.

3.3.1 Applying the RPA to obtain $\langle \rho_{\mathbf{q}}^H \rangle_{\rho}$

The first step of this calculation is to introduce, in the absence of chain-chain interactions at time t , the probability distribution $P_0 \{ \Delta \rho_{\mathbf{q}}^H, \Delta \rho_{\mathbf{q}}^D \}$:

$$P_0 \{ \Delta \rho_{\mathbf{q}}^H, \Delta \rho_{\mathbf{q}}^D \} \sim \exp \left[-\frac{1}{2} \sum_{\mathbf{q}} \begin{pmatrix} \Delta \rho_{-\mathbf{q}}^H & \Delta \rho_{-\mathbf{q}}^D \end{pmatrix} L_{\mathbf{q}}^{-1} \begin{pmatrix} \Delta \rho_{\mathbf{q}}^H \\ \Delta \rho_{\mathbf{q}}^D \end{pmatrix} \right], \quad (3.32)$$

where the quantities $\Delta \rho_{\mathbf{q}}^H$ and $\Delta \rho_{\mathbf{q}}^D$ are, respectively, given by

$$\Delta \rho_{\mathbf{q}}^H = \rho_{\mathbf{q}}^H - \langle \rho_{\mathbf{q}}^H \rangle_0 \quad \text{and} \quad \Delta \rho_{\mathbf{q}}^D = \rho_{\mathbf{q}}^D - \langle \rho_{\mathbf{q}}^D \rangle_0. \quad (3.33)$$

The meaning of eq 3.33 is that $P_0 \{ \Delta \rho_{\mathbf{q}}^H, \Delta \rho_{\mathbf{q}}^D \}$ describes the Gaussian fluctuations about the non zero means $\langle \rho_{\mathbf{q}}^H \rangle_0$ and $\langle \rho_{\mathbf{q}}^D \rangle_0$, undertaken by the density fields $\rho_{\mathbf{q}}^H$ and $\rho_{\mathbf{q}}^D$ in the absence of excluded volume interactions at time t . The means $\langle \rho_{\mathbf{q}}^H \rangle_0$ and $\langle \rho_{\mathbf{q}}^D \rangle_0$ may, naturally, be affected by the quenched variables, which themselves are affected by excluded volume interactions at earlier times (this will be the purpose of the subsequent calculation). Here, our aim is to introduce interactions into eq 3.33 and so to obtain the mean density fields in the presence of interactions at time t .

The matrix $L_{\mathbf{q}}$ reads

$$L_{\mathbf{q}} = \begin{pmatrix} T_{\mathbf{q}}^{HH} & T_{\mathbf{q}}^{HD} \\ T_{\mathbf{q}}^{HD} & T_{\mathbf{q}}^{DD} \end{pmatrix}, \quad (3.34)$$

with

$$T_{\mathbf{q}}^{AB} = \overline{\langle \Delta \rho_{-\mathbf{q}}^A \Delta \rho_{\mathbf{q}}^B \rangle_0^0} = \overline{\langle \rho_{-\mathbf{q}}^A \rho_{\mathbf{q}}^B \rangle_0^0} - \overline{\langle \rho_{-\mathbf{q}}^A \rangle_0^0} \overline{\langle \rho_{\mathbf{q}}^B \rangle_0^0}, \quad (3.35)$$

where the labels A and B can each be either H or D . The first term of eq 3.35 corresponds to the static correlation function $S_0^{AB}(q) = S_0^{AB}$ of a single chain; S_0^{HH} , S_0^{DD} , and S_0^{HD} are given in table 3.2 of section 3.2.3. The second term of eq 3.35 is time dependent and corresponds to $S_0^{AB}(q, t) = S_0^{AB}(t)$. This is because it depends on which variables, related to the Rouse modes, are considered quenched and which annealed over the time interval t . From another point of view, $\overline{\langle \rho_{-\mathbf{q}}^A \rangle_0^0} \overline{\langle \rho_{\mathbf{q}}^B \rangle_0^0}$ implies two separate averages over the annealed variables at time t ; if a chain is left twice to fluctuate locally (within the localising potential) from the initial stage at time zero, then, the two corresponding configurations after the separation time t will differ (and one possible configuration, among many, is the initial configuration). Equation 3.35 is, therefore, rewritten as

$$T_{\mathbf{q}}^{AB} = S_0^{AB}(q) - S_0^{AB}(q, t) = S_0^{AB} - S_0^{AB}(t) \quad (3.36)$$

The mean $\langle \rho_{\mathbf{q}}^H \rangle_{\rho}$, in the presence of interactions, can be estimated by enforcing incompressibility at time t . This practically means that one can substitute $\rho_{\mathbf{q}}^D$ and $\rho_{-\mathbf{q}}^D$ with $-\rho_{\mathbf{q}}^H$ and $-\rho_{-\mathbf{q}}^H$, respectively, in eq 3.33. After making these substitutions, $P_0 \{ \Delta \rho_{\mathbf{q}}^H, \Delta \rho_{\mathbf{q}}^D \}$ reduces to

$$P_{in} \{ \Delta \rho_{\mathbf{q}}^H, \Delta \rho_{\mathbf{q}}^D \} \sim \exp \left(- \sum_{\mathbf{q}} \left[\frac{T_{\mathbf{q}}^{HH} + T_{\mathbf{q}}^{DD} + 2T_{\mathbf{q}}^{HD}}{2 \det L_{\mathbf{q}}} \left(\left(\rho_{\mathbf{q}}^H - \langle \rho_{\mathbf{q}}^H \rangle_{\rho} \right)^2 + u(\mathbf{q}, t) \right) \right] \right) \quad (3.37)$$

where

$$u(\mathbf{q}, t) = \frac{\left(T_{\mathbf{q}}^{HH} T_{\mathbf{q}}^{DD} - (T_{\mathbf{q}}^{HD})^2 \right) \left(\langle \rho_{\mathbf{q}}^H \rangle_{\rho,0} + \langle \rho_{\mathbf{q}}^D \rangle_{\rho,0} \right)^2}{\left(T_{\mathbf{q}}^{HH} + T_{\mathbf{q}}^{DD} + 2T_{\mathbf{q}}^{HD} \right)^2}, \quad (3.38)$$

and

$$\langle \rho_{\mathbf{q}}^H \rangle_{\rho} = \frac{\langle \rho_{\mathbf{q}}^H \rangle_{\rho,0} (T_{\mathbf{q}}^{DD} + T_{\mathbf{q}}^{HD}) - \langle \rho_{\mathbf{q}}^D \rangle_{\rho,0} (T_{\mathbf{q}}^{HH} + T_{\mathbf{q}}^{HD})}{T_{\mathbf{q}}^{HH} + T_{\mathbf{q}}^{DD} + 2T_{\mathbf{q}}^{HD}}, \quad (3.39)$$

is the non zero mean after the introduction of EV interactions, at time $t' = t$. After substituting eq 3.39 into eq 3.31, the total coherent scattering function, $S^{tot}(q, t)$, is rewritten as

$$\overline{\langle \varphi_{-\mathbf{q}}^H \rangle_{\varphi}} \overline{\langle \rho_{\mathbf{q}}^H \rangle_{\rho}} = \frac{\overline{\langle \varphi_{-\mathbf{q}}^H \rangle_{\varphi}} \overline{\langle \rho_{\mathbf{q}}^H \rangle_{\rho,0}} (T_{\mathbf{q}}^{DD} + T_{\mathbf{q}}^{HD}) - \overline{\langle \varphi_{-\mathbf{q}}^H \rangle_{\varphi}} \overline{\langle \rho_{\mathbf{q}}^D \rangle_{\rho,0}} (T_{\mathbf{q}}^{HH} + T_{\mathbf{q}}^{HD})}{T_{\mathbf{q}}^{HH} + T_{\mathbf{q}}^{DD} + 2T_{\mathbf{q}}^{HD}}. \quad (3.40)$$

From this equation it is apparent that the development of an expression for $\overline{\langle \varphi_{-\mathbf{q}}^H \rangle_{\varphi} \langle \rho_{\mathbf{q}}^H \rangle_{\rho}}$ requires the calculation of $\overline{\langle \varphi_{-\mathbf{q}}^H \rangle_{\varphi} \langle \rho_{\mathbf{q}}^H \rangle_{\rho,0}}$ and $\overline{\langle \varphi_{-\mathbf{q}}^H \rangle_{\varphi} \langle \rho_{\mathbf{q}}^D \rangle_{\rho,0}}$. This is achieved by applying the RPA for a second time.

3.3.2 RPA to obtain $\overline{\langle \varphi_{-\mathbf{q}}^H \rangle_{\varphi} \langle \rho_{\mathbf{q}}^H \rangle_{\rho,0}}$ and $\overline{\langle \varphi_{-\mathbf{q}}^H \rangle_{\varphi} \langle \rho_{\mathbf{q}}^D \rangle_{\rho,0}}$

The starting point of this calculation is the introduction of the probability distribution $W_0 \{ \varphi_{\mathbf{q}}^H, \varphi_{\mathbf{q}}^D, \rho_{\mathbf{q}}^H, \rho_{\mathbf{q}}^D \}$ in the absence of any interactions between chains:

$$W_0 \{ \varphi_{\mathbf{q}}^H, \varphi_{\mathbf{q}}^D, \rho_{\mathbf{q}}^H, \rho_{\mathbf{q}}^D \} \sim \exp \left(-\frac{1}{2} \sum_{\mathbf{q}} \mathbf{w}_0^* K_{\mathbf{q}}^{-1} \mathbf{w}_0^T \right), \quad (3.41)$$

where $\mathbf{w}_0 = (\varphi_{\mathbf{q}}^H \quad \varphi_{\mathbf{q}}^D \quad \rho_{\mathbf{q}}^H \quad \rho_{\mathbf{q}}^D)$. The row vector \mathbf{w}_0^* and the column vector \mathbf{w}_0^T are the complex conjugate and transpose of \mathbf{w}_0 , respectively. The matrix $K_{\mathbf{q}}$ reads

$$K_{\mathbf{q}} = \begin{pmatrix} \overline{\langle \langle \varphi_{-\mathbf{q}}^H \varphi_{\mathbf{q}}^H \rangle_{\varphi,0} \rangle_{\rho,0}} & \overline{\langle \langle \varphi_{-\mathbf{q}}^H \varphi_{\mathbf{q}}^D \rangle_{\varphi,0} \rangle_{\rho,0}} & \overline{\langle \langle \varphi_{-\mathbf{q}}^H \rho_{\mathbf{q}}^H \rangle_{\varphi,0} \rangle_{\rho,0}} & \overline{\langle \langle \varphi_{-\mathbf{q}}^H \rho_{\mathbf{q}}^D \rangle_{\varphi,0} \rangle_{\rho,0}} \\ \overline{\langle \langle \varphi_{-\mathbf{q}}^D \varphi_{\mathbf{q}}^H \rangle_{\varphi,0} \rangle_{\rho,0}} & \overline{\langle \langle \varphi_{-\mathbf{q}}^D \varphi_{\mathbf{q}}^D \rangle_{\varphi,0} \rangle_{\rho,0}} & \overline{\langle \langle \varphi_{-\mathbf{q}}^D \rho_{\mathbf{q}}^H \rangle_{\varphi,0} \rangle_{\rho,0}} & \overline{\langle \langle \varphi_{-\mathbf{q}}^D \rho_{\mathbf{q}}^D \rangle_{\varphi,0} \rangle_{\rho,0}} \\ \overline{\langle \langle \rho_{-\mathbf{q}}^H \varphi_{\mathbf{q}}^H \rangle_{\varphi,0} \rangle_{\rho,0}} & \overline{\langle \langle \rho_{-\mathbf{q}}^H \varphi_{\mathbf{q}}^D \rangle_{\varphi,0} \rangle_{\rho,0}} & \overline{\langle \langle \rho_{-\mathbf{q}}^H \rho_{\mathbf{q}}^H \rangle_{\varphi,0} \rangle_{\rho,0}} & \overline{\langle \langle \rho_{-\mathbf{q}}^H \rho_{\mathbf{q}}^D \rangle_{\varphi,0} \rangle_{\rho,0}} \\ \overline{\langle \langle \rho_{-\mathbf{q}}^D \varphi_{\mathbf{q}}^H \rangle_{\varphi,0} \rangle_{\rho,0}} & \overline{\langle \langle \rho_{-\mathbf{q}}^D \varphi_{\mathbf{q}}^D \rangle_{\varphi,0} \rangle_{\rho,0}} & \overline{\langle \langle \rho_{-\mathbf{q}}^D \rho_{\mathbf{q}}^H \rangle_{\varphi,0} \rangle_{\rho,0}} & \overline{\langle \langle \rho_{-\mathbf{q}}^D \rho_{\mathbf{q}}^D \rangle_{\varphi,0} \rangle_{\rho,0}} \end{pmatrix} \quad (3.42)$$

with averages taken over the three different distributions; over the quenched variables and over the annealed variables at time zero and at time t .

The matrix elements of $K_{\mathbf{q}}$ are of three different forms: (i) matrix elements of the form $\overline{\langle \langle \varphi_{-\mathbf{q}}^A \varphi_{\mathbf{q}}^B \rangle_{\varphi,0} \rangle_{\rho,0}}$, which can be simply written as $\overline{\langle \varphi_{-\mathbf{q}}^A \varphi_{\mathbf{q}}^B \rangle_{\varphi,0}}$, since the density fields $\varphi_{\mathbf{q}}^{A,B}$ are independent of the chain configuration at time t and thus correspond to the static correlation functions S_0^{AB} , which are given by eqs 3.14, (ii) matrix elements of the form $\overline{\langle \langle \rho_{-\mathbf{q}}^A \rho_{\mathbf{q}}^B \rangle_{\varphi,0} \rangle_{\rho,0}}$, which can be expressed as $\overline{\langle \rho_{-\mathbf{q}}^A \rho_{\mathbf{q}}^B \rangle_{\rho,0}}$ since the density fields $\rho_{\mathbf{q}}^{A,B}$ are only associated with the chain configurations at time $t' = t$ (averages of this form equal S_0^{AB} as averages of the form $\overline{\langle \varphi_{-\mathbf{q}}^A \varphi_{\mathbf{q}}^B \rangle_{\varphi,0}}$ are time independent), and (iii) matrix elements of the form $\overline{\langle \langle \varphi_{-\mathbf{q}}^A \rho_{\mathbf{q}}^B \rangle_{\varphi,0} \rangle_{\rho,0}}$ that can be written as $\overline{\langle \varphi_{-\mathbf{q}}^A \rangle_{\varphi,0} \langle \rho_{\mathbf{q}}^B \rangle_{\rho,0}}$. From the latter form it is readily seen that these kind of averages correspond to the correlation

functions $S_0^{AB}(t)$. As a result of the above considerations, $K_{\mathbf{q}}$ (i.e. eq 3.42) is written as

$$K_{\mathbf{q}} = \begin{pmatrix} S_0^{HH} & S_0^{HD} & S_0^{HH}(t) & S_0^{HD}(t) \\ S_0^{HD} & S_0^{DD} & S_0^{HD}(t) & S_0^{DD}(t) \\ S_0^{HH}(t) & S_0^{HD}(t) & S_0^{HH} & S_0^{HD} \\ S_0^{HD}(t) & S_0^{DD}(t) & S_0^{HD} & S_0^{DD} \end{pmatrix} \quad (3.43)$$

When incompressibility at time $t' = 0$ is introduced (i.e. $\varphi_{\mathbf{q}}^D = -\varphi_{\mathbf{q}}^H$) EV interactions are imposed. These interactions are preserved in the system at later timescales. This means that certain aspects of the composition profile at $t' = 0$ are “frozen in” at $t' > 0$. The reduced distribution $W_{inc}\{\varphi_{\mathbf{q}}^H, \rho_{\mathbf{q}}^H, \rho_{\mathbf{q}}^D\}$ is

$$W_{inc}\{\varphi_{\mathbf{q}}^H, \rho_{\mathbf{q}}^H, \rho_{\mathbf{q}}^D\} \sim \exp\left(-\frac{1}{2} \sum_{\mathbf{q}} \mathbf{w}_{inc}^* B_{\mathbf{q}}^{-1} \mathbf{w}_{inc}\right), \quad (3.44)$$

where \mathbf{w}_{inc} is the row vector $\mathbf{w}_{inc} = (\varphi_{\mathbf{q}}^H \quad \rho_{\mathbf{q}}^H \quad \rho_{\mathbf{q}}^D)$. The matrix $B_{\mathbf{q}}^{-1}$ is given by

$$B_{\mathbf{q}}^{-1} = \begin{pmatrix} K_{\mathbf{q}11}^{-1} + K_{\mathbf{q}22}^{-1} - 2K_{\mathbf{q}12}^{-1} & K_{\mathbf{q}13}^{-1} - K_{\mathbf{q}23}^{-1} & K_{\mathbf{q}14}^{-1} - K_{\mathbf{q}24}^{-1} \\ K_{\mathbf{q}31}^{-1} - K_{\mathbf{q}32}^{-1} & K_{\mathbf{q}33}^{-1} & K_{\mathbf{q}34}^{-1} \\ K_{\mathbf{q}41}^{-1} - K_{\mathbf{q}42}^{-1} & K_{\mathbf{q}43}^{-1} & K_{\mathbf{q}44}^{-1} \end{pmatrix} \quad (3.45)$$

Its inverse, i.e. the matrix $B_{\mathbf{q}}$, contains the matrix elements of interest, namely $\overline{\langle \varphi_{-\mathbf{q}}^H \rangle_{\varphi} \langle \rho_{\mathbf{q}}^H \rangle_{\rho,0}}$ and $\overline{\langle \varphi_{-\mathbf{q}}^H \rangle_{\varphi} \langle \rho_{\mathbf{q}}^D \rangle_{\rho,0}}$. In general, $B_{\mathbf{q}}$ reads

$$B_{\mathbf{q}} = \begin{pmatrix} \overline{\langle \varphi_{-\mathbf{q}}^H \varphi_{\mathbf{q}}^H \rangle_{\varphi}} & \overline{\langle \varphi_{-\mathbf{q}}^H \rangle_{\varphi} \langle \rho_{\mathbf{q}}^H \rangle_{\rho,0}} & \overline{\langle \varphi_{-\mathbf{q}}^H \rangle_{\varphi} \langle \rho_{\mathbf{q}}^D \rangle_{\rho,0}} \\ \overline{\langle \rho_{-\mathbf{q}}^H \rangle_{\rho,0} \langle \varphi_{\mathbf{q}}^H \rangle_{\varphi}} & \overline{\langle \rho_{-\mathbf{q}}^H \rho_{\mathbf{q}}^H \rangle_{\rho,0}} & \overline{\langle \rho_{-\mathbf{q}}^H \rho_{\mathbf{q}}^D \rangle_{\rho,0}} \\ \overline{\langle \rho_{-\mathbf{q}}^D \rangle_{\rho,0} \langle \varphi_{\mathbf{q}}^H \rangle_{\varphi}} & \overline{\langle \rho_{-\mathbf{q}}^D \rho_{\mathbf{q}}^H \rangle_{\rho,0}} & \overline{\langle \rho_{-\mathbf{q}}^D \rho_{\mathbf{q}}^D \rangle_{\rho,0}} \end{pmatrix} \quad (3.46)$$

Using eq 3.45 one arrives at

$$\overline{\langle \varphi_{-\mathbf{q}}^H \rangle_{\varphi} \langle \rho_{\mathbf{q}}^H \rangle_{\rho,0}} = S_0^{HH}(t) - \frac{(S_0^{HD} + S_0^{HH})(S_0^{HD}(t) + S_0^{HH}(t))}{S_0^{HH} + S_0^{DD} + 2S_0^{HD}} \quad (3.47a)$$

$$\overline{\langle \varphi_{-\mathbf{q}}^H \rangle_{\varphi} \langle \rho_{\mathbf{q}}^D \rangle_{\rho,0}} = S_0^{HD}(t) - \frac{(S_0^{HD} + S_0^{HH})(S_0^{HD}(t) + S_0^{DD}(t))}{S_0^{HH} + S_0^{DD} + 2S_0^{HD}} \quad (3.47b)$$

We note, in passing, that

$$\overline{\langle \varphi_{\mathbf{q}}^H \varphi_{-\mathbf{q}}^H \rangle_{\varphi}} = \frac{S_0^{HH} S_0^{DD} - (S_0^{HD})^2}{S_0^{HH} + S_0^{DD} + 2S_0^{HD}} = S^{tot}(q), \quad (3.48)$$

as expected (i.e. the above expressions are consistent with the standard RPA expressions for incompressible blends [117, 118]). The final expression for the total coherent scattering function, $S^{tot}(q, t)$, in the presence of EV interactions between chains, is obtained by substituting eqs 3.47 back into eq 3.40. The final result is

$$S^{tot}(q, t) = \frac{\langle \varphi_{-\mathbf{q}}^H \rangle_\varphi \langle \rho_{\mathbf{q}}^H \rangle_\rho}{S_0^{HH} + S_0^{DD} + 2S_0^{HD}} - \frac{T_{\mathbf{q}}^{HH} T_{\mathbf{q}}^{DD} - (T_{\mathbf{q}}^{HD})^2}{T_{\mathbf{q}}^{HH} + T_{\mathbf{q}}^{DD} + 2T_{\mathbf{q}}^{HD}} \quad (3.49)$$

Equation 3.49 can be simplified in certain limits. For instance, if $t \rightarrow 0$, then $T_{\mathbf{q}}^{HH}, T_{\mathbf{q}}^{DD}, T_{\mathbf{q}}^{HD} \approx 0$ and thus eq 3.49 reduces to eq 3.48. Another example is the case of dilute labelled chains in an unlabelled matrix. In this case $S_0^{HD} = T_{\mathbf{q}}^{HD} = 0$, $S_0^{DD} \gg S_0^{HH}$, and $T_{\mathbf{q}}^{DD} \gg T_{\mathbf{q}}^{HH}$ leading to $S^{tot}(q, t) \approx S_0^{HH} - T_{\mathbf{q}}^{HH} \approx S_0^{HH}(t)$. Moreover, for a symmetric blend (that is, for a blend of labelled and unlabelled chains with identical degree of polymerisation, and volume fractions ϕ_H and $\phi_D = 1 - \phi_H$, respectively) the single chain correlation functions are the same for both labelled and unlabelled chains and so S_0^{AB} and $T_{\mathbf{q}}^{AB}$ reduce to

$$\begin{aligned} S_0^{HH} &= \phi_H S_0, & S_0^{DD} &= (1 - \phi_H) S_0, & S_0^{HD} &= 0, \\ T_{\mathbf{q}}^{HH} &= \phi_H T_{\mathbf{q}}, & T_{\mathbf{q}}^{DD} &= (1 - \phi_H) T_{\mathbf{q}}, & T_{\mathbf{q}}^{HD} &= 0, \end{aligned} \quad (3.50a)$$

with S_0 and $T_{\mathbf{q}} = S_0 - S_0(t)$ referring to both a labelled and an unlabelled chain. Under these simplifications, eq 3.49 reduces to $S^{tot}(q, t) = \phi_H (1 - \phi_H) S_0(t)$, or simply to $S^{tot}(q, t) \approx \phi_H S_0(t)$ for $\phi_H \ll 1$ (very diluted protonated chains).

3.3.3 Comparison with NSE data: the melt of symmetric stars

Expressions and parameters required for the calculation of $P(q, t)$

The computation of the total scattering signal, $P(q, t)$, i.e. the computation of eq 1.29, requires the computation of eqs 1.31 and 1.33. That is, one needs to calculate the following quantities: (1) the coherent scattering lengths, \tilde{b}_{coh_H} and \tilde{b}_{coh_D} , and the incoherent scattering lengths, \tilde{b}_{inc_H} and \tilde{b}_{inc_D} , of the protonated and deuterated “monomers”, (2) the total number of “monomers”, N_{tot} , and the volume fractions of the protonated and deuterated species ϕ_H and ϕ_D , respectively, and (3) the scattering functions $S^{tot}(q, t)$, $S^{tot}(q)$ and $S_{inc}(q, t)$.

The calculation of both the coherent and incoherent scattering lengths was detailed in section 3.1 (eqs 3.2 and 3.3). Moreover, in the same section the volume fractions of protonated and deuterated material were estimated; it was found that $\phi_H = 0.043$ and $\phi_D = 0.957$. For the melt of symmetric stars $N_{tot} = n_c f N_a$ where $f = 3$ and $N_a \approx 420$; the total number of chains is irrelevant since factors of n_c in the numerator and denominator of eq 1.29 cancel out.

With respect to $S^{tot}(q, t)$, its final expression (eq 3.49) depends on the (single chain) static and time dependant correlation functions S_0^{AB} and $S_0^{AB}(t)$, respectively. The static correlation functions are presented in table 3.2; the formulae for $S_0^{AB}(t)$, expressed in tube coordinates, are the following:

$$S_0^{HH}(t) = n_c f N_e^2 \int_0^{Z_H} ds \int_0^{Z_H} ds' \exp\left(\frac{-q^2}{6} \langle(\mathbf{r}_{\alpha,s,t} - \mathbf{r}_{\alpha,s',t'})^2\rangle\right) + n_c f (f-1) N_e^2 \int_0^{Z_H} ds \int_0^{Z_H} ds' \exp\left(\frac{-q^2}{6} \langle(\mathbf{r}_{\alpha,s,t} - \mathbf{r}_{\beta,s',t'})^2\rangle\right), \quad (3.51a)$$

$$S_0^{DD}(t) = n_c f N_e^2 \int_{Z_H}^{Z_t} ds \int_{Z_H}^{Z_t} ds' \exp\left(\frac{-q^2}{6} \langle(\mathbf{r}_{\alpha,s,t} - \mathbf{r}_{\alpha,s',t'})^2\rangle\right) + n_c f (f-1) N_e^2 \int_{Z_H}^{Z_t} ds \int_{Z_H}^{Z_t} ds' \exp\left(\frac{-q^2}{6} \langle(\mathbf{r}_{\alpha,s,t} - \mathbf{r}_{\beta,s',t'})^2\rangle\right), \quad (3.51b)$$

$$S_0^{HD}(t) = n_c f N_e^2 \int_0^{Z_H} ds \int_{Z_H}^{Z_t} ds' \exp\left(\frac{-q^2}{6} \langle(\mathbf{r}_{\alpha,s,t} - \mathbf{r}_{\alpha,s',t'})^2\rangle\right) + n_c f (f-1) N_e^2 \int_0^{Z_H} ds \int_{Z_H}^{Z_t} ds' \exp\left(\frac{-q^2}{6} \langle(\mathbf{r}_{\alpha,s,t} - \mathbf{r}_{\beta,s',t'})^2\rangle\right), \quad (3.51c)$$

where $Z_t = Z_H + Z_D$ is the total number of entanglements acting on an arm, and $\langle(\mathbf{r}_{\alpha,s,t} - \mathbf{r}_{\alpha,s',t'})^2\rangle$ and $\langle(\mathbf{r}_{\alpha,s,t} - \mathbf{r}_{\beta,s',t'})^2\rangle$ are the MSD correlation functions of table 2.2 of chapter 2 (c.f. section 2.3.2). The static collective scattering function, $S^{tot}(q)$, is given by eq 3.29, or equivalently by eq 3.18 with the label A (B) representing protonated (deuterated) species.

The total incoherent scattering function, $S_{inc}(q, t)$, is expressed in tube coordinates as

$$S_{inc}(q, t) = n_c \tilde{b}_{incH}^2 f N_e \int_0^{Z_H} ds \exp\left(\frac{-q^2}{6} \langle(\mathbf{r}_{\alpha,s,t} - \mathbf{r}_{\alpha,s,t'})^2\rangle\right) + n_c \tilde{b}_{incD}^2 f N_e \int_{Z_H}^{Z_t} ds \exp\left(\frac{-q^2}{6} \langle(\mathbf{r}_{\alpha,s,t} - \mathbf{r}_{\alpha,s,t'})^2\rangle\right), \quad (3.52)$$

where $\langle(\mathbf{r}_{\alpha,s,t} - \mathbf{r}_{\alpha,s,t'})^2\rangle$ is the segment MSD correlation function of table 2.2.

The MSD correlation functions, appearing in the integrals of eqs 3.51 and 3.52, contain two parameters, namely the tube diameter a and the entanglement relaxation time τ_e ; both a and τ_e can be treated as free parameters when fitting the NSE data, however, they are related through $a^2 = N_e b^2$ and $\tau_e = \tau_0 N_e^2$ (eq 1.50) and so, in practice, only one of them will serve as the fitting parameter in the comparison with the NSE data (we choose to treat a as the fitting parameter). For the segmental distance between protonated “monomers” and between deuterated “monomers” we use $b = 0.824\text{nm}$. Note that eq 1.50 can be rewritten as $\tau_e = N_e^2 / (\pi^2 W_R)$, where $W_R = 3k_B T / (\zeta_0 b^2)$ is the so-called Rouse rate. For all figures of the following section (i.e. for Figs. 3.9-3.11) we use $W_R = 15.184\text{ns}^{-1}$ since with this value $W_R b^4 = 7\text{nm}^4/\text{ns}$ as in Ref. [3]. Having specified b and W_R , for a given value of tube diameter, τ_e and N_e are determined; from N_e , the number of entanglements, $Z_H = N_H/N_e$ and $Z_D = N_D/N_e$, acting, respectively, on the protonated and deuterated sections of the arm is, in turn, determined. The values for Z_H and Z_D provide the limits in the integrals of eqs 3.51 and 3.52. These integrals are calculated numerically.

Results

In Figs. 3.9-3.10, rather than focusing on providing the best fit to the experimental data, we focus our attention on assessing how the theoretical prediction for $P(q, t)$ is affected by various factors; in particular, we examine how $P(q, t)$ is affected (i) by the inclusion of the chain-chain excluded volume interactions (c.f. left panel of Fig. 3.9), (ii) by the neglect of the incoherent scattering signal (c.f. right panel of Fig. 3.9), and (iii) by the use of the MSD correlation functions of Vilgis and Boué [120] instead of the MSD correlation functions that were developed in chapter 2, i.e. the expressions of table 2.2 (c.f. Fig. 3.10). The experimental data of Zamponi et al. [3] are shown in Figs. 3.9-3.10 with filled coloured circles; specifically, black, red, blue, and green circles correspond to $|\mathbf{q}| = 0.5\text{nm}^{-1}$, $|\mathbf{q}| = 0.77\text{nm}^{-1}$, $|\mathbf{q}| = 0.96\text{nm}^{-1}$, and $|\mathbf{q}| = 1.15\text{nm}^{-1}$, respectively. The same data, together with their error bars, are shown in Fig. 3.11. In this particular figure we take into account the early tube dilation (ETD) process that was described in section 2.4.1 of chapter 2.

In the left panel of Fig. 3.9, the theoretical predictions for $P(q, t)$, in both the presence (solid lines) and absence (dotted lines) of EV interactions (correlations), are presented. (Note that in the absence of EV interactions $S^{tot}(q, t) = S_0^{HH} - T_{\mathbf{q}}^{HH} = S_0^{HH}(t)$.) In this

particular plot, both the coherent and incoherent signals are accounted for. With respect to the tube diameter the value $a = 3.7\text{nm}$ was used. This plot demonstrates that the inclusion of EV interactions does not have any significant effect on the scattering signal, as expressed by the function $P(q, t)$. It is likely that the of-order 10% errors from neglect of interactions in the numerator and denominator of eq 1.29 cancel each other out, to a large extent. The right panel of Fig. 3.9 shows our predictions for $P(q, t)$ without (with) the inclusion of the incoherent signals, $I_{inc}(q, t)$ and $I_{inc}(q)$, as dotted (solid) lines. EV interactions between the chains are included in both calculations. As in the left panel of the same figure, we have used $a = 3.7\text{nm}$. From this plot it is evident that the coherent signal is dominating the scattering, since the inclusion of the incoherent terms $I_{inc}(q, t)$ and $I_{inc}(q)$, in eq 1.29, slightly changes the predicted $P(q, t)$. We note, however, that the deviation between solid and dotted lines becomes bigger with increasing $|\mathbf{q}|$ values; this is to be expected since with rising $|\mathbf{q}|$ motion at increasingly smaller lengthscales is probed (by the neutron beam).

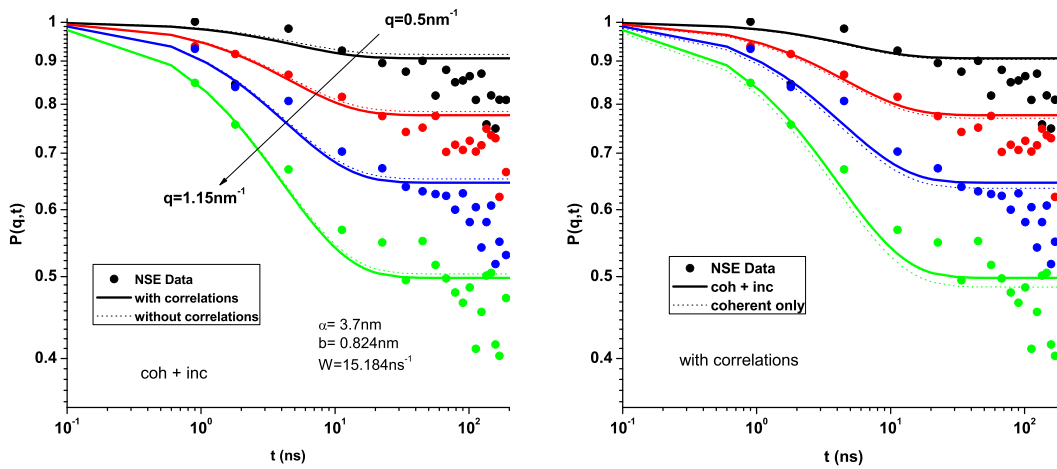


Figure 3.9: Theoretical (lines) and experimental (symbols) $P(q, t)$, for the PE star melt, at several $|\mathbf{q}|$. Black, red, blue, and green colours refer to $|\mathbf{q}| = 0.5\text{nm}^{-1}$, 0.77nm^{-1} , 0.96nm^{-1} , and 1.15nm^{-1} , respectively. Left: $P(q, t)$ in the presence (solid lines) and absence (dotted lines) of EV interactions (correlations) when both the coherent and incoherent signals are included. Right: $P(q, t)$ with and without the incoherent signal (solid and dotted lines, respectively), in the presence of correlations. The NSE data [3] are provided by Dr. M. Zamponi.

Figure 3.10 presents, with dotted lines, the predicted $P(q, t)$ when the MSD correlation

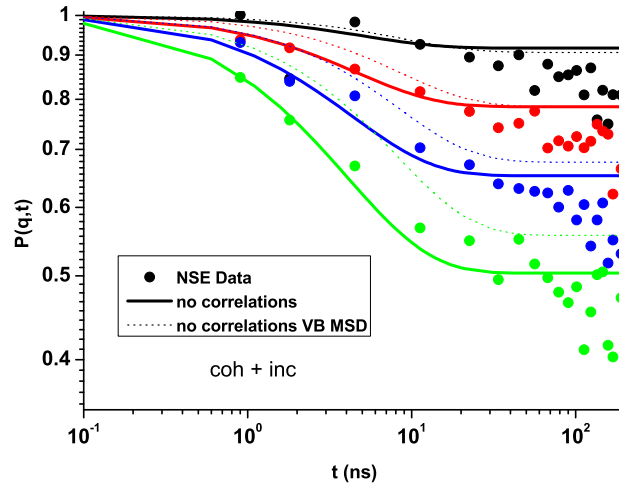


Figure 3.10: Theoretical $P(q, t)$ using the expressions of table 2.2 for the MSD correlation functions (solid lines). The same quantity using the expressions of Vilgis and Boué for the MSD functions (dotted lines). EV interactions (correlations) are disregarded. Both the coherent and incoherent signals are accounted for. NSE data are represented by filled circles. The correspondence between colours and q values is the same as in Fig. 3.9; a, b, W_R same as for Fig. 3.9. The NSE data [3] are provided by Dr. M. Zamponi.

function of Vilgis and Boué [120] is used. Note that for segments positioned on the same arm we use eq 2.28; for segments placed on different arms the factor $|s - s'|$ in eq 2.28 is substituted by the factor $(s + s')$. Moreover, following Ref. [3] W_R is multiplied by the factor $2/3$ to compensate for the fact that eq 2.28, actually, refers to a linear chain and not to a symmetric star and so it does not account for the enhanced friction due to the branch point; this modification, however, is unnecessary when one uses the expressions of tables 2.1 and 2.2. Figure 3.10 also includes, with solid lines, the obtained $P(q, t)$ when our expressions for the MSD correlations functions are used. In both cases, EV interactions between the chains are neglected, and both the coherent and incoherent signals are included. The experimental data are shown as filled symbols as in Fig. 3.9. From Fig. 3.10 it is clear that the theoretical NSE signal depends strongly on the choice of MSD correlation functions; for the two higher $|q|$ values (blue and green colours) much stronger localisation is predicted, throughout the entire NSE time window, when $\langle (\mathbf{r}_{s,t} - \mathbf{r}_{s',t'})^2 \rangle_{VB}$ is used. For $|q| = 0.96 \text{ nm}^{-1}$ (red colour) the plateau value of $P(q, t)$ is similar, nevertheless, the localisation in the Rouse regime is stronger

when $\langle (\mathbf{r}_{s,t} - \mathbf{r}_{s',t'})^2 \rangle_{VB}$ is used. The two choices give similar results at the lowest $|\mathbf{q}|$ (black line). The deviation between solid and dotted lines becomes bigger with increasing $|\mathbf{q}|$ because the expressions for the MSD, in S_0^{AB} and $S_0^{AB}(t)$, are multiplied by q^2 . Figure 3.10 indicates that the use of the Vilgis-Boue expressions in fitting NSE data (as is done in Ref. [3]) can give rise to errors.

In Figs. 3.9 and 3.10, the theoretical $P(q, t)$, in all considered cases, establishes a distinct plateau at times slightly longer than τ_e . At these times fast Rouse modes saturate and thus no further conformational relaxation is predicted, since our MSD correlation functions do not account, directly, for any other relaxation process. Apparently, the NSE data continue to decline even after $t > \tau_e$ indicating further relaxation of the branch point localisation. This additional relaxation can be incorporated in the MSD expressions of table 2.2 in a manner similar to the one used in sections 2.4.1 and 2.4.2 for the inclusion of early tube dilation and standard constraint release events in the comparison with the MD data. That is, the model parameters a , τ_e , and s entering in the expressions for the MSD correlation functions can be rescaled using eq 2.32 (the prefactors N_e in the integrals of eqs 3.51 and 3.52 are also rescaled appropriately).

Within the time window of the NSE experiment, however, standard constraint release (CR) only slightly affects the dynamics of the branch point; the upper time limit of the NSE experiment $t \approx 200\text{ns}$ is longer than τ_e about 1.5-2 decades (depending on the value of a used in the fitting), but is about six times lower than the Rouse relaxation time of an arm and thus deep contour length fluctuations of the arms, that convey the vast majority of standard CR events, are not activated yet. For this reason we set $\psi(t) = 1$ when we rescale our model parameters in the subsequent comparison with the NSE data (Fig. 3.11-thick solid lines). An additional reason to set the tube survival probability equal to unity is the big difference between the arm entanglement length of the simulated chains and the arm entanglement length of the real chains of the NSE experiment. Specifically, for an arm in the MD simulation $Z_a = 8$ while for an arm in the NSE experiment $Z_a \approx 20$ (the exact value of Z_a , as estimated from the NSE measurements, depends on the value of a – rheological measurements suggests a value of $Z_a \approx 14$ [3] which is, also, much bigger than the value of Z_a in the simulations). By setting $\psi(t) = 1$, therefore, a potentially overestimated contribution of CR effects, due to the fact that the deep CLF are activated earlier in the shorter arms of the MD simulation, is avoided.

To summarise this discussion, in an attempt to fit the NSE data, we will only include the early tube dilation (ETD) process described in section 2.4.1 and thus we will rescale the model parameters using eq 2.30. The early tube dilation function $g(t)$ (eq 2.31) is mapped in the time units of the NSE experiment (i.e. in ns) as follows: first, we set $g(t) = 1$ and use $a = 3.5\text{nm}$ (with a corresponding $\tau_e \approx 2.2\text{ns}$) to obtain a line that fits the NSE data at early timescales, up to $t \approx 10\text{ns}$ (c.f. dotted lines in Fig. 3.11). Then, using the value $\tau_e \approx 2.2\text{ns}$ we map the parameters, τ_g and t_0 , of eq 2.30 in real time units by requiring the ratios τ_g/τ_e and t_0/τ_e to be the same in both simulation and real units (ns). Under this mapping $\tau_g \approx 41.4\text{ns}$, which is about 0.05 times the Rouse relaxation time of an arm.

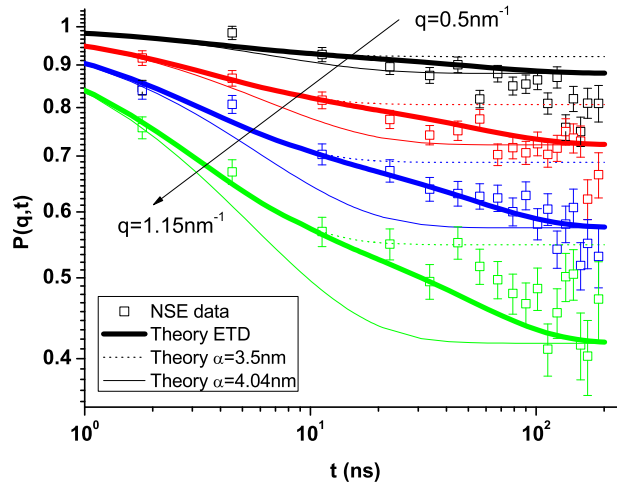


Figure 3.11: Predicted $P(q, t)$ when early tube dilation (ETD) is included (thick solid lines). The dotted and thin solid lines refer to $g(t) = 1$ (neglect of ETD) and are obtained using $a = 3.5\text{nm}$ and $a = 4.04\text{nm}$, respectively. NSE data, with their error bars, are shown with open squares. The correspondence between colours and q values is the same as in Figs. 3.9 and 3.10. The NSE data [3] are provided by Dr. M. Zamponi.

Figure 3.11 presents, with thick solid lines, the predicted $P(q, t)$ when early tube dilation is included. As aforementioned, the dotted lines correspond to $g(t) = 1$ and $a = 3.5\text{nm}$. Moreover, the thin solid lines refer to $g(t) = 1$ and $a_{ef} = 4.04\text{nm}$, which is the effective value of the tube diameter at $a/\sqrt{g(t \rightarrow \infty)}$. The NSE data, together with their error bars, are represented by open squares. The agreement, for $|q| = 0.77\text{nm}^{-1}$ and $|q| = 0.96\text{nm}^{-1}$ (red and blue colours, respectively), between the thick solid lines and the data is very good; for almost every data point the thick solid lines fall within the

error bars. For the lowest and the highest $|\mathbf{q}|$ values the agreement is poorer; towards the upper time limit of the experiment the localisation is slightly over-predicted (under-predicted) for $|\mathbf{q}| = 0.5\text{nm}^{-1}$ ($|\mathbf{q}| = 1.15\text{nm}^{-1}$). On the other hand, the dotted and thin solid lines, clearly, fail to describe the data, as expected. In the computation of $P(q, t)$ for this particular plot, EV interactions were included as well as the incoherent scattering signal (as demonstrated in Fig. 3.9, however, the neglect of interactions or the neglect of the incoherent scattering does not have a strong effect on the results). For the calculation of the MSD correlation functions the expressions of table 2.2 were used. Overall, the inclusion of the early tube dilation process provided a reasonable fit to the data. Comparing Figs. 3.11 and 3.9, and noting the quality of fits, it seems reasonable to conclude that the data have not reached a plateau in the experimental time window, and that the lack of a plateau can be explained by a form of early tube dilation, similar to that used in chapter 2.

3.4 Comparison with MD

In section 2.4 we compared MD simulation data for the MSD of a “simulation branch point”, of an entangled three arm symmetric star, with our theoretical expressions for the segmental MSD. In this section, and for the same system, we compare the MD data for both the coherent and the incoherent scattering functions with our theoretical predictions. In order to keep the same notation with the previous sections of this chapter, in what follows, we treat the “simulation branch point” (i.e. the branch point and its three closest neighbours on each arm) as the “labelled” section of the chain. Therefore, the theoretical expression that is used in the comparison against the MD data, for the (time dependent) coherent scattering function, is eq 3.51a. With respect to the (time dependent) incoherent scattering function the expression that is used, in the comparison against the data, corresponds to the first term of eq 3.52. The respective scattering functions at equilibrium are calculated using the same equations. For each case, we use the (appropriate) expression of table 2.2 for the MSD correlation functions.

For the calculation of the integrals of eqs 3.51a and 3.52 we use: (i) $N_e = a^2/b^2 \approx 11.1$, where a is the value of the undilated tube diameter before the onset of early tube dilation and CR, i.e. $a^2 = 38\sigma^2$ (c.f. section 2.4.1 and Fig. 2.7), and b is the segmental

distance between the simulation beads ($b = \sqrt{3.43}\sigma$), (ii) $Z_H = 3/N_e$, for the limits of the integrals, and (iii) eq 2.32 for the rescaling of the model parameters, in order to account for the effects of early tube dilation (ETD) and constraint release (CR). In practice one can retain the undilated variables s and s' and “dilate” the upper limit of the integrals, Z_H , using $N_e(t) = N_e / (g(t)\psi(t)^{\alpha_d})$.

The left panel of Fig. 3.12 presents the normalised incoherent scattering function, $S_{inc}(q, t)/S_{inc}(q)$, as a function of time, t , for several values of $|\mathbf{q}|$ (both t and $|\mathbf{q}|$ are expressed in terms of simulation units). The lowest $|\mathbf{q}|$ value is $0.1\sigma^{-1}$ (black colour) while the highest $|\mathbf{q}|$ value is $1\sigma^{-1}$ (orange colour). These two wavevectors correspond to lengthscales of $\approx 63\sigma$ and $\approx 6.3\sigma$, respectively (we note, for comparison, that the undilated tube diameter is $a = \sqrt{38}\sigma \approx 6.2\sigma$). A comparison between the data (open squares) and our predictions (thick lines for $\alpha_d = 1$ and thin lines for $\alpha_d = 4/3$) is also shown for eight values of $|\mathbf{q}|$ between the two aforementioned limits, i.e. for $|\mathbf{q}| = 0.2\sigma^{-1}, |\mathbf{q}| = 0.3\sigma^{-1}, \dots, |\mathbf{q}| = 0.9\sigma^{-1}$. Overall, the agreement between the MD data and our predictions, using $\alpha_d = 1$, is good for all examined $|\mathbf{q}|$ values.

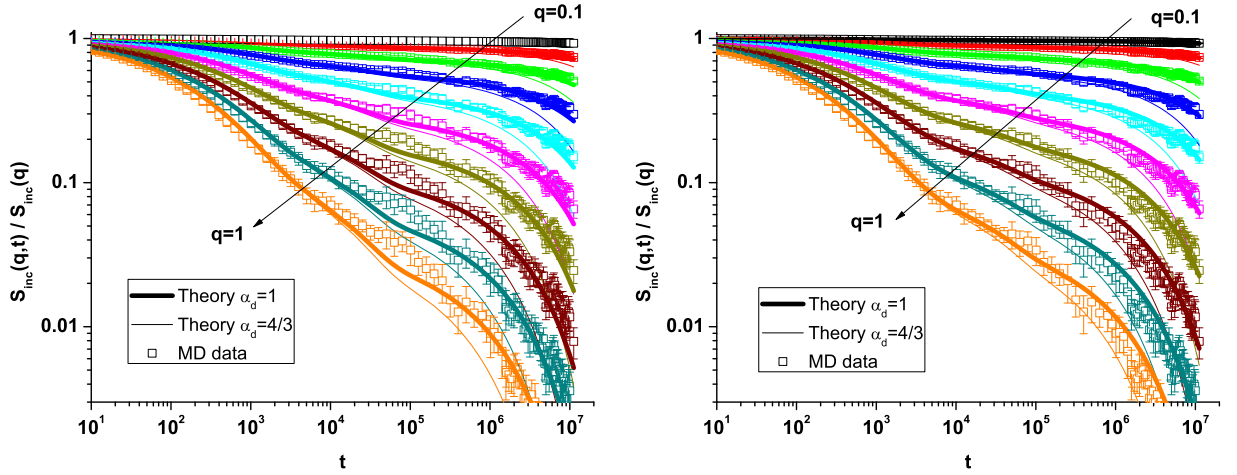


Figure 3.12: The normalised incoherent scattering function, as obtain from the MD simulations (open symbols with their error bars) and the theoretical expressions (lines) for several $|\mathbf{q}|$ values. Thick (thin) lines refer to $\alpha_d = 1$ ($\alpha_d = 4/3$). The theoretical predictions account for ETD and CR. Left: For $g(t)$ we use eq 2.31. Right: for $g(t)$ we use $\tilde{g}(t)$ (see text). The MD data are provided by P. Bačová and Dr. A. J. Moreno.

Note that, this plot may be considered, essentially, as a re-plot of the segmental MSD, presented in the left panel of Fig. 2.12, since the incoherent scattering function is only

related to the segmental dynamics (motion). For this reason these two plots share two common features. First, at times $t \gtrsim 5 \times 10^4 \tau_0^{MD}$, the MD data are better described using $\alpha_d = 1$. Second, in the time interval $4 \times 10^4 \tau_0^{MD} \lesssim t \lesssim 2 \times 10^5 \tau_0^{MD}$ the theoretical predictions, slightly, under-estimate the localisation of the segments. In this regime and for the higher values of $|\mathbf{q}|$, the theoretical lines are closer to the low limits of the error bars than the “actual” data points. Accordingly, in the left panel of Fig. 2.12, the theoretical lines for the MSD are closer to the upper limits of the error bars than the “actual” (MSD) data points.

To demonstrate that the discrepancy between the data and the theoretical predictions, in the time interval $4 \times 10^4 \tau_0^{MD} \lesssim t \lesssim 2 \times 10^5 \tau_0^{MD}$ is related to the ETD function, $g(t)$, we do the following: rather than using eq 2.31 for $g(t)$ we use the following expression: $\tilde{g}(t) = 0.8 + 0.2 \exp(-t/38075.5)$; our reason for considering this is that eq 2.31 was obtained as a best fit to both the star and Cayley tree data taken together. However, scattering data are only shown for the stars, so for a fair comparison we should consider the $g(t)$ that best fits the star MSD data, taken on their own. The right panel of Fig. 2.12 shows the outcome of this calculation. Clearly, in the aforementioned time regime, the MD data are better described in the plot of the right panel. The modest shift, of the theoretical curves, to the right at late times is expected since the value of $g^*(t \rightarrow \infty)$ is slightly higher than the value of $g(t \rightarrow \infty)$.

We now turn our attention in the comparison of the MD data and the theoretical predictions in the case of the coherent scattering function. Figure 3.13 presents the outcome of this comparison. As in Fig. 3.12, the MD data are represented by open symbols while our predictions are shown as thick and thin solid lines for $\alpha_d = 1$ and $\alpha_d = 4/3$, respectively. Black, red, blue, and dark cyan colours refer to $|\mathbf{q}| = 0.3\sigma^{-1}$, $|\mathbf{q}| = 0.4\sigma^{-1}$, $|\mathbf{q}| = 0.5\sigma^{-1}$, and $|\mathbf{q}| = 0.6\sigma^{-1}$, respectively. Although the error bars of the data are missing the agreement between MD simulations and theory can be considered relatively poor, especially, at early timescales. The reasons for this discrepancy are not understood yet; nevertheless, it is more likely that they are neither related to the semi-phenomenological approach that was used for the description of the so-called early tube dilation process, nor to the estimated (from the MD simulations) tube survival probability, since the deviation between the MD data and the theoretical predictions is big, even, at early timescales (at which the effects of ETD and CR are almost negligible). Indeed,

if we set $g(t) = \psi(t)^{\alpha_d} = 1$, then the theoretical results are indistinguishable from the solid lines of Fig. 3.13 up to $t \approx 6 \times 10^3 \tau_0^{MD}$ (at later timescales a clear plateau is formed as expected). A possible explanation for the discrepancy, then, is that at early times the Rouse model is not such a good model for the collective dynamics of the polymer chains. The model can provide a reasonably good description for the MSD of an individual monomer (Figs. 2.12 or 3.12) but runs into problems in describing the collective motion of several monomers at early times (as is required in the description of the coherent scattering of Fig. 3.13). This effect will be enhanced by the relatively stiff chains used in the simulations.

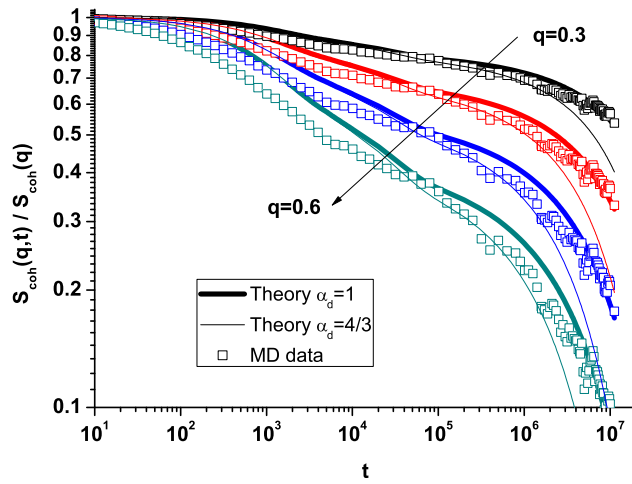


Figure 3.13: The normalised coherent scattering function, as obtain from the MD simulations (open symbols) and our theoretical expressions (lines) for several $|q|$ values. Thick (thin) lines refer to $\alpha_d = 1$ ($\alpha_d = 4/3$). The theoretical predictions account for ETD and CR. For the correspondence between colours and $|q|$ values see the text. The MD data are provided by P. Bačová and Dr. A. J. Moreno.

3.5 Conclusions and future work

This chapter was concerned with scattering from polymer melts. Particular attention was drawn to the interpretation of the NSE data of Zamponi et al. [3], which refer to scattering from the branch point region of molten (three arm) symmetric PE stars. Some aspects of the scattering behaviour of a blend of linear chains were also studied. For these

two systems the standard RPA was applied, in order (i) to examine the effects of chain-chain excluded volume (EV) interactions, and moreover, (ii) to determine the relative contribution between coherent and incoherent scattering signals, at equilibrium (that is, at time $t' = 0$). The application of the standard RPA demanded the calculation of the single chain structure factors in the absence of EV interactions; for both systems, these structure factors were obtained by using the method of Read [149]. This standard RPA showed that, for these two systems, a potential error of order 10% – 15% is possible in the interpretation of scattering data, if the EV interactions and/or the incoherent signal are disregarded.

For this reason a dynamic version of the standard RPA, which accounted for EV interactions both at equilibrium and after a time interval t , was developed. In the development of the dynamic RPA, it was assumed that, during the time interval t , there are some quenched variables shared between the two stages (namely, the configurations of the tubes and slow Rouse modes), and some annealed variables that fluctuate rapidly (fast Rouse modes). It was shown that the final expressions for the coherent scattering functions, $S(q, t)^{tot}$ and $S(q)^{tot}$, can be expressed in terms of the (static and time dependent) single chain structure factors in the absence of any chain-chain EV interactions (see equations below); this expression do not depend on the architecture of the chains since this type of information is absorbed in the structure factors. The Warner-Edwards (WE) picture of the tube [117, 118, 120, 121, 122, 124] was adopted for the evaluation of the structure factors. Thus the MSD correlation functions, which appeared in the expressions for the structure factors, were calculated by using the expressions developed in chapter 2. The respective expressions of Vilgis and Boué [120] were also used for comparison. The theoretical predictions for $P(q, t)$, the dynamic normalised scattering signal, were compared against the data of Zamponi et al. [3]. Finally, the theoretical expressions for the normalised incoherent and coherent scattering functions, $S_{inc}(q, t)/S_{inc}(q)$ and $S_{coh}(q, t)/S_{coh}(q)$ respectively, were compared with MD data. It was found that:

- I. For the melt of symmetric stars, the neglect of EV interactions has a negligible effect on $P(q, t)$. (See Fig. 3.9, left.) This is probably due to a cancelation of errors in the numerator and denominator of eq 1.29, since the standard RPA implies that the neglect of such interactions can give a potential error of 10% – 15%. The neglect of

the incoherent signal has also minor effects on $P(q, t)$. (See Fig. 3.9, right.)

- II. $P(q, t)$ is sensitive to the choice of MSD correlation functions (see Fig. 3.10): a considerable deviation is observed between $P(q, t)$ and $P_{VB}(q, t)$. ($P_{VB}(q, t)$ is the predicted scattering signal when the expressions of Vilgis and Boué [120] are used.) As shown in section 2.3.3 this deviation is attributed to the neglect of the mean path contribution to the MSD in the Vilgis-Boué expressions.
- III. The dynamic RPA provides a close quantitative match to the NSE measurements of Zamponi et al. [3] when early tube dilation is included in the MSD correlation functions (Fig. 3.11). CR can be ignored since at the time window of the experiment of Zamponi et al. deep CLF of the arms are not activated.
- IV. As regards the comparison with the MD simulations, a good agreement is seen for the incoherent scattering function, $S_{inc}(q, t)/S_{inc}(q)$, whereas for the coherent scattering function, $S_{coh}(q, t)/S_{coh}(q)$, the agreement is poor. A possible explanation is that the Rouse model is not such a good model for the collective dynamics of the polymer chains. The model can provide a reasonably good description for the MSD of an individual monomer (Figs. 2.12 or 3.12) but runs into problems in describing the collective motion of several monomers at early times (as is required in the description of the coherent scattering of Fig. 3.13).

NSE data are also available for the mixture of linear chains, which consists of a small fraction of (long centred) protonated chains in a deuterated matrix [84]. In this system CLF are masked since the ends of the labelled chains are deuterated; moreover, CR events are strongly suppressed due to the similar length of the labelled and matrix chains [84]. Although the signature of these relaxation mechanisms does not show up in this particular experiment, the application of the dynamic RPA to this system requires some extra attention: on the experimental time window the segments of the labelled sections are subjected to local reptative modes, therefore the slow Rouse modes can no longer be considered quenched; this means that the theoretical expressions for the MSD correlation functions (for linear chains one should set $f = 2$ in these expressions) are no longer valid as they do not incorporate local reptative motion. To apply the dynamic version of the RPA for this system one should include local reptation in the MSD expressions. Future work in this direction is required.

Finally, notice that the dynamic RPA expressions could be used in conjunction with structure factors obtained from single-chain simulations, e.g. from the slip-link model of Likhtman [150]. To explain this statement further I restate eqs 3.48 and 3.49, i.e. the RPA expressions for the dynamic coherent scattering function, $S^{tot}(q, t)$, and the static coherent scattering function, $S^{tot}(q)$, as follows:

$$S^{tot}(q) = n_c \frac{s_0^{HH} s_0^{DD} - (s_0^{HD})^2}{s_0^{HH} + s_0^{DD} + 2s_0^{HD}}$$

$$S^{tot}(q, t) = S^{tot}(q) - n_c \frac{[s_0^{HH} - s_0^{HH}(t)] [s_0^{DD} - s_0^{DD}(t)] - [s_0^{HD} - s_0^{HD}(t)]^2}{[s_0^{HH} - s_0^{HH}(t)] + [s_0^{DD} - s_0^{DD}(t)] + 2[s_0^{HD} - s_0^{HD}(t)]}$$

where $s_0^{HH}(t)$, $s_0^{DD}(t)$ and $s_0^{HD}(t)$ are the dynamic single chain structure factors, and s_0^{HH} , s_0^{DD} and s_0^{HD} are their static counterparts. (n_c is the total number of chains.) The message I wish to convey is the following: *instead of using the Warner and Edwards (WE) model, one can obtain the single chain structure factors from slip-link simulations and then use the above expressions, which account for EV interactions between the chains, to calculate the coherent scattering functions $S^{tot}(q, t)$ and $S^{tot}(q)$. In addition, one can extract the incoherent scattering functions, $S_{inc}(q, t)$ and $S_{inc}(q)$, from a slip-link simulation, and use them together with $S^{tot}(q, t)$ and $S^{tot}(q)$ to obtain the coherent and incoherent NSE signals (eqs 1.31 and 1.33) and, in turn, the dynamic normalised scattering signal $P(q, t)$ (eq 1.29). Compared to the WE model used in this chapter, the slip-link simulations provide a more realistic description of the single chain dynamics: structure factors obtained from such simulations would account for all possible conformational relaxation processes [150] (i.e. reptation, constraint release, counter length fluctuation, fast Rouse modes, and longitudinal modes), in contrast to the WE model which only accounts for local fluctuations within the tube (fast Rouse modes). We notice that slip-link simulations can provide a consistent description of NSE data from binary blends of linear polymer chains (i.e. blends of few labelled long chains in a matrix of shorter chains) over a large range of matrix molecular weights [94].*

Chapter 4

Modifying the pom-pom model for extensional viscosity overshoots

4.1 Introduction

This chapter is dedicated to the extensional behaviour of polymer melts with long-chain branching (LCB). Understanding the relationship between the LCB structure of commercial melts and their rheological response is of practical interest, since LCB has a significant effect on the processability of the melt. Specifically, long-chain branching is responsible for the strain hardening behaviour that commercial melts exhibit [151, 152, 153]. It is well established that this flow property, together with shear thinning, facilitates processing [151, 152]. Furthermore, strain hardening makes the processing operation less prone to instabilities [154, 155].

On the other hand the high and random branching of industrial melts makes the molecular modeling of their dynamics, even in the linear rheological regime, a difficult task. Nevertheless, concrete steps towards the development of a general theory for the rheology of arbitrary branched structures have been made [156, 157]. The so-called “BOB” (branch-on-branch) software [158] developed by Das et al. [157] is able to predict many aspects of the linear rheology of both model polymer melts [17, 157] (i.e. asymmetric stars, H-polymers, combs, linear-star blends and DendriMacs) and melts of industrial complexity [157] (e.g. metallocene-catalysed polyethylene melts). “BOB” has been recently refined by Read et al. [159] to account for fast flows. To predict

the nonlinear flow properties of a series of low-density polyethylenes (LDPEs) Read et al. mapped the priority and relaxation time distributions onto several “pom-pom” modes. Essentially, they represented the LDPEs by a set of pom-pom polymers [8], the idealised molecular structure presented in section 1.5.2.

As briefly discussed in section 1.5.2, the idea of “decoupling” the structure of an LCB melt into an equivalent set of pom-pom molecules (modes) was introduced by Inkson et al. [9] and refined by Blackwell et al. [102]. Within this approximation each mode is characterised by an orientation (reptation) relaxation time τ_{b_0} and a plateau modulus G_0 . These parameters can be readily obtained by matching the linear viscoelastic envelope (LVE) of a given melt using multiple Maxwell modes. In addition, each pom-pom mode has a stretch relaxation time τ_{s_0} and a priority q (the number of arms emerging from each branch point of a pom-pom). These two quantities serve as free parameters when fitting extensional viscosity data. Nevertheless, the selection of their values is restricted by the following physical arguments:

First, a long-chain branched molecule, like the one shown at the left panel of Fig. 4.1, relaxes hierarchically from outwards to inwards [2] so strands in the outer sections of the molecule do not stretch as much as strands in the inner sections. Consequently, modes that represent the inner parts are given high q values whereas modes that refer to the outer parts are decorated with low q values; this idea is illustrated schematically in the right panel of Fig. 4.1. Second, the stretch relaxation time can not exceed the reptation relaxation time and so $\tau_{b_0}/\tau_{s_0} \geq 1$. Third, going from faster modes (i.e. modes with lower τ_{b_0} values) to slower modes (higher τ_{b_0} values) the τ_{b_0}/τ_{s_0} ratio should decrease. This is because τ_{b_0}/τ_{s_0} is proportional to the number of entanglements that the backbone material experiences, and as relaxation occurs hierarchically one expects inner sections (represented by slower modes) to experience fewer entanglements than outer sections (represented by faster modes).

Using the multimode version of the original pom-pom theory (mPP), Inkson et al. were able to fit experimental data of the transient (both uniaxial and planar) extensional viscosity of several common industrial polymer melts [9]. However, the experimental data were obtained using a Mnstedt-type [160] or a Meissner-type [45] rheometer and thus much of the success of the mPP approach of Inkson et al. relies on the fact that the samples break before steady state is achieved. Data, obtained from such rheometers, in the

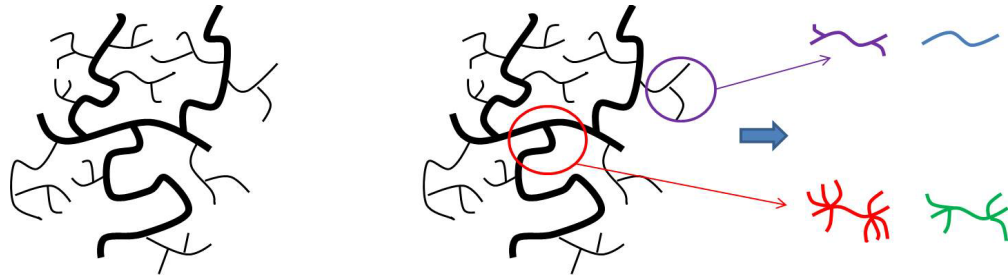


Figure 4.1: Left: A long chain branched (LCB) polymer. Right: A LCB polymer melt can be modelled as a series of individual pom-pom molecules. The inner parts of the LCB chain stretch more than the outer ones. Therefore the pom-pom molecules that represent the inner sections are decorated with higher q values.

vast majority of cases reveal only the sudden and extreme (at the highest rates) increase in the extensional viscosity which is attributed to strain hardening. After a particular time (Henky strain) in the hardening regime the samples break or become inhomogeneous [34] and reliable data are difficult to obtain. As a result, safe conclusions about the predictions of the mPP theory were not drawn beyond this point. To explain this statement further, we note that the constitutive equation of the original pom-pom model is able to predict the hardening behaviour (c.f. section 1.5.2), therefore one can use the mPP model and fit quantitatively the measured viscosity up to its maximum, i.e. up to the point at which the samples break; at this maximum and beyond, the mPP model predicts a clear viscosity plateau because stretch and orientation of the backbone are saturated, that is, $\lambda = q$ and $S_{xx} - S_{yy} = 1$, respectively; experimental data, however, are not available at these timescales and hence the prediction for a viscosity plateau is not justified.

As mentioned in section 1.2.6, the Filament Stretching Rheometer (FSR) [4, 5, 34] is able to reach Henky stains of order seven. As a result, it appears to be able to establish an effective steady state; as discussed in Ref. [34] even in this type of rheometer, however, a true steady-state flow condition is impossible to establish. The left panel of Fig. 4.2 presents the transient uniaxial extensional viscosity, of a commercial melt known as the DOW150R sample, as measured by the FSR device based in the Danish Technical University (DTU) [4, 5, 6, 7, 161, 162]. Throughout the rest of this chapter the study of the behaviour of the industrial melt, DOW150R, under a constant applied uniaxial extensional flow, will be referred to as the *normal case* (NC). In this figure, the strain rates (starting from the lowest which corresponds to the LVE) are: $\dot{\epsilon} = 0.0001\text{s}^{-1}$, $\dot{\epsilon} = 0.003\text{s}^{-1}$,

$\dot{\epsilon} = 0.01s^{-1}$, $\dot{\epsilon} = 0.03s^{-1}$, $\dot{\epsilon} = 0.1s^{-1}$ and $\dot{\epsilon} = 0.3s^{-1}$; hereafter, these rates are referred to as r1, r2, r3, r4, r5 and r6, respectively. The data demonstrate that the viscosity goes through a profound overshoot at the extensional (strain) rates $\dot{\epsilon} = 0.1s^{-1}$ and $\dot{\epsilon} = 0.03s^{-1}$; as briefly discussed in section 1.2.6, the existence of these overshoots is also supported by steady state extensional viscosity measurements in a cross-slot flow [60, 62]. Clearly, the constitutive equation of Inkson et al. [9] would fail to capture this kind of behaviour since it predicts a viscosity plateau after the initial hardening.

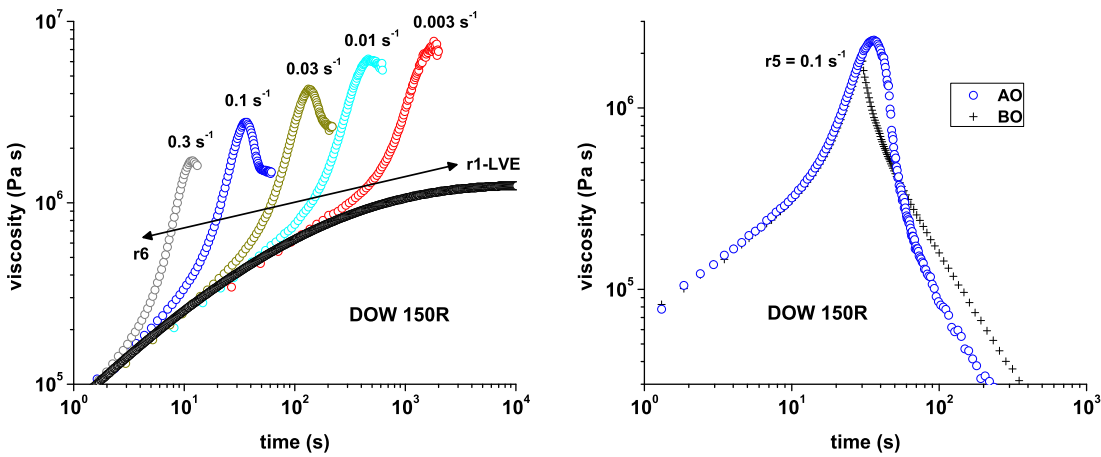


Figure 4.2: FSR measurements for the industrial sample DOW150R. Left: Uniaxial extensional viscosity [6], under steady flow, for several extensional rates. Right: The same quantity at $\dot{\epsilon} = 0.1s^{-1}$ [7]; black and blue symbols refer to flow cessation before the overshoot (**BO**) and after the overshoot (**AO**), respectively. The data are provided by Dr. Qian Huang and Prof. Ole Hassager.

Using the FSR rheometer, it is also possible to measure the relaxation of stress following cessation of the extensional flow [7, 162]. Throughout the rest of this chapter the study of the behaviour of the industrial melt under an uniaxial extensional flow, which is stopped at a particular time, will be referred to as the *relaxation case* (RC). The right panel of Fig. 4.2 shows the measured extensional viscosity of the DOW150R sample as a function of time for $\dot{\epsilon} = 0.1s^{-1}$ (the rate r5) in two cases [7]: (i) when the flow is ceased (stopped) before the overshoot and (ii) when the flow is stopped after the overshoot; in the text, hereafter, the former case is referred to as the **BO** (before overshoot) case while the latter case is referred to as the **AO** (after overshoot) case. In the right panel of Fig. 4.2, the data for the **BO** case and the **AO** case are presented with black and blue symbols, respectively. For the **BO** case the flow is stopped at a Henky strain of approximately

3.0 ($t \approx 30\text{s}$) while for the **AO** case at a Henky strain of approximately 4.5 ($t \approx 45\text{s}$). The purpose of this particular experiment is to provide information about the relaxation behaviour of the polymer melt both before and after the extensional viscosity overshoot. The relaxation data of the right panel of Fig. 4.2 indicate that the industrial melt relaxes faster in the **AO** case than in the **BO** case. In one of the following sections we demonstrate that the original pom-pom model is unable to predict this faster relaxation when the flow is “switched off” after the overshoot.

It is worth mentioning that Nielsen et al. [161] used the same FSR to study the response, under uniaxial extension, of a nearly monodisperse melt of polystyrene pom-pom molecules. The authors measured the extensional viscosity at six different strain rates, and they reported a clear overshoot only at the highest rate. However, in this particular experiment the steady state value of the viscosity was not determined. Furthermore, a bizarre (from the perspective of the pom-pom theory) effective value of $q = 2.5$ arms per branch point was proposed for this particular melt. Wagner and Rolon-Garrido [163] applied the molecular stretch function (MSF) constitutive model to fit the data in Nielsen et al. In their implementation of the MSF model they incorporated the idea of tube pressure [164] together with dynamic dilution, finite extensibility and branch point withdrawal (after the maximum stretch condition). Nevertheless, it is impossible to judge if the correct steady state is predicted by Wagner and Rolon-Garrido [163] since a steady state value is not achieved in the experiments of Ref. [161].

A recent modification of the original mPP theory is proposed in Refs. [6, 62] to enable extensional viscosity overshoots. To do so, Hoyle [62] introduced an additional relaxation time, τ^* , into the dynamic stretch equation of the original theory. This additional relaxation mechanism is driven from advection by the flow and depends upon the average backbone orientation \mathbf{S} . In addition to G_0 , q , τ_{b_0} and τ_{s_0} Hoyle introduced two more parameters for each mode: one to control the degree of alignment needed to trigger the additional relaxation mechanism and another one to control the steady state value of the viscosity. Despite the success of this approach [6, 62] at fitting the extensional data of the DOW150R sample, presented at the left panel of Fig. 4.2, this modification is phenomenological and lacks molecular origin. Moreover, it is not tested against the relaxation data presented at the right panel of Fig. 4.2. In this context, we note that their extra relaxation term in the stretch equation is proportional to flow rate. Thus, upon

cessation of flow, it is switched off and all relaxation times return to their original values. So it would seem impossible for their model to predict the different stress relaxation behaviour before and after the overshoot, even qualitatively.

Here, we propose a modification of the original pom-pom theory that enables extensional viscosity overshoots. Furthermore, we adopt the approach of Inkson et al. [9] to model the LCB melt as a collection of individual pom-pom modes and so we use a multimode version of our modified theory to fit the experimental data shown in Fig. 4.2. Contrary to previous modifications of the original theory [6, 62] the overshoot in our model is based on an underlying molecular reason, albeit handled within the semi-phenomenological framework of the pom-pom model. In particular, it arises from entanglement stripping at fast flows. Although in a melt of pom-pom molecules all kinds of entanglements can be stripped off (i.e. backbone-backbone, arm-arm, and backbone-arm entanglements) we note that the current modification is supposed to deal only with backbone-backbone entanglements.

4.2 The overshoot model

4.2.1 The physical concept

Central to the modification of the original model is the assumption that at fast flows some of the (backbone-backbone) entanglements can be stripped off and not be replaced by other entanglements; so the basic assumption of the overshoot model is that, in non-linear flows, there is loss of some entanglements.

For well entangled branched systems, the proposed molecular mechanism of entanglement stripping is as follows. While a flow (of whatever type) is present two opposing mechanisms operate in parallel. The first one is chain stretch which tends to increase the chain length. The second one is chain retraction, a direct consequence of chain stretch, which tends to keep the chain length to its equilibrium value. The latter mechanism involves relative motion of the chain and the surrounding entanglement mesh. Therefore entanglements can be stripped off and might not be replaced. In this context the point where a pom-pom reaches maximum extension (i.e. when $\lambda = q$) represents a

sudden increase in the rate of chain retraction, and therefore in the degree of entanglement stripping, and so can be responsible for a sudden loss of entanglements (although all retraction processes will do this to some extent). This idea is illustrated schematically in Fig. 4.3.

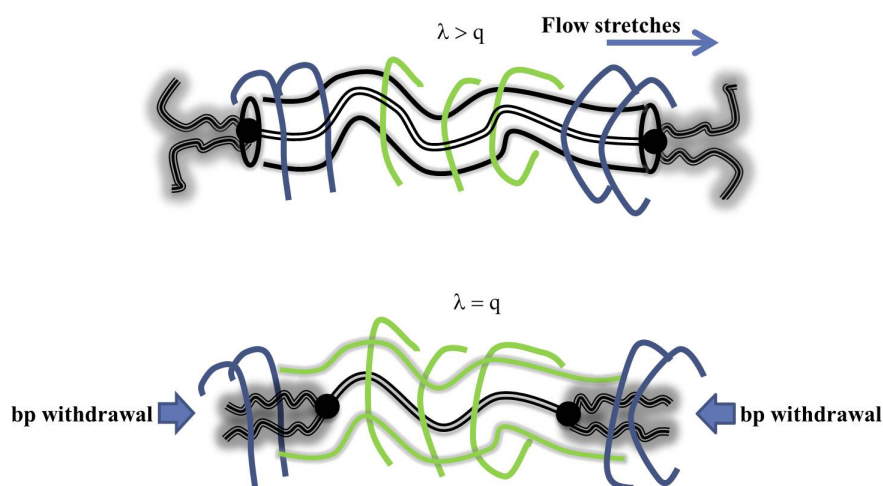


Figure 4.3: Up: A given backbone, prior to branch point withdrawal, entangles with both blue and green surrounding chains. The flow tends to stretch the backbone beyond the maximum stretch and so $\lambda > q$. Bottom: Branch point withdrawal occurs since the maximum stretch, $\lambda = q$, should be maintained. This process is instantaneous on the flow timescale and hence some entanglements (the blue ones) are stripped off. Here, the backbone only entangles with the green chains and so it is confined within a dilated tube.

From the conceptual point of view the qualitative consequences of entanglement stripping are the following: the backbone tube gradually dilates, and moreover the orientation and stretch relaxation times of the backbone (τ_b and τ_s respectively) speed up, as entanglement stripping goes on. So, in the current model, the above relaxation times are functions of the number of surviving entanglements at a given time and thus they are time dependent; these quantities are constant and given by $\tau_b = \tau_{b_0}$ and $\tau_s = \tau_{s_0}$ in the absence of entanglement stripping only.

At this point it should be clarified that the overshoot model (as was the case with the original pom-pom model) is developed with a view to describe the flow properties of randomly branched, polydisperse industrial melts but not of pom-pom melts; at a quantitative level, the rheology of monodisperse pom-pom melts can neither be described by the original model nor the overshoot model to be developed below. The evolutionary

equations for the relaxation times of orientation and stretch (eqs 4.3 below) have been derived on the basis of the aforementioned viewpoint.

4.2.2 Constitutive equation

To describe quantitatively the effect of entanglement stripping we introduce the dynamic variable $\Psi (= Z/Z_{eq})$, where Z and Z_{eq} denote, respectively, the number of entanglements acting on the backbone at time t and at time zero (i.e. at equilibrium before deformation is imposed). In other words, Ψ can be understood as the fraction of surviving entanglements at a particular time. Moreover, we introduce the parameter $\Psi_w (= Z_w/Z_{eq})$ which corresponds to the minimum fraction of surviving entanglements; Z_w is a constant denoting the minimum number of surviving entanglements. From the above, it is obvious that Ψ ranges between Ψ_w and unity. A differential equation for the time evolution of the fraction of surviving entanglements is proposed below (eq 4.9).

Here, we restrict our description to the experiments performed in the FSR rheometer, as opposed to a general deformation history. In these experiments, an initial flow of constant extension rate is applied. During the extensional flow, entanglement stripping may occur, and the tube gets wider. Following this, the flow may be stopped, and the melt relaxes. During the relaxation phase, chain retraction and entanglement stripping eventually stops, so that entanglements begin to be replaced and the tube gets thinner again. Thus, we consider one single phase of entanglement stripping, followed by one single phase of entanglement replacement (reformation). The left and right panels of Fig. 4.4 show the backbone tube at three different times during entanglement stripping ($d\Psi/dt < 0$) and entanglement reformation ($d\Psi/dt > 0$), respectively.

We first consider the dynamics of the pre-averaged backbone orientation, \mathbf{S} , and the dynamics of the pre-averaged stretch, λ , during entanglement stripping. Recall that the backbone tube is constructed by backbone-backbone entanglements only. In this sense, \mathbf{S} is the orientation tensor $\langle \mathbf{u}\mathbf{u} \rangle$ of a tube segment at the current degree of entanglement stripping. That is, if there is no entanglement stripping, \mathbf{u} is directed along the tube path (primitive path) defined by all backbone-backbone entanglements. When entanglement stripping occurs the tube becomes wider, and \mathbf{u} is directed along the tube path that is defined by the surviving backbone-backbone entanglements. We assume that

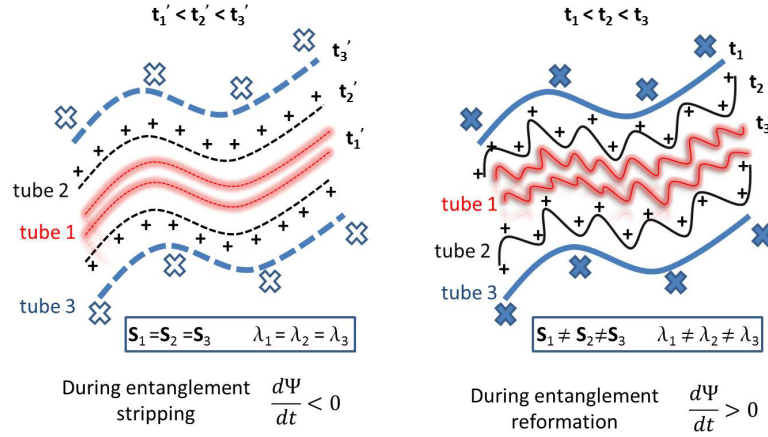


Figure 4.4: Left: The backbone tube at three different times during entanglement stripping. All tubes have undergone the same deformation history and identical fractional amount of chain retraction and thus $S_1 = S_2 = S_3$, $\lambda_1 = \lambda_2 = \lambda_3$. Right: The backbone tube at three different times during entanglement reformation. In this case “thinner” tubes equilibrate within “fatter” tubes, i.e. $S_1 \neq S_2 \neq S_3$, $\lambda_1 \neq \lambda_2 \neq \lambda_3$. The blue and black crosses represent the entanglements that form the blue and black tube, respectively.

entanglements are progressively removed. That is, the tube constraints broaden gradually from tube 1 to tube 2 to tube 3 and so on (c.f. the left panel of Fig. 4.4). In such a case, the deformation history experienced by the tube at current dilation (i.e. tube 3 at $t = t'_3$) is identical to that of the embedded tubes. Also, within the three tubes, the fractional amount of chain retraction (i.e. ratio of final to initial tube length) is identical. For these reasons we claim that all tubes have identical orientation and stretch, i.e. $S_1 = S_2 = S_3$ and $\lambda_1 = \lambda_2 = \lambda_3$. For the time evolution of the backbone orientation we consider the following differential equation:

$$\frac{d\mathbf{S}}{dt} = \mathbf{K} \cdot \mathbf{S} + \mathbf{S} \cdot \mathbf{K}^T - 2\mathbf{S}(\mathbf{K} : \mathbf{S}) - \frac{1}{\mathcal{B}\tau_b} \left(\mathbf{S} - \frac{\mathbf{I}}{3} \right), \quad (4.1)$$

where τ_b is the orientation relaxation time and $\mathcal{B} = \text{tr}\mathbf{A}, \lambda^2, 1$. In other words, eq 4.1 has three different versions which correspond to three different options for the timescale of orientation relaxation. The first version of eq 4.1 corresponds to $\mathcal{B} = \text{tr}\mathbf{A}$, i.e. in this version the orientation relaxation time is amplified by $\text{tr}\mathbf{A}$ (with \mathbf{A} given by eq 1.63). This version exactly corresponds to the original pom-pom model, as expressed in eq 1.63, but we have re-expressed the orientation dynamics in terms of \mathbf{S} rather than in terms of \mathbf{A} . In this context we note that \mathbf{S} , the orientation tensor of the tube, is the physically relevant

quantity, whilst \mathbf{A} was introduced solely as an approximate means to obtain \mathbf{S} .

The second version of eq 4.1 corresponds to $\mathcal{B} = \lambda^2$ whilst the third one corresponds to $\mathcal{B} = 1$. In the former version, the amplification of the orientation relaxation time by λ^2 implies that the chain diffuses in a stretched (backbone) tube. In the latter version, the orientation relaxation timescale is simply τ_b . It is obvious that the rate of tube reconfiguration in options A, B and C is $(\text{tr}\mathbf{A}\tau_b)^{-1}$, $(\lambda^2\tau_b)^{-1}$ and τ_b^{-1} , respectively. With regard to the time evolution of the backbone stretch we retain the differential equation of the original model, restated now:

$$\frac{d\lambda}{dt} = \lambda \mathbf{K} : \mathbf{S} - \frac{1}{\tau_s} (\lambda - 1). \quad (4.2)$$

In the current model, the relaxation times in eqs 4.1 and 4.2 are not time independent, but they are modified as follows:

$$\tau_b = \tau_{b_0} \exp(h(\Psi - 1)) \exp(-\nu(\lambda - 1)), \quad (4.3a)$$

$$\tau_s = \tau_{s_0} \exp(h(\Psi - 1)) \exp(-\nu(\lambda - 1)), \quad (4.3b)$$

where τ_{b_0} and τ_{s_0} are, respectively, the orientation and stretch relaxation time in the absence of entanglement stripping and drag-strain coupling (hereafter, referred to as the bare relaxation times). The factor $\exp(-\nu(\lambda - 1))$, where $\nu = 2/(q - 1)$, is due to the drag-strain coupling effect introduced by Blackwell et al. [102] (c.f. section 1.5.2). The other exponential term accounts for the dilution of the entanglement network due to entanglement stripping. It implies that the relaxation times speed up as entanglement stripping goes on. In this term, h is a parameter that accounts for the proportionality of the relaxation times on τ_a (the timescale for a complete arm retraction, c.f. eqs 1.62 and 1.64) and, in turn, on the arm entanglement length $Z_a = M_{w_a}/M_e$ (see eq 1.57). The factor of Ψ arises from the dilution of the entanglement network as follows:

$$\tau_b, \tau_s \propto \exp(\nu' Z_a) = \exp\left(\nu' \frac{M_{w_a}}{M_{e,0}} \Psi\right) = \exp(h\Psi) \quad (4.4)$$

where ν' is a numerical constant of order unity, and $M_{e,0}$ is the entanglement molecular weight in the limit of no entanglement loss. Since the current model only focuses on backbone structure, the use of the term arm entanglement length (or arm entanglements) can be confusing if the reader does not bear in mind that the model is developed with a view to describe the rheology of industrial resins rather than monodisperse pom-pom melts. From this perspective, the above term refers to the entanglement length

of the branching layers that are adjacent to the branch that the pom-pom backbone is supposed to represent. So, we are actually assuming that the degree of entanglement stripping is the same at a given branching layer and its adjoining branches. In practice, the degree of entanglement stripping will be similar, but not exactly the same. We make this assumption so as to avoid coupling between different pom-pom modes. To represent the physics more accurately, one might couple the relaxation time of one mode to the degree of entanglement stripping of other pom-pom modes (which would then represent the adjoining branches). This approach would involve further assumptions and approximations regarding the coupling terms, and we wish to avoid this. Finally, we note that eqs 4.3 are retained during entanglement reformation.

We now consider the dynamics of orientation and stretch during entanglement reformation. (See Fig. 4.4, right.) The arguments of identical deformation history and identical fractional amount of chain retraction, for all tubes, do not apply in this case (i.e. $\mathbf{S}_1 \neq \mathbf{S}_2 \neq \mathbf{S}_3$ and $\lambda_1 \neq \lambda_2 \neq \lambda_3$). Instead, as entanglements are reformed, the chain becomes localised by a thinner tube which locally equilibrates within a fatter (wider) tube. In this case, one should include an extra ‘‘correction’’ term in the equations that govern the time evolution of orientation and stretch, such that reformation (replacement) of entanglements does not increase the stress. These correction terms are obtained as follows. Let us consider the equilibration process of tube 1 (thin tube) within tube 2 (fat tube). According to Auhl et al. [14] for a thin tube equilibrated inside a fat tube, the orientation and stretch of the thin and fat tube are related through:

$$\lambda_1^2 \mathbf{S}_1 = \frac{1}{n} \lambda_2^2 \mathbf{S}_2 + \frac{1}{3} \left(1 - \frac{1}{n} \right) \mathbf{I}, \quad (4.5)$$

where \mathbf{I} is the unit tensor and n is the number of thin tube segments within each fat tube segment. Here, n can be approximated by the ratio of the entanglement stripping factors for the two tubes, i.e. by Ψ_1/Ψ_2 , and so the previous equation is re-expressed as

$$\lambda_1^2 \mathbf{S}_1 = \frac{\Psi_2}{\Psi_1} \lambda_2^2 \mathbf{S}_2 + \frac{1}{3} \left(1 - \frac{\Psi_2}{\Psi_1} \right) \mathbf{I}. \quad (4.6)$$

By taking the two tube diameters almost identical, assuming only a small change in Ψ , and noting that the trace of \mathbf{S} remains constant, it can be shown that the effective changes

in \mathbf{S} and λ due to a small change in Ψ arising from equation 4.6 are:

$$\left(\frac{d\mathbf{S}}{dt}\right)_+ = \left(\frac{\Psi\mathbf{I} - 3\Psi\mathbf{S}}{3\lambda^2\Psi^2}\right) \frac{d\Psi}{dt}. \quad (4.7a)$$

$$\left(\frac{d\lambda}{dt}\right)_+ = \left(\frac{1 - \lambda^2}{2\lambda\Psi}\right) \frac{d\Psi}{dt}. \quad (4.7b)$$

When $d\Psi/dt > 0$, eqs 4.7a and 4.7b should be added to the RHS of eqs 4.1 and 4.2, respectively.

Having discussed the dynamics of orientation and stretch, and the dynamics of their relaxation times, we now move on to derive an expression for the time evolution of entanglement stripping. This expression will not depend on whether we consider entanglement stripping or entanglement reformation. The number of entanglements, Z , at a given time is determined by two opposing factors: that is, on the one hand chain retraction causes entanglement stripping either before or after the maximum stretch (first term of eq 4.8), on the other hand, melt re-equilibration tends to keep the number of entanglements to its equilibrium value Z_{eq} (second term of eq 4.8). We assume melt re-equilibration occurs on the timescale of orientation relaxation. Thus, we express the time evolution of Z as follows:

$$\frac{dZ}{dt} = w(Z - Z_w) - \frac{1}{\mathcal{B}\tau_b}(Z - Z_{eq}), \quad (4.8)$$

where $\mathcal{B} = \text{tr}\mathbf{A}, \lambda^2, 1$ as in eq 4.1, and w is the retraction rate defined as the difference between the actual rate of stretching and the rate of stretching due to flow alone (c.f eq 4.10 below); in other words, the retraction rate is the difference between the chain stretch and the backbone tube stretch rates. Typically, the retraction rate is negative and so the first term on the RHS of eq 4.8 indicates loss of entanglements. On the other hand, the re-equilibration term of the above equation, i.e. the second term on the RHS of eq 4.8, is always negative (apart from equilibrium where $Z = Z_{eq}$) and hence it contributes to increases in the number of entanglements. Using the definitions $\Psi = Z/Z_{eq}$ and $\Psi_w = Z_w/Z_{eq}$, eq 4.8 is re-expressed as:

$$\frac{d\Psi}{dt} = w(\Psi - \Psi_w) - \frac{1}{\mathcal{B}\tau_b}(\Psi - 1), \quad (4.9)$$

where the minimum fraction of surviving entanglements, Ψ_w , determines the degree of entanglement stripping; by setting $\Psi_w = 0.2$, for example, one allows for up to 80% of entanglement loss. The explicit formula for the retraction rate is the following:

$$w = \frac{1}{\lambda} \left(\frac{d\lambda}{dt} - \lambda(\mathbf{K} : \mathbf{S}) \right). \quad (4.10)$$

By substituting eq 4.2 into the previous equation, one arrives at

$$w = \begin{cases} -\frac{1}{\tau_s} \frac{(\lambda-1)}{\lambda} & \text{for } \lambda < q, \\ -\mathbf{K} : \mathbf{S} & \text{for } \lambda \geq q \end{cases} \quad (4.11)$$

where τ_s is given by eq 4.3b. In what follows, the term that corresponds to the retraction rate prior to the maximum stretch ($\lambda < q$) is referred to as the normal chain retraction term. The $w = -\mathbf{K} : \mathbf{S}$ term is referred to as the branch point withdrawal retraction term.

Finally, the equation for the stress reads

$$\boldsymbol{\sigma} = 3G_0 \Psi \lambda^2 \mathbf{S}, \quad (4.12)$$

instead of $\boldsymbol{\sigma} = 3G_0 \lambda^2 \mathbf{S}$ (for a single mode) of the mPP model of Inkson et al. [9]. The extra factor of Ψ , in eq 4.12, accounts for the effective dilution of the entanglement network due to entanglement stripping. For completeness, we note that, in eqs 4.1 and 4.2, the flow terms (that is, the terms $\mathbf{K} : \mathbf{S}$ and $\mathbf{K} \cdot \mathbf{S} + \mathbf{S} \cdot \mathbf{K}^T$) are switched off during the relaxation stage. In other words, upon cessation of the flow, they are set equal to zero. The same applies to the branch point withdrawal retraction term, $w = -\mathbf{K} : \mathbf{S}$.

In summary, each mode is characterised by six parameters. The ones that already appear in Refs. [6, 9], namely, G_0 , τ_{b_0} , q , τ_{s_0} and two additional ones, namely, Ψ_w and h which denote the minimum fraction of surviving (backbone-backbone) entanglements and the number of arm entanglements before the onset of entanglement stripping, respectively. In contrast to Refs. [6, 9], there are three evolutionary equations per mode: one for the average backbone orientation, \mathbf{S} , a second one for the backbone stretch, λ , and a third one for the fraction of surviving entanglements, Ψ . Recall that we will consider (for now) three different options for the rate of backbone tube reconfiguration and hence we will consider all three versions of eqs 4.1 and 4.9 (the evolutionary equations for \mathbf{S} and Ψ , respectively). Therefore, we will essentially consider (for the moment) three different constitutive equations. All of them are presented in table 4.1. In what follows, the constitutive equations in which $\mathcal{B} = \text{tr}\mathbf{A}, \lambda^2, 1$ are referred to as options A, B and C, respectively.

Table 4.1: Overshoot model equation set.

<i>Backbone orientation and entanglement stripping- Option A</i>	
$\frac{d\mathbf{S}}{dt} = \mathbf{K} \cdot \mathbf{S} + \mathbf{S} \cdot \mathbf{K}^T - \frac{3}{\text{tr}\mathbf{A}\tau_b} \left(\mathbf{S} - \frac{\mathbf{I}}{3} \right) - 2\mathbf{S}(\mathbf{K} : \mathbf{S})$	
$\frac{d\Psi}{dt} = w(\Psi - \Psi_w) - \frac{1}{\text{tr}\mathbf{A}\tau_b} (\Psi - 1)$	
<i>Backbone orientation and entanglement stripping - Option B</i>	
$\frac{d\mathbf{S}}{dt} = \mathbf{K} \cdot \mathbf{S} + \mathbf{S} \cdot \mathbf{K}^T - \frac{1}{\lambda^2\tau_b} \left(\mathbf{S} - \frac{\mathbf{I}}{3} \right) - 2\mathbf{S}(\mathbf{K} : \mathbf{S})$	
$\frac{d\Psi}{dt} = w(\Psi - \Psi_w) - \frac{1}{\lambda^2\tau_b} (\Psi - 1)$	
<i>Backbone orientation and entanglement stripping - Option C</i>	
$\frac{d\mathbf{S}}{dt} = \mathbf{K} \cdot \mathbf{S} + \mathbf{S} \cdot \mathbf{K}^T - \frac{1}{\tau_b} \left(\mathbf{S} - \frac{\mathbf{I}}{3} \right) - 2\mathbf{S}(\mathbf{K} : \mathbf{S})$	
$\frac{d\Psi}{dt} = w(\Psi - \Psi_w) - \frac{1}{\tau_b} (\Psi - 1)$	
<i>Backbone stretch - options A, B, C</i>	
$\frac{d\lambda}{dt} = \begin{cases} \lambda\mathbf{K} : \mathbf{S} - \frac{1}{\tau_s}(\lambda - 1) & \text{for } \lambda < q, \\ 0 & \text{when } \lambda = q. \end{cases}$	
<i>Stress</i>	
$\boldsymbol{\sigma} = 3G_0\Psi\lambda^2\mathbf{S}$	
* τ_b and τ_s are given by eqs 4.3, w by eq 4.11, and \mathbf{A} by eq 1.63	
*upon flow cessation $\mathbf{K} : \mathbf{S} = 0$, $\mathbf{K} \cdot \mathbf{S} + \mathbf{S} \cdot \mathbf{K}^T = 0$, $d\lambda/dt = \frac{-(\lambda - 1)}{\tau_s}$ for $\lambda \geq q$	
*when $d\Psi/dt > 0$ eqs 4.7a and 4.7b are added, respectively, to eqs 4.1 and 4.2.	

4.3 Predictions of the model: single mode

4.3.1 The *relaxation case*: testing the three versions of the evolutionary equation of the backbone orientation

In table 4.1 we presented three different constitutive equations for the overshoot model, the so-called options A, B and C. In the absence of entanglement stripping, option A corresponds to the original pom-pom model. Here, we demonstrate that this option is the most deficient constitutive equation (among the three) for fitting the relaxation data of Fig. 4.2. To do so, we examine how the stress response of a single mode changes with respect to the three different versions of eq 4.1 which is the evolutionary equation for the orientation, \mathbf{S} .

In this section, entanglement stripping is omitted (that is, the fraction of surviving entanglements, Ψ , is in all three options unity). It is omitted as this section aims to highlight the effects of the three different versions of eq 4.1 on the stress response, not to examine the consequences of entanglement stripping. Since entanglement stripping is ignored, the (uniaxial) extensional viscosity only depends on the stretch, λ , and the (tube) orientation alignment, $S_{xx} - S_{yy}$ (which “measures” the alignment of the backbone tube relative to the flow direction, x).

The single mode under consideration is parameterized as follows: $G_0 = 72.88\text{Pa}$, $\tau_{b_0}/\tau_{s_0} = 2$, $q = 12$, $\Psi_w = 1$ and $h = 0$, where the values of the linear parameters, G_0 and τ_{b_0} , correspond to the slowest mode (15th) of the pom-pom spectrums of tables 4.2 and 4.3 below. The choice $\Psi_w = 1$ ensures that entanglement stripping is switched off in the model. Figure 4.5 shows the extensional viscosity as a function of time for all three options, i.e. for all three constitutive equations of table 4.1 (with $\Psi = 1$ in all options). Figure 4.6 shows the corresponding orientation alignment (left panel) and stretch (right panel). In these two figures the black, red and blue symbols refer, respectively, to options A, B and C. The strain rate is $\dot{\epsilon} = 0.1\text{s}^{-1}$. The stress relaxation phase starts at $t = t_{cf} \simeq 45\text{s}$ when the flow is stopped.

According to Fig. 4.5, the viscosity, for times up to t_{cf} , is unchanged irrespective of the chosen option. Then, it decays faster in option C than in the other two options. The

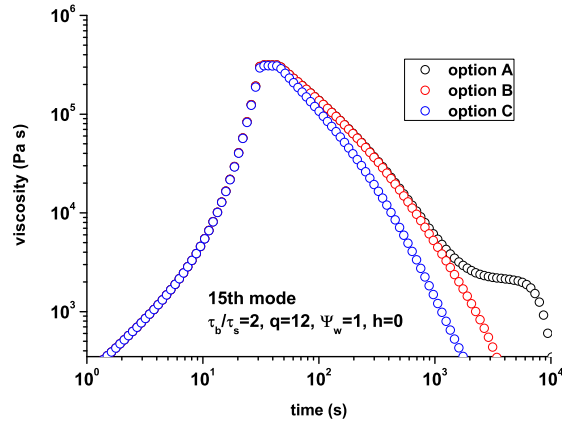


Figure 4.5: Uniaxial extensional viscosity vs time for the *relaxation case* (RC). The black, red and blue symbols refer to options A, B and C, respectively. The strain rate is $\dot{\epsilon} = 0.1\text{s}^{-1}$. The flow is ceased at $t = t_{cf} \simeq 45\text{s}$. $G_0 = 72.88\text{Pa}$, $\tau_{b0}/\tau_{s0} = 2$, $q = 12$, $\Psi_w = 1$ and $h = 0$. For all three options entanglement stripping is quenched since $\Psi_w = 1$.

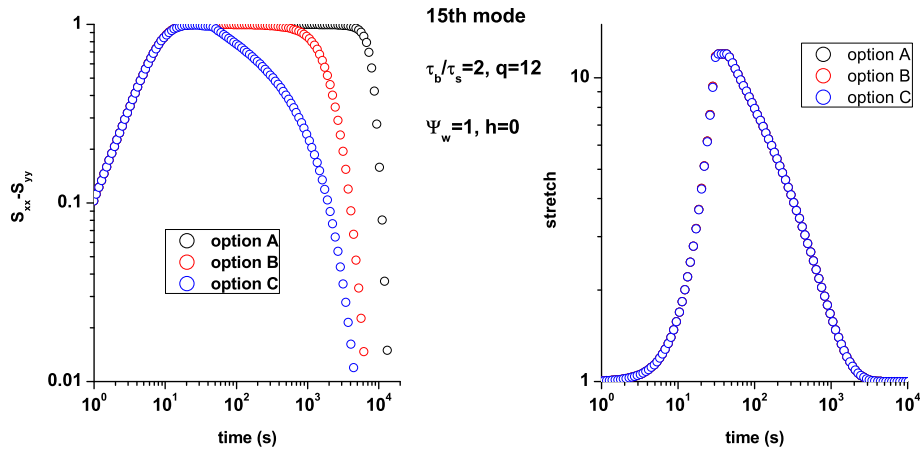


Figure 4.6: The corresponding orientation alignment, $S_{xx} - S_{yy}$ (left), and stretch, λ (right), of the viscosity curves of Fig. 4.5. The flow is ceased at $t = t_{cf} \simeq 45\text{s}$. The correspondence between colours and options is the same as in Fig. 4.5.

first two constitutive equations of table 4.1 give similar results up to $t \simeq 10^3\text{s}$ and then the viscosity, in option A, exhibits a plateau-like region until its final decay which occurs at $t \simeq 10^4\text{s}$. According to the right panel of Fig. 4.6, the stretch is the same for all three options and therefore the above features should solely depend on the orientation alignment, $S_{xx} - S_{yy}$. Indeed, the latter quantity shares the same qualitative features with the viscosity, as is readily seen from the left panel of Fig. 4.6.

Clearly, the amplification of the orientation relaxation time, τ_b , by $\text{tr}\mathbf{A}$, a quantity which is unbounded for high extension rates, renders the original pom-pom constitutive equation (that is, option A of table 4.1 with $\Psi = 1$) incapable of capturing the relaxation behaviour of the industrial melt: figure 4.5 shows that this option is very poorly behaved in relaxation after extensional flow; characteristically, the S_{xx} element of the orientation tensor, and in turn the alignment of the backbone tube relative to the flow direction, starts to decrease almost two decades after the cessation of the flow (due to the unnaturally large $\mathcal{B} = \text{tr}\mathbf{A}$ term in eq 4.1). In this context, we note that the quantity $\text{tr}\mathbf{A}$ carries *no physical meaning*. The quantity \mathbf{A} was originally introduced, within the differential version of the pom-pom model, as an approximate means to obtain the tube orientation \mathbf{S} . So, it is unreasonable that the quantity $\text{tr}\mathbf{A}$ should produce such a strong effect on the constitutive response. For this reason, option A must be rejected.

On the other hand, option B, in which τ_b is effectively increased by λ^2 , appears to be more appealing in terms of the underlying physics as the chain may diffuse (reptate) over a stretched tube. In this option and upon cessation of the flow, the tube orientation alignment, $S_{xx} - S_{yy}$, falls between the respective alignment of options A and C. For this reason, in the following section, we will compare options B and C more thoroughly for both the *normal case* and the *relaxation case*.

4.3.2 Normal case and relaxation case: comparing options B and C

To compare options B and C more carefully, we study the same mode (in terms of the parameters G_0 , τ_{b_0} and q) as the one studied in section 4.3.1 above. However, in this comparison we allow entanglement stripping. In particular, we set $\Psi_w = 0.5$. Moreover, we use slightly different values for h and τ_{b_0}/τ_{s_0} ; we set $h = 1$ and $\tau_{b_0}/\tau_{s_0} = 1.5$.

Figure 4.7 shows the extensional viscosity as a function of time for both the *normal case* (left panel) and the *relaxation case* (right panel). For the *normal case*, the corresponding fraction of surviving entanglements, Ψ , and orientation alignment, $S_{xx} - S_{yy}$, are, respectively, shown at panels **a** and **b** of Fig. 4.8. The respective quantities for the *relaxation case* are shown in panels **c** and **d** of Fig. 4.8. In these two figures the red curves correspond to option B while the blue curves refer to option C, as in Figs. 4.5 and 4.6. In panels referring to the *relaxation case*, the open circles correspond to cessation

of the flow at $t \simeq 45\text{s}$ (i.e. correspond to the **AO** case) whilst the lines correspond to cessation of the flow at $t \simeq 30\text{s}$ (i.e. correspond to the **BO** case).

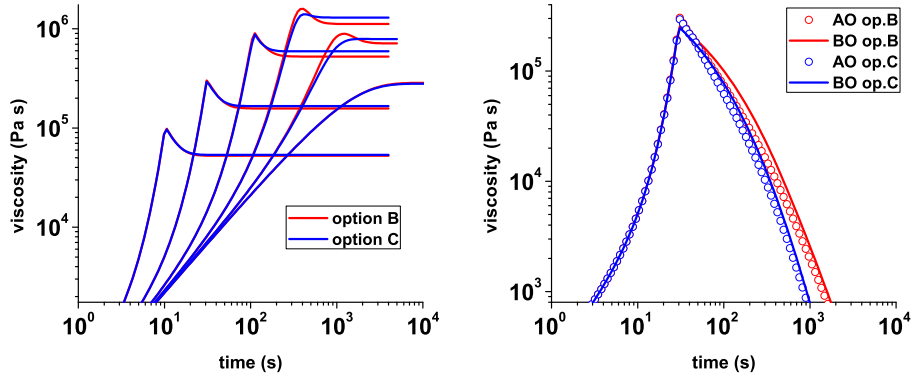


Figure 4.7: Uniaxial extensional viscosity vs time for options B and C (red and blue colours, respectively). Left: the *normal case*. Right: the *relaxation case*. In the right panel, open symbols refer to the **AO** case while lines refer to the **BO** case. The mode is parameterised by $G_0 = 72.88\text{Pa}$, $\tau_{b_0}/\tau_{s_0} = 1.5$, $q = 12$, $\Psi_w = 0.5$, $h = 1$.

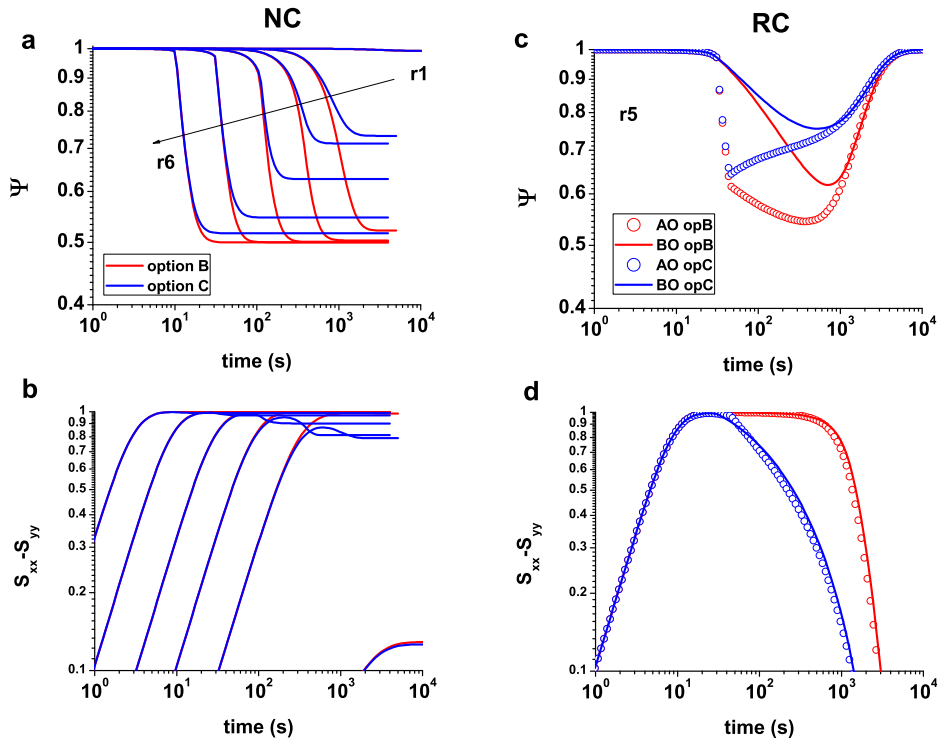


Figure 4.8: The corresponding Ψ , τ_s , $S_{xx} - S_{yy}$ and λ of the viscosity curves of the right panel of Fig. 4.7 (i.e. for the *relaxation case*).

From the left panel of Fig. 4.7, which refers to the *normal case*, we notice that option B gives in general larger overshoots and thus lower steady states than option C.

Nevertheless, at the two highest rates (r_5 and r_6) the difference between the two options is almost negligible for this particular parameter set. The tendency of option B for larger overshoots arises from the higher entanglement stripping that is achieved in this option (c.f. panel **a** of Fig. 4.8), as in the re-equilibration term of eq 4.9 (second term on the RHS) the orientation relaxation time is amplified by λ^2 . Apart from the degree of entanglement stripping, another difference between the two options is the overshoots in the orientation alignment. As seen from panel **b** of Fig. 4.8, such overshoots are only observed in option C. They compensate for the lower entanglement stripping in this option, so that both options produce similar stress (viscosity) for this particular parameter set.

From the right panel of Fig. 4.7, which is concerned with the *relaxation case*, we note the following: although option B produces higher entanglement stripping than option C (c.f. panel **c** of Fig. 4.8), the viscosity, in both cases (**BO** and **AO**), decays moderately faster in option C than in option B. This is because the orientation alignment relaxes more rapidly in option C than in the other option (see panel **d** of Fig. 4.8). The viscosity always decays more rapidly in option C than in option B, unless the mode is parameterised by a combination of very low values of Ψ_w and of (relatively) high values of h (below 0.2 and above 2, respectively). Then, the higher entanglement stripping in the constitutive equation B compensates for the faster orientation relaxation in the constitutive equation C so that the viscosity relaxes slightly faster in option B.

In short, for moderate values of Ψ_w and relative low values of h the differences between the two options are not significant. However, for the *normal case* and for lower values of Ψ_w or higher values of h the differences will be stronger; that is, option B will give much larger overshoots than option C. For the *relaxation case*, option C in general produces slightly faster stress relaxation than option B. We note that, in the comparison with the FSR data, combinations of values of Ψ_w and h that produce the reverse behaviour are not considered, as they lead to a very poor agreement between the predictions of the multimode overshoot model and the FSR measurements (in the *normal case*).

The concluding remark of this section is as follows. Compared to option C, option B, the constitutive equation in which the orientation relaxation time is amplified by the square of the stretch, seems more appropriate (from the conceptual point of view) for modelling the flow properties of monodisperse pom-pom melts (since the backbone would have to diffuse over a stretched tube). Nevertheless, the overshoot model is developed

with a view to describe the rheology of melts of industrial complexity only. From the perspective of fitting real relaxation data, option C, the constitutive equation in which the orientation relaxation time is simply τ_b , is superior to option B since it relaxes slightly faster after extensional flow. In particular, multimode versions of both constitutive equations B and C can provide a reasonable fit to the *normal case* FSR data, however the use of the latter constitutive equation (option C) also facilitates the comparison with the FSR relaxation data. Besides the purely practical reason, i.e. the facilitation of the data fitting, there is also a physical reason indicating that the use of option C might be permitted: in long chain branched polymers, conformational relaxation occurs hierarchically by thermally activated contour length fluctuations and not by reptation. Thus, the branching layer of the architecturally complex polymer that the pom-pom backbone is supposed to represent does not have to diffuse over a stretched tube (it is a diffusion argument based on the reptation process which gives rise to the factor λ^2 in option B). For these reasons, in what follows, option C will be adopted.

4.3.3 Option C: varying the values of the model parameters

Before we attempt to fit the experimental data of Fig. 4.2, using a multimode version of the overshoot model, we investigate how a single mode behaves with respect to variations in the values of the (non-linear) model parameters. Specifically, we consider the effects of changing the value of τ_{b_0}/τ_{s_0} , q , Ψ_w and h in this model. Recall that τ_{b_0}/τ_{s_0} is the ratio of the bare orientation and stretch relaxation times, q is the priority number (i.e. the number of arms emerging from each branch point), Ψ_w is the minimum fraction of surviving entanglements, and h is (approximately) the number of arm entanglements before the onset of entanglement stripping (see eq 4.4 and discussion below it). Notice that, in the absence of entanglement loss and drag-strain coupling, the parameter τ_{b_0}/τ_{s_0} is proportional to the number of backbone entanglements.

Here, we chose two reference modes, a fast one and a slow one, which will (in practice) correspond to typical fast and slow modes from the Maxwell spectrum for the experimental data. For the slow mode, G_0 is about a decade smaller while τ_{b_0} is approximately a decade longer (compared to G_0 and τ_{b_0} of the fast mode). Moreover, for the reference slow (fast) mode we select $\tau_{b_0}/\tau_{s_0} = 1.5(1.5)$, $q = 12(8)$, $\Psi_w = 0.5(0.5)$

and $h = 1(1)$. In Fig. 4.9 we examine how the uniaxial extensional viscosity changes with τ_{b_0}/τ_{s_0} . Figures 4.10, 4.11 and 4.12 refer to variations in q , Ψ_w and h , respectively. In all plots of Figs. 4.9-4.12, black curves correspond to the reference modes and are obtained using the aforementioned values. The red (blue) curves refer to a decrease (an increase) in the value of the respective parameter of the reference mode. Moreover, panels **a** and **c** correspond, respectively, to the slow and fast mode in the *normal case* (NC); panels **b** and **d** refer, respectively, to the slow and fast mode in the *relaxation case* (RC).

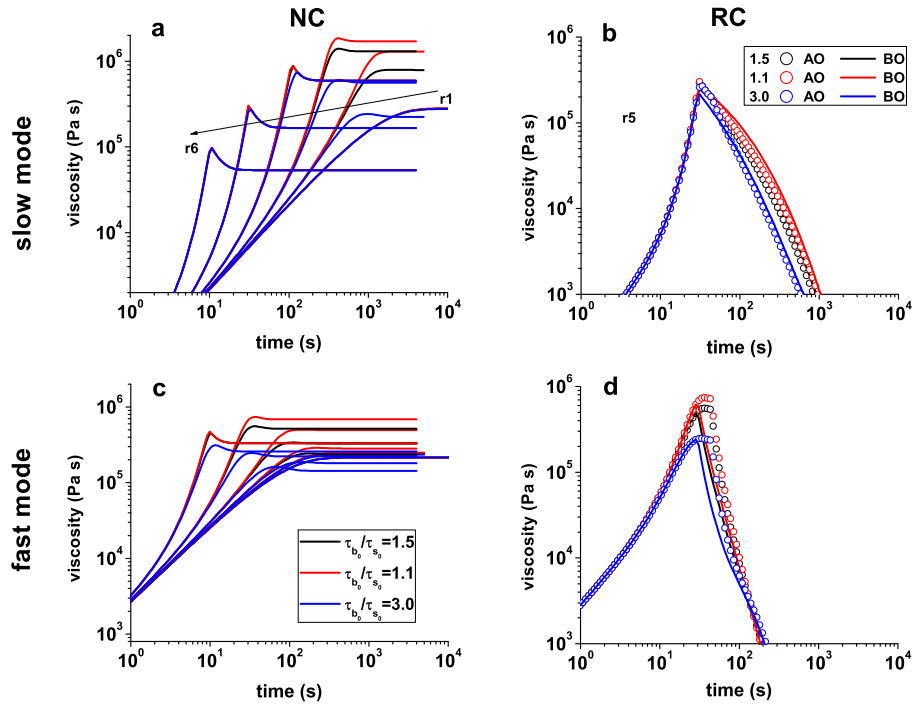


Figure 4.9: Transient uniaxial extensional viscosity vs time of the reference modes with varying τ_{b_0}/τ_{s_0} (see labels). Panels **a** and **c**: *normal case* (NC) for the slow mode and the fast mode, respectively. Panels **b** and **d**: *relaxation case* (RC) for the slow mode and the fast mode, respectively. For the parameterisation of the reference modes see the text.

To begin the discussion of Figs. 4.9-4.12, we note that, for the *normal case*, the maximum stretch condition is always reached at the three highest rates (r_4 , r_5 and r_6) for the slow mode, and at the highest rate for the fast mode; this is not the case, however, for the blue line in panel **c** of Fig. 4.9. In all other occasions maximum stretch is not achieved.

According to panels **a** and **c** of Fig. 4.9, the ratio of the bare orientation and stretch relaxation times, τ_{b_0}/τ_{s_0} , in general controls the hardening at those extension rates where

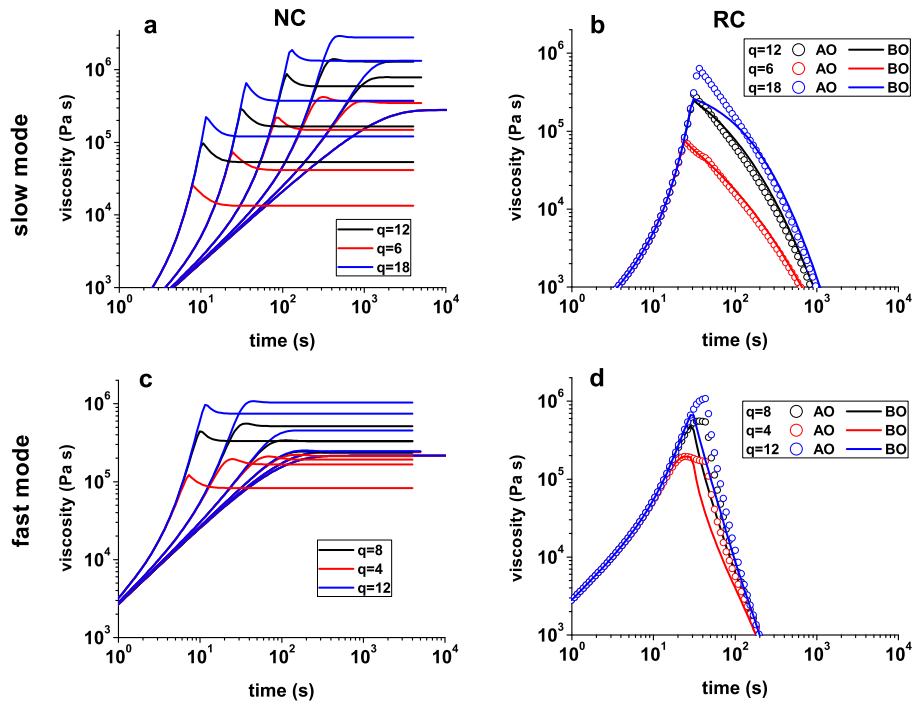


Figure 4.10: Same as Fig. 4.9 with varying q (see labels).

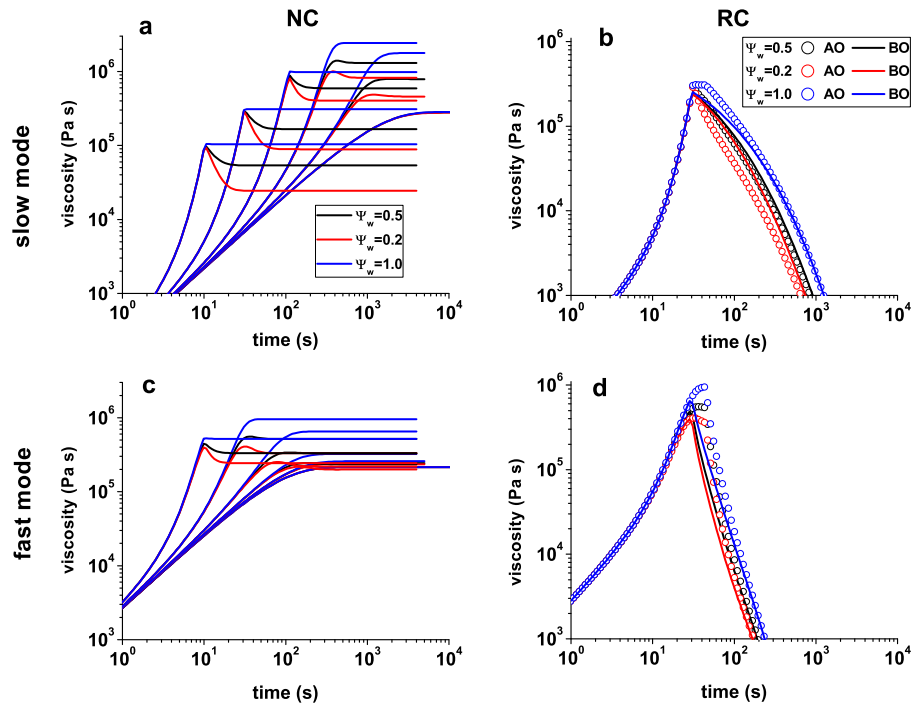


Figure 4.11: Same as Figs. 4.9 and 4.10 with varying Ψ_w (see labels).

the maximum stretch condition is not reached (of course this does not apply to the lowest rates for the fast mode at which no significant stretching occurs). In particular, increases in τ_{b_0}/τ_{s_0} lead to lower hardening since increases in this parameter correspond to a decrease in stretch relaxation time; in other words, with increasing τ_{b_0}/τ_{s_0} , the relaxation term in

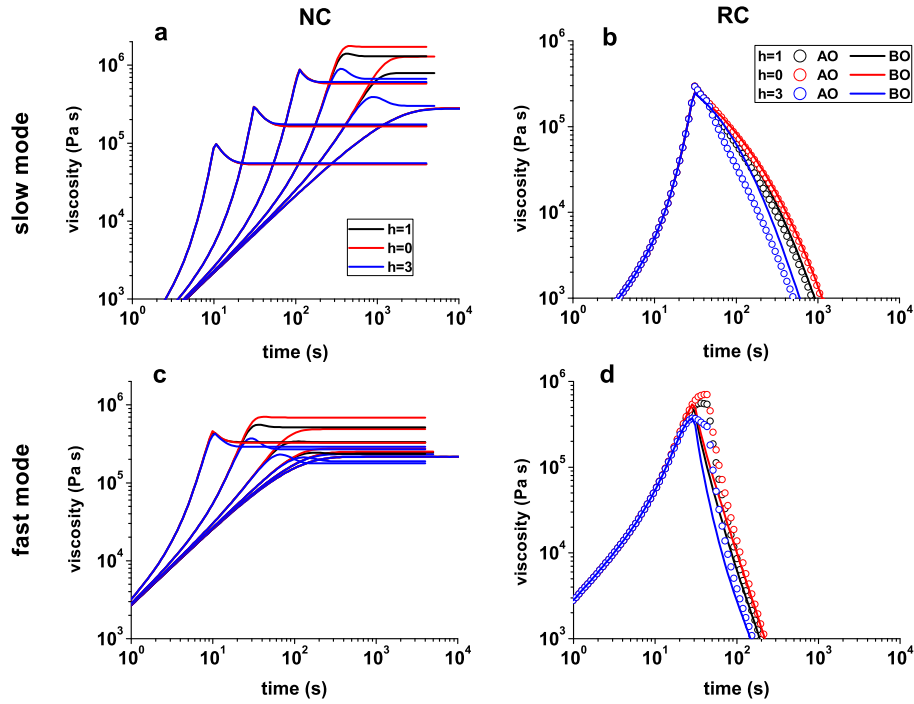


Figure 4.12: Same as Figs. 4.9- 4.11 with varying h (see labels).

eq 4.2 (second term on the RHS) becomes bigger restricting the build up of stretch. On the contrary, decreases in the τ_{b_0}/τ_{s_0} ratio give rise to a higher degree of strain hardening. At rates at which maximum extensibility is achieved, the viscosity is practically unaffected by the value of the ratio; here, the flow term, i.e. the first term on the RHS of eq 4.2, dominates the relaxation term and so variations in the bare stretch relaxation time, τ_{s_0} , are irrelevant.

We now turn the discussion to the *relaxation case*. From panels **b** and **d** of Fig. 4.9, it is apparent that, with increasing τ_{b_0}/τ_{s_0} and upon cessation of the flow, the viscosity decays faster in both the **BO** and **AO** case. This behaviour is attributed to both the decrease of stretch relaxation time and the higher entanglement stripping. Moreover, we notice that, during the relaxation phase of the fast mode, symbols (**AO** case) lie on the right side of lines (**BO** case) of the same colour. In contrast, in panel **b**, which refers to the slow mode, the order is the reverse. The same trends are seen in the respective panels of Figs. 4.10-4.12, and they will be discussed separately at the end of this section. Finally, due to the much lower value of bare stretch relaxation time, τ_{s_0} , stress relaxation occurs more rapidly in the fast mode than in the slow mode; that is, all curves of panel **d**, upon cessation of the flow, are shifted to the left compared to the respective curves of panel **b**. This behaviour is also seen in panels **b** and **d** of Figs. 4.10-4.12.

We now consider variations in the priority variable, q , shown in Fig. 4.10. From panels **a** and **c** of this figure, which refer to the *normal case*, it is evident that, for both modes and for all extension rates at which significant stretching occurs, increases in q lead to an increase in extensional viscosity; that is, increases in this parameter correspond to a higher level of hardening, in line with the original pom-pom theory [8]. Furthermore, one observes that changes in the priority number do not affect the stress response in a qualitative level. This also applies to the *relaxation case*.

Figure 4.11 shows the stress response of the two modes on variations in the minimum fraction of surviving entanglements, Ψ_w . Notice that decreases (increases) in this parameter correspond to higher (lower) entanglement stripping. We embark on the discussion with the *normal case* (panels **a** and **c**), and first consider occasions at which the maximum stretch condition is reached. Here, the dominant contribution to the viscosity overshoot comes from entanglement stripping (i.e. the decrease in the fraction of surviving entanglements, Ψ), yet there is a small contribution from an overshoot in the orientation alignment, $S_{xx} - S_{yy}$. Therefore, by adjusting Ψ_w , one can readily control the magnitude of the overshoot and, in turn, the viscosity steady state; decreases in Ψ_w lead to larger overshoots and hence to lower steady states. When the maximum stretch condition is not fulfilled, higher entanglement stripping (with decreasing Ψ_w) contributes to larger overshoots in two ways: first, through the decrease of Ψ , and second through the corresponding decrease in the stretch relaxation time which typically leads to an overshoot in stretch. Finally, from panels **a** and **c**, it is obvious that, for $\Psi_w = 1$, the predictions of the current model are qualitatively similar to the predictions of the original model; that is, the viscosity (after its maximum) displays a distinct plateau as entanglement stripping is switched off.

Concerning the relaxation behaviour of the slow mode (panel **b**), in particular the **AO** case, we observe the following two features: first, in the time interval between viscosity (stretch) maximum and cessation of the flow (i.e. in the interval $31s \lesssim t \lesssim 45s$) the viscosity decays faster with decreasing Ψ_w since the level of entanglement stripping increases. For $\Psi_w = 1$, entanglement stripping is switched off and so the viscosity remains constant in the aforementioned interval. Second, upon cessation of the flow, the viscosity continues to drop faster with decreasing Ψ_w . This is because lower values of Ψ_w and, in turn, lower values of Ψ lead to faster stretch and orientation relaxation times

and thus they lead to a more rapid relaxation behaviour. The latter feature is also seen in the **BO** case.

Figure 4.12 deals with variations in the number of arm entanglements, h . For the *normal case* we note the following: first, when maximum stretch is achieved, the value of the parameter h has in practice a negligible effect on the viscosity. Second, when the maximum stretch condition is not fulfilled, the response to increases in h is similar to the response to increases in τ_{b_0}/τ_{s_0} or/and similar to the response to decreases in Ψ_w ; specifically, higher values of h speed up the stretch relaxation time, causing in turn lower stretch and hence less strain hardening.

We now turn the discussion to the *relaxation case* starting from the slow mode (c.f. panel **b** of Fig. 4.12). With regard to the **AO** case, in the time window between viscosity maximum and flow cessation, the relaxation behaviour is independent of h ; this is due to the fact that the minimum fraction of surviving entanglements, Ψ_w , is fixed and so entanglement stripping is of similar strength for all considered values of h . Upon cessation of the flow and for both cases (**AO** and **BO**), the viscosity decays faster with increasing h since the orientation and stretch relaxation speeds up. The same comment applies to the relaxation behaviour of the fast mode.

Comparison of the relaxation before and after the overshoot

According to all **b** panels of Figs. 4.9-4.12, the overshoot model predicts that, during the relaxation phase of the slow mode, the viscosity curves which correspond to cessation of flow after the overshoot (open circles/**AO** case) drop below the respective curves that correspond to cessation of flow before the overshoot (solid lines/**BO** case). This behaviour is qualitatively consistent with the experimental results of the right panel of Fig. 4.2. It is not seen at all in the case of the fast mode. The only exception for the slow mode is seen at Fig. 4.11, for $\Psi_w = 1$, where the blue open circles do not cross the blue line during the relaxation stage; this demonstrates that the original pom-pom model is unable to reproduce the faster stress relaxation behaviour seen at the experimental data when the flow is ceased after the overshoot.

We now demonstrate, with the help of Fig. 4.13 below, that entanglement stripping due to branch point withdrawal causes the aforementioned behaviour of the model. Panels **a**,

b, **c** and **d** in Fig. 4.13 present, respectively, the fraction of surviving entanglements, Ψ , the stretch relaxation time, τ_s , the tube orientation alignment, $S_{xx} - S_{yy}$, and the stretch, λ , against time, for both the slow mode (green colour) and the fast mode (red colour). They are obtained by using $\Psi_w = 0.2$ (i.e. by using the same parameterisation as the one used for obtaining the red curves of Fig. 4.11). Open symbols refer to the **AO** case whilst lines refer to the **BO** case.

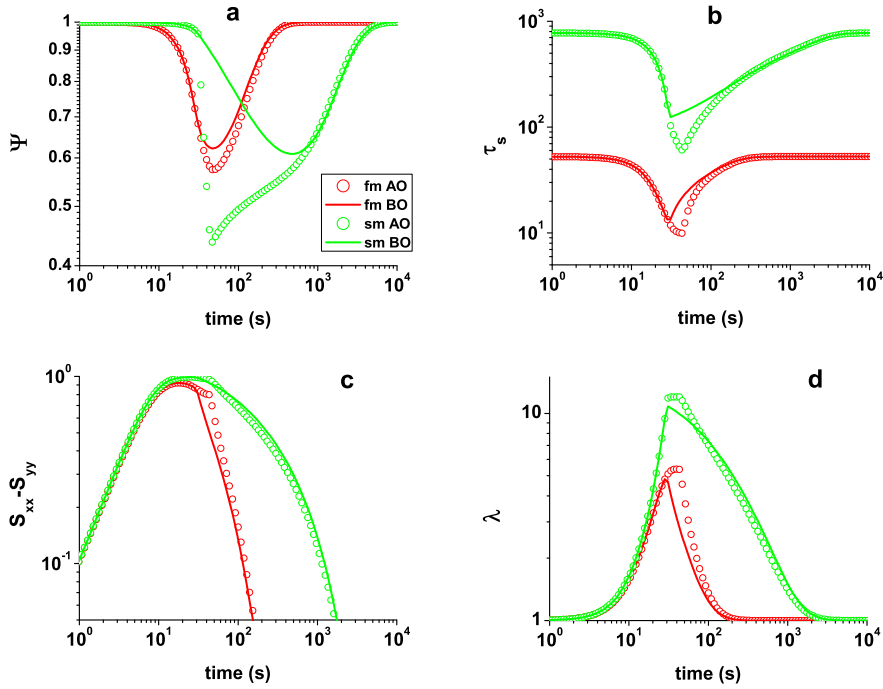


Figure 4.13: Relaxation behaviour of the fast and slow modes. Panels **a**, **b**, **c** and **d** depict Ψ , τ_s , $S_{xx} - S_{yy}$ and λ , respectively. The results for the fast (slow) mode are shown with green (red) colour and are obtained using $\tau_{b_0}/\tau_{s_0} = 1.5(1.5)$, $q = 12(8)$, $\Psi_w = 0.2(0.2)$ and $h = 1(1)$. Symbols correspond to the **AO** case while lines to the **BO** case.

Focussing specifically on the green symbols and curves in Fig. 4.13, which correspond to the slow mode, we note the following. Panel **d** demonstrates that maximum extensibility in stretch is achieved only in the **AO** case, in the time interval $31\text{s} \lesssim t \lesssim 45\text{s}$ (after which the flow is stopped). During this time interval, a large amount of entanglement stripping occurs (panel **a**), so that Ψ is greatly reduced both in its overall value, and in comparison to the before overshoot (**BO**) case. The result is a significant drop in the stretch relaxation time (panel **b**) and a corresponding drop in the orientation relaxation time. The reduction in these relaxation times is much stronger when flow is ceased after the overshoot (**AO** case) as compared to when the flow is ceased before the

overshoot. Consequently, both the orientation (panel **c**) and the stretch (panel **d**) relax faster in the **AO** case compared to the **BO** case, to the extent that in both cases the lines and symbols cross. Because both orientation and stretch exhibit this crossing, the stress relaxation response also exhibits the crossing behaviour.

The fast mode (red lines and symbols) shows similar trends but, since it does not reach its maximum extensibility, the effects are not so strong, and no crossing of the **AO** and **BO** relaxation curves ensues.

4.3.4 A rough guide for fitting data with the overshoot model

Here, we briefly discuss the effects of the different parameters (τ_{b_0}/τ_{s_0} , q , Ψ_w , h) from the perspective of fitting (uniaxial) extensional viscosity data from an industrial melt. To fit such data one needs a spectrum of modes (c.f. section 4.4 below). Therefore, one should bear in mind that at a given rate, $\dot{\epsilon}$, several modes may contribute. Thus, the matching of the viscosity data (at a given rate) could possibly require adjustments to the parameters of more than one mode. In this context, we notice that it is useful to identify the rates at which each mode contributes; this can be achieved by comparing $\dot{\epsilon}$ against the reciprocal stretch relaxation times $1/\tau_{s_0 i}$. With respect to the effects of the different parameters on the response of a single mode we note the following:

- I. At rates $\dot{\epsilon} \gtrsim 1/\tau_{s_0}$, the most efficient way to control hardening, during start up of the flow, is by adjusting the parameters τ_{b_0}/τ_{s_0} and q (the ratio of bare orientation and stretch relaxations times and the priority number, respectively). Increases in the former parameter lead to weaker hardening while increases in the latter parameter lead to higher level of hardening.
- II. As regards the overshoots, at rates at which the maximum stretch is achieved, their magnitude is readily controlled by Ψ_w , the minimum fraction of surviving entanglements; by decreasing the value of Ψ_w one gets larger overshoots and thus lower steady state viscosity. In such occasions, and for given values of the parameters τ_{b_0}/τ_{s_0} and Ψ_w , variations (over a reasonable range, i.e. 1-2 units) in h , the number of arm entanglements, do not typically influence the magnitude of the overshoot unless Ψ_w is low (that is, $0.1 \lesssim \Psi_w \lesssim 0.3$). At rates at which no

maximum stretch is achieved the overshoot can be controlled by both Ψ_w and h ; decreases in Ψ_w act in the same direction as increases in h , that is, such variations lead to larger overshoots.

- III. As Ψ_w approaches unity the predictions tend to the original pom-pom model. In other words, overshoots weaken as Ψ_w increases; they disappear when $\Psi_w = 1$.
- IV. As regards the stress relaxation behaviour (*relaxation case*), we notice that increases (decreases) in h (Ψ_w) lead to much faster relaxation in the **AO** case (i.e. flow cessation after the overshoot) than in the **BO** case (i.e. flow cessation before the overshoot). Such changes in the parameters, from the perspective of achieving much more rapid relaxation in the **AO** case than in the **BO** case, are meaningful for the slowest modes. For fast modes, though stress relaxes quicker in the **AO** case, the **AO** and **BO** curves do never cross each other during the early and intermediate stages of the relaxation phase.

4.4 Predictions of the model: multimode version

4.4.1 The full model

Here, we attempt to fit the FSR data of Fig. 4.2 using a multimode (15 modes) version of the overshoot model developed in section 4.2.2, which, hereafter, will be referred to as the full model. Figure 4.14 compares the predictions of the full model (lines) with the experimental data (symbols) for the uniaxial extensional viscosity. The left panels (i.e. **a** and **c**) refer to the *normal case* while the right panels (i.e. **b** and **d**) refer to the *relaxation case*. For the latter case the comparison is restricted to the second highest rate $\dot{\epsilon} = 0.1s^{-1}$ (i.e. to r5). In panels **b** and **d**, the blue and black curves correspond to the **AO** and **BO** case, respectively. The theoretical curves in the upper and bottom panel of Fig. 4.14 are obtained using the so-called SET I and SET II parameterisation of table 4.2, respectively. In both sets only the six slowest modes are active in terms of non-linear parameters, i.e. there are six stretching modes with $q \neq 1$.

As readily seen from the upper panel of Fig. 4.14, SET I fails to capture simultaneously all the experimental data. In more details, according to panel **a**, SET I captures well the

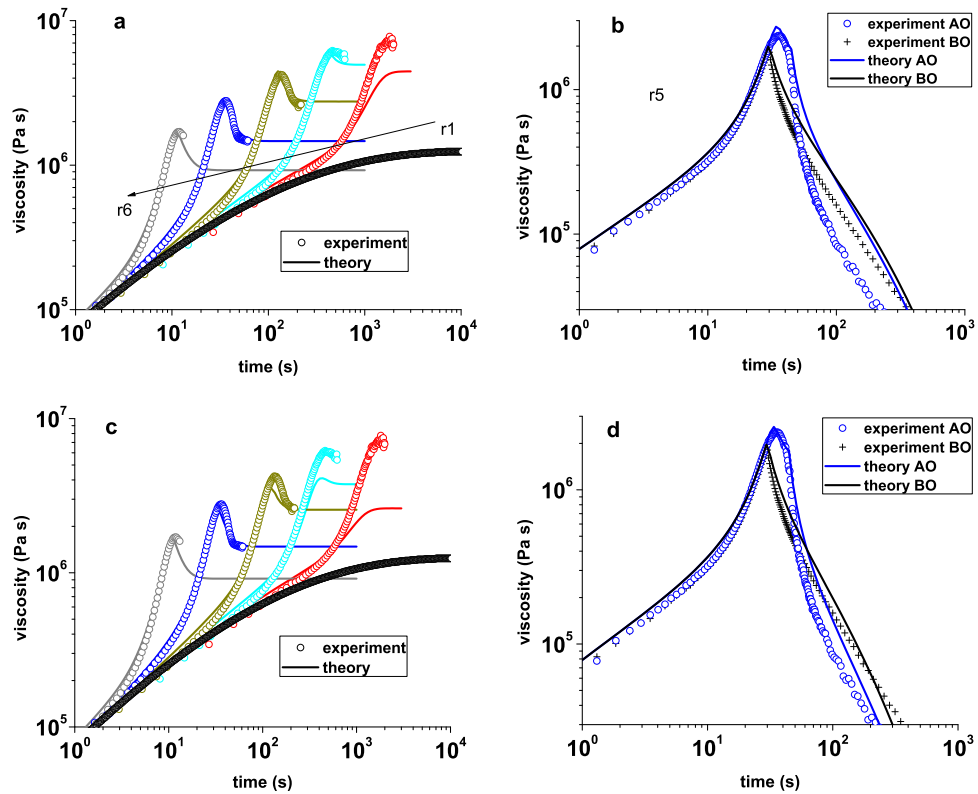


Figure 4.14: Comparison between the predictions of the full version of the overshoot model (lines) and the experimental data (symbols) for the DOW150R sample. Upper panel: Using SET I of table 4.2. Bottom panel: Using SET II of table 4.2. The plots on the left (right) side refer to the *normal case (relaxation case)*. For the correspondence between curves and represented quantities in the *relaxation case* see the labels. The data are provided by Dr. Qian Huang and Prof. Ole Hassager.

onset of strain hardening at all rates. Furthermore, it fits nicely the observed overshoots and steady states at r_4 and r_5 . It underestimates the degree of hardening, however, at the lowest rate (compare red line with red symbols). Foremost, it fails to capture the relaxation behaviour of the DOW150R sample (c.f. panel **b**). The full version of the model, with this parameterisation, predicts that relaxation after the overshoot is faster than before the overshoot, though is not as fast as the measurements indicate and so the blue and black lines of panel **b** do not cross significantly.

It is possible to improve the predictions of the full model in the *relaxation case* by using an alternative parameterisation, i.e. SET II of table 4.2. This spectrum is constructed by taking into consideration the following two facts: first, the slower modes are the ones that strongly determine a faster stress relaxation behaviour in the **AO** case (this feature

of the model was demonstrated in Fig. 4.13). Second, an increase (decrease) in the value of h (Ψ_w) speeds up the stress relaxation after the overshoot (c.f. Figs. 4.11 and 4.12). Therefore, in SET II, and for the three slowest modes, we use higher values of h than in SET I; nevertheless, for these modes, we do not decrease Ψ_w since a very low value for this parameter, i.e. $\Psi_w = 0.1$, has already been used in SET I.

The outcome of this alternative fit is presented in panels **c** and **d** of Fig. 4.14. Clearly, compared to SET I, this alternative parameterisation compares much better with the relaxation data (c.f. panel **d**). In contrast, it underestimates the degree of strain hardening at r4, at r3 and (predominantly) at r2. The predictions for r5 and r6 are practically the same. The systematic underestimation of the amount of strain hardening with decreasing strain rate is associated with the speed up of the stretch relaxation time; that is, compared to SET I, SET II under-predicts the degree of strain hardening as the higher values of h (in this set) do not allow the build up of stretch, especially at the lower rates. This limitation of the full model prevents us from fitting all measurements simultaneously using a single parameterisation. One can either fit the data of the *normal case* or the data of the *relaxation case*. In the next section we will present a minimal version of the overshoot model, which compares relatively well with all experimental data when a single set of parameters is used.

4.4.2 Minimal model

According to eq 4.3b, drag-strain coupling and entanglement stripping contribute to the speed up of the stretch relaxation time, τ_s , when the flow is active (i.e. in the *normal case*). In particular, with increasing stretch, λ , and decreasing fraction of surviving entanglements, Ψ , the stretch relaxation time reduces through the $\exp(-\nu(\lambda - 1))$ and $\exp(h(\Psi - 1))$ term, respectively.

Having this in mind, in the minimal model, we disregard entanglement stripping before the maximum stretch condition. That is, we set the normal chain retraction term, $w = -(\lambda - 1)/(\lambda\tau_s)$, equal to zero while $\lambda < q$. Here, branch point withdrawal is the only process that contributes to entanglement stripping. Hence, the $\exp(h(\Psi - 1))$ term in eq 4.3b does not contribute to the decrease of the stretch relaxation time until the onset of the aforementioned process.

Figure 4.15 compares the full and minimal model for the *normal case*, and for the slowest mode of parameterisation SET II; for this set, this mode is the one that mainly contributes to the hardening at the lowest non-linear rate. Figure 4.16 shows the respective comparison for the *relaxation case*. In Figs. 4.15 and 4.16, the predictions of the full and minimal model are presented by the magenta and black curves, respectively. Panels **a**, **b**, **c**, and **d** show the uniaxial extensional viscosity, the fraction of surviving entanglements, the stretch, and the stretch relaxation time, respectively. Note that, the relaxation times of orientation and stretch are equal since the ratio of the bare orientation and stretch relaxation times is unity, i.e. $\tau_{b_0}/\tau_{s_0} = 1$. In Fig. 4.16, symbols and lines refer, respectively, to cessation of the flow after (AO) and before the overshoot (BO).

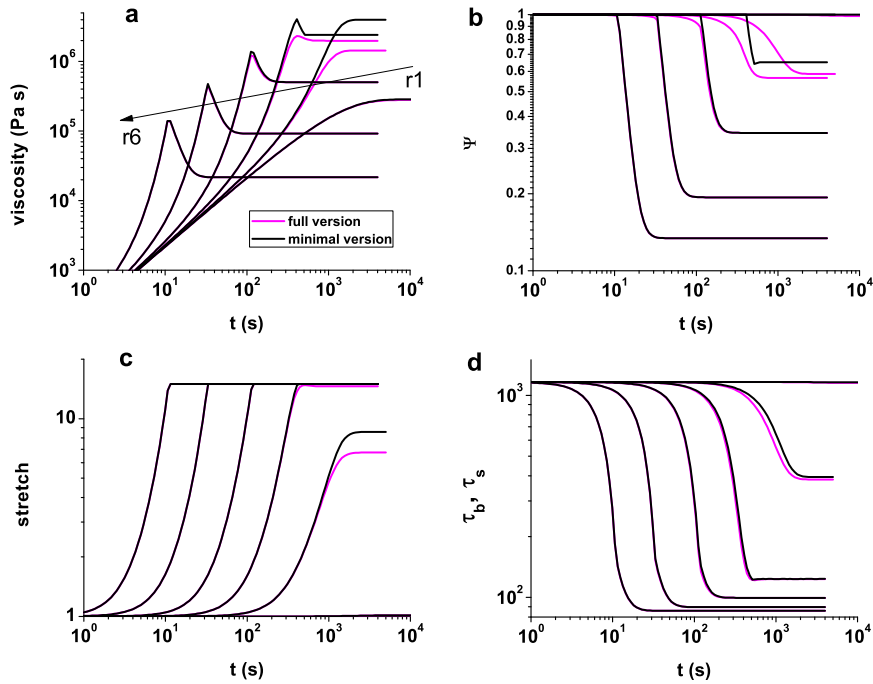


Figure 4.15: A comparison between the full and the minimal model for the *normal case*, and for the slowest mode of the SET II spectrum of table 4.2. The full (minimal) model is represented by magenta (black) lines. Panel **a** presents the uniaxial extensional viscosity. Panels **b**, **c** and **d** show Ψ , λ and τ_b , respectively. Here, $\tau_b = \tau_s$.

Figure 4.15 shows that, at the lowest non-linear rate (r2) where maximum stretch is not achieved, the minimal model predicts significantly higher strain hardening than the full model (c.f. panel **a**). This behaviour is attributed to the neglect of normal chain retraction in the minimal model: due to this neglect, in comparison with the full model, the minimal model gives higher stretch and higher fraction of surviving entanglements (i.e. Ψ is unity)

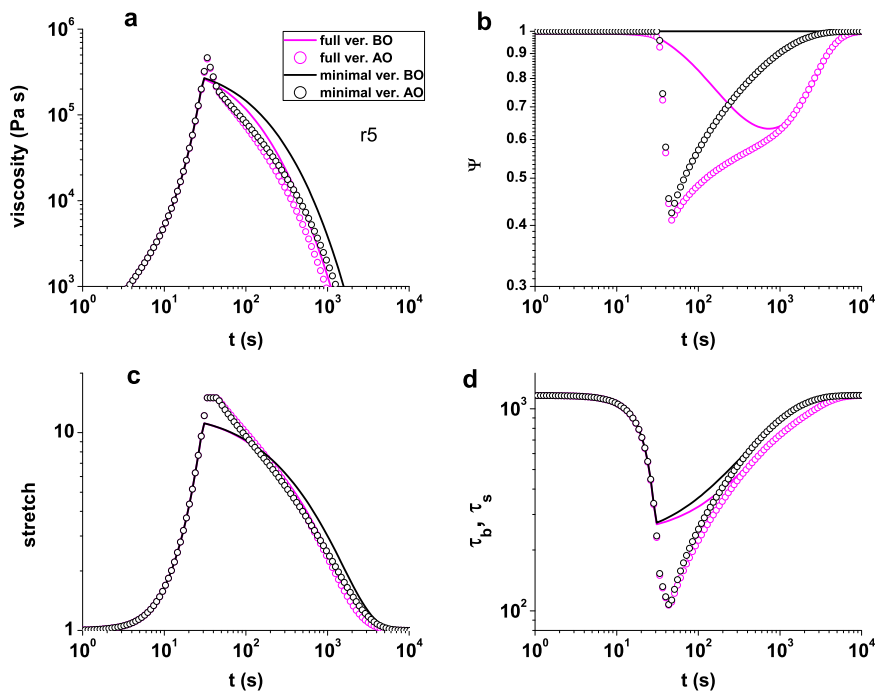


Figure 4.16: Same as Fig. 4.15 for the *relaxation case*. Symbols correspond to the **AO** case while lines to the **BO** case.

at this rate, as readily seen from panels **b** and **c**.

With respect to the *relaxation case* (Fig. 4.16) we notice, from panel **a**, that in both cases (**BO** and **AO**) the viscosity decays faster in the full model than in the minimal model. The difference between the predictions of the two models is bigger in the **BO** case since entanglement stripping does not occur at all in the case of the minimal model. For this reason, mainly, the area between the black symbols and the black line is bigger than the respective area between the two magenta curves. According to panel **b**, and with respect to the **AO** case, the neglect of the normal retraction term results in a more abrupt increase of Ψ in the minimal model, upon cessation of the flow. This trend, in turn, affects the respective relaxation times (panel **d**), that is, τ_b and τ_s increase more gradually toward their equilibrium values in the case of the full version; the latter statement also applies to the **BO** case. For this reason one would expect orientation and stretch relaxation, in both cases (**BO** and **AO**), to occur more rapidly in the full model. In fact, this is the case for the relaxation dynamics of the orientation (not shown), and also for the relaxation dynamics of the stretch when the flow is stopped before the overshoot (c.f. black and magenta lines in panel **c**). Nevertheless, stretch relaxation occurs slightly faster in the case of the minimal version, at times immediately after flow cessation, or at an equal rate

for both versions, at later times and up to $t \approx 10^3$ s, when the flow is switched off after the overshoot. This happens because the stretch correction term, i.e. eq 4.7b, in the case of the minimal model significantly contributes to the relaxation dynamics due to the abrupt upturn of Ψ ; specifically, the relaxation dynamics is controlled by:

$$\frac{d\lambda}{dt} = -\frac{(\lambda - 1)}{\tau_s \lambda} - \left(\frac{\lambda^2 - 1}{2\lambda\Psi} \right) \frac{d\Psi}{dt}, \quad (4.13)$$

and so in the case of the minimal version, though the first term of this expression produces a slower relaxation rate than in the case of the full version, the second term (correction term) contributes significantly to the relaxation process giving a faster rate of relaxation in the minimal model or an equal rate of relaxation between the two versions.

Having explained the main differences between the two versions, we now move on to compare the predictions of a multimode version of the minimal model with the experimental data. Figure 4.17 shows the outcome of this comparison; it should be considered as the analogous figure of Fig. 4.14 and so colours, symbols, etc. are used in exactly the same way as in Fig. 4.14. Moreover, it was obtained using 15 modes from which the last six were active in terms of non-linear parameters. The complete set of parameters that was used for the minimal model is presented in table 4.3.

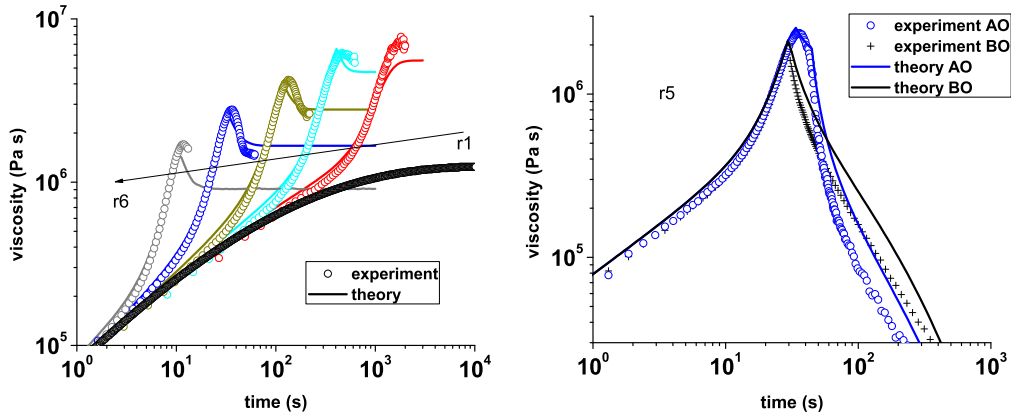


Figure 4.17: Same as Fig. 4.14 using the minimal model and the parameterisation of table 4.3. The data are provided by Dr. Qian Huang and Prof. Ole Hassager.

According to the left panel of Fig. 4.17, which refers to the *normal case*, the hardening, at the lowest rate is moderately underestimated. Nevertheless, at the lowest rate the predictions of the minimal model agree much better with the data compared to the predictions of the full model. With respect to r4 and r5 (dark yellow and blue colours,

respectively), the steady state value of the viscosity is lightly over-predicted. We note that for these rates the cross-slot flow measurements [60, 62] indicate that the steady state is even lower than the apparent steady state of the FSR data. Finally, at the highest rate the maximum is slightly underestimated. At this rate, a steady state is not achieved in the FSR; the prediction of the minimal model for the steady state lies somewhat above the measured value from the cross-slot experiment. As regards the *relaxation case*, which is shown at the right panel of Fig. 4.17, the predictions of the minimal model are in qualitative agreement with the data. That is, the model forecasts that the relaxation is faster in the **AO** case than in the **BO** case in accordance with the data. Moreover, the area between the black and blue symbols is about the same with the area between the black and blue lines, after the respective intersection points. However, the model predictions are not in a quantitative agreement with the data. Overall, the minimal version of the overshoot model provides a reasonable, but not perfect, fit to all experimental data with a single parameterisation set.

Table 4.2: Parameterisation for the full version of the model

DOW150R at 160°C, 15 modes, SET I							DOW150R at 160°C, 15 modes, SET II					
Mode	$G_{0_i}(Pa)$	$\tau_{b_{0_i}}(s)$	$\frac{\tau_{b_{0_i}}}{\tau_{s_{0_i}}}$	q	Ψ_w	h	$G_{0_i}(Pa)$	$\tau_{b_{0_i}}(s)$	$\frac{\tau_{b_{0_i}}}{\tau_{s_{0_i}}}$	q	Ψ_w	h
1	104459.99	0.0041	1.0	1	1.0	0.0	104459.99	0.0041	1.0	1	1.0	0.0
2	6810.18	0.0101	1.0	1	1.0	0.0	6810.18	0.0101	1.0	1	1.0	0.0
3	28071.50	0.0248	1.0	1	1.0	0.0	28071.50	0.0248	1.0	1	1.0	0.0
4	17859.70	0.0607	1.0	1	1.0	0.0	17859.70	0.0607	1.0	1	1.0	0.0
5	13952.96	0.1488	1.0	1	1.0	0.0	13952.96	0.1488	1.0	1	1.0	0.0
6	10726.20	0.3646	1.0	1	1.0	0.0	10726.20	0.3646	1.0	1	1.0	0.0
7	7647.08	0.8937	1.0	1	1.0	0.0	7647.08	0.8937	1.0	1	1.0	0.0
8	5493.66	2.1904	1.0	1	1.0	0.0	5493.66	2.1904	1.0	1	1.0	0.0
9	3534.60	5.3686	1.0	1	1.0	0.0	3534.60	5.3686	1.0	1	1.0	0.0
10	2538.33	13.1583	2.2	8	0.8	1.0	2538.33	13.1583	2.2	8	0.8	2.0
11	1224.37	32.2508	2.0	9	0.1	0.8	1224.37	32.2508	1.8	9	0.1	1.0
12	900.99	79.0463	1.8	10	0.1	0.6	900.99	79.0463	1.7	10	0.1	0.85
13	351.45	193.7415	1.3	11	0.1	0.4	351.45	193.7415	1.3	11	0.1	0.8
14	132.10	474.8578	1.05	13	0.1	0.3	132.10	474.8578	1.1	13	0.1	0.75
15	72.88	1163.8699	1.0	18	0.1	0.0	72.88	1163.8699	1.0	15	0.1	0.7

Table 4.3: Parameterisation for the minimal model

DOW150R at 160°C, 15 modes						
Mode	$G_{0_i}(Pa)$	$\tau_{b_{0_i}}(s)$	$\frac{\tau_{b_{0_i}}}{\tau_{s_{0_i}}}$	q	Ψ_w	h
1	104459.99	0.0041	1.0	1	1.0	0.0
2	6810.18	0.0101	1.0	1	1.0	0.0
3	28071.50	0.0248	1.0	1	1.0	0.0
4	17859.70	0.0607	1.0	1	1.0	0.0
5	13952.96	0.1488	1.0	1	1.0	0.0
6	10726.20	0.3646	1.0	1	1.0	0.0
7	7647.08	0.8937	1.0	1	1.0	0.0
8	5493.66	2.1904	1.0	1	1.0	0.0
9	3534.60	5.3686	1.0	1	1.0	0.0
10	2538.33	13.1583	3.0	6	0.8	2.0
11	1224.37	32.2508	2.5	7	0.8	1.0
12	900.99	79.0463	2.3	8	0.1	0.65
13	351.45	193.7415	1.75	9	0.1	0.6
14	132.10	474.8578	1.1	10	0.1	0.55
15	72.88	1163.8699	1.0	15	0.1	0.5

4.4.3 Comments on the pom-pom spectra

According to tables 4.2 and 4.3, the 15 modes overshoot model requires 90 parameters to function. This is not entirely the case despite the fact that each mode consists of six parameters. In fact, regardless of their exact number, about two thirds of the modes are inactive in terms of the non-linear parameter, q , the priority number. That is, for these modes the priority number and, in turn, the stretch, λ , is unity; τ_{b_0}/τ_{s_0} , the ratio of bare orientation and stretch relaxation times, is unity too. Since the stretch is at its equilibrium value, the retraction process (expressed either by normal chain retraction or branch point withdrawal) and, in turn, the entanglement stripping process is inactive in the model. This practically means that the minimum fraction of surviving entanglements, Ψ_w , and the number of arm entanglements prior to the onset entanglement stripping, h , can be set to unity and zero, respectively. Hence, between the non-stretching modes, only the linear parameters, G_0 and τ_{b_0} , differ. This fact significantly reduces the total number of parameters of the multimode overshoot model; for instance, the fitting parameters in tables 4.2 and 4.3 are in practice 58 and not 90.

It is obvious that the number of fitting parameters can be further reduced by using fewer modes. Compared to the fit in Fig. 4.17, multimode versions of the minimal model with 10 or 12 modes (which are comprised of 3 or 4 stretching modes, respectively) can achieve quite similar fits. We note that, as the density (number) of modes decreases, (i) the fitting procedure becomes easier (since the number of parameters reduces), but (ii) the smoothness of the theoretical curves decreases. The density of modes used in this study (i.e. 15) is a compromise between the factors (i) and (ii) above. Nevertheless, the exact number of modes and the precise values of the fitting parameters do not necessarily provide a precise description of the molecular structure, neither do they faithfully reflect the underlying molecular physics. In reality, the modes are coupled in their dynamics and thus the physics of the real system (industrial melt) is most likely to be much richer than the physics suggested by the standard decoupling approximation.

Finally we note that the size of the overshoot model parameter space is restricted by the following physical constraints: τ_{b_0}/τ_{s_0} and h must decrease, whereas q must increase, towards the centre of a long chain branched (LCB) molecule. These constraints arise from the hierarchical character of the relaxation of a LCB molecule.

4.5 Conclusions and future work

This chapter dealt with the non-linear viscoelastic flow properties of industrial melts under (uniaxial) extensional flow. It aimed at developing a basic model for the description of the Filament Stretching Rheometer (FSR) data of the industrial melt DOW150R [6, 7]. These data reveal that (i) the viscosity can overshoot under continuous applied flow, and (ii) the stress relaxation, at $\dot{\epsilon} = 0.1\text{s}^{-1}$, is significantly faster when the flow is ceased after the overshoot (**AO** case) than in the case in which the flow is stopped before the overshoot (**BO** case). The basic model, the so-called overshoot model, that was introduced for the aforementioned purpose is essentially a variant of the pom-pom model [8] that allows entanglement stripping. It was argued that, within the framework of this model, an extensional viscosity overshoot arises from entanglement stripping, which in turn originates from the relative motion between a given test backbone and the matrix backbones, during the processes of normal chain retraction or/and branch point withdrawal. In the so-called full version of the model, entanglement stripping due to

(both) normal retraction and branch point withdrawal was accounted for. A minimal version, which only accounted for entanglement stripping due to branch-point withdrawal, was also considered.

In both the full and minimal model the constitutive equation is comprised of three evolutionary differential equations: one for the pre-averaged backbone orientation, \mathbf{S} , a second one for the pre-averaged backbone stretch, λ , and a third one for the fraction of surviving (backbone-backbone) entanglements, Ψ (see eqs 4.1, 4.2 and 4.9, respectively). Apart from the usual parameters (i.e. the plateau modulus, G_0 , the bare orientation relaxation time, τ_{b_0} , the ratio of bare orientation and stretch relaxation times, τ_{b_0}/τ_{s_0} , and the priority number, q [8, 9, 102, 103]), the overshoot model contains two additional parameters, namely the minimum fraction of surviving entanglements, Ψ_w , and the number of arm entanglements prior to the onset of entanglement loss, h .

For the rate of tube reconfiguration (that is, the inverse of the timescale for orientation relaxation), three different options were considered and so three different constitutive equations, the so-called options A, B and C, were essentially examined. It was shown that option A, the option most commonly used in differential pom-pom models, behaves very poorly in relaxation after extensional flow due to the un-physically low rate of tube reconfiguration (c.f. Figs. 4.5 and 4.6). From the perspective of modelling the flow properties of industrial melts, Option C (the constitutive equation in which the rate of tube reconfiguration is simply the inverse of the orientation relaxation time, τ_b) is superior to Option B, the constitutive equation in which the rate of tube reorientation is $(\lambda^2\tau_b)^{-1}$.

By using option C and a single mode, the study of the stress response of the full model has shown the following: in general, higher strain hardening can be achieved by increasing q and Ψ_w or/and by decreasing τ_{b_0}/τ_{s_0} and h . (ii) At rates at which the maximum stretch condition is fulfilled, the magnitude of the overshoots can be readily controlled by Ψ_w ; decreases in this parameter lead to higher entanglement stripping and, in turn, to larger overshoots. (iii) At rates at which the maximum stretch is not achieved, the overshoots can be controlled by both Ψ_w and h ; that is, lower values of Ψ_w and higher values of h give larger overshoots. Features (i)-(iii) above can be seen in Figs. 4.9-4.12 in panels that refer to the *normal case* (c.f. section 4.3.4 also). (iv) Compared to the **BO** case, the model predicts much faster stress relaxation in the **AO** case, in qualitative agreement with the measurements. We saw that, within the framework of the model, this behaviour is related

to the high and sudden entanglement loss due to branch point withdrawal (c.f. 4.13).

To provide a quantitative fit to the experimental data we adopted the method of Inkson et al. [9]. That is, we represented the melt by a superposition of individual pom-pom modes. Although the multimode full model matched a fair amount of the experimental data it proved to be ineffective to fit all data with a single parameterisation. On the other hand, the multimode minimal model provided a reasonable, but not perfect, fit to all data.

However, the superior performance of the minimal model in fitting the experimental data of the DOW150R sample does not necessarily render the minimal model superior to the full model from the physical point of view. The physical reason, if any, behind the superior performance of the minimal model is not obvious. It may be that there is actually a fundamental difference between (i) the stretch relaxation process (via branch point hopping), which involves contour length fluctuations at the same time as stretch relaxation, and (ii) branch-point withdrawal, which is a sudden process involving, in some sense, a change of state of the molecules. Whilst this is speculative, it does point towards the form of the minimal model. An alternative (and perhaps more likely) possibility is to note that in reality the different layers of a branched molecule are coupled, and this may give rise to additional effects not captured in the decoupled multimode model.

In order to draw safer conclusions about the superior performance of the minimal model, it would be sensible to test the predictive power of both models for other industrial samples, such as the HDB6, for which experimental data are available [6]. Furthermore, both models could be tested in other types of simple flows (e.g. shear) or/and complex flows like the cross-slot flow. For the latter type of flow, the constitutive equations of the full and minimal model could be incorporated into finite element flow solvers in order to test if they can predict the double cusping patterns (in the birefringence images) along the outflow centre line [6, 62, 100].

In conclusion, it was shown that the incorporation of entanglement stripping in the multimode pom-pom formalism can provide a practical and flexible tool for fitting viscosity (stress) data of industrial melts, which exhibit overshoots under steady extensional flow. Yet, the difficulty in fitting all data simultaneously (i.e. measurements of stress under steady extensional flow and measurements of stress relaxation following the steady flow) may be an indication that the real industrial melt is significantly more

complex than suggested by the multimode pom-pom formulation; different sections of different molecules are, in reality, coupled in their dynamics, a fact which is wholly ignored in the multimode model. Moreover, the fact remains that some molecular mechanisms, such as constraint release (CR), are not presently represented within the semi-phenomenological framework of the pom-pom model. A molecular model that would account for the coupled dynamics between the modes, and would describe CR events and entanglement stripping in a more fundamental way, would be more realistic than the overshoot model developed here. A microscopic description of CR events in a monodisperse pom-pom melt is the subject of the following chapter.

Chapter 5

Constraint Release events in a pom-pom melt

5.1 A pom-pom molecule with constraint release under shear and uniaxial extensional flows

In section 1.5.2 we saw that the pom-pom model [8] is typically used for the molecular modelling of long chain branched polymers. In the context of this model, constraint release (CR) events are accounted for in an indirect manner by utilizing the (semi-phenomenological) dynamic dilution hypothesis [2]. The aim of this chapter is to include constraint release in a melt of pom-pom molecules in an explicit manner, i.e. by using a microscopic description of CR events, and investigate the effects of such events on the rheological properties of the melt. In particular, CR events are modelled as random Rouse-like hops (“kinks”) of the primitive chain in common with Refs. [10, 11, 12, 13, 90].

Two cases will be examined. The first one, referred hereafter as the 1CR model, focuses on convective constraint release (CCR) events, i.e. the hops that a backbone undertakes when matrix backbones are dragged away (in non-linear flows) from a given test backbone with subsequent release of entanglements. In the second case (2CR model), some of the CR events between a given backbone and surrounding arm material, which are mediated by the arm retraction process, are also modelled; as regards this case, in the formulation to be developed below (section 5.1.3) the physical picture of the thin and fat tubes, proposed

in Refs. [14, 15], is used. For both cases the effects of CR events on the rheological response of the melt (to shear and uniaxial extensional flows) will be studied.

5.1.1 An alternative model for the pom-pom molecule

To incorporate constraint release in a melt of pom-poms, one could modify the constitutive equation of the original model or could use other existing models (for linear chains) that provide the aforementioned microscopic description of CR events, and moreover, have the potential to treat the dynamics of branched molecules. A possible model is the one proposed by Read in Ref. [13], based on earlier works of Likhtman, Milner and McLeish [10, 11] and the GLaMM model of Graham et al. [12], since (i) it represents constraint release by means of Rouse hops, and (ii) it was introduced for an infinite long linear chain which was assumed to stretch uniformly by a factor λ ; indeed, this a good assumption for a pom-pom molecule since the friction is dominated by the two branch points and thus the whole backbone is stretched uniformly; differences in the local stretch along the backbone vanish rapidly on the timescale of the bare Rouse relaxation time of the molecule.

The equation of motion, for the position vector $\mathbf{R}(s, t) = \mathbf{R}$ of a tube segment, in this model was written as

$$\frac{\partial \mathbf{R}}{\partial t} = \mathbf{K} \cdot \mathbf{R} + \frac{3\nu\eta\lambda}{2\theta\phi^2} \frac{\partial^2 \mathbf{R}}{\partial s^2} + \mathbf{g} + \tilde{w}s \frac{\partial \mathbf{R}}{\partial s}, \quad (5.1)$$

where the terms on the right side refer to the flow, constraint release, random noise due to CR events and chain retraction, respectively. This equation is similar to the Rouse model (eq. 1.41) with the inclusion of a flow and a retraction term. The quantity ν represents the frequency of the Rouse hops while η , θ and ϕ are functions of the stretch λ and are related to changes of the tube properties, that is, they describe changes in the length of the Rouse hops, the tube diameter, and the tube persistence length, respectively. Here, the length of the hops and the tube diameter are kept constant and so $\eta = \theta = 1$. Moreover, ϕ is set equal to λ ; according to Ref. [13], setting $\phi = \lambda$ means that the variable s measures uniform steps of order N_e along the chain, in the manner of the GLaMM model of Graham et al. [12]. It is worth mentioning that by setting $\phi = \lambda$, $\eta = 1$, and $\theta = 1$ one ensures that the model results of Ref. [13] are very similar to those of the GLaMM model. Finally, \tilde{w} is the retraction rate and, within the model, controls relaxation of the stretch.

In more recent work, Read, Jagannathan and Likhtman [124] showed that a more physically consistent picture, especially at lengthscales closer to the tube diameter, was to consider the tube as a mean-path of the chain, which introduces a bending energy term into the equations (as we showed in chapter 2 for star polymers). A Fourier mode solution, including bending energy terms is possible [15]. However, since we will mostly be concerned with lengthscales larger than the thin tube diameter, and to keep things simple, we will use a Fourier mode solution based on the methods of the Read paper [13]. The main difference is that we will here have sharp boundaries in Fourier space, rather than the more gentle crossovers that one gets with the bending energy formulation.

The evolution equation that governs the dynamics of the system in Fourier space is derived as follows [13]. By defining the Fourier modes as

$$\mathbf{R}_p(t) = \int_{-\infty}^{+\infty} ds \mathbf{R}(s, t) e^{ips}, \quad \mathbf{R}(s, t) = \frac{1}{2\pi} \int_{-\infty}^{+\infty} dp \mathbf{R}_p(t) e^{-ips}, \quad (5.2)$$

eq 5.1 is transformed to

$$\frac{\partial}{\partial t} \mathbf{R}_p(t) = \mathbf{K} \cdot \mathbf{R}_p(t) - \frac{3\nu}{2\lambda} p^2 \mathbf{R}_p(t) + \mathbf{g}_p(t) - \tilde{w} \left(\mathbf{R}_p(t) + p \frac{\partial \mathbf{R}_p(t)}{\partial p} \right). \quad (5.3)$$

Moreover, by using the tensors

$$\mathbf{Q}_p = \frac{1}{2\pi} \int_{-\infty}^{+\infty} dp' \langle \mathbf{R}_p \mathbf{R}_{p'} \rangle, \quad \mathbf{C}_p = \frac{3p^2}{\alpha_0^2} \mathbf{Q}_p, \quad (5.4)$$

and eq 5.3 in the expression:

$$\frac{\partial}{\partial t} \langle \mathbf{R}_p(t) \mathbf{R}_{p'}(t) \rangle = \left\langle \left(\frac{\partial}{\partial t} \mathbf{R}_p(t) \right) \mathbf{R}_{p'}(t) \right\rangle + \left\langle \mathbf{R}_p(t) \left(\frac{\partial}{\partial t} \mathbf{R}_{p'}(t) \right) \right\rangle \quad (5.5)$$

one ends up with an equation that describes in Fourier space the dynamic behavior of the system, via the time evolution of the tensor \mathbf{C}_p :

$$\frac{\partial}{\partial t} \mathbf{C}_p = \mathbf{K} \cdot \mathbf{C}_p + \mathbf{C}_p \cdot \mathbf{K}^T - \frac{3\nu}{\lambda} p^2 (\mathbf{C}_p - \mathbf{I}) + \tilde{w} \left(\mathbf{C}_p - p \frac{\partial \mathbf{C}_p}{\partial p} \right), \quad (5.6)$$

where the terms on the right side are associated with changes due to the flow (first two terms), constraint release events, and chain retraction, respectively. Since the particular model focuses on infinitely long chains it does not provide a detailed description of the orientational relaxation of the chain, that is, the model disregards the full reptation spectrum of relaxations. Nevertheless, a single orientational (reptation) relaxation time can be introduced in the model by adding to eq 5.6 a term of the form $-\frac{1}{\lambda^2 \tau_b} (\mathbf{C}_p - \lambda^2 \mathbf{I})$;

in this expression the reptation time of the chain is amplified by a factor of λ^2 in respect to the reptation time, τ_b , of the unstretched chain. To obtain eq 5.6 the following pre-averaging expressions are used:

$$\langle g_{p\alpha} R_{p'\beta} \rangle = \frac{2\pi\nu a^2}{\lambda} \Delta_p \delta(p+p') \delta_{\alpha\beta}, \quad (5.7)$$

$$\left\langle \frac{1}{\lambda} \mathbf{R}_p \mathbf{R}_{p'} \right\rangle \approx \frac{1}{\lambda} \langle \mathbf{R}_p \mathbf{R}_{p'} \rangle, \quad \langle \tilde{w} \mathbf{R}_p \mathbf{R}_{p'} \rangle \approx \tilde{w} \langle \mathbf{R}_p \mathbf{R}_{p'} \rangle. \quad (5.8)$$

In eq 5.7 the indices α, β denote cartesian coordinates, a is the tube diameter and $\Delta_p = 1$ for $-\pi \leq p \leq \pi$. The closure approximations of eq 5.8, which imply a pre-averaging approximation, are similar to those in the models of Milner et al. [11] and Graham et al. [12].

The retraction rate, \tilde{w} , and the CCR rate, ν , are written as

$$\tilde{w} = -\frac{(\lambda-1)}{\tau_s \lambda}, \quad (5.9a)$$

$$\nu = c_\nu \left(-\tilde{w} + \frac{1}{\lambda^2 \tau_b} \right). \quad (5.9b)$$

Equation 5.9b counts the contributions to CR events from stretch relaxation (chain retraction) and from reptation; in other words it determines the rate at which the chain ends of a given test chain pass the tube segments of surrounding chains (or vice-versa). The constraint release parameter, c_ν , is usually given a value of 0.1 [11, 12, 13]; it accounts for the fact that several chain ends (of matrix chains) are typically required to pass sections of the test chain for the latter to undertake a hop of order the tube diameter [11]. For $\theta = 1$, the expression for the stress is identical to the respective expression of the pom-pom model, that is, the stress is given by

$$\sigma = G_0 3\lambda^2 \mathbf{S} = G_0 \mathbf{A}, \quad (5.10)$$

where \mathbf{S} is the orientation tensor; the tensor \mathbf{A} is defined as

$$\mathbf{A} = 3\lambda^2 \mathbf{S} = \frac{1}{\pi} \int_0^\pi dp \mathbf{C}_p. \quad (5.11)$$

The stretch is obtained from the expression $\mathbf{A} = 3\lambda^2 \mathbf{S}$ by making use of the fact that $\text{tr} \mathbf{S} = 1$, where tr denotes a matrix trace; hence the explicit formula for the stretch is

$$\lambda^2 = \frac{1}{3} \text{tr} \mathbf{A}. \quad (5.12)$$

In all calculations to be presented below we will use $G_0 = 1\text{Pa}$.

The following section is concerned with the 1CR model. A maximum stretch condition is added to the equations described in this section and the flow properties of the melt are examined. Section 5.1.3 deals with the 2CR model, which also considers the CR events that arise from release of entanglements between the backbones and the much faster relaxing arms. The numerical solution, for both models, is detailed in Appendix D.

5.1.2 A simple CCR rate for the pom-pom backbone: the 1CR model

As a first improvement compared to the existing pom-pom theory we are going to include CCR events. We assume that these events occur at rate ν and represent the hops that the backbone makes when the constraints from the matrix backbones are released. Such hops take place in the presence of strong flows; this is because matrix backbones are convected by the flow and so they are dragged away from the backbone of a test chain; this relative motion between the matrix backbones and the test backbone is followed by release of the mutual entanglements. Similarly to the original model the theory presented in this section will be valid for flows that do not stretch the arms of the molecule.

Since Read's constitutive equation (eq 5.6) includes CR and retraction the only thing we are required to do, in order to apply it to a pom-pom melt, is to impose a maximum stretch condition. As discussed in section 1.5.2, the maximum stretch condition implies that $d\lambda/dt$ is zero when λ reaches q . Starting from the definition of λ , i.e. from eq 5.12, and by differentiating with respect to time one arrives at the appropriate retraction rate, \tilde{w} , which is needed to keep $\lambda = q$:

$$\begin{aligned}
\lambda^2(t) &= \frac{1}{3} \text{tr} \mathbf{A} \\
2\lambda \left(\frac{d\lambda}{dt} \right) &= \frac{1}{3\pi} \int_0^\pi dp \frac{\partial}{\partial t} \text{tr} \mathbf{C}_p \\
\frac{d\lambda}{dt} = 0 &= \frac{1}{6\pi\lambda} \left(2\pi \mathbf{K} : \mathbf{A} - \frac{3\nu}{\lambda} \int_0^\pi dp p^2 \text{tr} (\mathbf{C}_p - \mathbf{I}) \right) - \\
&\quad \frac{1}{6\pi\lambda} \left[\frac{\pi}{\tau_b} \text{tr} (\mathbf{A} - \lambda^2 \mathbf{I}) + \tilde{w} \pi \left(\text{tr} \mathbf{A} - \frac{1}{\pi} \int_0^\pi p \frac{\partial}{\partial p} \text{tr} \mathbf{C}_p \right) \right] \\
\Leftrightarrow \tilde{w} &= \frac{-2\pi \mathbf{K} : \mathbf{A} + \frac{3c_\nu}{\lambda^3 \tau_b} \left(-\pi^3 + \int_0^\pi dp p^2 \text{tr} \mathbf{C}_p \right)}{\frac{3c_\nu}{\lambda} \left(-\pi^3 + \int_0^\pi dp p^2 \text{tr} \mathbf{C}_p \right) + \pi \text{tr} \mathbf{A} - \int_0^\pi p \frac{\partial}{\partial p} \text{tr} \mathbf{C}_p}. \quad (5.13)
\end{aligned}$$

Note that $\text{tr} (\mathbf{A} - \lambda^2 \mathbf{I}) = 0$ according to eq 5.12. Equation 5.13 is used when $\lambda \geq q$ and

serves as the maximum stretch condition; for $\lambda < q$, the retraction rate is given by eq 5.9a.

Figure 5.1 presents the predictions of the current theory, under shear and uniaxial extensional (continuous) flows, for the parameterisation $q = 5$, $\tau_b = 100\text{s}$, and $\tau_s = 1\text{s}$. In particular, the upper panel of Fig. 5.1 shows the viscosity as a function of time in the cases of shear flow (left) and extensional flow (right). The bottom panel of the same figure illustrates the corresponding values of the backbone stretch. The correspondence between flow rates and colours is: 0.01s^{-1} (black), 0.1s^{-1} (red), 0.5s^{-1} (blue), 1s^{-1} (magenta), 2s^{-1} (dark yellow), and 5s^{-1} (dark cyan). The results for the viscosity can be compared qualitatively with the predictions of the original pom-pom model that are shown in Fig. 1.15 of chapter 1; from this perspective both models display the same behaviour; they predict shear-thinning and extensional hardening during start up of the flow.

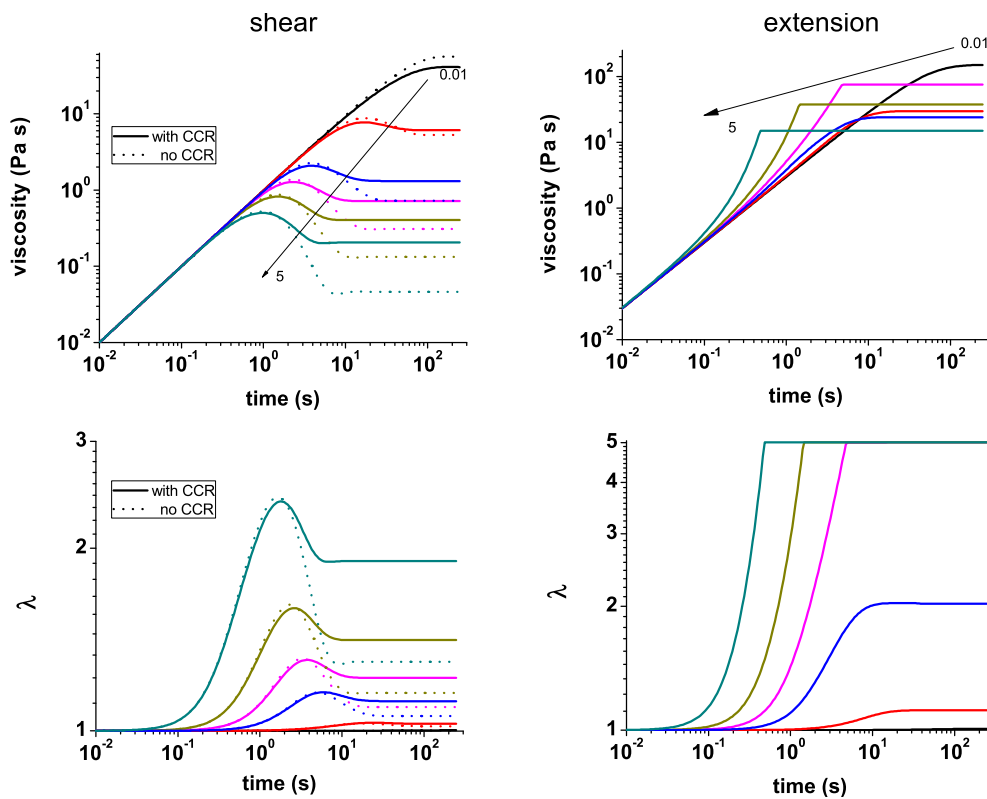


Figure 5.1: The 1CR model using $q = 5$, $\tau_b = 100\text{s}$, and $\tau_s = 1\text{s}$. Top panel: Shear (left) and elongational (right) viscosities. Bottom panel: The corresponding values of λ . The correspondence between rates and colours is: 0.01s^{-1} (black), 0.1s^{-1} (red), 0.5s^{-1} (blue), 1s^{-1} (magenta), 2s^{-1} (dark yellow), and 5s^{-1} (dark cyan). For the shear case, the dotted lines correspond to the model predictions when CCR events are ignored.

In more details, shear-thinning occurs as the magnitude of $\eta(t, \dot{\gamma})$ in the non-linear regime (high shear rates) is smaller than the respective values in the linear regime (low shear rates). Furthermore, for all shear rates that exceed τ_b^{-1} , both theories predict an overshoot in the shear viscosity and therefore in the shear stress $\sigma_{xy}(t)$; in general, under shear flow and without CCR, we expect $\sigma_{xy}(t)$ to increase until the tubes are rotated and aligned to the flow direction (*x direction*) and afterwards to decrease to its steady-state value since there is no stress component in the *xy* “direction”; this behavior of σ_{xy} is responsible for the observed overshoot in $\eta(t, \dot{\gamma})$, for all flow rates that are strong enough to orient the tubes, i.e. for $\dot{\gamma} \gtrsim \tau_b^{-1}$.

However, in our model, we include CCR events and therefore we anticipate an enhanced contribution to $\sigma_{xy}(t)$ after the maximum, i.e. after tube alignment with the flow. This is because CCR produces kinks which weaken the tube alignment, and moreover increases the tube length (in turn the chain stretch). Therefore, the incorporation of CCR should at least produce a less shear-thinning behavior (i.e. should weaken the maximum appearing in $\eta(t, \dot{\gamma})$) compared to the original pom-pom theory. To test the validity of this argument, we could compare the predictions of the two models using the same parameterisation. Alternatively, we can just switch off the CCR mechanism in our model, that is, we can set $c_\nu = 0$, and compare our predictions with and without CCR; the dotted lines in the left panels of Fig. 5.1 present the model predictions when CCR is ignored; by comparing the solid and dotted lines of the left panels of Fig. 5.1 we conclude that the maxima in the shear viscosity and the corresponding stretch are weaker when CCR is active, for all rates at which an overshoot is seen. Finally, we note that for all examined shear rates the stretch did not reach the maximum stretch condition.

As regards the extensional flow we notice that strain hardening occurs, during start up of the flow, for extensional rates that are of order $\tau_s^{-1} \gtrsim 1\text{s}^{-1}$. In our predictions some hardening even appears at $\dot{\epsilon} = 0.5\text{s}^{-1}$. For the highest three strain rates the maximum stretch condition is achieved. As a consequence, at these rates, the viscosity remains constant as soon as λ reaches q ; this is due to the fact that the chain can not be stretched further since branch point withdrawal occurs. At steady state, strain-softening occurs since $\eta(t, \dot{\epsilon})$ is below $\eta(t, \dot{\epsilon} = 0.01\text{s}^{-1})$ for all non-linear extension rates. We also note that the neglect of CCR events changes only slightly the predictions of our model (not shown); this is to be expected since under extension the chain is under much higher

tension than under shear and thus the formation of disoriented kinks becomes unlikely. In conclusion, the 1CR model predicts qualitatively the same behaviour as the original pom-pom model, that is, if maximum extensibility is achieved then the viscosity forms a distinct plateau. In the next section, we also include CR events due to release of backbone-arm entanglements in order to investigate if the inclusion of such events can give a qualitative different behaviour in extension; for instance, if the inclusion of such events can predict the overshoots that were discussed in chapter 4.

5.1.3 Modeling two CR rates in a pom-pom melt: the 2CR model

In the previous section CCR events were modeled, but the embedded structure inside the backbone's tube was omitted. In a melt of pom-pom molecules the backbone does not only entangle with the other backbones but also entangles with the arms of the matrix molecules. Thus the situation resembles approximately the binary blend of long and short linear chains that was shown schematically in Fig. 1.13; since the backbones relax much slower than the arms they can be thought of as the long linear chains while the arms can be thought of as the short linear chains that release their constraints on the backbone at a rate ν_{fast} . This mechanism represents the omitted structure of the previous section. Here, we assume that $\nu_{fast} \propto \tau(0.5)^{-1}$, that is, we suppose that "kinks" are produced when an arm tip reaches (via the arm retraction process) the middle of the arm. It should be stressed that this is a simplification, an initial model to be developed further; in reality there is a continuous spectrum of constraint release times (rates) associated with the arms. We also include the CCR events that occur at a rate ν_{slow} which is slower than ν_{fast} . For $\tau(0.5)$ the expression of the original pom-pom model is used:

$$\tau(s_\ell) = \tau_{pre} \exp \left[\frac{15}{4} Z_a \left(\frac{(1 - s_\ell)^2}{2} - (1 - \phi_b^{\alpha_d}) \frac{(1 - s_\ell)^3}{3} \right) \right], \quad (5.14)$$

where Z_a denotes the arm entanglement length, ϕ_b is the volume fraction of backbone material (c.f. eq 1.60), and α_d is the dilution exponent which is assumed unity throughout this chapter (although this will not significantly affect the results in a qualitative sense); τ_{pre} is approximated by the Rouse time of an arm $\tau_{R_a} = \tau_e Z_a^2$.

Following a similar procedure to that applied for a binary blend of short and long linear chains [14, 15], which successfully predicted the linear and non-linear rheology

of a polyisoprene bi-disperse melt, we shall represent the two kind of entanglements by two different tubes: (i) a thin (skinny) tube, with Z_{thin} entanglement segments, which represents all the entanglements between a given pom-pom molecule and the matrix chains, and (ii) a fat tube, with Z_{fat} entanglement segments, that replaces the topological constraints between a given pom-pom and the matrix backbones only. Here, Z_{thin}^2 is defined as $Z_{thin} = Z_b + 2qZ_a$ where Z_b and Z_a denote the number of entanglements (of all kind) acting on the backbone and an arm of a given pom-pom, respectively; moreover, the diameters of the thin and fat tubes are denoted as a and a_{fat} , respectively. Within the framework of the theories of Auhl et al. [14] and Read et al. [15], (i) the two diameters are related through:

$$a_{fat}^2 = a^2 n, \quad (5.15)$$

where n denotes the number of thin tube segments within a fat tube segment; $n = 1/\phi_L^{\alpha_d}$, with $\phi_L^{\alpha_d}$ being the volume fraction of long chains. In our case, $\phi_L^{\alpha_d} = \phi_b$. Also, (ii) the thin tube locally equilibrates inside the fat tube. Instead of one stretch parameter λ , two stretches exist in this case: λ_{thin} and λ_{fat} the stretch of the thin and fat tube, respectively; according to Auhl et al. [14] “if there is stretch in the fat tube, and the thin tube is equilibrated within it, then a stretch in the thin tube is imposed”, that is, λ_{thin} and λ_{fat} are related through:

$$\lambda_{thin}^2 = \phi_b \lambda_{fat}^2 + (1 - \phi_b). \quad (5.16)$$

In this context, the description of the physics of stretch relaxation is a bit more complicated than the description of the respective physics of the 1CR system.

Since the thin tube equilibrates inside the fat tube, the maximum stretch condition should be imposed on λ_{thin} . In other words the thin tube is allowed to stretch but λ_{thin} should not exceed q . If $\lambda_{thin} \geq q$, then branch point withdrawal takes place in the skinny tube; the timescale for this process is approximately the bare Rouse time of the molecule, which is effectively instantaneous on the (examined) flow timescales. Another stretch relaxation mechanism occurs when λ_{fat} exceeds q . Using the argument of the skinny tube relaxing in the fat tube, we expect λ_{fat} to reach q earlier than λ_{thin} . When this happens branch point withdrawal occurs in the fat tube. In this case the friction dominating the process comes from the entanglements of the fast relaxing matrix arms that get in the way. However, the appropriate timescale for withdrawal of the branch point along the fat tube is not clear, and we could consider two possible scenarios.

We might suggest that the appropriate timescale is the constraint release Rouse time of the thin tube (i.e. the time for the thin tube to completely reorganise itself subject to local CR hops). This timescale is:

$$\tau_{CR} = \tau_{obs} Z_{thin}^2 = \frac{2\tau(0.5)}{3\pi^2 c_\nu} Z_{thin}^2, \quad (5.17)$$

where $\tau_{obs} = 2\tau(0.5)/(3\pi^2 c_\nu)$ is the life time of the obstacles (i.e. the fast relaxing arms) and Z_{thin} is the number of thin tube entanglements. Using $q = 3$, $\phi_b = 0.3$, $Z_b = 25$, $Z_a = (1 - \phi_b) Z_b / (2q\phi_b) \approx 10$ and $\tau_e = 10^{-7}$ s, eq 5.17 gives $\tau_{CR} \approx 1.5$ s; the Figs. 5.2 and 5.3 below have been obtained using $\tau_{CR} = 1$ s. As noted earlier, the assumption $\tau_{obs} \propto \tau(0.5)$ is a simplification of the more realistic physical picture of a continuous spectrum of CR rates; depending on s_ℓ , τ_{CR} could span a wide range of values, e.g., for $\tau_{obs} \propto \tau(0.25)$ and $\tau_{obs} \propto \tau(0.75)$ one gets $\tau_{CR} \approx 0.1$ s and $\tau_{CR} \approx 35$ s, respectively.

On the other hand, Ref. [14] demonstrated that in binary blends of linear chains, stretch relaxation along the fat tube could be achieved by motion of the chain along the thin tube. (The timescale for this was the ratio of the bare Rouse relaxation time of a long chain and the volume fraction of long chains, i.e. $\tau_R/\phi_L^{\alpha d}$.) This process would also allow the linear chain sections of a branched polymer to redistribute their stretch along the fat tube. However, for branch point withdrawal, there must additionally be some local tube reorganisation near the branch point, to allow for equilibration of chain stretch at either side of the branch point. We might estimate a timescale for this by balancing the spring constant of the pom-pom backbone, $k_b = 3k_B T / (Z_b a^2)$, with the friction constant, ζ_{bp} , associated with local diffusion of the branch points over a distance of order the fat tube diameter, that is $\zeta_{bp} = k_B T / D_{bp} = 3k_B T \tau_{exp} / a_{fat}^2$; in the latter expression, τ_{exp} is the time taken for the branch point to explore the width of the fat tube; this timescale is not clear, for instance, one could assume: $\tau_{exp} = \tau_{obs} n^2$ or $\tau_{exp} = \tau(0)$ (i.e., the time taken for a complete retraction of an arm, thereby the time taken for the branch point to execute a diffusive step of order a_{fat}). Hence, the effective relaxation time for withdrawal of the branch point along the fat tube is

$$\tau_{eff} = \frac{\zeta_{eff}}{k_b} = \frac{\zeta_b + \zeta_{bp}}{k_b} = \frac{\tau_{R,pp}}{\phi_b} + Z_b \phi_b \tau_{exp}, \quad (5.18)$$

where $\zeta_b/k_b = \tau_{R,pp}/\phi_b$ and $\tau_{R,pp}$ is the bare Rouse time of the pom-pom, which can be approximated by the expression: $\tau_{R,pp} = \tau_e Z_b (Z_b + 2Z_a)$ [52]. The first term of eq 5.18 is similar to τ_{eff} in the case of a binary blend of long and short linear chains [14] and

is associated with the friction resisting the motion of the backbone chain along the thin tube; the second term accounts for the extra friction due to the branch points. The exact value of τ_{eff} depends on τ_{exp} . By using the aforementioned parameterisation for q , ϕ_b , etc., and $\tau_{exp} = \tau_{obs} n^2$ (with $\tau_{obs} = 2\tau(0.5)/(3\pi^2 c_\nu)$), eq 5.18 gives $\tau_{eff} \approx 0.01s$ while for $\tau_{exp} = \tau(0)$ gives $\tau_{eff} \approx 1s$; as a compromise, in our calculations we have used $\tau_{eff} = 0.1s$.

While λ_{thin} and λ_{fat} are both less than q the stretch of the fat tube (consequently of the thin tube) can relax by virtue of diffusive steps, as discussed in section 1.5.2. Specifically, the arms of the pom-pom molecule are very fast relaxing objects (compared to the backbones) and each time an arm fully retracts (at $t = \tau_a = \tau(0)$) the branch point can make a diffusive hop of magnitude of order the diameter of the fat tube. The friction dominating this motion is coming from the branch points (because the branch points can only hop when the attached arms are fully relaxed) and not from the fast relaxing matrix arms that get in the way. For this kind of process the characteristic stretch relaxation time of the fat tube is τ_s (c.f. eq 1.64).

According to the arguments discussed in the three previous paragraphs the retraction rate for the 2CR model reads:

$$\tilde{w} = \begin{cases} \tilde{w}_t & \text{if } \lambda_{thin} > q \\ -\frac{(\lambda_{fat}-1)}{\tau_s \lambda_{fat}} - \frac{(\lambda_{fat}-q)}{\tilde{\tau} \lambda_{fat}} & \text{if } \lambda_{fat} > q, \lambda_{thin} < q \\ -\frac{(\lambda_{fat}-1)}{\tau_s \lambda_{fat}} & \text{if } \lambda_{fat}, \lambda_{thin} < q \end{cases}$$

where $\tilde{\tau}$ can either be τ_{CR} or τ_{eff} . The term \tilde{w}_t , corresponds to the case of branch-point withdrawal in the thin tube, and ensures that the maximum stretch condition, $\lambda_{thin} = q$, is fulfilled; the derivation of an equation for \tilde{w}_t is similar to the derivation of eq 5.13. The second expression, which is valid while $\lambda_{fat} > q$, and $\lambda_{thin} < q$, i.e. while branch point withdrawal in the fat tube happens, has two terms. The first one is a single retraction term that tends to keep the stretch of the fat tube to its equilibrium value of unity. This term's contribution to \tilde{w} will be small since τ_s is much bigger than $\tilde{\tau}$. The second term refers to branch point withdrawal in the fat tube; $\tilde{\tau}$ can either be the CR Rouse relaxation time of the thin tube, τ_{CR} , or the effective relaxation time τ_{eff} ; in our calculations below we consider both options. The third expression is used while λ_{fat} and $\lambda_{thin} < q$; it models stretch relaxation, towards the equilibrium value of unity, due to diffusive (hopping) branch point motion.

We now need to consider how the thin and fat tubes may be represented within the \mathbf{C}_p variable structure. The arguments for this representation are based on the ideas of Auhl et al. [14] for a bi-disperse melt of long and short linear chains. That is, one can consider a fat tube segment, with end-to-end vector \mathbf{R} , with n thin tube segments, with end-to-end vector \mathbf{r} , equilibrating within it; assuming Gaussian statistics it is proven [14] that

$$\langle r_\alpha r_\beta \rangle = \frac{1}{n^2} \langle R_\alpha R_\beta \rangle + \frac{1}{3} a^2 (1 - n^{-1}) \delta_{\alpha\beta}. \quad (5.19)$$

Let

$$\mathbf{A}_{thin} = \frac{3}{a^2} \langle \mathbf{r}\mathbf{r} \rangle, \quad \mathbf{A}_{fat} = \frac{3}{na^2} \langle \mathbf{R}\mathbf{R} \rangle. \quad (5.20)$$

If the thin tube equilibrates inside the fat tube, then by use of eqs 5.20 one can reexpress eq 5.19 as

$$\mathbf{A}_{thin} = \frac{1}{n} \mathbf{A}_{fat} + (1 - n^{-1}) \mathbf{I}. \quad (5.21)$$

We now need to represent this structure in terms of the tensor \mathbf{C}_p . In the current model the variable p describes different lengthscales in Fourier space, that is, big values of p correspond to small lengthscales in real space whereas lower values of p refer to larger lengthscales in real space. In this context we can introduce a cutoff value of p , namely p_c , such that structure for $p < p_c$ describes the fat tube; taking this idea into consideration, if the thin tube is equilibrated in the fat one then $\mathbf{C}_p = \mathbf{I}$ for $p > p_c$. In view of eq 5.11 and the aforementioned arguments, \mathbf{A}_{thin} is written as

$$\begin{aligned} \mathbf{A}_{thin} &= \frac{1}{\pi} \int_0^\pi dp \mathbf{C}_p = \frac{1}{\pi} \left(\int_0^{p_c} dp \mathbf{C}_p + \int_{p_c}^\pi dp \mathbf{I} \right), \\ &= \frac{1}{\pi} \int_0^{p_c} dp \mathbf{C}_p + \left(1 - \frac{p_c}{\pi} \right). \end{aligned} \quad (5.22)$$

By comparing the latter equation with eq 5.19 one finds that $\mathbf{A}_{fat} = n/\pi \int_0^{p_c} dp \mathbf{C}_p$ and that $n = \pi/p_c$; from Auhl et al. [14] we also know that $n = 1/\phi_L^{\alpha_d}$ and thus we arrive at $p_c = \pi\phi_b$, since the volume fraction of long chains in the case of the binary blend corresponds (in our case) to ϕ_b and moreover we have assumed that $\alpha_d = 1$. We are now in the position to present the analogous expressions to eqs 5.11 and 5.12, for the \mathbf{A} tensor and the stretch of the thin and fat tubes:

$$\mathbf{A}_{thin} = \frac{1}{\pi} \int_0^\pi dp \mathbf{C}_p, \quad \lambda_{thin}^2 = \frac{1}{3} \text{Tr} \mathbf{A}_{thin}, \quad (5.23a)$$

$$\mathbf{A}_{fat} = \frac{1}{p_c} \int_0^{p_c} dp \mathbf{C}_p, \quad \lambda_{fat}^2 = \frac{1}{3} \text{Tr} \mathbf{A}_{fat}, \quad (5.23b)$$

To summarise this paragraph, it is possible to represent the physics implied by eq 5.19, i.e. the physics of a thin tube equilibrating within a fat tube, by imposing particular spectrum of relaxation times for the \mathbf{C}_p variables. For $p > p_c$, \mathbf{C}_p is relaxed quickly by CR events due to the fast relaxing arms, but for $p < p_c$ the tensor \mathbf{C}_p is relaxed slowly; the region $p < p_c$ solely represents the dynamics of the fat tube structure.

Another issue that arises from the distinction of p space in two regions is what the appropriate CR rate should be in each region. In particular, we would like to represent CR dynamics by an equation similar to eq 5.6, i.e. an expression of the form

$$\frac{\partial}{\partial t} \mathbf{C}_p = + \dots - \frac{3\nu(p)}{\lambda} p^2 (\mathbf{C}_p - \mathbf{I}) + \dots \quad (5.24)$$

with the only exception that ν is a function of the variable p in this case. Above, we defined the effective rates of thin and fat tube hops as ν_{fast} and ν_{slow} , respectively. These rates are given by

$$\nu_{fast} = c_\nu \left(-\tilde{w} + \frac{1}{\tau(0.5)} \right), \quad \nu_{slow} = c_\nu \left(-\tilde{w} + \frac{1}{\tau_b \lambda_{fat}^2} \right). \quad (5.25)$$

Recall that \tilde{w} is typically negative. For the thin tube region ($p > p_c$) it is evident that the appropriate hop rate should be ν_{fast} since it represents the loss and creation of constraints at length scales of the thin tube. The choice ν_{slow} for the fat tube region ($p < p_c$) is the obvious one, but it is not the correct one. For $p < p_c$ we need an effective rate, ν_{ef} , which is the rate of CR hops acting at the lengthscale of the thin tube which gives the same large scale dynamics as hops at a rate, ν_{slow} , acting at fat tube lengthscale.

This effective rate is estimated as follows. There are Z_{fat} fat tube segments and Z_{thin} thin tube segments, with $Z_{fat} = Z_{thin}/n = Z_{thin}\phi_b$; here, the thin tube is a hypothetical tube which undergoes CR events at a rate ν_{ef} . The constraint release Rouse time of the fat tube, $\tau_{CR,f}$, and the respective time of the hypothetical thin tube, $\tau_{CR,t}$, are:

$$\tau_{CR,f} = \frac{2}{3\pi^2\nu_{slow}} Z_{fat}^2, \quad \tau_{CR,t} = \frac{2}{3\pi^2\nu_{ef}} Z_{thin}^2. \quad (5.26)$$

For the two rates to produce the same large scale dynamics we require $\tau_{CR,f} = \tau_{CR,t}$; this leads to the expression for the effective rate, which is $\nu_{ef} = \nu_{slow}/\phi_b^2$. However, as we integrate forward in time eq 5.24, ν_{slow} changes in every time step (according to eq 5.25, \tilde{w} and λ_{fat} are functions of time) and thus in general we could encounter occasions where $\nu_{ef} > \nu_{fast}$ (nevertheless, this is not the case in the calculations to be presented below).

In this case we chose $\nu_{ef} = \nu_{fast}$, i.e. we chose the minimum value between ν_{ef} and ν_{fast} ; if we had chosen to keep ν_{ef} that would have meant that the friction acting on the fat tube would come from the CR events of the arms and not from the CR events of the backbones. So, generally, $\nu(p)$ reads

$$\nu(p) = \begin{cases} \nu_{fast} & \text{for } p > p_c \\ \text{Min}(\nu_{ef}, \nu_{fast}) & \text{for } p < p_c \end{cases} \quad (5.27)$$

The results, of this section's theory, for uniaxial extension and shear are presented in Figs. 5.2 and 5.3, respectively. Specifically, the upper panel of these figures presents the viscosity while the bottom panels show the corresponding stretch in the thin tube (left) and in the fat tube (right). The lowest six rates are the same as the ones in Fig. 5.1; the highest three rates in Figs. 5.2 and 5.3 are: 10s^{-1} (wine colour), 50s^{-1} (orange), and 100s^{-1} (grey). Figures 5.2 and 5.3 have been obtained using the parameterisation: $q = 3$, $\phi_b = 0.3$, $Z_b = 25$, $Z_a \approx 10$, $\tau_b = 100\text{s}$, $\tau_s = 10\text{s}$, $\tau_{CR} = 1\text{s}$, $\tau_{eff} = 0.1\text{s}$ and $\tau(0.5) = 0.0001\text{s}$; the timescales are rounded off so that they are approximately the values obtained for $Z_b = 25$, $q = 3$ and $\tau_e = 10^{-7}\text{s}$. In both figures, the solid lines refer to $\tilde{\tau} = \tau_{CR}$ while the dotted lines to $\tilde{\tau} = \tau_{eff}$.

From Fig. 5.2 we observe that at all rates, apart the lowest one, extensional hardening occurs during start-up of the flow; moreover, a steady state strain thinning behaviour is also seen. By inspecting the results, we notice that the amount of hardening depends strongly on the relaxation time $\tilde{\tau}$ at intermediate rates (blue, magenta and dark yellow colours). In particular, the hardening is significantly weaker in the case in which $\tilde{\tau} = \tau_{eff}$ than in the case in which $\tilde{\tau} = \tau_{CR}$. This is due to the fact that τ_{eff} is one order of magnitude faster than τ_{CR} and therefore the process of branch point withdrawal in the fat tube becomes more effective; notice the difference in the fat tube stretch between the two cases; if τ_{eff} is used, then λ_{fat} is kept close to the value of the maximum stretch at these rates (c.f. the dotted lines, at these rates, in the right bottom panel). On the other hand, the four highest rates are of similar order of $1/\tau_{eff}$ and thus the difference between the solid and dotted lines is either small ($\dot{\epsilon} = 5\text{s}^{-1}$) or negligible (three highest rates). Although the maximum stretch is imposed on λ_{thin} we notice that an effective ‘‘maximum stretch’’, which depends on the flow-rate and the relaxation time $\tilde{\tau}$, is seen at λ_{fat} ; this is because λ_{fat} and λ_{thin} are coupled through eq 5.16; in fact, we have checked that eq 5.16 holds in the current ‘‘simulations’’. It is worth mentioning that no overshoot is

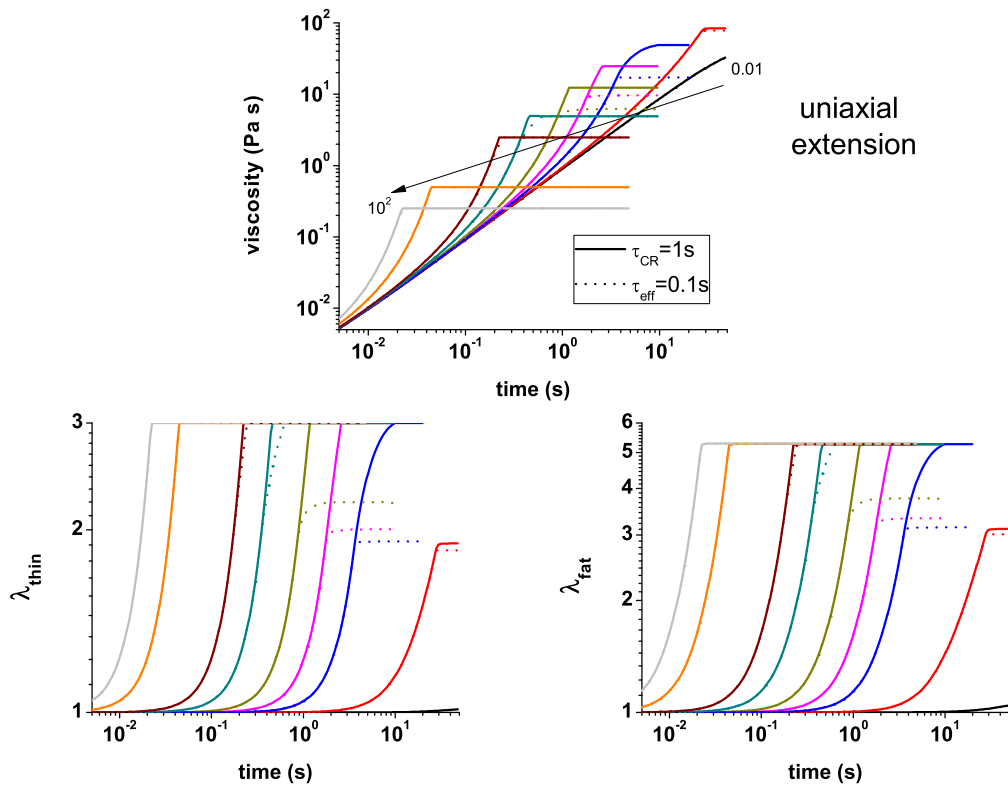


Figure 5.2: The 2CR model under uniaxial extension. Top: Viscosity vs time. Bottom: λ_{thin} and λ_{fat} (left and right side, respectively). The correspondence between colours and rates at the lowest six rates is the same as in Fig. 5.1. The highest three rates are 10s^{-1} , 50s^{-1} , 100s^{-1} and are represented by wine, orange and grey colours, respectively. At all panels the solid (dotted) lines refer to $\tilde{\tau} = \tau_{CR}$ ($\tilde{\tau} = \tau_{eff}$). For the parameterisation see the text.

seen at all examined rates. As regards the shear case (Fig. 5.3), we observe shear thinning behaviour, as expected. As for the elongational flow situation, λ_{fat} and λ_{thin} are lower in the case in which $\tilde{\tau} = \tau_{eff}$ than in the case in which $\tilde{\tau} = \tau_{CR}$; however, the difference between the solid and dotted lines is significant even at high rates since shear flow does not stretch tube segments as much as extensional flow does; with the exception of the three lowest rates, at which branch point withdrawal in the fat tube does not occur, the deviation between solid and dotted lines is negligible at the highest rate only.

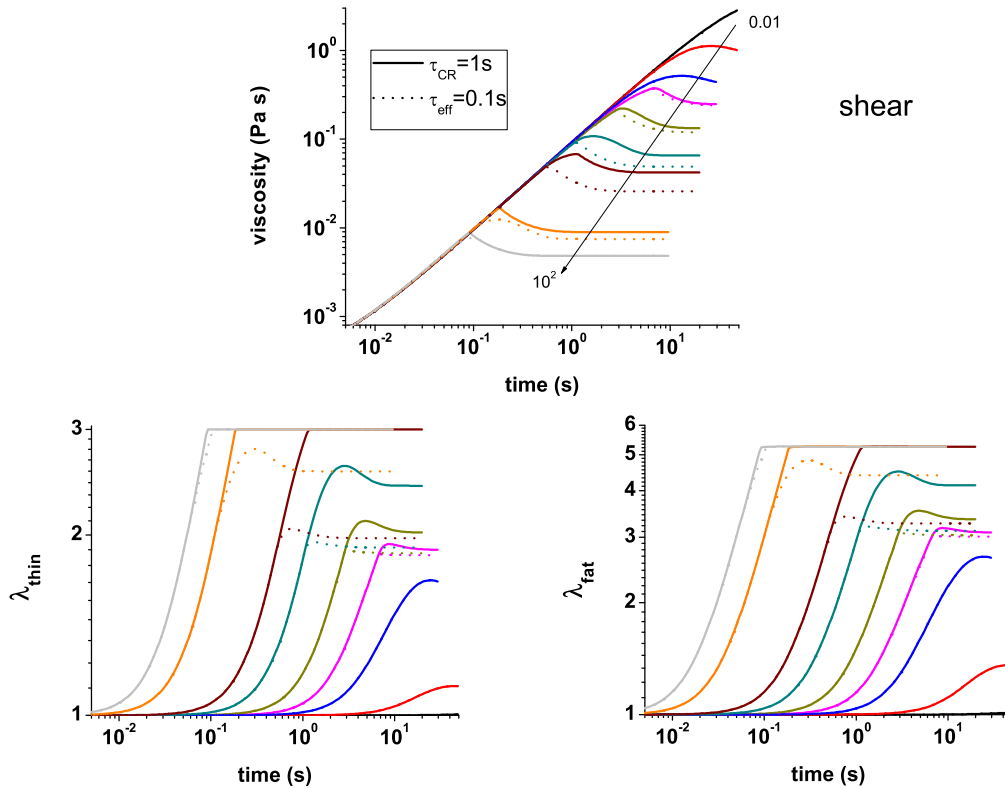


Figure 5.3: Same as Fig. 5.2 but for continuous shear flow.

5.2 Conclusions and future work

This chapter dealt with the inclusion of constraint release (CR) events in a melt of pom-pom molecules. The microscopic description of the CR events was based upon the conjecture that CR events produce local hops of the tube. This conjecture gives rise to a dynamical equation similar to the Rouse model [10, 11, 12, 13, 90]. Building upon the model of Read [13], the effects of CR events on the non-linear viscoelastic properties of the melt were examined.

Two particular cases were investigated. In the first one (1CR model) the attention was drawn on the CCR events which arise from relative motion between the pom-pom backbones. In the second one (2CR model) CR events due to relative motion between the backbones and surrounding arms were also taken into account. In the latter case it was assumed that CR events occur when arm retraction reaches the middle of an arm. In the description of the dynamics of the 2CR system the physical picture of thin and fat tubes was adopted, following Auhl et al. [14] and Read et al. [15]. In the context of these theories, the thin tube equilibrates inside the fat tube. Moreover, if stretch is imposed on

the fat tube, then stretch is induced in the thin tube.

Concerning the 2CR system a maximum stretch condition was imposed on the thin tube stretch, λ_{thin} . Branch point withdrawal in the fat tube was assumed to take place while $\lambda_{fat} \geq q$ and $\lambda_{thin} < q$. For this particular situation, two different mechanisms for stretch relaxation towards q were considered. As regards the first one, it was assumed that the friction dominating the branch point withdrawal process arises from the surrounding relaxing arms that get in the way. Hence, the relaxation timescale for this process was considered to be the CR-Rouse relaxation time of the whole thin tube, i.e. $\tilde{\tau} = \tau_{CR}$. In the second mechanism, following Ref. [14], it was supposed that λ_{fat} can relax via motion of the chain along the thin tube. The characteristic timescale for this process, $\tilde{\tau} = \tau_{eff}$, was associated with (i) the chain (backbone) friction, and (ii) the friction due to local motion of the branch points in the fat tube (c.f. eq 5.18). However, the exact value of τ_{eff} is not clear. With the chosen parameterisation, which corresponds to (i) well entangled arms, (ii) well self-entangled backbones, and (iii) a thin tube that is approximately 2-3 times more entangled than the fat tube, $0.01s \lesssim \tau_{eff} \lesssim 1s$, depending on the adopted timescale for branch point exploration of the fat tube. Here, the value 0.1s was used, that is, $\tau_{eff} = 0.1\tau_{CR}$. The main conclusions are outlined below:

- I. For both flows the 1CR model behaves similarly to the original pom-pom model in a qualitative sense; that is, during start-up of the flow it displays extensional hardening and shear thinning behaviour. For shear flow we saw that the inclusion of CCR events has a dramatic effect on the steady state value of the viscosity. Specifically, the inclusion of CCR events leads to much higher steady state values and so it weakens the maximum of the viscosity vs time curves at all non-linear shear rates.
- II. It was found that the 2CR model exhibits the same qualitative characteristics as the 1CR model: that is, it predicts strain hardening at elongation and thinning in shear. Although the maximum stretch is imposed on λ_{thin} , an effective maximum stretch is achieved in λ_{fat} . The latter depends, in general, on the flow rate and $\tilde{\tau}$. In extension, it was found that λ_{fat} stays close to q , at intermediate flow rates, in the case in which stretch relaxation occurs via motion of the chain along the thin tube. In contrast, in the case in which $\tilde{\tau} = \tau_{CR}$ the effective maximum stretch in λ_{fat} was achieved at $\lambda_{fat} \approx 2q$ for all examined rates, except the two lowest ones. Extensional viscosity

overshoots were not observed.

III. In all cases it was found that eq 5.16 is fulfilled. This suggests that one could set $C_p = \mathbf{I}$ for $p > p_c$ and possibly simplify the equations of the 2CR model.

There is strong experimental and theoretical evidence that branch polymers with long-chain branches, such as a pom-pom molecule, behave similarly under uniaxial and planar extensional flow [9, 63]. As future work, it could easily be verified if this is also the case for the 1CR and the 2CR model. Also, the influence of the number of arms on the stress response of the melt could be studied readily. Another future task is the comparison of the predictions of the 1CR and 2CR models with the experimental evidence of Nielsen et al. [161] and Rasmussen et al. [162] for a PS melt of pom-pom molecules.

However, the long term goal is to make the current model more realistic by taking into account the distribution of relaxation times along the arms. In other words, the 2CR model should be generalised to a continuous spectrum of CR rates. A plausible way of modeling this effect is to think of the backbone chain as being constrained by a nested tube structure, i.e. as being trapped within a tube which is itself trapped within a fatter tube etc. An attempt to combine/unify this nested tube structure with the overshoot model of chapter 4 is of interest.

Chapter 6

Concluding Remarks and future work

The scope of this thesis was to examine the dynamics and the flow properties of branched polymers by means of molecular theories. Particular attention was paid to (i) the local branch point motion and (ii) the modelling of the rheological properties of industrial melts. In the following, each topic is separately discussed.

6.1 Local branch point motion in branched polymers

With respect to this topic, the main subject of this thesis (see chapters 2 and 3) was to provide a theoretical framework for the description of the local motion of a branch point at early timescales, i.e. at times considerably shorter than the time taken for the arm retraction process to reach the branch point. Symmetric stars were considered due to their simplicity in respect to other branched molecules, and the abundance in (i) mean square displacement (MSD) data from Molecular Dynamics (MD) simulations and (ii) scattering data from Neutron Spin Echo (NSE) experiments, with which the theoretical predictions could be compared.

Building upon the Rouse model [71] and the Warner-Edwards picture of the tube [121, 122, 124], I derived analytical expressions for the mean square displacement (MSD) correlation functions for well entangled chains. These expressions describe the fluctuations of the actual chain about the mean path. It was found that the segmental MSD correlation function compares well with simulation data, obtained either in the presence or absence of standard constraint release (CR), after allowing for tube dilation

at timescales above the entanglement relaxation time. (When arm retraction and, in turn, CR were quenched some form of early tube dilation was allowed. Constraint release, when active, was considered to provide an additional rescaling of the tube diameter over and above the early tube dilation process.) Moreover, a dynamic version of the Random Phase Approximation, which incorporated the early tube dilation process in the MSD functions, successfully captured the decline of the NSE scattering data after the Rouse regime. (See Fig. 3.11.) The physical interpretation of these two findings is as follows: while the very deep contour length fluctuations of the arms are not yet activated, the dynamics of the branch point is governed by fluctuations (transverse motion) about the mean path. These fluctuations evolve within a “tube” that gradually dilates as a function of time (c.f. Fig. 2.9).

Limitations and future work

The expansion of the position vector and the fluctuation term in eigenmodes (eqs 2.4 and 2.22) will be different for other polymer architectures since the boundary conditions (apart one) are dependant on the polymer topology. This will of course reflect on the expressions for the MSD correlation functions. So one could attempt to extend the presented model to other branched polymer structures, obtain the MSD functions and compare them with the expressions derived here. However, the good agreement between the simulation data and the model, for the MSD of the central branch point of the Cayley tree, suggests that the analytical MSD functions developed here could provide a reasonable description of the local branch point dynamics of more complex architectures, provided that the arms emerging from the branch point are symmetric.

An outstanding issue with the theoretical framework developed here is the molecular origin of the so-called early tube dilation process. Visual inspection of branch point trajectories, in the MD simulations with fixed ends, indicated that the branch point can make short excursions along the tubes of each arm (called diving modes [132]). Another plausible scenario is that, the slight increase of the simulation data at timescales above the entanglement relaxation time, is caused by tension equilibration along the constraining chains, a process of redistribution of segments along the mean path. An important question to be answered in this case is whether the increase in the MSD simulation data is caused by longitudinal motion of a chain section upon which the branch point resides or is

a result of transverse motion (about the mean path) within a dilated tube due to softening of the confining potential.

The inclusion of longitudinal motion in the MSD functions is necessary if one wishes to model the dynamics of segments that are not positioned in the vicinity of the branch point. Besides longitudinal motion, the aforementioned task requires the inclusion of the arm retraction process. Another avenue of future research could be related to the incorporation of bending modes in the model: that is, one could consider a free energy that, apart from bending of the mean path, penalises bending of the actual chain also. The omission of this piece of physics may explain the discrepancies between the simulation data and the theoretical predictions for the normalised coherent scattering function (Fig. 3.13).

6.2 Constitutive modelling of industrial complexity melts

The understanding of the flow properties of industrial melts is a significant step towards synthesizing polymers by design. Industrial melts like LDPE have varied random long chain branching due to the synthesis technique used. As a result the constitutive modelling of their flow properties, even in the linear rheological regime, is a demanding task [157]. Typically, in the non-linear regime, such polymer melts manifest severe extensional hardening even at relatively slow flow rates. They also exhibit shear thinning as melts of linear polymers. By considering a melt of monodisperse pom-pom molecules, McLeish and Larson [8] captured the qualitative rheological behavior of LDPEs in both shear and extension. Inkson et al. [9] demonstrated that a multimode version of the pom-pom model is able to account quantitatively for LDPE rheology in three different geometries of flows. However, their model is incapable of capturing new FSR (Filament Stretching Rheometer) data that indicate a viscosity overshoot under steady (uniaxial) extensional flow [6]. In this thesis (c.f. chapter 4) it was shown that a variant of the multimode pom-pom model that includes entanglement stripping compares well with the aforementioned FSR data. Compared to other modified versions of the original model [6], which also enable extensional viscosity overshoots, the version developed here provides an underlying molecular reason for the viscosity overshoot. This is entanglement stripping which within the framework of the model originates from the relative motion between a given test backbone and the matrix backbones, during the processes of normal chain retraction

or/and branch point withdrawal.

Using the FSR rheometer, it is also possible to measure the relaxation of stress following cessation of the extensional flow [6, 7]. I demonstrated that the so-called constitutive equation A, in which the evolutionary equation for the backbone orientation corresponds to the equation of the original differential version of the pom-pom model, behaves very poorly in relaxation after extensional flow due to the un-physically low rate of tube reconfiguration. So, I have attempted to match all experimental data for the sample DOW150R (i.e. measurements of stress under steady extensional flow and measurements of stress relaxation following the steady flow) using an alternative constitutive equation in which the rate of tube reconfiguration is simply the inverse of the orientation relaxation time. Although the full version of the model was found to be ineffective to fit all data with a single parameterisation, it was shown that a minimal version of the model can provide a reasonable, but not perfect, fit to all data.

Limitations and future work

Further data comparison is required in order to assess the superior performance of the minimal model before any definitive conclusions can be drawn. In this sense, both models must be tested in other types of simple flows (e.g. shear) or/and complex flows like the cross-slot flow [6, 62, 100]. However, the fact remains that the decoupling of different sections of a connected molecule is a crude approximation. In reality the different layers of a branched molecule are coupled in their dynamics, and this can give rise to additional effects not captured in the decoupled multimode model. The difficulty in fitting all data simultaneously does point towards this direction. Efforts to couple the dynamics of different layers of branched polymers are limited [165] and, moreover, a detailed tube model for the non-linear rheology of branched polymers has not yet been developed in general. There is a necessity of more precise treatment of the input physics in such tube models. A consideration of the local influence of CR events (arising from relative motion between backbones and surrounding arms) is essential in this context. Some preliminary calculations in chapter 5 suggest that both convective and thermal CR events are not related to the extensional viscosity overshoots. Before any definitive conclusions can be drawn, however, the model developed in chapter 5 should be generalised to a continuous spectrum of CR rates.

Appendices

A Unentangled stars.

A.1 ‘Diagonal’ terms which contain $\Psi_{p'}^c \Psi_p^c$ and $\Psi_{q'}^{s_i} \Psi_q^{s_i}$ and ‘non diagonal’ terms which contain $\Psi_{q'}^{s_i} \Psi_p^c$ and $\Psi_{q'}^{s_i} \Psi_q^{s_j}$.

If one multiplies eq 2.7 with the sums

$$\sum_{\alpha=1}^f \int_0^{N_a} \sum_{p'} \Psi_{p'}^c(\ell) d\ell, \sum_{\alpha=1}^f \int_0^{N_a} \sum_{q'} \Psi_{q'}^{s_1}(\alpha, \ell) d\ell, \dots, \sum_{\alpha=1}^f \int_0^{N_a} \sum_{q'} \Psi_{q'}^{s_{f'}}(\alpha, \ell) d\ell,$$

will get terms that contain products of all possible combinations of the eigenmodes Ψ_p^c and $\Psi_q^{s_i}$. For example the rhs of eq 2.7 includes ‘diagonal’ terms which contain products of the form $\Psi_{p'}^c \Psi_p^c$ and $\Psi_{q'}^{s_i} \Psi_q^{s_i}$, and ‘non diagonal’ terms with products like $\Psi_{q'}^{s_i} \Psi_p^c$ and $\Psi_{q'}^{s_i} \Psi_q^{s_j}$.

The contribution of the ‘diagonal’ terms $\Psi_{p'}^c \Psi_p^c$ and $\Psi_{q'}^{s_i} \Psi_q^{s_i}$ is

$$\begin{aligned} \Psi_{p'}^c \Psi_p^c &\rightarrow -k \sum_{\alpha=1}^f \int_0^{N_a} \sum_{p'} \sum_p \left(\frac{p\pi}{N_a} \right)^2 \mathbf{X}_p^c \Psi_{p'}^c \Psi_p^c d\ell \\ &= -k \sum_{p'} \sum_p \mathbf{X}_p^c \left(\frac{p\pi}{N_a} \right)^2 \sum_{\alpha=1}^f \int_0^{N_a} \cos \left(\frac{p'\pi\ell}{N_a} \right) \cos \left(\frac{p\pi\ell}{N_a} \right) d\ell \\ &= - \sum_p k_p^c \mathbf{X}_p^c \end{aligned}$$

and

$$\begin{aligned}
 \Psi_{q'}^{s_i} \Psi_q^{s_i} &\rightarrow -k \sum_{\alpha=1}^f \int_0^{N_a} \sum_{q'} \sum_q \left(\frac{(2q-1)\pi}{2N_a} \right)^2 \mathbf{X}_q^{s_i} \Psi_{q'}^{s_i} \Psi_q^{s_i} d\ell \\
 &= -k \sum_{q'} \sum_q \left[\mathbf{X}_q^{s_i} \left(\frac{(2q-1)\pi}{2N_a} \right)^2 \right. \\
 &\quad \left. \times \underbrace{\sum_{\alpha=1}^f s_{i\alpha}^2}_{f} \int_0^{N_a} \sin \left(\frac{(2q'-1)\pi\ell}{2N_a} \right) \sin \left(\frac{(2q-1)\pi\ell}{2N_a} \right) d\ell \right] \\
 &= - \sum_q k_q^{s_i} \mathbf{X}_q^{s_i},
 \end{aligned}$$

respectively. The contribution of the “non diagonal” terms is

$$\begin{aligned}
 \Psi_{q'}^{s_i} \Psi_p^c &\rightarrow -k \sum_{\alpha=1}^f \int_0^{N_a} \sum_{q'} \sum_p \left(\frac{p\pi}{N_a} \right)^2 \mathbf{X}_p^c \Psi_{q'}^{s_i} \Psi_p^c d\ell \\
 &= -k \sum_{q'} \sum_p \left[\mathbf{X}_p^c \left(\frac{p\pi}{N_a} \right)^2 \right. \\
 &\quad \left. \times \underbrace{\sum_{\alpha=1}^f s_{i\alpha}}_0 \int_0^{N_a} \sin \left(\frac{(2q'-1)\pi\ell}{2N_a} \right) \cos \left(\frac{p\pi\ell}{N_a} \right) d\ell \right] \\
 &= 0
 \end{aligned}$$

$$\begin{aligned}
 \Psi_{q'}^{s_i} \Psi_q^{s_j} &\rightarrow -k \sum_{\alpha=1}^f \int_0^{N_a} \sum_{q'} \sum_q \left(\frac{(2q-1)\pi}{2N_a} \right)^2 \mathbf{X}_q^{s_j} \Psi_{q'}^{s_i} \Psi_q^{s_j} d\ell \\
 &= -k \sum_{q'} \sum_q \left[\mathbf{X}_q^{s_j} \left(\frac{(2q-1)\pi}{2N_a} \right)^2 \right. \\
 &\quad \left. \times \underbrace{\sum_{\alpha=1}^f s_{i\alpha} s_{j\alpha}}_0 \int_0^{N_a} \sin \left(\frac{(2q'-1)\pi\ell}{2N_a} \right) \sin \left(\frac{(2q-1)\pi\ell}{2N_a} \right) d\ell \right] \\
 &= 0
 \end{aligned}$$

From these calculations it is apparent that only the “diagonal” terms survive because of eqs 2.6a and 2.6c. Since p, q, p', q', i and j are dummy indices we anticipate terms containing the products $\Psi_{q'}^{s_i} \Psi_p^c$ and $\Psi_{p'}^c \Psi_q^{s_i}$ to give the same contribution. The same applies to terms with $\Psi_{q'}^{s_i} \Psi_q^{s_j}$ and $\Psi_{q'}^{s_j} \Psi_q^{s_i}$.

A.2 Mean square displacement correlation functions.

In this Appendix we deal with unentangled stars. Specifically, we are interested in deriving the expressions for the MSD of segments positioned on the same and on different arms, that is, we seek to calculate, respectively, the correlation functions $\langle (\mathbf{r}_{\alpha,\ell,t} - \mathbf{r}_{\alpha,\ell',t'})^2 \rangle = \langle \mathbf{r}_{\alpha,\ell,t} \cdot \mathbf{r}_{\alpha,\ell,t} \rangle + \langle \mathbf{r}_{\alpha,\ell',t'} \cdot \mathbf{r}_{\alpha,\ell',t'} \rangle - 2 \langle \mathbf{r}_{\alpha,\ell,t} \cdot \mathbf{r}_{\alpha,\ell',t'} \rangle$ and $\langle (\mathbf{r}_{\alpha,\ell,t} - \mathbf{r}_{\beta,\ell',t'})^2 \rangle = \langle \mathbf{r}_{\alpha,\ell,t} \cdot \mathbf{r}_{\alpha,\ell,t} \rangle + \langle \mathbf{r}_{\beta,\ell',t'} \cdot \mathbf{r}_{\beta,\ell',t'} \rangle - 2 \langle \mathbf{r}_{\alpha,\ell,t} \cdot \mathbf{r}_{\beta,\ell',t'} \rangle$. Therefore, we need to calculate $\langle \mathbf{r}_{\alpha,\ell,t} \cdot \mathbf{r}_{\alpha,\ell',t'} \rangle$ and $\langle \mathbf{r}_{\alpha,\ell,t} \cdot \mathbf{r}_{\beta,\ell',t'} \rangle$. Using eq 2.4, $\langle \mathbf{r}_{\alpha,\ell,t} \cdot \mathbf{r}_{\alpha,\ell',t'} \rangle$ is calculated as follows

$$\begin{aligned}
 & \langle \mathbf{r}_{\alpha,\ell,t} \cdot \mathbf{r}_{\alpha,\ell',t'} \rangle = \\
 & \left\langle \left[\sum_p \mathbf{X}_p^c(t) \Psi_p^c(\ell) + \sum_q \left(\mathbf{X}_q^{s_1}(t) \Psi_q^{s_1}(\alpha, \ell) + \dots + \mathbf{X}_q^{s_{f'}}(t) \Psi_q^{s_{f'}}(\alpha, \ell) \right) \right] \right. \\
 & \left. \left[\sum_{p'} \mathbf{X}_{p'}^c(t') \Psi_{p'}^c(\ell') + \sum_{q'} \left(\mathbf{X}_{q'}^{s_1}(t') \Psi_{q'}^{s_1}(\alpha, \ell') + \dots + \mathbf{X}_{q'}^{s_{f'}}(t') \Psi_{q'}^{s_{f'}}(\alpha, \ell') \right) \right] \right\rangle \\
 & = \sum_{p,p'} \underbrace{\langle \mathbf{X}_p^c(t) \cdot \mathbf{X}_{p'}^c(t') \rangle}_{\text{eq 2.11a}} \Psi_p^c(\ell) \Psi_{p'}^c(\ell') + \sum_{q,q'} \underbrace{\left(\langle \mathbf{X}_q^{s_1}(t) \cdot \mathbf{X}_{q'}^{s_1}(t') \rangle \right)}_{\text{eq 2.11b}} \Psi_q^{s_1}(\alpha, \ell) \Psi_{q'}^{s_1}(\alpha, \ell') + \\
 & \dots + \underbrace{\left(\langle \mathbf{X}_q^{s_{f'}}(t) \cdot \mathbf{X}_{q'}^{s_{f'}}(t') \rangle \right)}_{\text{eq 2.11b}} \Psi_q^{s_{f'}}(\alpha, \ell) \Psi_{q'}^{s_{f'}}(\alpha, \ell') \\
 & = \frac{2N_a b^2}{f\pi^2} \sum_p \left[\frac{1}{p^2} \Psi_p^c(\ell) \Psi_p^c(\ell') \exp(-\tilde{t}_{R_a} p^2) \right] + \frac{8N_a b^2}{f\pi^2} \sum_q \left[\frac{1}{(2q-1)^2} \times \right. \\
 & \left. \left(\Psi_q^{s_1}(\alpha, \ell) \Psi_q^{s_1}(\alpha, \ell') + \dots + \Psi_q^{s_{f'}}(\alpha, \ell) \Psi_q^{s_{f'}}(\alpha, \ell') \right) \exp\left(\frac{-\tilde{t}_{R_a} (2q-1)^2}{4}\right) \right] \\
 & = \frac{2N_a b^2}{f\pi^2} \left[\int_0^\infty \frac{\cos\left(\frac{p\pi\ell}{N_a}\right) \cos\left(\frac{p\pi\ell'}{N_a}\right)}{p^2} \exp(-\tilde{t}_{R_a} p^2) dp + \right. \\
 & \left. \underbrace{\left(s_{1\alpha}^2 + \dots + s_{f'\alpha}^2 \right)}_{f-1} \int_0^\infty \frac{\sin\left(\frac{p\pi\ell}{N_a}\right) \sin\left(\frac{p\pi\ell'}{N_a}\right)}{p^2} \exp(-\tilde{t}_{R_a} p^2) dp \right] \\
 & = \frac{N_a b^2}{\pi^2} \int_0^\infty \frac{\exp(-\tilde{t}_{R_a} p^2)}{p^2} \left[\cos\left(\frac{p\pi|\ell - \ell'|}{N_a}\right) - \left(\frac{f-2}{f}\right) \cos\left(\frac{p\pi(\ell + \ell')}{N_a}\right) \right] dp \\
 & = -\frac{N_a b^2}{\pi^{1.5}} \sqrt{\tilde{t}_{R_a}} \exp\left(\frac{-\pi^2|\ell - \ell'|^2}{4N_a^2 \tilde{t}_{R_a}}\right) - \frac{b^2|\ell - \ell'|}{2} \Phi\left(\frac{\pi|\ell - \ell'|}{2N_a \sqrt{\tilde{t}_{R_a}}}\right) + \\
 & \frac{N_a b^2 \left(\frac{f-2}{f}\right)}{\pi^{1.5}} \sqrt{\tilde{t}_{R_a}} \exp\left(\frac{-\pi^2(\ell + \ell')^2}{4N_a^2 \tilde{t}_{R_a}}\right) + \frac{b^2(\ell + \ell') \left(\frac{f-2}{f}\right)}{2} \Phi\left(\frac{\pi(\ell + \ell')}{2N_a \sqrt{\tilde{t}_{R_a}}}\right), \tag{A.1}
 \end{aligned}$$

where $\Phi(x) = \frac{2}{\sqrt{\pi}} \int_0^x e^{-u^2} du$ is the error function. A similar calculation for $\langle \mathbf{r}_{\alpha,\ell,t} \cdot \mathbf{r}_{\beta,\ell',t'} \rangle$ can be performed to obtain

$$\begin{aligned}
 & \langle \mathbf{r}_{\alpha,\ell,t} \cdot \mathbf{r}_{\beta,\ell',t'} \rangle = \\
 & \left\langle \left[\sum_p \mathbf{X}_p^c(t) \Psi_p^c(\ell) + \sum_q \left(\mathbf{X}_q^{s_1}(t) \Psi_q^{s_1}(\alpha, \ell) + \dots + \mathbf{X}_q^{s_{f'}}(t) \Psi_q^{s_{f'}}(\alpha, \ell) \right) \right] \cdot \right. \\
 & \left. \left[\sum_{p'} \mathbf{X}_{p'}^c(t') \Psi_{p'}^c(\ell') + \sum_{q'} \left(\mathbf{X}_{q'}^{s_1}(t') \Psi_{q'}^{s_1}(\beta, \ell') + \dots + \mathbf{X}_{q'}^{s_{f'}}(t') \Psi_{q'}^{s_{f'}}(\beta, \ell') \right) \right] \right\rangle \\
 & = \sum_{p,p'} \underbrace{\langle \mathbf{X}_p^c(t) \cdot \mathbf{X}_{p'}^c(t') \rangle}_{\text{eq 2.11a}} \Psi_p^c(\ell) \Psi_{p'}^c(\ell') + \sum_{q,q'} \left(\underbrace{\langle \mathbf{X}_q^{s_1}(t) \cdot \mathbf{X}_{q'}^{s_1}(t') \rangle}_{\text{eq 2.11b}} \Psi_q^{s_1}(\alpha, \ell) \Psi_{q'}^{s_1}(\beta, \ell') + \right. \\
 & \left. \dots + \underbrace{\langle \mathbf{X}_q^{s_{f'}}(t) \cdot \mathbf{X}_{q'}^{s_{f'}}(t') \rangle}_{\text{eq 2.11b}} \Psi_q^{s_{f'}}(\alpha, \ell) \Psi_{q'}^{s_{f'}}(\beta, \ell') \right) \\
 & = \frac{2N_a b^2}{f\pi^2} \sum_p \left[\frac{1}{p^2} \Psi_p^c(\ell) \Psi_p^c(\ell') \exp(-\tilde{t}_{R_a} p^2) \right] + \frac{8N_a b^2}{f\pi^2} \sum_q \left[\frac{1}{(2q-1)^2} \times \right. \\
 & \left. \left(\Psi_q^{s_1}(\alpha, \ell) \Psi_q^{s_1}(\beta, \ell') + \dots + \Psi_q^{s_{f'}}(\alpha, \ell) \Psi_q^{s_{f'}}(\beta, \ell') \right) \exp\left(\frac{-\tilde{t}_{R_a} (2q-1)^2}{4}\right) \right] \\
 & = \frac{2N_a b^2}{f\pi^2} \left[\int_0^\infty \frac{\cos\left(\frac{p\pi\ell}{N_a}\right) \cos\left(\frac{p\pi\ell'}{N_a}\right)}{p^2} \exp(-\tilde{t}_{R_a} p^2) dp + \right. \\
 & \left. \underbrace{(s_{1\alpha} s_{1\beta} + \dots + s_{f'\alpha} s_{f'\beta})}_{-1} \int_0^\infty \frac{\sin\left(\frac{p\pi\ell}{N_a}\right) \sin\left(\frac{p\pi\ell'}{N_a}\right)}{p^2} \exp(-\tilde{t}_{R_a} p^2) dp \right] \\
 & = \frac{2N_a b^2}{f\pi^2} \int_0^\infty \frac{\cos\left(\frac{p\pi(\ell+\ell')}{N_a}\right)}{p^2} \exp(-\tilde{t}_{R_a} p^2) dp \\
 & = -\frac{2N_a b^2}{f\pi^{1.5}} \sqrt{\tilde{t}_{R_a}} \exp\left(\frac{-\pi^2(\ell+\ell')^2}{4N_a^2 \tilde{t}_{R_a}}\right) - \frac{b^2(\ell+\ell')}{f} \Phi\left(\frac{\pi(\ell+\ell')}{2N_a \sqrt{\tilde{t}_{R_a}}}\right) \tag{A.2}
 \end{aligned}$$

From eqs A.1 and A.2 the correlation functions $\langle \mathbf{r}_{\alpha,\ell,t} \cdot \mathbf{r}_{\alpha,\ell,t} \rangle$ and $\langle \mathbf{r}_{\alpha,\ell',t'} \cdot \mathbf{r}_{\alpha,\ell',t'} \rangle$ are readily obtained. The results are

$$\langle \mathbf{r}_{\alpha,\ell,t} \cdot \mathbf{r}_{\alpha,\ell,t} \rangle = \left(\frac{f-2}{f} \right) b^2 \ell \tag{A.3a}$$

$$\langle \mathbf{r}_{\alpha,\ell',t'} \cdot \mathbf{r}_{\alpha,\ell',t'} \rangle = \left(\frac{f-2}{f} \right) b^2 \ell' = \langle \mathbf{r}_{\beta,\ell',t'} \cdot \mathbf{r}_{\beta,\ell',t'} \rangle. \tag{A.3b}$$

Using eqs A.1, A.2 and A.3 we arrive at the final expressions for $\langle (\mathbf{r}_{\alpha,\ell,t} - \mathbf{r}_{\alpha,\ell',t'})^2 \rangle$ and $\langle (\mathbf{r}_{\alpha,\ell,t} - \mathbf{r}_{\beta,\ell',t'})^2 \rangle$, which are given by

$$\langle (\mathbf{r}_{\alpha,\ell,t} - \mathbf{r}_{\alpha,\ell',t'})^2 \rangle = \frac{2N_a b^2 \sqrt{\tilde{t}_{R_a}}}{\pi^{1.5}} \left[\exp\left(\frac{-\pi^2 |\ell - \ell'|^2}{4N_a^2 \tilde{t}_{R_a}}\right) - \left(\frac{f-2}{f}\right) \exp\left(\frac{-\pi^2 (\ell + \ell')^2}{4N_a^2 \tilde{t}_{R_a}}\right) \right] + b^2 |\ell - \ell'| \Phi\left(\frac{\pi |\ell - \ell'|}{2N_a \sqrt{\tilde{t}_{R_a}}}\right) - \left(\frac{f-2}{f}\right) b^2 (\ell + \ell') \left[\Phi\left(\frac{\pi (\ell + \ell')}{2N_a \sqrt{\tilde{t}_{R_a}}}\right) - 1 \right],$$

and

$$\langle (\mathbf{r}_{\alpha,\ell,t} - \mathbf{r}_{\beta,\ell',t'})^2 \rangle = \frac{b^2 (\ell + \ell')}{f} \left[(f-2) + 2\Phi\left(\frac{\pi (\ell + \ell')}{2N_a \sqrt{\tilde{t}_{R_a}}}\right) \right] + \frac{4N_a b^2 \sqrt{\tilde{t}_{R_a}}}{f \pi^{1.5}} \exp\left(\frac{-\pi^2 (\ell + \ell')^2}{4N_a^2 \tilde{t}_{R_a}}\right).$$

These are the expressions presented in the first and second row of table 2.1, respectively.

I mention that in the derivation of eqs A.1 and A.2 I have approximated the sums by integrals, and I have assumed that $2p - 1 = 2p$ (and $2q - 1 = 2q$) which physically means that the fast Rouse modes (i.e. large p, q) dominate the dynamics. Moreover, I have used eqs 2.11 for the evaluation of the correlation function of the mode amplitudes and the trigonometric identities

$$2 \cos(\tilde{A}) \cos(\tilde{B}) = \cos(\tilde{A} - \tilde{B}) + \cos(\tilde{A} + \tilde{B}) \quad (\text{A.4a})$$

$$2 \sin(\tilde{A}) \sin(\tilde{B}) = \cos(\tilde{A} - \tilde{B}) - \cos(\tilde{A} + \tilde{B}) \quad (\text{A.4b})$$

Finally, the integrals that appear in the final step of the derivation of eqs A.1 and A.2 are evaluated by making use of the formula

$$\int_0^\infty \frac{\cos(Ax) \exp(-Bx^2)}{x^2} dx = -\sqrt{\pi B} \exp\left(\frac{-A^2}{4B}\right) - \frac{A\pi}{2} \Phi\left(\frac{A}{2\sqrt{B}}\right), \quad A, B \geq 0 \quad (\text{A.5})$$

B Entangled stars: Mean square displacement correlation functions.

To obtain the MSD correlation functions for entangled chains, one needs to calculate the averages $\langle \Delta_{\alpha,\ell,t} \cdot \Delta_{\alpha,\ell',t'} \rangle$ and $\langle \Delta_{\alpha,\ell,t} \cdot \Delta_{\beta,\ell',t'} \rangle$, where $\Delta_{\alpha,\ell,t}$ is the fluctuation term given by eq 2.22. These averages are calculated in an identical fashion to eqs A.1 and A.2 of Appendix A.2. However, one has to make use of eqs 2.23 instead of eqs 2.11. In particular, $\langle \Delta_{\alpha,\ell,t} \cdot \Delta_{\alpha,\ell',t'} \rangle$ and $\langle \Delta_{\alpha,\ell,t} \cdot \Delta_{\beta,\ell',t'} \rangle$ are calculated as follows:

$$\begin{aligned}
 & \langle \Delta_{\alpha,\ell,t} \cdot \Delta_{\alpha,\ell',t'} \rangle = \\
 & \left\langle \left[\sum_p \mathbf{Y}_p^c(t) \Psi_p^c(\ell) + \sum_q \left(\mathbf{Y}_q^{s_1}(t) \Psi_q^{s_1}(\alpha, \ell) + \dots + \mathbf{Y}_q^{s_{f'}}(t) \Psi_q^{s_{f'}}(\alpha, \ell) \right) \right] \cdot \right. \\
 & \left. \left[\sum_{p'} \mathbf{Y}_{p'}^c(t') \Psi_{p'}^c(\ell') + \sum_{q'} \left(\mathbf{Y}_{q'}^{s_1}(t') \Psi_{q'}^{s_1}(\alpha, \ell') + \dots + \mathbf{Y}_{q'}^{s_{f'}}(t') \Psi_{q'}^{s_{f'}}(\alpha, \ell') \right) \right] \right\rangle \\
 & = \frac{2N_a b^2}{f\pi^2} \left[\int_0^\infty \frac{\cos\left(\frac{p\pi\ell}{N_a}\right) \cos\left(\frac{p\pi\ell'}{N_a}\right)}{p^2 + \left(\frac{\sqrt{h_s} N_a}{\pi}\right)^2} \exp\left(-\tilde{t}_{Ra} \left[p^2 + \left(\frac{\sqrt{h_s} N_a}{\pi}\right)^2 \right] \right) dp + \right. \\
 & \quad \left. \underbrace{(s_{1\alpha}^2 + \dots + s_{f'\alpha}^2)}_{f-1} \int_0^\infty \frac{\sin\left(\frac{p\pi\ell}{N_a}\right) \sin\left(\frac{p\pi\ell'}{N_a}\right)}{p^2 + \left(\frac{\sqrt{h_s} N_a}{\pi}\right)^2} \exp\left(-\tilde{t}_{Ra} \left[p^2 + \left(\frac{\sqrt{h_s} N_a}{\pi}\right)^2 \right] \right) dp \right] \\
 & = \frac{N_a b^2}{\pi^2} \int_0^\infty \frac{\cos\left(\frac{p\pi|\ell-\ell'|}{N_a}\right)}{p^2 + \left(\frac{\sqrt{h_s} N_a}{\pi}\right)^2} \exp\left(-\tilde{t}_{Ra} \left[p^2 + \left(\frac{\sqrt{h_s} N_a}{\pi}\right)^2 \right] \right) dp - \\
 & \quad \frac{N_a b^2}{\pi^2} \left(\frac{f-2}{f}\right) \int_0^\infty \frac{\cos\left(\frac{p\pi(\ell+\ell')}{N_a}\right)}{p^2 + \left(\frac{\sqrt{h_s} N_a}{\pi}\right)^2} \exp\left(-\tilde{t}_{Ra} \left[p^2 + \left(\frac{\sqrt{h_s} N_a}{\pi}\right)^2 \right] \right) dp \\
 & = \frac{b^2 \sqrt{N_s}}{4} \left[2 \cosh\left(\frac{|\ell-\ell'|}{\sqrt{N_s}}\right) - \exp\left(\frac{-|\ell-\ell'|}{\sqrt{N_s}}\right) \Phi\left(\frac{N_a \sqrt{\tilde{t}_{Ra}}}{\pi \sqrt{N_s}} - \frac{\pi|\ell-\ell'|}{2N_a \sqrt{\tilde{t}_{Ra}}}\right) \right] - \\
 & \quad \frac{b^2 \sqrt{N_s}}{4} \left[\exp\left(\frac{|\ell-\ell'|}{\sqrt{N_s}}\right) \Phi\left(\frac{N_a \sqrt{\tilde{t}_{Ra}}}{\pi \sqrt{N_s}} + \frac{\pi|\ell-\ell'|}{2N_a \sqrt{\tilde{t}_{Ra}}}\right) \right] - \frac{b^2 \sqrt{N_s}}{4} \left(\frac{f-2}{f}\right) \\
 & \quad \times \left[2 \cosh\left(\frac{(\ell+\ell')}{\sqrt{N_s}}\right) - \exp\left(\frac{-(\ell+\ell')}{\sqrt{N_s}}\right) \Phi\left(\frac{N_a \sqrt{\tilde{t}_{Ra}}}{\pi \sqrt{N_s}} - \frac{\pi(\ell+\ell')}{2N_a \sqrt{\tilde{t}_{Ra}}}\right) \right] + \\
 & \quad \frac{b^2 \sqrt{N_s}}{4} \left(\frac{f-2}{f}\right) \left[\exp\left(\frac{(\ell+\ell')}{\sqrt{N_s}}\right) \Phi\left(\frac{N_a \sqrt{\tilde{t}_{Ra}}}{\pi \sqrt{N_s}} + \frac{\pi(\ell+\ell')}{2N_a \sqrt{\tilde{t}_{Ra}}}\right) \right], \tag{B.6}
 \end{aligned}$$

and

$$\begin{aligned}
 & \langle \Delta_{\alpha,\ell,t} \cdot \Delta_{\beta,\ell',t'} \rangle = \\
 & \left\langle \left[\sum_p \mathbf{Y}_p^c(t) \Psi_p^c(\ell) + \sum_q \left(\mathbf{Y}_q^{s_1}(t) \Psi_q^{s_1}(\alpha, \ell) + \dots + \mathbf{Y}_q^{s_{f'}}(t) \Psi_q^{s_{f'}}(\alpha, \ell) \right) \right] \cdot \right. \\
 & \left. \left[\sum_{p'} \mathbf{Y}_{p'}^c(t') \Psi_{p'}^c(\ell') + \sum_{q'} \left(\mathbf{Y}_{q'}^{s_1}(t') \Psi_{q'}^{s_1}(\beta, \ell') + \dots + \mathbf{Y}_{q'}^{s_{f'}}(t') \Psi_{q'}^{s_{f'}}(\beta, \ell') \right) \right] \right\rangle \\
 & = \frac{2N_a b^2}{f\pi^2} \left[\int_0^\infty \frac{\cos\left(\frac{p\pi\ell}{N_a}\right) \cos\left(\frac{p\pi\ell'}{N_a}\right)}{p^2 + \left(\frac{\sqrt{h_s} N_a}{\pi}\right)^2} \exp\left(-\tilde{t}_{Ra} \left[p^2 + \left(\frac{\sqrt{h_s} N_a}{\pi}\right)^2 \right] \right) dp + \right. \\
 & \quad \left. \underbrace{(s_{1\alpha} s_{1\beta} + \dots + s_{f'\alpha} s_{f'\beta})}_{-1} \int_0^\infty \frac{\sin\left(\frac{p\pi\ell}{N_a}\right) \sin\left(\frac{p\pi\ell'}{N_a}\right)}{p^2 + \left(\frac{\sqrt{h_s} N_a}{\pi}\right)^2} \exp\left(-\tilde{t}_{Ra} \left[p^2 + \left(\frac{\sqrt{h_s} N_a}{\pi}\right)^2 \right] \right) dp \right] \\
 & = \frac{2N_a b^2}{f\pi^2} \int_0^\infty \frac{\cos\left(\frac{p\pi(\ell+\ell')}{N_a}\right)}{p^2 + \left(\frac{\sqrt{h_s} N_a}{\pi}\right)^2} \exp\left(-\tilde{t}_{Ra} \left[p^2 + \left(\frac{\sqrt{h_s} N_a}{\pi}\right)^2 \right] \right) dp \\
 & = \frac{b^2 \sqrt{N_s}}{2f} \left[2 \cosh\left(\frac{(\ell+\ell')}{\sqrt{N_s}}\right) - \exp\left(\frac{-(\ell+\ell')}{\sqrt{N_s}}\right) \Phi\left(\frac{N_a \sqrt{\tilde{t}_{Ra}}}{\pi \sqrt{N_s}} - \frac{\pi(\ell+\ell')}{2N_a \sqrt{\tilde{t}_{Ra}}}\right) \right] - \\
 & \quad \frac{b^2 \sqrt{N_s}}{2f} \left[\exp\left(\frac{(\ell+\ell')}{\sqrt{N_s}}\right) \Phi\left(\frac{N_a \sqrt{\tilde{t}_{Ra}}}{\pi \sqrt{N_s}} + \frac{\pi(\ell+\ell')}{2N_a \sqrt{\tilde{t}_{Ra}}}\right) \right], \tag{B.7}
 \end{aligned}$$

where $\Phi(x) = \frac{2}{\sqrt{\pi}} \int_0^x e^{-u^2} du$ is the error function. As in the respective derivations in Appendix A.2 we approximated the sums as integrals. Furthermore, we assumed that the dynamics of the chain within the localising potential is governed by fast Rouse modes, i.e. the approximations $2p - 1 = 2p$ and $2q - 1 = 2q$ have been made. In this case the integrals in the final step of the above derivations are evaluated using the formula

$$\begin{aligned}
 & \int_0^\infty \frac{\cos(Ax) \exp(-Bx^2)}{x^2 + C^2} dx = \frac{\pi}{2C} \exp(BC^2) \cosh(AC) - \frac{\pi}{4C} \exp(BC^2) \\
 & \quad \times \left[\exp(-CA) \Phi\left(C\sqrt{B} - \frac{A}{2\sqrt{B}}\right) + \exp(CA) \Phi\left(C\sqrt{B} + \frac{A}{2\sqrt{B}}\right) \right], \tag{B.8}
 \end{aligned}$$

where $A, B \geq 0$ and $C > 0$.

The results for $\langle \Delta_{\alpha,\ell,t} \cdot \Delta_{\alpha,\ell',t'} \rangle$ and $\langle \Delta_{\alpha,\ell,t} \cdot \Delta_{\beta,\ell',t'} \rangle$ can be expressed in tube coordinates using the transformation rules $\tilde{t}_{Ra} = \tilde{t}_e N_e^2 (N_a^2)^{-1}$, $a^2 = N_e b^2 = \sqrt{N_s k_b^{-1}} b^2$ (recall that $N_s = h_s^{-1}$) and $s = \ell N_e^{-1}$ leading to

$$\begin{aligned}
 & \langle \Delta_{\alpha,s,t} \cdot \Delta_{\alpha,s',t'} \rangle = \frac{a^2 \sqrt{k_b}}{2} \left[\cosh\left(\frac{|s-s'|}{\sqrt{k_b}}\right) - \left(\frac{f-2}{f}\right) \cosh\left(\frac{(s+s')}{\sqrt{k_b}}\right) \right] - \\
 & \quad \frac{a^2 \sqrt{k_b}}{4} \left[(\Omega_-^A(s, s', \tilde{t}_e) + \Omega_+^A(s, s', \tilde{t}_e)) + \left(\frac{f-2}{f}\right) (\Omega_-^B(s, s', \tilde{t}_e) + \Omega_+^B(s, s', \tilde{t}_e)) \right] \tag{B.9}
 \end{aligned}$$

and

$$\langle \Delta_{\alpha,s,t} \cdot \Delta_{\beta,s',t'} \rangle = \frac{a^2 \sqrt{k_b}}{2f} \left[2 \cosh \left(\frac{(s+s')}{\sqrt{k_b}} \right) - \Omega_+^B(s, s', \tilde{t}_e) - \Omega_-^B(s, s', \tilde{t}_e) \right], \quad (\text{B.10})$$

respectively, with

$$\Omega_-^A(s, s', \tilde{t}_e) = \exp \left(\frac{-|s-s'|}{\sqrt{k_b}} \right) \Phi \left(\frac{\sqrt{\tilde{t}_e}}{\pi \sqrt{k_b}} - \frac{\pi |s-s'|}{2\sqrt{\tilde{t}_e}} \right), \quad (\text{B.11a})$$

$$\Omega_+^A(s, s', \tilde{t}_e) = \exp \left(\frac{|s-s'|}{\sqrt{k_b}} \right) \Phi \left(\frac{\sqrt{\tilde{t}_e}}{\pi \sqrt{k_b}} + \frac{\pi |s-s'|}{2\sqrt{\tilde{t}_e}} \right), \quad (\text{B.11b})$$

$$\Omega_-^B(s, s', \tilde{t}_e) = \exp \left(\frac{-(s+s')}{\sqrt{k_b}} \right) \Phi \left(\frac{\sqrt{\tilde{t}_e}}{\pi \sqrt{k_b}} - \frac{\pi (s+s')}{2\sqrt{\tilde{t}_e}} \right), \quad (\text{B.11c})$$

$$\Omega_+^B(s, s', \tilde{t}_e) = \exp \left(\frac{(s+s')}{\sqrt{k_b}} \right) \Phi \left(\frac{\sqrt{\tilde{t}_e}}{\pi \sqrt{k_b}} + \frac{\pi (s+s')}{2\sqrt{\tilde{t}_e}} \right). \quad (\text{B.11d})$$

From equations B.9 and B.10 we also obtain

$$\langle \Delta_{\alpha,s,t} \cdot \Delta_{\alpha,s,t} \rangle = \frac{a^2 \sqrt{k_b}}{2} \left[1 - \left(\frac{f-2}{f} \right) \exp \left(\frac{-2s}{\sqrt{k_b}} \right) \right], \quad (\text{B.12a})$$

$$\langle \Delta_{\alpha,s',t'} \cdot \Delta_{\alpha,s',t'} \rangle = \frac{a^2 \sqrt{k_b}}{2} \left[1 - \left(\frac{f-2}{f} \right) \exp \left(\frac{-2s'}{\sqrt{k_b}} \right) \right] = \langle \Delta_{\beta,s',t'} \cdot \Delta_{\beta,s',t'} \rangle. \quad (\text{B.12b})$$

Having obtained equations B.9, B.10 and B.12 the contribution of the fluctuations terms $\langle (\Delta_{\alpha,s,t} - \Delta_{\alpha,s',t'})^2 \rangle$ and $\langle (\Delta_{\alpha,s,t} - \Delta_{\beta,s',t'})^2 \rangle$ to the respective MSD are calculated readily. The results for segments positioned on the same and on different arms are given by

$$\begin{aligned} \langle (\Delta_{\alpha,s,t} - \Delta_{\alpha,s',t'})^2 \rangle &= a^2 \sqrt{k_b} - \frac{a^2 \sqrt{k_b}}{2} \left(\frac{f-2}{f} \right) \left[\exp \left(\frac{-2s}{\sqrt{k_b}} \right) + \exp \left(\frac{-2s'}{\sqrt{k_b}} \right) \right] - \\ &\frac{a^2 \sqrt{k_b}}{2} \left[2 \cosh \left(\frac{|s-s'|}{\sqrt{k_b}} \right) - \Omega_-^A(s, s', \tilde{t}_e) - \Omega_+^A(s, s', \tilde{t}_e) \right] + \frac{a^2 \sqrt{k_b}}{2} \left(\frac{f-2}{f} \right) \\ &\times \left[2 \cosh \left(\frac{(s+s')}{\sqrt{k_b}} \right) - \Omega_-^B(s, s', \tilde{t}_e) - \Omega_+^B(s, s', \tilde{t}_e) \right], \text{ and} \end{aligned} \quad (\text{B.13a})$$

$$\begin{aligned} \langle (\Delta_{\alpha,s,t} - \Delta_{\beta,s',t'})^2 \rangle &= a^2 \sqrt{k_b} - \frac{a^2 \sqrt{k_b}}{2} \left(\frac{f-2}{f} \right) \left[\exp \left(\frac{-2s}{\sqrt{k_b}} \right) + \exp \left(\frac{-2s'}{\sqrt{k_b}} \right) \right] - \\ &\frac{a^2 \sqrt{k_b}}{f} \left[2 \cosh \left(\frac{(s+s')}{\sqrt{k_b}} \right) - \Omega_-^B(s, s', \tilde{t}_e) - \Omega_+^B(s, s', \tilde{t}_e) \right], \end{aligned} \quad (\text{B.13b})$$

respectively. At equilibrium (i.e. at $\tilde{t}_e = 0$), these expression reduce to eqs 2.26a and 2.26b, respectively.

C Tube survival probability from the simulations.

C.1 The correlation function $\Psi_{s_\ell}^{MD}(t)$ for the Cayley tree.

In this Appendix the extension of equation 2.33 for the Cayley tree is discussed. In the case of the three arm symmetric star the three indices $\alpha, \beta, \gamma \in \{1, 2, 3\}$ denote the three arms. Moreover, two numerical coefficients, namely B' and C' , are required. These coefficients provide the weight of the correlation between the arm α and the two other arms β and γ , which in this particular case is $-1/2$ for both arms. In the Cayley tree, however, there are more than three arms and so some extra care is needed in the definition of $\Psi_{s_\ell}^{MD}(t)$. Specifically, each (long) arm of the Cayley tree is divided into two different sections, an inner and an outer. The former contains the portion of the chain between the central branch point and the branch point of the side arm. The latter includes the portion of the chain between the branch point of the side arm and the free end of the (long) arm. Moreover, one has to consider the side arm. The different sections of the Cayley tree are indicated with dashed black arrows in the upper panel of Fig. C.1 (c.f. panel II).

Depending on the position of $\mathbf{u}_{\alpha, s_\ell, 0}$ three different cases emerge:

- I $\mathbf{u}_{\alpha, s_\ell, 0}$ is positioned on the outer section α of the long arm. In this case the tangent vector is correlated with the end-to-end vector $\mathbf{R}_{\alpha, t}^e$ of section α and with the end-to-end vector $\mathbf{R}_{\beta, t}^e$ of the inner section β of the long arm. The weight of the correlation between sections α and β is $B' = -1$, hence $\Psi_{s_\ell}^{MD}(t) = \langle \mathbf{u}_{\alpha, s_\ell, 0} \cdot (\mathbf{R}_{\alpha, t}^e - \mathbf{R}_{\beta, t}^e) \rangle$.
- II $\mathbf{u}_{\alpha, s_\ell, 0}$ is positioned on the inner section α of the long arm. In this case the tangent vector is correlated, apart from $\mathbf{R}_{\alpha, t}^e$, with the end-to-end vectors of the inner sections β and γ of the other two long arms. The weight of each of these correlations is $-1/2$, as for the star. Thus, $B' = C' = -1/2$. However, in this particular case a third prefactor D' is required. This prefactor provides the weight of the correlation between $\mathbf{u}_{\alpha, s_\ell, 0}$ and the end-to-end vector $\mathbf{R}_{\delta, t}^e$ of the outer section δ of the same arm. $D' = -1$ so $\Psi_{s_\ell}^{MD}(t) = \langle \mathbf{u}_{\alpha, s_\ell, 0} \cdot (\mathbf{R}_{\alpha, t}^e - \frac{1}{2}\mathbf{R}_{\beta, t}^e - \frac{1}{2}\mathbf{R}_{\gamma, t}^e - \mathbf{R}_{\delta, t}^e) \rangle$,
- III $\mathbf{u}_{\alpha, s_\ell, 0}$ is positioned on the side arm α . This case is treated in a manner similar to the symmetric star. Thus, $\mathbf{u}_{\alpha, s_\ell, 0}$ is correlated, except from $\mathbf{R}_{\alpha, t}^e$, with the end-to-

end vectors of the inner and outer parts of the attached long arm and so $\Psi_{s_\ell}^{MD}(t) = \langle \mathbf{u}_{\alpha, s_\ell, 0} \cdot (\mathbf{R}_{\alpha, t}^e - \frac{1}{2}\mathbf{R}_{\beta, t}^e - \frac{1}{2}\mathbf{R}_{\gamma, t}^e) \rangle$.

The upper panel of Fig. C.1 illustrates schematically these three cases while the bottom panel of the same figure presents the case of the symmetric star. In this schematic illustration $\mathbf{u}_{\alpha, s_\ell, 0}$ is positioned within the red coloured arm/section of the chain. The different arms/sections are denoted by the indices $\alpha, \beta, \gamma, \delta$, etc. Furthermore, the numbers labelling particular sections are the weights of the correlation between these sections and the red coloured portion of the chain, In other words these numbers are the prefactors B', C' , etc. used in eq 2.33. The non “self” (i.e. $\mathbf{u}_{\alpha, s_\ell, 0}$ with $\mathbf{R}_{\alpha, t}^e$) and non zero correlations are indicated with solid blue arrows.

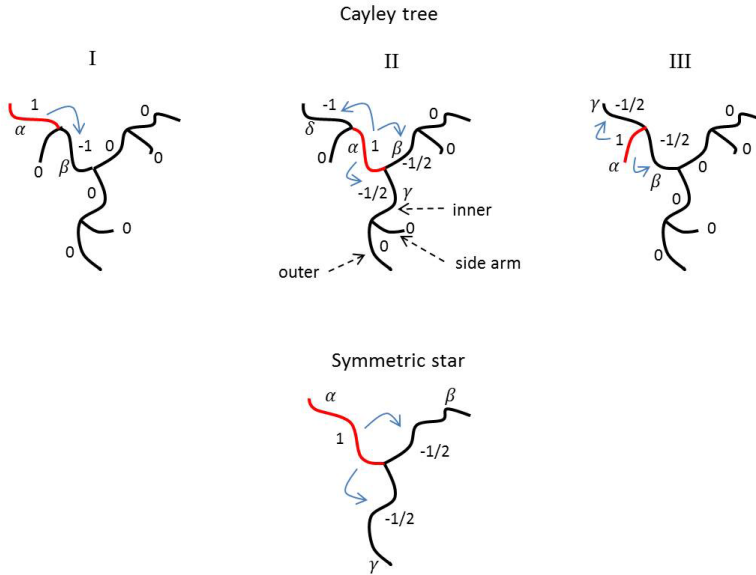


Figure C.1: Upper: Schematic representation of the correlations used for $\Psi_{s_\ell}^{MD}(t)$ of the Cayley tree. The red colour highlights the section of the chain in which $\mathbf{u}_{\alpha, s_\ell, 0}$ is embedded. Panels I, II and III refer to the respective cases discussed in the text. The dashed black arrows in panel II indicate the position of the inner and outer sections of the long arm and the position of the side arm on the molecule. Different sections are denoted by $\alpha, \beta, \gamma, \delta$, etc. Moreover, numbers labelling particular sections are the prefactors used in the analogous correlation function of eq 2.33 for the Cayley tree. Bottom: Schematic representation of the correlations used for $\Psi_{s_\ell}^{MD}(t)$ of the three arm symmetric star. In this case α, β, γ refer to different arms. The numbers labelling the arms β and γ are the prefactors B', C' used in eq 2.33.

C.2 Relaxation spectra and the fit of $\psi(t)$ to KWW functions.

In this Appendix the relaxation spectra $[s_\ell; \tau_\ell]$, as obtained from the simulations, of the symmetric star and of the Cayley tree are presented. Moreover, from these relaxation spectra the tube survival probabilities for all arms (parts) of the star (Cayley tree), i.e. the functions $\Xi_{\alpha,\beta,\gamma}(t)$ introduced in subsection 2.4.2, are constructed by fitting the spectra to stretched exponential (KWW) functions.

Table 1 presents $[s_\ell; \tau_{s_\ell}]$ of an arm of the symmetric star. (It also shows the values of β used in eq 2.34.) Obviously, the relaxation spectrum of the other two arms is identical since the molecule is symmetric. The procedure for obtaining $[s_\ell; \tau_{s_\ell}]$ has been described in subsection 2.4.2. The same procedure is followed for obtaining the respective spectrum of the Cayley tree. As illustrated in Fig. C.1 of Appendix C.1 the long arm of the Cayley tree is divided into two parts, an inner and an outer. Furthermore, a shorter side arm is attached to each long arm. The relaxation spectrums of these sections of the Cayley tree are shown in table 2. Individual values of β were used for each segment (not shown). With respect to the long arm s_ℓ spans the chain length, running from 0 (central branch point) to 1 (arm tip). In a similar manner, at the branch point of the side arm $s_\ell = 0$ and at the arm tip of the side arm $s_\ell = 1$. We note that the relaxation times τ_{s_ℓ} of both tables 1 and 2 are expressed in simulation units, τ_0^{MD} .

Table 1: The relaxation spectrum of the 888 star
as obtained from the simulations.

s_ℓ	$\tau_{s_\ell} (\tau_0^{MD})$	β	s_ℓ	$\tau_{s_\ell} (\tau_0^{MD})$	β
0.955	1963.3	0.477	0.605	1.794×10^6	0.755
0.905	14295.7	0.663	0.555	2.454×10^6	0.792
0.855	70135.6	0.649	0.505	3.256×10^6	0.758
0.805	186334.0	0.709	0.455	5.880×10^6	0.803
0.755	387779.0	0.748	0.405	7.119×10^6	0.978
0.705	679654.0	0.803	0.355	1.289×10^7	0.813
0.655	999064.0	0.758	0.305	1.886×10^7	0.832

From the data presented in tables 1 and 2 (the individual values of β , however, are not considered), the tube survival probability of each arm (part) of the star (Cayley tree) can

Table 2: The relaxation spectrum of the Cayley tree as obtained from the simulations.

outer		inner		side	
s_ℓ	$\tau_{s_\ell}(\tau_0^{MD})$	s_ℓ	$\tau_{s_\ell}(\tau_0^{MD})$	s_ℓ	$\tau_{s_\ell}(\tau_0^{MD})$
0.955	1337.0	0.455	4.83756×10^7	0.820	1515.0
0.905	13897.0	0.405	8.59760×10^7	0.620	14670.0
0.855	52538.0	0.355	9.97643×10^7	0.420	53863.0
0.805	177762.0	0.305	1.09860×10^8	0.220	216842.0
0.755	344709.0	0.255	1.52558×10^8	0.02	832773.0
0.705	545827.0	0.205	4.62460×10^8	0.0	1.52558×10^8
0.655	1.40402×10^6				
0.605	2.82788×10^6				
0.555	6.92447×10^6				
0.505	1.29450×10^7				

be constructed by fitting the $(1 - s_\ell)$ vs τ_{s_ℓ} curves to a stretched KWW function:

$$\Xi_\alpha(t) = \exp \left[- \left(\frac{t}{\tau_{\Xi_\alpha}} \right)^{\beta_{\Xi_\alpha}} \right]. \tag{C.14}$$

From this procedure one obtains two values, one for τ_{Ξ_α} and another one for β_{Ξ_α} , for each arm (part) of the star (Cayley tree). For an arm of the symmetric star these values are $\tau_{\Xi_\alpha} = 10887400.0\tau_0^{MD}$ and $\beta_{\Xi_\alpha} = 0.365865$. These parameters are identical for every arm hence $\Xi_\alpha(t) = \Xi_\beta(t) = \Xi_\gamma(t)$. The respective parameters for the outer and inner parts and the side arm of the Cayley tree are given in table 3. Using the fitted functions $\Xi_{\alpha,\beta,\gamma}(t)$ one can estimate the total tube survival probability, $\psi(t)$, using eq 2.35. The estimated $\psi(t)$, for both the star and the Cayley tree, is plotted in Fig. 2.11.

Table 3: KWW parameters for the functions $\Xi_\alpha(t), \Xi_\beta(t), \Xi_\gamma(t)$ of the different sections of the Cayley tree.

outer		inner		side	
$\tau_\Xi(\tau_0^{MD})$	β_Ξ	$\tau_\Xi(\tau_0^{MD})$	β_Ξ	$\tau_\Xi(\tau_0^{MD})$	β_Ξ
861556.0	0.395767	333549000.0	0.845396	74373.1	0.442203

D Numerical solution for the 1CR and 2CR models

This Appendix summarises the way in which the equations of section 5.1 were dealt with numerically. To compute the quantities of interest, i.e. the stress and the stretch, one needs to integrate forward in time eq 5.6, which is a nonlinear partial differential equation. The \mathbf{C}_p are subject to the initial condition $\mathbf{C}_p = \mathbf{I}$, at $t = 0$, and the boundary conditions $\mathbf{C}_p = 0$ for $p > \pi$ and $p < -\pi$. In practice, one can make use of the symmetry $\mathbf{C}_p = \mathbf{C}_{-p}$ and only deal with one of the $-\pi \leq p \leq 0$ and $0 \geq p \geq \pi$ domains; here, we chose to compute the \mathbf{C}_p in the latter domain. This is achieved by using a finite difference scheme, in which the elements of the \mathbf{C}_p tensor are defined on regularly spaced values of $\ln p = x$ at

$$p_i = \exp(x_i) \quad \text{with} \quad (\text{D.15a})$$

$$x_i = x_{min} + \left(i - \frac{1}{2}\right) \Delta x, \quad \text{for } i = 0, m, \quad (\text{D.15b})$$

where $\Delta x = (x_{max} - x_{min})/m$; $x_{max} = \ln \pi$ while $x_{min} = \ln p_{min}$; for p_{min} we have used the cut-off value of 10^{-6} . Within this discretisation scheme $x_{min} = x_{i=0} + 0.5\Delta x$ and $x_{max} = x_{i=m} + 0.5\Delta x$. The \mathbf{C}_{m+1} matrix elements are set equal to zero.

The \mathbf{C}_p (\mathbf{C}_x) structure up to p_{min} (x_{min}) is treated as follows. We introduce the tensor \mathbf{A}_0 :

$$\mathbf{A}_0 = \frac{1}{p_{min}} \int_0^{p_{min}} dp \mathbf{C}_p \quad (\text{D.16})$$

with the time evolution of the \mathbf{C}_p being obtained from eq 5.6 after ignoring the CR contribution since it contains a p^2 term, that is, in this case the evolution equation of \mathbf{C}_p is

$$\frac{\partial \mathbf{C}_p}{\partial t} = \mathbf{K} \cdot \mathbf{C}_p + \mathbf{C}_p \cdot \mathbf{K}^T - \frac{1}{\lambda^2 \tau_b} (\mathbf{C}_p - \lambda^2 \mathbf{I}) + \tilde{w} \left(\mathbf{C}_p - p \frac{\partial \mathbf{C}_p}{\partial p} \right), \quad (\text{D.17})$$

thus $\partial \mathbf{A}_0 / \partial t$ reads

$$\frac{\partial \mathbf{A}_0}{\partial t} = \mathbf{K} \cdot \mathbf{A}_0 + \mathbf{A}_0 \cdot \mathbf{K}^T - \frac{1}{\lambda^2 \tau_b} (\mathbf{A}_0 - \lambda^2 \mathbf{I}) + \tilde{w} (2\mathbf{A}_0 - \mathbf{C}_{p_{min}}). \quad (\text{D.18})$$

To obtain the retraction term (last term of the latter equation) we have integrated by parts $\int_0^{p_{min}} dp p \partial \mathbf{C}_p / \partial p$. In the numerical solution, the $\mathbf{C}_{p_{min}}$ term is approximated by $(\mathbf{C}_{p=0} + \mathbf{C}_{p=1})/2$; in practice, we use $(\mathbf{C}_{x=0} + \mathbf{C}_{x=1})/2$ since we work out the solution in terms of \mathbf{C}_x .

For $p > p_{min}$ ($x > x_{min}$) we integrate forward in time, using a first order Euler method, the expression

$$\frac{\partial}{\partial t} \mathbf{C}_x = \mathbf{K} \cdot \mathbf{C}_x + \mathbf{C}_x \cdot \mathbf{K}^T - \frac{3\nu}{\lambda} \exp(2x) (\mathbf{C}_x - \mathbf{I}) - \frac{1}{\lambda^2 \tau_b} (\mathbf{C}_x - \lambda^2 \mathbf{I}) + \tilde{w} \left(\mathbf{C}_x - \frac{\partial \mathbf{C}_x}{\partial x} \right), \quad (\text{D.19})$$

which is eq 5.6 (with the inclusion of the reptation term) reexpressed in terms of \mathbf{C}_x . The form of flow term $\mathbf{K} \cdot \mathbf{C}_x + \mathbf{C}_x \cdot \mathbf{K}^T$, in both shear and uniaxial extension, is readily obtained using the matrixes of table 1.1 (the same applies to the flow terms of eq D.18). The derivative $\partial \mathbf{C}_x / \partial x$ is evaluated using a first order upwind finite difference scheme [166]:

$$\frac{\partial \mathbf{C}_x}{\partial x} = \text{upwx}_i = \begin{cases} (\mathbf{C}_{x=i} - \mathbf{C}_{x=i-1}) / \Delta x & \text{if } \tilde{w} > 0 \\ (\mathbf{C}_{x=i+1} - \mathbf{C}_{x=i}) / \Delta x & \text{if } \tilde{w} \leq 0 \end{cases} \quad (\text{D.20})$$

If $\tilde{w} \leq 0$, which is typically the case, then we use the second expression of eq D.20 for $i = 0, \dots, m$. On the other hand, if $\tilde{w} > 0$, then we use the the first expression of eq D.20 for $i = 2, \dots, m$; for $i = 1$ we use $(\mathbf{C}_{x=1} - \mathbf{A}_0) / \Delta x$ while for $i = 0$ the derivative is set to zero.

It is apparent from eq 5.13 that in order to evaluate the retraction rate at the maximum stretch condition one needs to compute integrals of the form $\int_0^\pi dp p (\partial \text{tr} \mathbf{C}_p / \partial p)$, $\int_0^\pi dp p^2 \text{tr} \mathbf{C}_p$; the former integral is computed as follows

$$\begin{aligned} \int_0^\pi dp p \left(\frac{\partial}{\partial p} \text{tr} \mathbf{C}_p \right) &= \int_0^{p_{min}} dp p \left(\frac{\partial}{\partial p} \text{tr} \mathbf{C}_p \right) + \int_{x_{min}}^{x_{max}} dx \exp(x) \left(\frac{\partial}{\partial x} \text{tr} \mathbf{C}_x \right) \\ &= p_{min} (\text{tr} \mathbf{C}_{p_{min}} - \text{tr} \mathbf{A}_0) + \sum_{i=1}^m \exp(x_i) \text{tr}(\text{upwx}_i) \Delta x, \end{aligned} \quad (\text{D.21})$$

while the CR integral is evaluated as

$$\begin{aligned} \int_0^\pi dp p^2 \text{tr} \mathbf{C}_p &= \underbrace{\int_0^{p_{min}} dp p^2 \text{tr} \mathbf{C}_p}_{\approx 0} + \int_{x_{min}}^{x_{max}} dx \exp(3x) \text{tr} \mathbf{C}_x \\ &= \sum_{i=1}^m \exp(3x_i) \text{tr} \mathbf{C}_{x_i} \Delta x. \end{aligned} \quad (\text{D.22})$$

In the 2CR model, in particular in the calculation of the retraction rate for branch point withdrawal in the thin tube, the above integrals are computed in a similar fashion; however, we split the integrals into the following three domains: $0 \leq p \leq p_{min}$,

$x_{min} < x \leq x_c$ and $x_c < x \leq x_{max}$, where $x_c = \ln p_c$. With respect to the reptation term in the 2CR model we assume that it takes place in the fat tube; this particular choice does not have an effect on the results of the previous section, since at the timescales of interest orientation relaxes locally via the CR events and not via reptation. As regards the prefactor λ in eq 5.24, which is related with the CR dynamics in the thin and fat tubes, for each tube we use the respective stretch.

For the 1CR model and the 2CR model, $m = 601$ and $m = 101$, respectively; in both cases, a converged solution can be found with significantly fewer modes. For the finite difference scheme to be stable we require $\Delta x > \tilde{w}\Delta t$ or equivalently $\Delta t < (x_{max} - x_{min})/m|\tilde{w}|$; in addition, $\Delta t < 1/\nu_{fast}$ in the case of the two CR rates; taking into consideration these requirements we have used $\Delta t = 5 \times 10^{-4}$ for the 1CR model and $\Delta t = 5 \times 10^{-7}$ for the 2CR model. Finally, we quote the basic structure of the algorithms, which is the following:

```

for  $t = 0$ ,  $\rightarrow$   $\lambda = 1$ ,  $\mathbf{C}_x = 1$ ,  $\mathbf{A}_0 = 1$ ,  $\tilde{w} = 0$ 
do  $t = t + \Delta t$ 
  update  $\mathbf{A}_0, \mathbf{C}_x$ 
  update  $\lambda$ 
  update  $\tilde{w}$ 
  compute  $\sigma$ 
end do

```

E Nomenclature

Abbreviation	Definition	Chapter
CSER	Cross-slot extensional rheometer.	1, 4
CLF	Contour length fluctuations	1, 3
CR	Constraint release.	1-5
CR-Rouse	Constraint-release Rouse (process).	1
DE	Doi and Edwards (tube model).	1
DEMG	Marrucci-Grizzuti (tube model).	1
DCPP	Double convected pom-pom (model).	1, 4
eq	Equation.	1-5
ETD	Early tube dilation.	2, 3
EV	Excluded volume (interactions).	3
Fig.	Figure.	1-5
FSR	Filament stretching rheometer.	1, 4, 5
HI	Hydrodynamic interactions.	1
LDPE	Low density polyethylene.	1,4
LCB	Long chain branching.	1,4
MC	Monte Carlo (simulations).	1
MD	Molecular Dynamics (simulations).	1, 2, 3
MSD	Mean square displacement.	1, 2, 3
mPP	multimode pom-pom (model).	1, 4
NSE	Neutron spin echo (technique).	1, 2, 3
PP	Primitive path.	1
SAOS	Small-amplitude oscillatory shear.	1
SER	Sentmanat extension rheometer.	1,4
XPP	Extended pom-pom (model).	1, 4

Symbol	Definition. [Units (if non-dimensionless).]	Chapter
A	Arbitrary tensor variable in the dumbbell model (eq 1.39).	1
	Auxiliary tensor in the pom-pom model. (See eq 1.63.)	1, 4
	Arbitrary tensor variable. (See eq 5.11.)	5
\mathbf{A}_{fat}	Arbitrary tensor variable representing fat tube structure.	5
\mathbf{A}_{thin}	Arbitrary tensor variable representing thin tube structure.	5
a	Tube diameter. [m]	1, 2, 3
	Tube diameter of the thin tube. [m]	5
$a_{ef}(t)$	Effective tube diameter during dynamic dilution. [m]	1
a_{fat}	Tube diameter of the fat tube. [m]	5
\mathcal{B}	Arbitrary variable. (See eqs 4.1 and 4.9.)	4
b	Kuhn length. [m]	1, 2, 3
b_i	Scattering length (amplitude) of the nucleus i . [m]	1
$b_i^{coh} = \langle b_i \rangle_{isot}^{spin}$	The scattering length, b_i , averaged over isotopes and spin states, i.e. the coherent scattering length of nucleus i . [m]	1, 3
b_i^{inc}	Incoherent scattering length of the nucleus i . [m]	1, 3
$\tilde{b}_{coh,H}, \tilde{b}_{inc,H}$	Coherent and incoherent scattering length of the protonated ($-[CH_2 - CHD - CHD - CH_2]-$) “monomers” in the NSE experiment. [m]	1, 3
$\tilde{b}_{coh,D}, \tilde{b}_{inc,D}$	Coherent and incoherent scattering length of the deuterated ($-[CD_2 - CD_2 - CD_2 - CD_2]-$) “monomers” in the NSE experiment. [m]	1, 3
c	Monomer concentration. [kg m^{-3}]	1
c_ν	Constraint release parameter. (See eq 5.9b.)	5
\mathbf{C}_p	Arbitrary tensor variable. (See eqs 5.4 and 5.6.)	5
D	Rate of deformation (strain rate) tensor. [s^{-1}]	1
D_{bp}	Diffusion coefficient of a branch point. [$\text{m}^2 \text{s}^{-1}$]	1, 5
D_{CM}	Diffusion coefficient of a Rouse chain. [$\text{m}^2 \text{s}^{-1}$]	1
f	Number of arms in a polymer star.	2, 3
f'	$f - 1$.	2, 3
f	Elastic force. (Vector.) [kg m s^{-2}]	1
f_ν	ν -component of the force f . [kg m s^{-2}]	1

Symbol	Definition	Chapter
\mathbf{f}_ℓ	Spring force acting on segment ℓ : Rouse model for linear chains, see eq 1.40. (Vector.) [kg m s ⁻²]	1
$\mathbf{g}_\ell(t)$	Random force acting on segment ℓ : Rouse model for linear chains, see eq 1.41. (Vector.) [kg m s ⁻²]	1
$g_{\ell\mu}(t)$	μ -component of the force $\mathbf{g}_\ell(t)$ at time t . [kg m s ⁻²]	1
$\mathbf{g}_p(t)$	Fourier transform of $\mathbf{g}_\ell(t)$ (See eq 1.45). [kg m s ⁻²]	1
$\mathbf{g}(\alpha, \ell, t)$	Random force acting on segment ℓ in arm α at time t : Rouse model for star polymers. (Vector.) [kg m s ⁻²]	2
$\mathbf{g}_p^c, \mathbf{g}_q^{s_i}$	Fourier transforms of $\mathbf{g}(\alpha, \ell, t)$. (See eqs 2.9.) [kg m s ⁻²]	2
$G(t)$	Stress relaxation modulus. [kg m ⁻¹ s ⁻²]	1
$G(t, \gamma)$	Non-linear stress relaxation modulus. [kg m ⁻¹ s ⁻²]	1
G_0	Elastic modulus of a perfectly elastic solid. [kg m ⁻¹ s ⁻²] G_0 is also the plateau modulus in the Maxwell model.	1, 4
G_{0_i}	Plateau modulus of the i th Maxwell mode. [kg m ⁻¹ s ⁻²] Plateau modulus of the i th pom-pom mode. [kg m ⁻¹ s ⁻²]	1 4
G_N^0	Plateau modulus in the tube model. [kg m ⁻¹ s ⁻²]	1
G', G''	Storage and loss moduli measured in SAOS. [kg m ⁻¹ s ⁻²]	1
G_γ	Propagator of block γ . (See eq 3.26a.)	3
$g(t)$	ETD function. (See eq 2.31.)	2, 3
H_γ	Coterm of block γ . (See eq 3.26b.)	3
h	Parameter in the overshoot model. (See eqs 4.3 and 4.4.)	4
h_s	Variable that controls the strength of the localising springs.	2
$h(\gamma)$	Damping function.	1
\mathbf{I}	Identity tensor.	1, 5
I_{abs}	Absolute scattering measured in experiments. [m ⁻¹]	1
$I_{coh}(q, t), I_{coh}(q)$	Dynamic and static coherent signal in NSE. [m ⁻¹]	1, 3
$I_{inc}(q, t), I_{inc}(q)$	Dynamic and static incoherent signal in NSE. [m ⁻¹]	1, 3
J_γ	Self-term of block γ . (See eq 3.26c.)	3
$\mathbf{K}(\mathbf{r}, t) = \mathbf{K}$	Velocity gradient tensor. [s ⁻¹]	1, 4, 5
k	Spring constant. [kg s ⁻²]	1-5
k_B	Boltzmann constant. [kg m ² s ⁻² K ⁻¹]	1-5

Symbol	Definition	Chapter
k_b	Parameter that equals N_s/N_e^2 . The value 1/4 is used.	2
	Spring constant of the pom-pom backbone. [kg s^{-2}]	5
k_p	Spring constant of mode p (linear polymers). [kg s^{-2}]	1
k_p^c	Spring constant of mode p of the cosine eigenmode. [kg s^{-2}]	2
k_q^{si}	Spring constant of mode q of the i th sine eigenmode. [kg s^{-2}]	2
$L(t), L$	Contour length of the PP at time t and equilibrium. [m]	1, 4
M_e	Entanglement molecular weight. [kg mol^{-1}]	1-5
M_w	Molecular weight of a chain. [kg mol^{-1}]	1-5
M_{w_a}	Arm molecular weight. [kg mol^{-1}]	1-5
M_{w_b}	Backbone molecular weight. [kg mol^{-1}]	1, 4
M_{w_c}	Critical molecular weight for entanglement in linear chains. [kg mol^{-1}]	1 1
$M_{w,L}$	Molecular weight of the long chains in bimodal blends of linear polymer melts. [kg mol^{-1}]	1
$M_{w,S}$	Molecular weight of the short chains. [kg mol^{-1}]	1
m_{mon}	Molar mass of a monomer. [kg mol^{-1}]	1, 3
N	Degree of polymerisation of a linear chain.	1
N_a	Degree of polymerisation of the arm.	1-5
N_D	Degree of polymerisation of the deuterated part of the arm.	3
N_D^*	Degree of polymerisation of the matrix linear chains.	3
N_e	Degree of polymerisation between entanglements.	1-5
N_H	Degree of polymerisation of the protonated part of the arm.	3
N_s	Degree of polymerisation of (virtual) anchoring chain.	2
N_{tot}	Total number of monomers in the system.	1, 3
n	Number of thin tube segments per fat tube segment.	5
n_c	Total number of chains in the system.	1,3
\mathbf{n}_s	Neutron spin. Vector (in classical mechanics). [$\text{kg m}^2 \text{s}^{-1}$]	1
$P(q, t)$	Normalised scattering signal in the NSE.	1, 3
Q_γ	Normalised wavevector for block γ .	3
\mathbf{q}	Scattering wavevector. [m^{-1}]	1, 3
$q = \mathbf{q} $	Magnitude of the scattering wavevector. [m^{-1}]	1, 3

Symbol	Definition	Chapter
q	Priority number, i.e. the number of arms emerging from each branch point of a pom-pom molecule.	1, 4
\mathbf{R}	End-to-end vector of a linear polymer chain. [m]	1
R_μ	μ -component of \mathbf{R} . [m]	1
$\mathbf{R}(s, t) = \mathbf{R}$	Position vector of a tube segment. [m]	5
\mathbf{R}_p	Fourier transform of $\mathbf{R}(s, t)$. [m]	5
\mathbf{R}	End-to-end vector of a fat tube segment. [m]	5
R_α	α -component of \mathbf{R} . [m]	5
\mathbf{R}_{pp}	End-to-end vector of the primitive path. [m]	1
$\mathbf{R}_{\alpha,\ell}$	Position vector of a localising spring. [m]	2
$\mathbf{R}_{\alpha,t}^e$	End-to-end vector of arm α of the star polymer. [m]	2
\mathbf{r}	End-to-end vector of a thin tube. [m]	5
r_α	α -component of \mathbf{r} . [m]	5
$\mathbf{r}_{\alpha,\ell,t}$	Position vector of segment ℓ in arm α at time t . [m]	2, 3
$\widehat{\mathbf{r}}_{\alpha,\ell}$	Position vector of segment ℓ in arm α on the mean path. [m]	2
$\mathbf{r}_\ell(t)$	Position vector of segment ℓ in a linear chain. [m]	1
\mathbf{S}	Orientation tensor of the primitive path.	1
	Orientation tensor of the backbone tube.	1, 4
$S_0^{AB}(q, t)$	The notation $S_0^{AB}(t)$ is used also. $S_0^{AB}(q, t) = n_c s_0^{AB}(q, t)$.	3
$S_0^{AB}(q)$	The notation S_0^{AB} is used also. Static counterpart of the correlation function $S_0^{AB}(q, t)$.	3
S_{cor}	See eq 3.29.	3
$S_{inc}(q, t)$	Dynamic incoherent scattering function (eq 1.32).	1, 3
$S^{tot}(q, t)$	Dynamic coherent scattering function (eq 1.30a).	1, 3
$S^{tot}(q)$	Static coherent scattering function (eq 1.30b).	1, 3
$s_0^{AB}(q, t)$	The notation $s_0^{AB}(t)$ is used also. Single chain structure factors. The labels A and B can each be either H or D .	3
$s_0^{AB}(q)$	The notation s_0^{AB} is used also. Static counterpart of $s_0^{AB}(q, t)$.	3
s_ℓ	Fractional coordinate that runs along an arm.	1, 2, 5
s	Tube coordinate. Spans the chain length of an arm.	2, 3
$s_{i\alpha}, s_{j\alpha}$	Numerical coefficients for the sine eigenmodes (eqs 2.6).	2

Symbol	Definition	Chapter
T	Temperature. [K]	1-3, 5
$T_{\mathbf{q}}^{AB}$	Correlation functions in the dynamic RPA. (See eq 3.36.)	3
\tilde{t}_e	Normalised time: t/τ_e .	1-3
$\tilde{t}_R, \tilde{t}_{R_a}$	Normalised times t/τ_R and t/τ_{R_a} .	1-3
$\mathbf{u}_\ell(t)$	Linear chain. Tangent unit vector at the ℓ th segment at time t .	1
$\mathbf{u}_{\alpha,\ell,t}$	Unentangled stars. Tangent unit vector at the ℓ th segment in arm α at time t .	2
$\mathbf{u}_{\alpha,s_\ell,t}$	Same as above for entangled stars.	2
W_R	Rouse rate given by $3k_B T/(\zeta_0 b^2)$. [s^{-1}]	3
w	Retraction rate in the overshoot model (eqs 4.10 and 4.11). [s^{-1}]	4
\tilde{w}	Retraction rate in the 1CR and the 2CR model. [s^{-1}]	5
\tilde{w}_t	Retraction rate for branch point withdrawal in the thin tube. [s^{-1}]	5
$\mathbf{X}_p(t)$	Linear chains. Normal mode p . Vector. (See eq 1.43a.) [m]	1
$\mathbf{X}_p^c(t)$	Unentangled stars. Normal mode p for the cosine eigenmode. Vector. [m]	2
$\mathbf{X}_q^{si}(t)$	Normal mode q for the i th sine eigenmode. Vector. [m]	2
$\mathbf{Y}_p^c(t)$	Entangled stars. Normal mode p for the cosine eigenmode. Vector. [m]	2
$\mathbf{Y}_q^{si}(t)$	Normal mode q for the i th sine eigenmode. Vector. [m]	2
Z	Entanglement length of a linear chain.	1
	Number of backbone-backbone entanglements at time t .	4
Z_w	Minimum number of surviving backbone entanglements.	4
Z_a	Number of arm entanglements (arm entanglement length).	1-5
Z_b	Number of backbone entanglements.	1-3, 5
Z_H	Entanglement length of the protonated part of the arm.	3
Z_D	Entanglement length of the deuterated part of the arm.	3
Z_D^*	Entanglement length of a deuterated matrix chain.	3
Z_L, Z_S	Entanglement length of the long and short chains.	1
Z_{fat}	Number of fat tube entanglements.	5
Z_{thin}	Number of thin tube entanglements.	5
Z_t	$Z_H + Z_D$.	3

Symbol	Definition	Chapter
α_d	Dilution exponent. Unity or 4/3.	1-3, 5
$\gamma, \dot{\gamma}$	Strain and strain rate in shear flow. $\dot{\gamma}$ has units of s^{-1} .	1, 5
γ	Index denoting blocks.	3
$\Delta_{\alpha,\ell,t}$	Fluctuation of the ℓ th segment in arm α about the mean path. [m]	2
$\Delta_{\alpha,s,t}$	$\Delta_{\alpha,\ell,t}$ expressed in tube coordinates. Vector. [m]	2
$\Delta \mathbf{r}^2$	Segmental mean square displacement. [m^2]	1, 2
$\Delta \rho_{\mathbf{q}}^A$	Fluctuations of the density variables $\rho_{\mathbf{q}}^A$ about the mean. Label A can be either H or D .	3
$\epsilon, \dot{\epsilon}$	Strain and strain rate in extensional flow. $\dot{\epsilon}$ has units of s^{-1} .	1, 4, 5
ζ_0	Friction coefficient of a bead (Rouse segment). [$kg\ s^{-1}$]	1, 2, 3
ζ_{bp}	Effective friction of a branch point. [$kg\ s^{-1}$]	1, 5
ζ_p	Friction coefficient of normal mode p . [$kg\ s^{-1}$]	2
$\eta(\dot{\gamma}, t)$	Viscosity in steady shear flow. [$kg\ m^{-1}\ s^{-1}$]	1, 5
$\eta^+(\dot{\epsilon}, t)$	Viscosity in steady (uniaxial) extensional flow. [$kg\ m^{-1}\ s^{-1}$]	1, 4, 5
η, η_0	Newtonian viscosity and zero shear viscosity. [$kg\ m^{-1}\ s^{-1}$]	1
λ	Wavelength of a neutron beam (section 1.3). [m^{-1}]	1
	Stretch of the pom-pom backbone.	1, 4, 5
λ_{fat}	Stretch of the fat tube.	5
λ_{thin}	Stretch of the thin tube.	5
$\nu, \nu(p)$	Constraint release rate in the 1CR and the 2CR model. [s^{-1}]	5
ν_{ef}	Effective CR rate for the fat tube. [s^{-1}]	5
ν_{fast}	CR rate for the thin tube. [s^{-1}]	5
ν_{slow}	CR rate for the fat tube. [s^{-1}]	5
$\Xi_{\alpha}(t)$	Tube survival probability of arm α .	2
ξ	Normalised coordinate for unentangled chains. Linear polymers $\xi = \ell/N$. Star polymers $\xi = \ell/N_a$.	1, 2
ρ	Polymer density. [$kg\ m^{-3}$]	1, 3
$\rho_{\mathbf{q}}$	Fourier transformed density variables in a homopolymer melt.	3
$\rho_{\mathbf{q}}^A$	Fourier transformed density variables at time t , for species A in a copolymer melt or blend. The label A can be either H or D .	3

Symbol	Definition	Chapter
σ	Polymer contribution to the stress. [$\text{kg m}^{-1} \text{s}^{-2}$]	1
	Stress of the pom-pom backbone. [$\text{kg m}^{-1} \text{s}^{-2}$]	1, 4, 5
$\sigma_{\mu\nu}$	Matrix elements of the σ tensor, i.e. the xx, xy, etc. coefficients of tensor σ in xyz coordinate system. [$\text{kg m}^{-1} \text{s}^{-2}$]	1, 4, 5
σ	Length unit in the MD simulations. [m]	1, 2, 3
τ	Terminal relaxation time in the Maxwell model. [s]	1
τ_a	Time taken for a complete arm retraction. [s]	1-5
τ_b	Orientation relaxation time. [s]	1-5
$\tau_{b,L}$	Orientation relaxation time of the long linear chains. [s]	1
$\tau_{b,S}$	Orientation relaxation time of the short linear chains. [s]	1
τ_{b0}/τ_{s0}	Ratio of the bare orientation and stretch relaxation times.	4
τ_e	Entanglement relaxation time. [s]	1-5
τ_{exp}	Timescale for the branch point to explore the width of the fat tube.[s]	5
τ_{eff}	Effective relaxation time for withdrawal of the branch point along the fat tube. [s]	5
τ_i	Terminal relaxation time of the i th Maxwell mode. [s]	1
τ_{obs}	Reptation timescale of the short chains. [s]	1
	Relaxation time of the fast relaxing arms. [s]	5
τ_p	Relaxation time of the p th mode. (See eq 1.44.) [s]	1
τ_p^c	Relaxation time of the p th mode of the cosine eigenmode. [s]	2
$\tau_q^{s_i}$	Relaxation time of the q th mode of the i th sine eigenmode. [s]	2
τ_{pre}	Timescale for shallow CLF of the arm. [s]	1, 5
τ_R	Rouse relaxation time of a linear chain. [s]	1
τ_{Ra}	Rouse relaxation time of the arm. [s]	2, 3
τ_{CR}	Constraint release relaxation time of a tube. [s]	1, 5
$\tau_{CR,f}$	CR relaxation time of the fat tube. [s]	5
$\tau_{CR,t}$	CR relaxation time of the hypothetical thin tube (eq 5.26). [s]	5
τ_s	Stretch relaxation time. [s]	1-5
τ_{s_ℓ}	Relaxation time of the s_ℓ -th arm segment from the MD. [s]	2
$\tau(s_\ell)$	Theoretical relaxation time of the s_ℓ -th arm segment. [s]	1, 5

Symbol	Definition	Chapter
τ_0	Segmental relaxation time. [s]	1, 3
τ_0^{MD}	Time unit in the MD simulations. [s]	1, 2, 3
$\Phi(x)$	Error function. (See table 2.2.)	2
$\varphi_{\mathbf{q}}^A$	Fourier transformed density variables at time zero, for species A in a copolymer melt or blend. The label A can be either H or D .	3
ϕ_L	Precession angle (eq 1.28). [rad]	1
	Volume fraction of long chains in a binary blend of linear chains.	5
$\phi(s_\ell)$	Fraction of unrelaxed arm material.	1
ϕ_a, ϕ_b	Pom-pom melt. Volume fractions of arm and backbone material.	1, 5
ϕ_H, ϕ_D	Volume fractions of protonated and deuterated material.	1, 3
χ	Flory interaction parameter.	3
Ψ	Fraction of surviving entanglements. (See eq 4.9.)	4
Ψ_w	Minimum fraction of surviving entanglements.	4
$\Psi_p^c(\ell)$	Cosine eigenmode. (See eq 2.5a.)	2
$\Psi_q^{s_i}(\alpha, \ell)$	i th sine eigenmode. (See eq 2.5b.)	2
$\psi_\ell^{R_{hc}}(t)$	Half correlator for the unentangled (Rouse) stars (2.14).	2
$\psi_\ell^{R_{ic}}(t)$	Full correlator for the unentangled (Rouse) stars (2.15).	2
$\Psi_{s_\ell}^{MD}(t)$	Full correlator for the entangled stars in the MD (eq 2.33).	2
$\psi(t)$	Tube survival probability.	1, 2, 3
$\langle \dots \rangle_{\varphi, 0}$	No EV interactions. Average over the annealed variables at $t' = 0$.	3
$\langle \dots \rangle_\varphi$	Average over the annealed variables at $t' = 0$. Accounts for EV interactions between the annealed variables at $t' = 0$.	3
$\langle \dots \rangle_{\rho, 0}$	No EV interactions. Average over the annealed variables at $t' = t$.	3
$\langle \dots \rangle_\rho$	Average over the annealed variables at $t' = t$. Accounts for EV interactions between the annealed variables at $t' = t$	3
$\overline{(\dots)}^0$	Average over the quenched variables in the non-interacting limit.	3
$\overline{(\dots)}$	Average over the quenched variables with EV interactions.	3

Bibliography

- [1] P. Bačová, L.G.D. Hawke, D.J. Read, and A.J. Moreno. Dynamics of branched polymers: A combined study by molecular dynamics simulations and tube theory. *Macromolecules*, 46(11):4633–4650, 2013.
- [2] T.C.B. McLeish. Tube theory of entangled polymer dynamics. *Advances in Physics*, 51(6):1379–1527, 2002.
- [3] M. Zamponi, W. Pyckhout-Hintzen, A. Wischnewski, M. Monkenbusch, L. Willner, G. Kali, and D. Richten. Molecular observation of branch point motion in star polymer melts. *Macromolecules*, 43(1):518–524, 2010.
- [4] A. Bach, H.K. Rasmussen, and O. Hassager. Extensional viscosity for polymer melts measured in the filament stretching rheometer. *Journal of Rheology*, 47(2):429–441, 2003.
- [5] H.K. Rasmussen, J.K. Nielsen, A. Bach, and O. Hassager. Viscosity overshoot in the start-up of uniaxial elongation of low density polyethylene melts. *Journal of Rheology*, 49(2):369–381, 2005.
- [6] D.M. Hoyle, Q. Huang, D. Auhl, D. Hassell, H.K. Rasmussen, A.L. Skov, O.G. Harlen, O. Hassager, and T.C.B. McLeish. Transient overshoot extensional rheology of long-chain branched polyethylenes: Experimental and numerical comparisons between filament stretching and cross-slot flow. *Journal of Rheology*, 57(1):293–313, 2013.
- [7] Q. Huang. *Molecular Rheology of Complex Fluids*. PhD thesis, Technical University of Denmark, 2013.

- [8] T.C.B. McLeish and R.G. Larson. Molecular constitutive equations for a class of branched polymers: The pom-pom polymer. *Journal of Rheology*, 42(1):81–110, 1998.
- [9] N.J. Inkson, T.C.B. McLeish, O.G. Harlen, and D.J. Groves. Predicting low density polyethylene melt rheology in elongational and shear flows with “pom-pom” constitutive equations. *The Journal of Rheology*, 43(4):873–896, 1999.
- [10] A.E. Likhtman, S.T. Milner, and T.C.B. McLeish. Microscopic theory for the fast flow of polymer melts. *Physical Review Letters*, 85(21):4550–4553, 2000.
- [11] S.T. Milner, T.C.B. McLeish, and A.E. Likhtman. Microscopic theory of convective constraint release. *Journal of Rheology*, 45(2):539–563, 2001.
- [12] R.S. Graham, A.E. Likhtman, T.C.B. McLeish, and S.T. Milner. Microscopic theory of linear, entangled polymer chains under rapid deformation including chain stretch and convective constraint release. *Journal of Rheology*, 47(5):1171–1200, 2003.
- [13] D.J. Read. Convective constraint release with chain stretch: Solution of the rouse-tube model in the limit of infinite tubes. *Journal of Rheology*, 48(2):349–377, 2004.
- [14] D. Auhl, P. Chambon, T.C.B. McLeish, and D.J. Read. Elongational flow of blends of long and short polymers: Effective stretch relaxation time. *Physical review letters*, 103(13):136001, 2009.
- [15] D.J. Read, K. Jagannathan, S.K. Sukumaran, and D. Auhl. A full-chain constitutive model for bidisperse blends of linear polymers. *Journal of Rheology*, 56(4):823–873, 2012.
- [16] K. Orfanou, H. Iatrou, D.J. Lohse, and N. Hadjichristidis. Synthesis of well-defined second (g-2) and third (g-3) generation dendritic polybutadienes. *Macromolecules*, 39(13):4361–4365, 2006.
- [17] L.R. Hutchings, S.M. Kimani, D.M. Hoyle, D.J. Read, C. Das, T.C.B. McLeish, T. Chang, H. Lee, and D. Auhl. In silico molecular design, synthesis,

- characterization, and rheology of dendritically branched polymers: Closing the design loop. *ACS Macro Letters*, 1(3):404–408, 2012.
- [18] F. Snijkers, K. Ratkanthwar, D. Vlassopoulos, and N. Hadjichristidis. Viscoelasticity, nonlinear shear start-up, and relaxation of entangled star polymers. *Macromolecules*, 46(14):5702–5713, 2013.
- [19] S. Agostini and L.R. Hutchings. Synthesis and temperature gradient interaction chromatography of model asymmetric star polymers by the macromonomer approach. *European Polymer Journal*, 49(9):2769 – 2784, 2013.
- [20] J.R. Fried. *Polymers in Aerospace Applications*. RAPRA review reports: RAPRA Technology Limited. iSmithers Rapra Publishing, 2010.
- [21] R. Stauber and L. Vollrath. *Plastics in Automotive Engineering: Exterior Applications*. Hanser Gardner Publications, 2007.
- [22] L.A. Sukhareva, V.S. Âkovlev, and O.A. Legonkova. *Polymers for Packaging and Containers in Food Industry*. New Concepts in Polymer Science. VSP, 2008.
- [23] S. Ebnesajjad. *Plastic Films in Food Packaging: Materials, Technology and Applications*. Plastics Design Library. Elsevier Science, 2012.
- [24] K. Cantor. *Blown Film Extrusion*. Hanser Gardner Publications, 2nd edition, 2011.
- [25] P.G. de Gennes. Reptation of a polymer chain in the presence of fixed obstacles. *Journal of Chemical Physics*, 55(2):572–579, 1971.
- [26] M. Doi and S.F. Edwards. *The Theory of Polymer Dynamics*. International series of monographs on physics. Oxford University Press, Oxford, 1st ed., 1986.
- [27] M. Doi. *Introduction to Polymer Physics*. Oxford Science Publications. Clarendon Press, Oxford, 1995.
- [28] M. Rubinstein and R.H. Colby. *Polymer Physics*. Oxford University Press, Oxford, 2003.
- [29] J.M. Dealy and R.G. Larson. *Structure and Rheology of Molten Polymers*. Hanser Gardner Publications, 2006.

- [30] F.A. Morrison. *Understanding Rheology*. Topics chemical engineering : A series of textbooks and monographs. Oxford University Press, 2001.
- [31] N. Phan-Thien. *Understanding Viscoelasticity: Basics of Rheology*. Advanced Texts in Physics. Springer, 2002.
- [32] P. Tapadia and S.Q. Wang. Nonlinear flow behavior of entangled polymer solutions: Yieldlike entanglement-disentanglement transition. *Macromolecules*, 37(24):9083–9095, 2004.
- [33] S.Q. Wang, Y. Wang, S. Cheng, X. Li, X. Zhu, and H. Sun. New experiments for improved theoretical description of nonlinear rheology of entangled polymers. *Macromolecules*, 46(8):3147–3159, 2013.
- [34] G.H. McKinley and T. Sridhar. Filament-stretching rheometry of complex fluids. *Annual Review of Fluid Mechanics*, 34:375–415, 2002.
- [35] P.P. Tas. *Film Blowing: from Polymer to Product*. PhD thesis, Eindhoven University of Technology, 1994.
- [36] R.I. Tanner. *Engineering Rheology*. Oxford University Press, Oxford, 2nd edition, 2000.
- [37] R.I. Tanner. A theory of die-swell revisited. *Journal of Non-Newtonian Fluid Mechanics*, 129(2):85–87, 2005.
- [38] R.G. Larson. *Constitutive Equations for Polymer Melts and Solutions*. Biotechnology Series. Butterworths, Boston, 1988.
- [39] J. Ramirez and A.E. Likhtman. Reptate: Rheology of entangled polymers, toolkit for analysis of theory and experiment. Developed at the University of Reading and at the University of Leeds. 2009. <http://www.reptate.com/>.
- [40] L.J. Fetters, A.D. Kiss, D.S. Pearson, G.F. Quack, and F.J. Vitus. Rheological behavior of star-shaped polymers. *Macromolecules*, 26(4):647–654, 1993.
- [41] T.C.B. McLeish, J. Allgaier, D.K. Bick, G. Bishko, P. Biswas, R. Blackwell, B. Blottire, N. Clarke, B. Gibbs, D.J. Groves, A. Hakiki, R.K. Heenan, J.M. Johnson, R. Kant, D.J. Read, and R.N. Young. Dynamics of entangled h-polymers:

- Theory, rheology, and neutron-scattering. *Macromolecules*, 32(20):6734–6758, 1999.
- [42] Suneel, R.S. Graham, and T.C.B. McLeish. Characterisation of an industrial polymer melt through either uniaxial extension or exponential shear data: An application of the pom-pom model. *Applied Rheology*, 13(1):19–25, 2003.
- [43] J. Meissner. Dehnungsverhalten von polyäthylen-schmelzen. *Rheologica Acta*, 10(2):230–242, 1971.
- [44] H.M. Laun and H. Münstedt. Comparison of the elongational behaviour of a polyethylene melt at constant stress and constant strain rate. *Rheologica Acta*, 15(10):517–524, 1976.
- [45] J. Meissner and J. Hostettler. A new elongational rheometer for polymer melts and other highly viscoelastic liquids. *Rheologica Acta*, 33(1):1–21, 1994.
- [46] J.S. Schulze, T.P. Lodge, C.W. Macosko, J. Hepperle, H. Münstedt, H. Bastian, D. Ferri, D.J. Groves, Y.H. Kim, M. Lyon, T. Schweizer, T. Virkler, E. Wassner, and W. Zoetelief. A comparison of extensional viscosity measurements from various rme rheometers. *Rheologica Acta*, 40(5):457–466, 2001.
- [47] H. Münstedt. New universal extensional rheometer for polymer melts. measurements on a polystyrene sample. *Journal of Rheology*, 23(4):421–436, 1979.
- [48] H. Münstedt, S. Kurzbeck, and L. Egersdörfer. Influence of molecular structure on rheological properties of polyethylenes. part ii. elongational behavior. *Rheologica Acta*, 37(1):21–29, 1998.
- [49] M. Sentmanat. Miniature universal testing platform: from extensional melt rheology to solid-state deformation behavior. *Rheologica Acta*, 43(6):657–669, 2004.
- [50] M. Sentmanat, B.N. Wang, and G.H. McKinley. Measuring the transient extensional rheology of polyethylene melts using the ser universal testing platform. *Journal of Rheology*, 49(3):585–606, 2005.

- [51] H. Münstedt and D. Auhl. Rheological measuring techniques and their relevance for the molecular characterization of polymers. *Journal of Non-Newtonian Fluid Mechanics*, 128(1):62–69, 2005.
- [52] H. Lentzakis, D. Vlassopoulos, D.J. Read, H. Lee, T. Chang, P. Driva, and N. Hadjichristidis. Uniaxial extensional rheology of well-characterized comb polymers. *Journal of Rheology*, 57(2):605–625, 2013.
- [53] M. Kolte, H.K. Rasmussen, and O. Hassager. Transient filament stretching rheometer. *Rheologica Acta*, 36(3):285–302, 1997.
- [54] M.R. Mackley, R.T.J. Marshall, and J.B.A.F. Smeulders. The multipass rheometer. *Journal of Rheology*, 39(6):1293–1309, 1995.
- [55] M.W. Collis and M.R. Mackley. The melt processing of monodisperse and polydisperse polystyrene melts within a slit entry and exit flow. *Journal of Non-Newtonian Fluid Mechanics*, 128(1):29–41, 2005.
- [56] N. Clemeur, R.P.G. Rutgers, and B. Debbaut. Numerical simulation of abrupt contraction flows using the double convected pom-pom model. *Journal of Non-Newtonian Fluid Mechanics*, 117(23):193–209, 2004.
- [57] N. Clemeur, R.P.G. Rutgers, and B. Debbaut. Numerical evaluation of three dimensional effects in planar flow birefringence. *Journal of Non-Newtonian Fluid Mechanics*, 123(23):105–120, 2004.
- [58] K.D. Coventry and M.R. Mackley. Cross-slot extensional flow birefringence observations of polymer melts using a multi-pass rheometer. *Journal of Rheology*, 52(2):401–415, 2008.
- [59] D.G. Hassell, D. Auhl, T.C.B. McLeish, and M.R. Mackley. The effect of viscoelasticity on stress fields within polyethylene melt flow for a cross-slot and contraction - expansion slit geometry. *Rheologica Acta*, 47(7):821–834, 2008.
- [60] D. Auhl, D.M. Hoyle, D. Hassell, T.D. Lord, O.G. Harlen, M.R. Mackley, and T.C.B. McLeish. Cross-slot extensional rheometry and the steady-state extensional response of long chain branched polymer melts. *Journal of Rheology*, 55(4):875–900, 2011.

- [61] D.G. Hassell, D. Hoyle, D. Auhl, O. Harlen, M.R. Mackley, and T.C.B. McLeish. Effect of branching in cross-slot flow: the formation of w cusps. *Rheologica Acta*, 48(5):551–561, 2009.
- [62] D.M. Hoyle. *Constitutive modelling of branched polymer melts in non-linear response*. PhD thesis, University of Leeds, 2011.
- [63] H.M. Laun and H. Schuch. Transient elongational viscosities and drawability of polymer melts. *Journal of Rheology*, 33(1):119–175, 1989.
- [64] V.F. Sears. Neutron scattering lengths and cross sections. *Physics Review*, 3(3):26–37, 1992.
- [65] B.J. Gabrys. *Applications of Neutron Scattering to Soft Condensed Matter*. Gordon and Breach Science Publishers, Amsterdam, 2000.
- [66] T. Imae, T. Kanaya, M. Furusaka, and N. Torikai. *Neutrons in Soft Matter*. Wiley, New Jersey, 2011.
- [67] R.M. Moon, T. Risse, and W.C. Koehler. Polarization analysis of thermal-neutron scattering. *Physical Review*, 181(2):920–931, 1969.
- [68] F. Mezei. *Neutron Spin Echo*. Lecture Notes in Physics Vol. 128, Springer, Berlin, 1980.
- [69] R. Gähler, R. Golub, K. Habicht, T. Keller, and J. Felber. Space-time description of neutron spin echo spectrometry. *Physica B*, 229(1):1–17, 1996.
- [70] D. Richter, M. Monkenbusch, A. Arbe, and J. Colmenero. Neutron spin echo in polymer systems. *Advances in Polymer Science*, 174:1–221, 2005.
- [71] P.E. Rouse. A theory of the linear viscoelastic properties of dilute solutions of coiling polymers. *J. Chem. Phys*, 21(7):1272–1280, 1953.
- [72] R.B. Bird, C.F. Curtiss, R.C. Armstrong, and O. Hassager. *Dynamics of Polymeric Liquids - Volume 2; Kinetic Theory*. John Wiley and Sons, New York, 1977.
- [73] G.C. Berry and T.G. Fox. The viscosity of polymers and their concentrated solutions. In *Fortschritte der Hochpolymeren-Forschung*, volume 5/3 of *Advances in Polymer Science*, pages 261–357. Springer Berlin Heidelberg, 1968.

- [74] R.H. Colby, L.J. Fetters, and W.W. Graessley. The melt viscosity-molecular weight relationship for linear polymers. *Macromolecules*, 20(9):2226–2237, 1987.
- [75] B.H. Zimm. Dynamics of polymer molecules in dilute solution: viscoelasticity, flow birefringence and dielectric loss. *Journal of Chemical Physics*, 24(2):269–278, 1956.
- [76] P. Ahlrichs, R. Everaers, and B. Dünweg. Screening of hydrodynamic interactions in semidilute polymer solutions: A computer simulation study. *Physical Review E*, 64(4):040501, 2001.
- [77] S. Onogi, T. Masuda, and K. Kitagawa. Rheological properties of anionic polystyrenes. i. dynamic viscoelasticity of narrow-distribution polystyrenes. *Macromolecules*, 3(2):109–116, 1970.
- [78] M. Fukuda, K. Osaki, and M. Kurata. Nonlinear viscoelasticity of polystyrene solutions. i. strain-dependent relaxation modulus. *Journal of Polymer Science: Polymer Physics Edition*, 13(8):1563–1576, 1975.
- [79] K. Osaki. On the damping function of shear relaxation modulus for entangled polymers. *Rheologica Acta*, 32(5):429–437, 1993.
- [80] M. Bercea, C. Peiti, B. Simionescu, and P. Navard. Shear rheology of semidilute poly(methyl methacrylate) solutions. *Macromolecules*, 26(25):7095–7096, 1993.
- [81] A.E. Likhtman and T.C.B. McLeish. Quantitative theory for linear dynamics of linear entangled polymers. *Macromolecules*, 35(16):6332–6343, 2002.
- [82] S.T. Milner and T.C.B. McLeish. Reptation and contour-length fluctuations in melts of linear polymers. *Physical Review Letters*, 81(3):725, 1998.
- [83] A. Wischnewski, M. Monkenbusch, L. Willner, D. Richter, A. E. Likhtman, T. C. B. McLeish, and B. Farago. Molecular observation of contour-length fluctuations limiting topological confinement in polymer melts. *Physical Review Letters*, 88(5):058301, 2002.
- [84] M. Zamponi, M. Monkenbusch, L. Willner, A. Wischnewski, B. Farago, and D. Richter. Contour length fluctuations in polymer melts: A direct molecular proof. *EPL (Europhysics Letters)*, 72(6):1039, 2005.

- [85] G. Marrucci and N. Grizzuti. Fast flows of concentrated polymers: Predictions of the tube model of chain stretching. *Gazzetta Chimica Italiana*, 118:179–185, 1988.
- [86] D.S. Pearson, A.D. Kiss, L.J. Fetters, and M. Doi. Flow-induced birefringence of concentrated polyisoprene solutions. *Journal of Rheology*, 33(3):517–535, 1989.
- [87] V. Tirtaatmadja and T. Sridhar. A filament stretching device for measurement of extensional viscosity. *Journal of Rheology*, 37(6):1081–1102, 1993.
- [88] X. Ye, R.G. Larson, C. Pattamaprom, and T. Sridhar. Extensional properties of monodisperse and bidisperse polystyrene solutions. *Journal of Rheology*, 47(2):443–468, 2003.
- [89] M.H. Wagner, S. Kheirandish, and O. Hassager. Quantitative prediction of transient and steady-state elongational viscosity of nearly monodisperse polystyrene melts. *Journal of Rheology*, 49(6):1317–1327, 2005.
- [90] M. Doi, W.W. Graessley, E. Helfand, and D.S. Pearson. Dynamics of polymers in polydisperse melts. *Macromolecules*, 20(8):1900–1906, 1987.
- [91] J.L. Viovy, M. Rubinstein, and R.H. Colby. Constraint release in polymer melts: tube reorganization versus tube dilation. *Macromolecules*, 24(12):3587–3596, 1991.
- [92] G. Marrucci. Dynamics of entanglements: A nonlinear model consistent with the cox-merz rule. *Journal of Non-Newtonian Fluid Mechanics*, 62(2-3):279–289, 1996.
- [93] D.W. Mead, R.G. Larson, and M. Doi. A molecular theory for fast flows of entangled polymers. *Macromolecules*, 31(22):7895–7914, 1998.
- [94] M. Zamponi, A. Wischniewski, M. Monkenbusch, L. Willner, D. Richter, A.E. Likhtman, G. Kali, and B. Farago. Molecular observation of constraint release in polymer melts. *Physical Review Letters*, 96(23):238302, 2006.
- [95] D.S. Pearson and E. Helfand. Viscoelastic properties of star-shaped polymers. *Macromolecules*, 17(4):888–895, 1984.

- [96] R.C. Ball and T.C.B. McLeish. Dynamic dilution and the viscosity of star polymer melts. *Macromolecules*, 22(5):1911–1913, 1989.
- [97] R.H. Colby and M. Rubinstein. Two-parameter scaling for polymers in solvents. *Macromolecules*, 23(10):2753–2757, 1990.
- [98] M. Rubenstein. Theoretical challenges in polymer dynamics. In T.C.B. McLeish, editor, *Theoretical Challenges in the Dynamics of Complex Fluids*, Nato Science Series E: (closed) Series, pages 21–52. Kluwer, 1997.
- [99] S.T. Milner and T.C.B. McLeish. Parameter-free theory for stress relaxation in star polymer melts. *Macromolecules*, 30(7):2159–2166, 1997.
- [100] D.M. Hoyle, O. G. Harlen, D. Auhl, and T. C. B. McLeish. Non-linear step strain of branched polymer melts. *Journal of Rheology*, 53(4):917–942, 2009.
- [101] C.D. Chodankar, J.D. Schieber, and D.C. Venerus. Evaluation of rheological constitutive equations for branched polymers in step shear strain flows. *Rheologica Acta*, 42(1-2):123–131, 2003.
- [102] R.J. Blackwell, T.C.B. McLeish, and O.G. Harlen. Molecular drag-strain coupling in branched polymer melts. *Journal of Rheology*, 44(1):121–136, 2000.
- [103] R.S. Graham, T.C.B. McLeish, and O.G. Harlen. Using the pom-pom equations to analyze polymer melts in exponential shear. *Journal of Rheology*, 45(1):275–290, 2001.
- [104] S.G. Kalogrianitis and J.W. van Egmond. Full tensor optical rheometry of polymer fluids. *Journal of Rheology*, 41(2):343–364, 1997.
- [105] W.M.H. Verbeeten, G.W.M. Peters, and F.P.T. Baaijens. Differential constitutive equations for polymer melts: The extended pom–pom model. *Journal of Rheology*, 45(4):823–843, 2001.
- [106] N. Clemeur, R.P. Rutgers, and B. Debbaut. On the evaluation of some differential formulations for the pom-pom constitutive model. *Rheologica Acta*, 42(3):217–231, 2003.

- [107] H.C. Öttinger. Thermodynamic admissibility of the pompon model for branched polymers. *Rheologica Acta*, 40(4):317–321, 2001.
- [108] K. Lee, M.R. Mackley, T.C.B. McLeish, T.M. Nicholson, and O.G. Harlen. Experimental observation and numerical simulation of transient “stress fangs” within flowing molten polyethylene. *Journal of Rheology*, 45(6):1261–1277, 2001.
- [109] K. Binder, editor. *Monte Carlo and Molecular Dynamics Simulations in Polymer Science*. Oxford University Press, New York, 1995.
- [110] J.M. Haile. *Molecular Dynamics Simulation: Elementary Methods*. A Wiley-Interscience publication. Wiley, New York, 1997.
- [111] D. Frenkel and B. Smit. *Understanding Molecular Simulation: From Algorithms to Applications*. Computational science series. Elsevier Science, 2001.
- [112] K. Kremer and G.S. Grest. Dynamics of entangled linear polymer melts: A molecular-dynamics simulation. *The Journal of Chemical Physics*, 92:5057, 1990.
- [113] Q. Zhou and R.G. Larson. Direct calculation of the tube potential confining entangled polymers. *Macromolecules*, 39(19):6737–6743, 2006.
- [114] Z. Wang, A.E. Likhtman, and R.G. Larson. Segmental dynamics in entangled linear polymer melts. *Macromolecules*, 45(8):3557–3570, 2012.
- [115] S.K. Sukumaran and A.E. Likhtman. Modeling entangled dynamics: Comparison between stochastic single-chain and multichain models. *Macromolecules*, 42(12):4300–4309, 2009.
- [116] R. Auhl, R. Everaers, G.S. Grest, K. Kremer, and S.J. Plimpton. Equilibration of long chain polymer melts in computer simulations. *The Journal of Chemical Physics*, 119(24):12718–12728, 2003.
- [117] D.J. Read. Calculation of scattering from stretched copolymers using the tube model: a generalisation of the rpa. *The European Physical Journal B*, 12(3):431–449, 1999.

- [118] D.J. Read. Calculation of scattering from stretched copolymers using the tube model: Incorporation of the effect of elastic inhomogeneities. *Macromolecules*, 37(13):5065–5092, 2004.
- [119] N. Clarke and T.C.B. Mcleish. The dynamic structure factor of a star polymer in a concentrated solution. *Macromolecules*, 26(19):5264–5266, 1993.
- [120] T.A. Vilgis and F. Boue. Brownian motion of chains and crosslinks in a permanently linked network: The dynamic form factor. *Journal of Polymer Science, Part B: Polymer Physics*, 26(11):2291–2302, 1988.
- [121] R.T. Deam and S.F. Edwards. The theory of rubber elasticity. *Philos. Trans. Roy. Soc. London Ser. A*, 280:317–353, 1976.
- [122] M. Warner and S.F. Edwards. Neutron scattering from strained polymer networks. *Journal of Physics A: Mathematical and General*, 11(8):1649–1655, 1978.
- [123] B. Mergell and R. Everaers. Tube models for rubber-elastic systems. *Macromolecules*, 34(16):5675–5686, 2001.
- [124] D.J. Read, K. Jagannathan, and A.E. Likhtman. Entangled polymers: Constraint release, mean paths, and tube bending energy. *Macromolecules*, 41(18):6843–6853, 2008.
- [125] J.H. Lee, L.J. Fetters, and L.A. Archer. Branch-point motion in asymmetric star polymers. *Macromolecules*, 38(10):4484–4494, 2005.
- [126] J.H. Lee, L.J. Fetters, and L.A. Archer. Stress relaxation of branched polymers. *Macromolecules*, 38(26):10763–10771, 2005.
- [127] Q. Zhou and R.G. Larson. Direct molecular dynamics simulation of branch point motion in asymmetric star polymer melts. *Macromolecules*, 40(9):3443–3449, 2007.
- [128] Y. Masubuchi, T. Yaoita, Y. Matsumiya, and H. Watanabe. Primitive chain network simulations for asymmetric star polymers. *Journal of Chemical Physics*, 134(19):194905, 2011.

- [129] B.H. Zimm and R.W. Kilb. Dynamics of branched polymer molecules in dilute solution. *Journal of Polymer Science*, 37:19–42, 1959.
- [130] H. Watanabe, H. Yoshida, and T. Kotaka. Model calculation for viscoelastic and dielectric relaxation functions of non-entangled star chains with arm length distribution. *Polymer Journal*, 22(2):153–161, 1990.
- [131] S.D. Anogiannakis, C. Tzoumanekas, and D.N. Theodorou. Microscopic description of entanglements in polyethylene networks and melts: Strong, weak, pairwise, and collective attributes. *Macromolecules*, 45(23):9475–9492, 2012.
- [132] J. Klein. Dynamics of entangled linear, branched, and cyclic polymers. *Macromolecules*, 19(1):105–118, 1986.
- [133] J. Qin, S.T. Milner, P.S. Stephanou, and V.G. Mavrantzas. Effects of tube persistence length on dynamics of mildly entangled polymers. *Journal of Rheology*, 56(4):707–723, 2012.
- [134] Y. Matsumiya, H. Watanabe, and K. Osaki. Comparison of dielectric and viscoelastic relaxation functions of cis-polyisoprenes: Test of tube dilation molecular picture. *Macromolecules*, 33(2):499–506, 2000.
- [135] H. Watanabe, Y. Matsumiya, E. Van Ruymbeke, D. Vlassopoulos, and N. Hadjichristidis. Viscoelastic and dielectric relaxation of a cayley-tree-type polyisoprene: Test of molecular picture of dynamic tube dilation. *Macromolecules*, 41(16):6110–6124, 2008.
- [136] S.F. Edwards. The theory of polymer solutions at intermediate concentrations. *Proceedings of the Physical Society (London)*, 88(2):265–280, 1966.
- [137] P.G. de Gennes. Theory of x-ray scattering by liquid macromolecules with heavy atom labels. *J. Physics France*, 31:235–238, 1970.
- [138] S. Panyukov and Y. Rabin. Statistical physics of polymer gels. *Physics Reports*, 269(1-2):1–131, 1996.
- [139] S. Panyukov and Y. Rabin. Polymer gels: Frozen inhomogeneities and density fluctuations. *Macromolecules*, 29(24):7960–7975, 1996.

- [140] S.V. Panyukov and I.I. Potemkin. Statics and dynamics of the “liquid-” and “solidlike” degrees of freedom in lightly cross-linked polymer networks. *Journal de Physique II*, 7(2):273–289, 1997.
- [141] M.G. Brereton and T.A. Vilgis. The random phase approximation for polymer melts with quenched degrees of variables. *J. Physics I France*, 2:581–598, 1992.
- [142] K.K. Müller-Nedebock, S.F. Edwards, and T.C.B. McLeish. Scattering from deformed polymer networks. *Journal of Chemical Physics*, 111(17):8196–8208, 1999.
- [143] L. Leibner. Theory of microphase separation in block copolymers. *Macromolecules*, 13(6):1602–1617, 1980.
- [144] T. Ohta and K. Kawasaki. Equilibrium morphology of block copolymer melts. *Macromolecules*, 19(10):2621–2632, 1986.
- [145] I.I. Potemkin and S.V. Panyukov. Microphase separation in correlated random copolymers: Mean-field theory and fluctuation corrections. *Physical Review E*, 57(6):6902–6912, 1998.
- [146] T. Araki, Q. Tran-Cong, and M. Shibayama. *Structure and properties of multiphase polymeric materials*. Marcel Dekker Inc., New York, 1998.
- [147] G.H. Fredrickson. *The Equilibrium Theory of Inhomogeneous Polymers*. Clarendon Press, Oxford, 2006.
- [148] M. Heinrich, W. Pyckhout-Hintzen, J. Allgaier, D. Richter, E. Straube, T.C.B. McLeish, A. Wiedenmann, R.J. Blackwell, and D.J. Read. Small-angle neutron scattering study of the relaxation of a melt of polybutadiene h-polymers following a large step strain. *Macromolecules*, 37(13):5054–5064, 2004.
- [149] D.J. Read. Mean field theory for phase separation during polycondensation reactions and calculation of structure factors for copolymers of arbitrary architecture. *Macromolecules*, 31(3):899–911, 1998.
- [150] A.E. Likhtman. Single-chain slip-link model of entangled polymers: simultaneous description of neutron spin-echo, rheology, and diffusion. *Macromolecules*, 38(14):6128–6139, 2005.

- [151] M. Gahleitner. Melt rheology of polyolefins. *Progress in Polymer Science*, 26(6):895–944, 2001.
- [152] R.A. Bubeck. Structure-property relationships in metallocene polyethylenes. *Materials Science and Engineering R: Reports*, 39(1):1–28, 2002.
- [153] D. Auhl, J. Stange, H. Münstedt, B. Krause, D. Voigt, A. Lederer, U. Lappan, and K. Lunkwitz. Long-chain branched polypropylenes by electron beam irradiation and their rheological properties. *Macromolecules*, 37(25):9465–9472, 2004.
- [154] C.J.S. Petrie and M.M. Denn. Instabilities in polymer processing. *AIChE Journal*, 22:209–236, 1976.
- [155] R.G. Larson. Instabilities in viscoelastic flows. *Rheologica Acta*, 31(3):213–263, 1992.
- [156] S.J. Park and R.G. Larson. Modeling the linear viscoelastic properties of metallocene-catalyzed high density polyethylenes with long-chain branching. *The Journal of Rheology*, 49(2):523–536, 2005.
- [157] C. Das, N.J. Inkson, D.J. Read, M.A. Kelmanson, and T.C.B. McLeish. Computational linear rheology of general branch-on-branch polymers. *The Journal of Rheology*, 50(2):207–234, 2006.
- [158] Bob : Branched on branched software. <http://sourceforge.net/projects/bob-rheology>.
- [159] D.J. Read, D. Auhl, C. Das, J. den Doelder, M. Kapnistos, I. Vittorias, and T.C.B. McLeish. Linking models of polymerization and dynamics to predict branched polymer structure and flow. *Science*, 333(6051):1871–1874, 2011.
- [160] H. Münstedt and H.M. Laun. Elongational behaviour of a low density polyethylene melt - ii. transient behaviour in constant stretching rate and tensile creep experiments. comparison with shear data. temperature dependence of the elongational properties. *Rheologica Acta*, 18(4):492–504, 1979.
- [161] J.K. Nielsen, H.K. Rasmussen, M. Denberg, K. Almdal, and O. Hassager. Nonlinear branch-point dynamics of multiarm polystyrene. *Macromolecules*, 39(25):8844–8853, 2006.

- [162] H.K. Rasmussen, A.L. Skov, J.K. Nielsen, and P. Laillé. Elongational dynamics of multiarm polystyrene. *Journal of Rheology*, 53(2):401–415, 2009.
- [163] M.H. Wagner and V.H. Roln-Garrido. Verification of branch point withdrawal in elongational flow of pom-pom polystyrene melt. *Journal of Rheology*, 52(5):1049–1068, 2008.
- [164] G. Marrucci and G. Ianniruberto. Interchain pressure effect in extensional flows of entangled polymer melts. *Macromolecules*, 37(10):3934–3942, 2004.
- [165] R.J. Blackwell, O.G. Harlen, and T.C.B. McLeish. Theoretical linear and nonlinear rheology of symmetric treelike polymer melts. *Macromolecules*, 34(8):2579–2596, 2001.
- [166] W.H. Press, S.A. Teukolsky, W.T. Vetterling, and B.P. Flannery. *Numerical Recipes in FORTRAN 77: The Art of Scientific Computing*. Cambridge University Press, Cambridge, 2nd edition, 1992.